Characterisation of the immune response to calcium phosphate particulates; implications for osteoarthritis and bone tissue engineering

Olwyn Mahon

B.A (Hons) Neuroscience

M.Sc. Immunology

A thesis submitted to

Trinity College Dublin

for the degree of

Doctor of Philosophy

Supervisor: Prof. Aisling Dunne

Co-Supervisor: Prof. Daniel Kelly

Molecular Immunology Group

School of Biochemistry and Immunology

Trinity College Dublin

2020

Declaration of Authorship

I declare that this thesis has not been submitted as an exercise for a degree at this or any other university and it is entirely my own work, except where otherwise stated. I agree to deposit this thesis in the University's open access institutional repository or allow the library to do so on my behalf, subject to Irish Copyright Legislation and Trinity College Library conditions of use and acknowledgement.

_____

Olwyn Mahon

Acknowledgements

Firstly, I would like to extend my sincere thanks to my supervisor Prof. Aisling Dunne who has been the most wonderful and encouraging mentor and friend. Thank you for your time and patience with me, always keeping me focused and pushing me to do my best. I could not have imagined having a better advisor and mentor for my time here.

I would also like to extend my profound thanks to my co-supervisor and mentor, Prof. Danny Kelly. I am sincerely grateful for the time you have invested in me, and your trust in me with this project. It has been an honour to learn from you over the years, and I greatly appreciate your input to this project. Few people are lucky enough to have a supervisor who is equal parts brilliant, knowledgeable and kind, but somehow I have been blessed with two.

I would also like to thank our collaborator Prof. Geraldine McCarthy for all her input and guidance over the years.

To all the past and present members of the Dunne lab who made the lab such a welcoming and enjoyable place to work. A particular thanks to Clare, Emma, Nicole and Sharee who patiently taught me how everything works during my first few years and always offered words of encouragement. Thanks to Glyn for always providing a source of entertainment and company in the office on the long experiment days. You have all, not only been ideal co-workers, but also brilliant friends throughout my time in the lab. Thanks to the current lab members, Hannah, Sinead, Eva and our newest member, Lianne, for all their support.

To all of the past and present Stevenson and McLoughlin lab members, thanks for making the lab such a friendly work environment. Thanks to Michelle and Simon who were always around for highly entertaining chats! Keenan and Orla, my original office huns, I couldn't have asked for better friends, both in and out of work. A special thanks to Eoin for his constant advice and support, whether it was about seahorse experiments or help with my never ending computer problems. I am extremely grateful to Stephen, I am very lucky to have had your constant support and friendship. Thank you so much for all you have taught me, and for continuing to be an excellent role model. I wish you all the best in your new position in UCD, you will be massively missed here. Thanks to Tracey for all your kind words and support throughout the last few years. Thanks to Emilio for all your encouraging words, advice and friendship over the last 2 years. Andrew, Jonah, Claudia and Mei, thank you for always providing such a friendly environment to work in and always making the time for a chat. Richard…… my knowledge of Muay thai and Rob Lipsett has certainly increased since meeting you. Thank you for being a great support and I know I can now parry, swivel or roundhouse my way out of anything.

A special thanks to Jenny and Alanna for their unwavering support and friendship. Whether I needed someone to celebrate with, or someone to vent to, I could always rely on you both.

Thanks to all the staff in TBSI, our tech support team Liam and Noel, who endured constant phone calls from me to come fix something in the lab. To Barry Moran for all his flow cytometry assistance and Gaby in the school office, who always knew when I needed tea and biscuits. A special thanks to everyone in the teaching lab, Glynis, Audrey, Martha, Brian, Edith, Trudy, Roisin and Bernie. All of you have supported me at some point during this PhD, your constant guidance, support, encouragement and positivity was much appreciated.

I would also like to acknowledge and extend my sincerest thanks to all members of TCBE whom have been a huge part of my journey. There's so many individuals to name but you all made the lab environment exciting and stimulating to work in, both academically and personally. Everyone was so willing to help or to share their knowledge. It has been a privilege to be part of this last for the last 4 year and watch so many wonderful people come and go. I am lucky to have made so many friends and memories for life. I would especially like to thank Jessie, Rossana, Pedro and Julia. I could not have asked for better people to share this journey with since starting together in 2015 with you all. Thank you for pushing me to try my hardest and always reminding me that the end was nearly in sight. A big thanks to Dave and Stan for all their help with this project and always answering my never-ending questions. Farhad, Ian, Ross, Pierluca and Kian, thanks for always being around for some fun and some office drinks. Delighted to be joining you in the 'lads only' office. Mathieu… mon amie, thank you for always making me try speak more french and finish the week with a nice Friday pint. Grace, you're a superstar! Thanks for being a non-stop support and always knowing when I needed a break.
To Sophia, whose friendship I value more than she knows. Thank you for your constant encouragement and making me feel like I can achieve anything. You were always there, whether I needed cheering up, or the occasional 'one' glass of wine!
To Alix and Robbie, who never minded me being their third wheel in their relationship. I am so lucky to have met you both on this journey.
I would also like to thank all my friends in particular Sinead K, Sinead McK, Kyle and Aoife, Rachel and Sorcha. You have been such a support group and I could not have asked for better friends.

I would finally like to thank my family whose unwavering support has made it possible for me to do this PhD. Their positive influence, insurmountable patience and encouragement has allowed me to arrive to this point. I am very grateful to my sister, Julia, who encouraged me throughout the challenges I have faced. Thanks for putting up

with my grumpiness over the last 4 years. I would like to thank my mum for giving me advice to overcome obstacles on this journey. Thanks for all your support, looking after me and making sure I'm always well fed. She always put my needs first and gave me the space and encouragement to explore what it was I wanted to do. To my Dad, who always encouraged me to take every opportunity that came my way and do whatever truly made me happy. I love you all dearly and hope I have made you all proud. I dedicate my thesis to them.

Abstract

Early trauma, resulting in focal areas of cartilage damage with injury to the underlying subchondral bone (osteochondral damage) often progresses to arthritis. These so called osteochondral defects (OCDs) can arise from an acute traumatic injury to the knee or an underlying disorder of the bone. If left untreated, localised OCDs can become widespread and often progress to more severe damage, as is the case in Osteoarthritis (OA). It is now widely accepted that cartilage damage in OA is associated with inflammation and a number of 'damage' or 'danger' associated molecules have been identified that contribute to this phenotype. They include hyaluronic acid fragments, basic calcium phosphate (BCP) crystals and members of the S100 family of proteins. As joint damage progresses, total joint replacement (TJR) is required to relieve pain and restore joint function, however TJRs themselves are associated with long-term complications such as periprosthetic osteolysis (PO) which is driven by implant-derived wear debris particles that are generated over time causing inflammation and eventual implant failure. With this in mind, efforts are underway to **(i)** improve the biocompatibility and durability of orthopaedic implants and **(ii)** to develop tissue engineering strategies that can repair early osteochondral damage, before OA progresses. The most promising approach is to develop biomaterial scaffolds that promote self-repair and regeneration of damaged tissue. However, as with traditional implant materials, tissue engineered constructs can also impact host immune responses and it has become increasingly apparent that engineering a pro-regenerative immune response following scaffold implantation is integral to functional tissue regeneration.

This study aimed to investigate the direct effects of endogenous and exogenous calcium phosphate particulates in human macrophages. These particulates include OA-associated BCP crystals and hydroxyapatite (HA), which is commonly used as a coating for orthopaedic implants and bone tissue engineering applications. The data presented here demonstrates that BCP crystals drive pro-inflammatory M1 macrophage polarization and metabolic reprogramming, causing cells to derive energy from glycolysis rather than oxidative phosphorylation, a phenomenon that is emerging as a key regulator of macrophage phenotype. This study therefore, not only provides further insight into how OA-associated DAMPs impact on immune cell function, but also

highlights metabolic reprogramming as a potential therapeutic target for calcium crystal-related arthropathies.

This study also examined the specific signalling pathways activated by wear particles in primary human macrophages. As was the case for BCP crystals, HA and PMMA (i.e. bone cement) particles were found to drive M1 macrophage polarization and this was shown to be dependent on activation of the membrane proximal kinase, Spleen Tyrosine Kinase (Syk), in addition to members of the mitogen-activated protein kinase (MAPK) family of signalling molecules. Pre-treatment of macrophages with Syk or MAPK inhibitors, not only prevented macrophage polarization, but also attenuated production of key pro-inflammatory mediators that have been specifically implicated in periprosthetic osteolysis and osteoclast differentiation. While further investigation is required, this study identifies these molecules as potential therapeutic targets to treat, or possibly prevent wear debris induced inflammation.

Finally, an immune modulating scaffold for bone defect healing containing nanoHA particles was developed. In contrast to micron sized HA particles, the in-house generated nano particles were shown to preferentially polarize human macrophages towards an M2 phenotype. Furthermore, nano-particle-mediated IL-10 induction by macrophages resulted in enhanced mesenchymal stem cell (MSC) osteogenesis *in vitro*, demonstrating for the first time, a direct pro-osteogenic role for this cytokine. Implantation of particle-functionalised scaffolds into a rat femoral defect resulted in a more anti-inflammatory, pro-regenerative phenotype at the site of implantation, compared to the pro-inflammatory, fibrotic environment observed with micron-HA functionalised scaffolds. The anti-inflammatory response induced by nanoHA particles also correlated with enhanced tissue vascularisation and increased bone repair demonstrating that nano HA particles have inherent immune-modulatory properties.

Overall, this study demonstrates that a greater understanding of the immune response to particulate matter generated from endogenous processes in the joint, or from biomaterial implants is required. This may allow for the identification of novel therapeutic targets for joint-associated inflammation or for the development of superior implant materials that can ultimately be used to improve the bone tissue repair and regeneration process in a disease that is becoming steadily more prevalent as the aging population increases.

Publications

Mahon, O.R., Browe, D. C., Gonzalez-Fernandez, T., Pitacco, P., Von Euw, S., Cunningham, K. T., Mills, K.H.G., D. J. Kelly, and A. Dunne. Nano-particle mediated M2 macrophage polarization enhances bone formation and MSC osteogenesis in an IL-10 dependent manner. *Biomaterials* **239**:119833 **(2020).**
Doi: 10.1016/j.biomaterials.2020.119833

Mahon, O.R., G. M. McCarthy., D.J Kelly., A. Mahon, O.R., G. M. McCarthy., D.J Kelly., A. Dunne. Osteoarthritis-associated basic calcium phosphate crystals alter immune cell metabolism and promote M1 macrophage polarization. *Osteoarthritis and Cartilage* (in press) **(2020)**
Doi: 10.1016/j.joca.2019.10.010

Browe, D. C., **Mahon, O.R**., A. Dunne, C. T. Buckley, and D. J. Kelly. Glyoxal cross-linking of solubilised extracellular matrix to produce highly porous, elastic and chondro-permissive scaffolds for orthopaedic tissue engineering. *J Biomed Mater Res A.* **107:**2222-2234 **(2019)**

Silveira, A. A. A.,* **Mahon, O. R.,*** C. C. Cunningham, E. M. Corr, R. Mendonça, S. T. O. Saad, F. F. Costa, A. Dunne, and N. Conran. S100A8 acts as an autocrine priming signal for heme-induced human Mϕ pro- inflammatory responses in hemolytic inflammation. J*. Leukoc. Biol.* 1–9 **(2019)**
*Equal contribution

Mahon, O. R., S. O'Hanlon, C. C. Cunningham, G. M. McCarthy, C. Hobbs, V. Nicolosi, D. J. Kelly, and A. Dunne. Orthopaedic implant materials drive M1 macrophage polarization in a spleen tyrosine kinase and mitogen-activated protein kinase-dependent manner. *Acta Biomater*. **65**: 426–435 **(2018)**

Mahon, O. R., and A. Dunne. Disease-associated particulates and joint inflammation; mechanistic insights and potential therapeutic targets. *Front. Immunol.* **9**: 1–8 **(2018)**

Cunniffe, G. M., P. J. Díaz-Payno, E. J. Sheehy, S. E. Critchley, H. V. Almeida, P. Pitacco, S. F. Carroll, **Mahon, O.R.**, A. Dunne, T. J. Levingstone, C. J. Moran, R. T. Brady, F. J. O'Brien, P. A. J. Brama, and D. J. Kelly. Tissue-specific extracellular matrix scaffolds for the regeneration of spatially complex musculoskeletal tissues. *Biomaterials* **188:** 63–73 **(2018)**

Cunniffe, G. M., P. J. Diaz-Payno, J. S. Ramey, **Mahon, O.R.,** A. Dunne, E. M. Thompson, F. J. O'Brien, and D.J. Kelly. Growth plate extracellular matrix-derived scaffolds for large bone defect healing. *Eur. Cell.Mater*. **33**: 130–142 **(2017)**

Browe, D. C., **Mahon, O.R.,** Díaz-Payno, P.J., Dunne, A., Moran, C.J., Buckley. C. T. and Kelly. D.J. A Method to rapidly isolate Chondro-progenitor cells from Infrapatellar Fat Pad Tissue for Single-Stage Cartilage Regeneration Strategies. American Journal of Sports Medicine (manuscript submitted)

Mahon, O.R.,* Browe, D. C.,* Díaz-Payno, P.J., Kelly. D.J. and Dunne, A., ECM scaffolds derived from diverse tissue sources differentially influence macrophage and Mesenchymal stem cell phenotype (manuscript in preparation).
*Equal contribution

Conference Proceedings

Bioengineering in Ireland, 26th Annual Conference, January 2020, Carlow, Ireland. **Olwyn R. Mahon,** Browe, D.C., Von Euw, S., Kelly, D.J. and Dunne, A. **Oral Presentation** - Engineering immunomodulating scaffold for bone tissue regeneration

Irish Society for Immunology, September 2019, Dublin, Ireland. **Olwyn R. Mahon**, Browe, D.C., Gonzalez-Fernandez, T, Pitacco, P., Kelly, D.J. and Dunne, A. **Poster Presentation -** Nanoparticle mediated metabolic reprogramming and M2 macrophage polarization enhances bone formation and mesenchymal stem cell osteogenesis in an IL-10 dependent manner.

Trinity Biomedical Sciences Institute research symposium, September 2019, Trinity College Dublin. **Olwyn R. Mahon,** Browe, D.C., Gonzalez-Fernandez, T, Pitacco, P., Kelly, D.J. and Dunne, A. **Poster Presentation -** Engineering immunomodulating scaffolds by modulating particle size.

Tissue Engineering and Regenerative Medicine International Society, May 2019, Rhodes, Greece. **Olwyn R. Mahon**, Browe, D.C., Gonzalez-Fernandez, T, Pitacco, P., Kelly, D.J. and Dunne, A. **Oral Presentation -** Engineering immunomodulating scaffolds by modulating particle size.

Bioengineering in Ireland, 25th Annual Conference, January 2019, Limerick, Ireland. **Olwyn R. Mahon,** Browe, D.C., Gonzalez-Fernandez, T, Pitacco, P., Kelly, D.J. and Dunne, A. **Oral Presentation** - Engineering immunomodulating scaffolds by modulating particle size.

Irish Society for Immunology, September 2018, Dublin, Ireland. **Olwyn R. Mahon**, Browe, D.C., Gonzalez-Fernandez, T, Pitacco, P., Kelly, D.J. and Dunne, A. **Poster Presentation -** The relationship between hydroxyapatite particles size and macrophage polarization: implications for biomaterial design strategies.

TERMIS World Congress, September 2018, Kyoto, Japan. **Olwyn R. Mahon** , Browe, D.C., Gonzalez-Fernandez, T, Pitacco, P., Kelly, D.J. and Dunne, A. **Poster Presentation -** Immune modulating scaffolds for bone tissue engineering.

7th International Conference on Osteoimmunology: Interactions of the Immune and Skeletal Systems, May 2018, Chania, Greece. **Olwyn R. Mahon**, Browe, D.C., Gonzalez-Fernandez, T, Pitacco, P., Kelly, D.J. and Dunne, A. **Poster Presentation-** Immune modulating scaffolds for bone tissue engineering.

World Congress of Biomechanics, July 2018, Dublin, Ireland. **Olwyn R. Mahon**, Browe, D.C., Gonzalez-Fernandez, T, Kelly, D.J. and Dunne, A. **Poster Presentation -** Macrophage phenotype and innate immune cytokines influence the osteogenic differentiation of mesenchymal stem cells.

Bioengineering in Ireland, 24th Annual Conference, January 2018, Meath, Ireland. **Olwyn R. Mahon**, Browe, D.C., Gonzalez-Fernandez, T, Kelly, D.J. and Dunne, A. **Oral Presentation -** Macrophage phenotype and innate immune cytokines influence the osteogenic differentiation of mesenchymal stem cells.

Matrix Biology 4th Annual meeting, November, 2017 Dublin, Ireland. **Olwyn R. Mahon**, Browe, D.C., Gonzalez-Fernandez, T, Kelly, D.J., McCarthy, G and Dunne, A. Matrix Biology 4th Annual meeting, November, 2017 Dublin, Ireland. **Oral Presentation -** Assessment of the immune response to extracellular matrix derived implant materials.

American College of Rheumatology Annual Meeting, November 2017, San Diego, California, USA**. Olwyn R. Mahon**, McCarthy, G, O'Hanlon, S, Gonzalez-Fernandez, T, Kelly, D.J., and Dunne, A. **Oral Presentation -** Osteoarthritis-Associated Calcium-Containing Crystals and Biomaterial Microparticles Both Drive M1 Macrophage Polarization in a Syk and MAP Kinase-Dependent Manner.

Irish Society for Immunology, September 2017, Dublin, Ireland. **Olwyn R. Mahon**, Gonzalez-Fernandez, T, Kelly, D.J., McCarthy, G and Dunne, A. **Poster Presentation -** Generating an M2 pro-regenerative macrophage phenotype using nanoHA particles for bone tissue engineering.

Tissue Engineering and Regenerative Medicine International Society, June 2017, Davos, Switzerland. **Olwyn R. Mahon**, Tomas Gonzalez-Fernandez, Daniel J. Kelly, Geraldine McCarthy and Aisling Dunne. **Oral Presentation -**Generating an M2 pro-regenerative macrophage phenotype using nanoHA particles for bone tissue engineering.

Bioengineering in Ireland, 23rd Annual Conference, January 2017, Belfast, Ireland. **Olwyn R. Mahon,** Tomas Gonzalez-Fernandez, Daniel J. Kelly, Geraldine McCarthy and Aisling Dunne. **Oral Presentation -** Generating an M2 pro-regenerative macrophage phenotype using nanoHA particles for bone tissue engineering.

British Society for Immunology, December 2016 Liverpool. **Olwyn R. Mahon**, Tomas Gonzalez-Fernandez, Daniel J. Kelly, Geraldine McCarthy and Aisling Dunne. **Poster presentation -** Orthopaedic wear debris-associated particulates drive pro-inflammatory gene expression and cytokine production in primary human macrophages.

Irish Society for Immunology, September 2016 Cork. **Olwyn R. Mahon**, Tomas Gonzalez-Fernandez, Daniel J. Kelly, Geraldine McCarthy and Aisling Dunne. **Oral presentation -** Orthopaedic wear debris-associated particulates drive pro-inflammatory gene expression and cytokine production in primary human macrophages and dendritic cells.

Awards

January 2020: Finalist for the Engineers Ireland Biomedical research medal (26th Annual Conference of the Section of Bioengineering of Royal Academy of Medicine in Ireland)

September 2019: 2nd Place poster presentation (Trinity Biomedical Sciences Institute Research Symposium)

September 2018: Best poster presentation (Irish Society for Immunology)

May 2018: 1,000 euro Travel award (7th International Conference on Osteoimmunology)

September 2018: Tebu-Bio Travel Grant (400 euro)

November 2017: Best podium presentation (4th annual Matrix Biology Ireland Conference)

Abbreviations

2-DG	2-deoxy-D-glucose
AC	Articular cartilage
ATP	Adenosine Triphosphate
ANG1	Angiopoetin 1
APC	Antigen Presenting Cell
ATP	Adenosine Triphosphate
BCP	Basic Calcium Phosphate
BSA	Bovine Serum Albumin
BMDC	Bone Marrow Derived Dendritic Cell
BMDM	Bone Marrow Derived Macrophage
CD	Cluster of differentiation
DAMP	Danger Associated Molecular Pattern
DAPI	4',6-diamidino-2-phenylindole
DC	Dendritic cell
DMEM	Dulbecco's Modified Eagle's Medium
DMOAD	Disease Modifying Osteoarthritic Drug
DMOG	Dimethyloxallyl Glycine
DMSO	Dimethyl sulfoxide
DNA	Deoxyribonucleic Acid
DTT	Dithiothreitol
DQ-Ova	DQ Ovalbumin
ECM	Extracellular matrix
ERK	Extracellular signal-Regulated Kinase
FCS	Foetal calf serum
ECL	Enhanced Chemiluminescent HRP Substrate
EDTA	Ethylenediaminetetraacetic acid
ELISA	Enzyme-Linked Immunosorbent Assay
ER	Endoplasmic Reticulum
ETC	Electron Transport Chain

FBS	Foetal Bovine Serum
FCCP	Carbonyl cyanide-4-(trifluoromethoxy)phenylhydrazone
FMO	Fluorescence-Minus-One
FOXP3	Forkhead Box P3
FSC	Forward Scatter
GAGs	Glycosaminoglycans
GM-CSF	Granulocyte-Monocyte Colony-Stimulating Factor
HA	Hydroxyapatite
HIF1α	Hypoxia Inducible Factor 1α
HSLB	High Stringency Lysis Buffer
IκB	Inhibitor of κB
IKK	IκB Kinase
IL	Interleukin
LPS	Lipopolysaccharide
MACS	Magnetic-Activated Cell Sorting
MAPK	Mitogen Activated Protein Kinase
MHC	Major Histocompatibility Complex
MFI	Mean Fluorescence Intensity
MMP	Matrix Metalloproteinase
MS	Multiple Sclerosis
mTOR	Mammalian Target of Rapamycin
NADPH	Nicotinamide Adenine Dinucleotide Phosphate-Oxidase
NET	Neutrophil Extracellular Trap
NF-κB	Nuclear Factor κB
NLR	NOD-like receptor
NO	Nitric Oxide
OA	Osteoarthritis
OCDs	Osteochondral Defects
OCP	Osteoclast Precursor
OCR	Oxygen Consumption Rate
OPG	Osteoprotegrin
PAMP	Pathogen Associated Molecular Pattern

PBMC	Peripheral Blood Mononuclear Cell
PBS	Phosphate Buffered Saline
PFA	Paraformaldehyde
PI3K	Phosphatidylinositol-3 Kinase
PMA	Phorbol 12-myristate 13-acetate
PRR	Pattern Recognition Receptor
PVDF	Polyvinylidene difluoride
RA	Rheumatoid Arthritis
RNA	Ribonucleic Acid
ROS	Reactive Oxygen Species
RPMI	Roswell Park Memorial Institute
SD	Standard Deviation
SEM	Standard Error of the Mean
siRNA	Small Interfering RNA
SLE	Systemic Lupus Erythematosus
SRC	Spare Respiratory Capacity
SSC	Side Scatter
TCA	Tricarboxylic acid
TCR	T cell Receptor
TGF β	Transforming Growth Factor β
Th cell	T-Helper Cell
TIMP	Tissue inhibitors of MMPs
TIR	Toll/Interleukin 1 Receptor
TJA	Total Joint Arthroplasty
TLR	Toll-Like Receptor
Treg	Regulatory T Cell
GP	Growth Plate
HA	Hydroxyapatite
IFN	Interferon
IL	Interleukin
LPS	Lipopolysaccharide
MAPK	Mitogen Activated Protein Kinase

MATS	Membrane Affinity-Triggered Signalling
M-β-CD	Methyl-β-cyclodextrin
M-CSF	Macrophage Colony Stimulating Factor
mg	milligram
ml	millilitre
mM	millimolar
MMP	Matrix metalloproteinase
Mo	Monocyte-derived
MSCs	Mesenchymal stem/stromal cell
ng	nanogram
NLRP3	NOD-like receptor family, pyrin domain containing 3
OA	Osteoarthritis
OC	Osteoclast
OCP	Osteoclast Precursor
OPG	Osteoprotegrin
PBMC	Peripheral Blood Mononuclear Cell
PBS	Phosphate Buffer Saline
PFA	Paraformaldehyde
pg	Picogram
PGE	Prostaglandin E
PMMA	Polymethyl methacrylate
PO	Periprosthetic Osteolysis
RANK	Receptor activator or NF-κB
RANKL	Receptor activator of NF-κB ligand
ROS	Reactive Oxygen Species
SDS	Sodium dodecyl sulphate
Syk	Spleen Tyrosine Kinase
TJA	Total Joint Arthroplasty
TNF	Tumour necrosis factor
TRAP	Tartrate Resistant acid Phosphatase
UHMWPE	Ultrahigh molecular weight polyethylene
VEGF	Vascular Endothelial Growth Factor

µg	microgram
µM	microMolar

Table of contents

Chapter 1: Introduction

1.1 Osteoarthritis

Osteoarthritis (OA), or degenerative arthritis is the most prevalent form of arthritis and can affect one or more joints in the body. 9.6 % of men and 18% of women over the age of 60 suffer from OA (1). Patients generally present with pain, stiffness and loss of joint mobility and the disease is most common in, but not restricted to, knee and hip joints. The principal risk factors are age, obesity, joint injury and repetitive physical activities that put strain on the joints (2). The principle pathological changes are progressive cartilage degradation, synovitis and subchondral bone remodelling which are accompanied by increased bone turnover and the formation of bony growths or projections along the joint margin known as osteophytes (Figure 1.1) (2). While OA is often regarded as merely a disease of the cartilage, it should be noted that the synovium contributes considerably to disease pathology, with synovial activation and inflammation, known as synovitis, observed in up to 50 % of patients at any stage of disease progression (3).

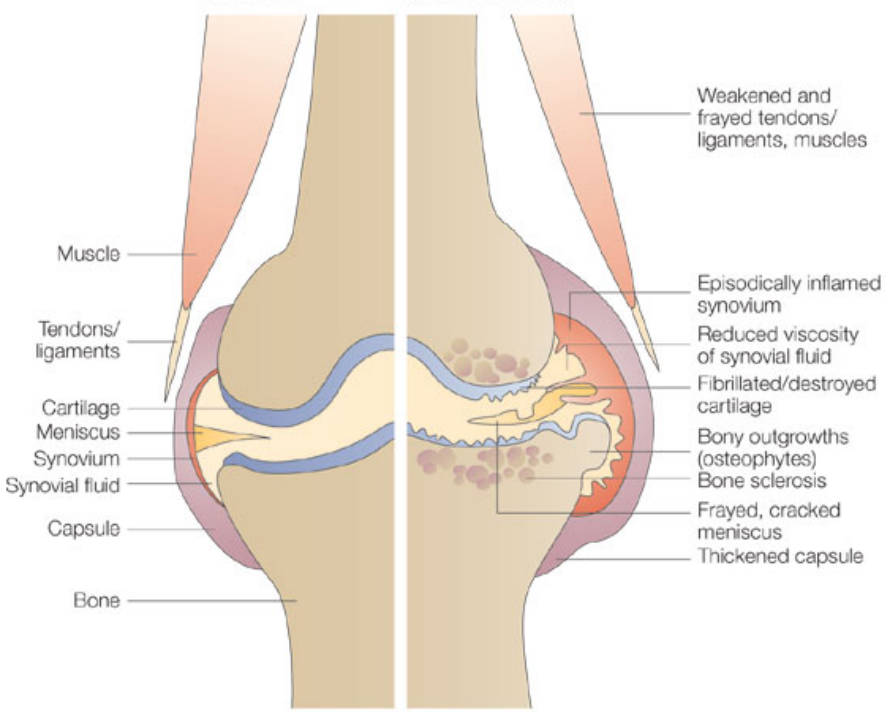

Figure 1.1 Healthy versus osteoarthritic joint. Left: Healthy joint with normal cartilage and no synovial inflammation. Right: Osteoarthritic joint with inflamed synovium, fibrillated cartilage, osteophytes and bone sclerosis. Image adapted from (4).

While it is unclear how damage to the joint is initiated in OA, early trauma resulting in focal areas of cartilage damage with injury to the underlying subchondral bone (osteochondral damage) often progresses to arthritis. These so called osteochondral defects (OCDs) can arise from an acute traumatic injury to the knee or an underlying disorder of the bone. If left untreated, localised OCDs can become widespread and often progress to more severe damage, as is the case in OA. Additionally, hyaline cartilage degradation, which is a central disease motif is understood to be triggered by altered chondrocyte metabolism and dysregulated homeostasis between the catabolic effects of the myeloid lineage bone resorptive cells (osteoclasts) and the anabolic mesenchymal cells (osteoblasts) which promote the formation of bone (5).

Articular cartilage and underlying bone are very different tissues in their make-up and structure within the synovial joint (Figure 1.2). This architecture allows for synovial joints to function correctly and achieve movement at the point of contact of the articulating bones. In healthy joints, the epiphysis of bone is covered with a thin layer of strong, smooth articular cartilage. A very thin layer of viscous joint fluid, called synovial fluid, separates and lubricates the two cartilage-covered bone surfaces. A thin synovial membrane encapsulates the joint surfaces and is responsible for the production of synovial fluid. The function of the articular cartilage and synovial fluid is to provide a lubricated, smooth surface that can both reduce and transfer biomechanical loads onto the subchondral bone beneath. Articular cartilage is a specialized tissue that consists of a solid matrix phase and an interstitial fluid phase. The solid matrix phase consists of proteoglycans and type II collagen. Sulphated glycosaminoglycans (sGAGs) in the proteoglycan are hydrophillic, negatively charged macromolecules, which attract water into the tissue causing an osmotic swelling pressure and also produce a repulsive force. These forces are balanced by a dense mesh of collagen fibres restricting the proteoglycans (6). Articular cartilage has a hierarchical zonal structure consisting of superficial, middle and deep zones (7). Articular cartilage is extensively damaged in OA and is the most obvious pathological feature prior to joint dysfunction. Chondrocytes are the cells responsible for the synthesis and maintenance of cartilage through a process called chondrogenesis (5). Under normal physiological conditions chondrocytes maintain a low turnover rate of cartilage matrix production (2), however homeostatic

changes can result in functional abnormality of chondrocytes and phenotypic shifts that result in articular cartilage damage leading to disease initiation and progression. Furthermore, chondrocyte apoptosis has been shown to be elevated in OA joints, leading to limited cartilage repair and reduced matrix deposition by chondrocytes post disease initiation (2).

Typically, the underlying bone is divided into two layers: subchondral bone plate and subarticular spongiosa, confining the bone marrow. Given the limited capacity of articular cartilage to self-repair (due to its avascular nature), extensive loss of the hyaline cartilage at the surface occurs and therefore the underlying subchondral bone can become extensively damaged. Subchondral bone remodelling involving subchondral plate thickening, formation of bony projections (osteophytes) and development of bone cysts occurs (8, 9). While cartilage damage is thought to the initial event in OA, animal models of OA in addition to human clinical data have demonstrated that enhanced subchondral bone turnover may impact cartilage metabolism (10, 11) thereby propagating disease progression.

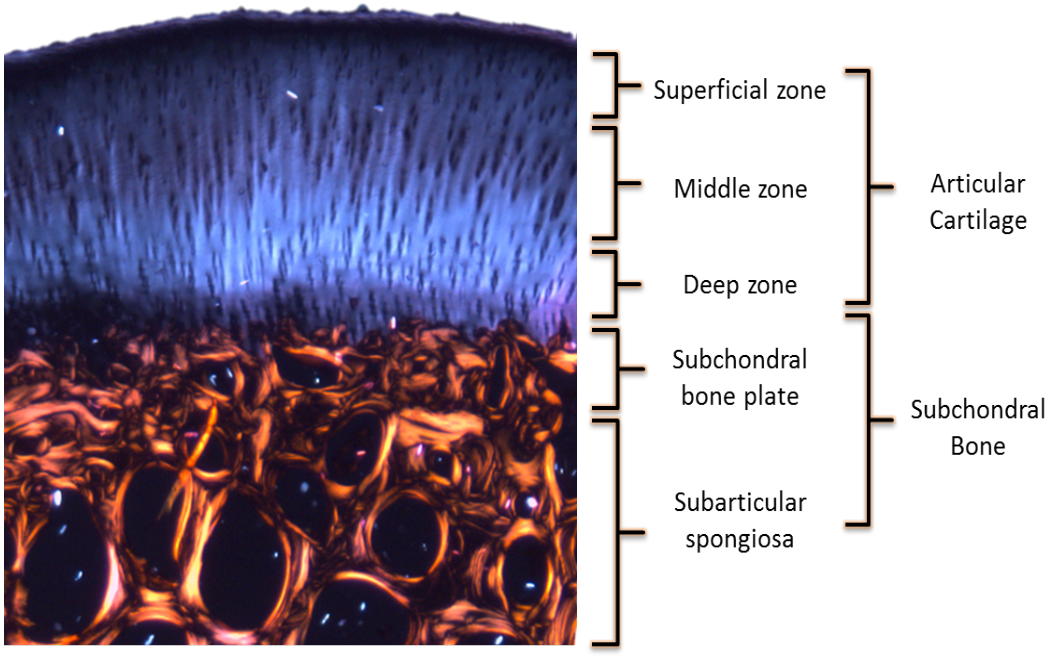

Figure 1.2 Haematoxylin and eosin stained histological sample of an osteochondral tissue under polarized light microscopy: Image taken by Pedro Diaz-Payno, Trinity Centre for Bioengineering.

The synovium is the soft tissue found between the articular capsule and the joint and has a role in joint homeostasis. It consists of dense bundles of collagen fibres connected to the bones around the joint and fibroblastic synovial cells which secrete the major constituents of synovial fluid i.e. hyaluronic acid and lubricin, which serve to lubricate the joint and reduce friction between the surface of the bones. In OA, the concentration and composition of these molecules may become altered which can directly affect cartilage (12). In addition to fibroblasts, the synovium also consists of synovial macrophages, that when activated, secrete pro-inflammatory cytokines and proteases that drive synovitis and further cartilage destruction (13). Interestingly, it has been reported that synovitis and inflammation may occur prior the development of significant radiographic changes and cartilage loss (14).

1.1.1 Innate immunity in Osteoarthritis

OA has traditionally been considered a non-inflammatory condition, in large part due to the use of OA tissues as controls for rheumatoid arthritis (RA) studies, with the latter exhibiting very high levels of inflammatory proteins and histological abnormalities. It is now becoming increasingly apparent that inflammation may play a substantial role in OA and is prominent even at the early stages of the disease (15). Unlike RA, where both the innate and adaptive immune system are involved in disease pathogenesis, it is primarily the innate immune response that contributes to inflammation in OA (16, 17). Macrophages within the synovial membrane become activated by altered conditions in the joint, such as the generation of cartilage fragments by aberrant MMP activity. Activated macrophages then produce inflammatory mediators, which in turn activate chondrocytes, enhance MMP production and propagate cartilage degradation (18). Synovial macrophage depletion using clodronate liposomes results in a reduction of aggrecan degradation and synovial MMP expression in the collagenase-induced OA model (19, 20), further supporting the role for innate cells in the pathogenesis of OA.

IL-1β and TNFα are the most extensively studied cytokines that have been implicated in the pathogenesis of OA. These cytokines can be produced by cells of the synovium and

have been found to be increased in the synovial fluid of OA patients compared to healthy controls (21). Furthermore, enhanced immunostaining for IL-1β and TNFα is observed in synovial biopsies from early stage OA patients (22). IL-1β and TNFα have also been shown to induce the production of MMPs which can lead to ECM degradation. Inflammatory mediators such as ICAM, VEGF, NF-κB and COX2 are also highly expressed in early stage OA patient samples compared to late stage tissue biopsies. IL-1β has been shown to induce cartilage damage through upregulation of MMP in chondrocytes in addition to suppressing the synthesis of collagen and aggrecan (23). Despite a pathogenic role for IL-1 in OA, therapeutic blockade of IL-1 using an IL-1R antagonist has not proved effective, with only marginal reduction in symptoms and no improvement in articular cartilage destruction observed (24).

TNFα has also been found to be elevated in the synovial fluid of patients with OA and is also known to contribute to catabolic processes (25, 26). While clinical efficacy has been observed in RA patients treated with the anti-TNFα monoclonal antibody, Infliximab, non-significant improvements in pain and physical function were reported in patients with OA of the hand (27).

1.1.2 Matrix Metalloproteases in Osteoarthritis

While pro-inflammatory cytokines and chemokines can drive the progression of OA, the major hallmark of OA is degradation of articular cartilage by proteolytic enzymes such as MMPs and aggrecanases, or ADAMTS. Aggrecan is known to be important in the maintenance of collagen in the ECM and its loss or proteolysis results in cartilage degradation. A number of members of the ADAMTS family are reported to degrade aggrecan in vitro, however, ADAMTS-4 and -5 are considered to be the principal aggrecanases involved in OA (28). ADAMTS-5 deficient mice, for example, were found to develop less severe cartilage damage in both the surgically induced model of OA and the antigen-induced arthritis model (29, 30), further highlighting the importance of aggrecanases in the development of OA.

MMPs are capable of degrading a number of ECM proteins and their normal function is to facilitate tissue remodelling. MMP activity is carefully regulated by a family of endogenous tissue inhibitors of MMPs (TIMPs), and an imbalance in the levels of MMPs versus TIMPs has been associated with cartilage loss in OA joints (31). Studies have also demonstrated that the severity of cartilage damage correlates with MMP activity, specifically in relation to MMP-1, MMP-3 and MMP-13, which are highly expressed in the synovial fluid of OA patients (32, 33). MMP-1 and MMP-13 are capable of degrading collagen type II, while MMP-3 can cleave fibronectin and laminin in addition to various other ECM components (34). Studies using MMP-3 deficient mice demonstrated reduced aggrecan cleavage and collagen loss (35, 36) while MMP-13-/- mice were protected from cartilage degradation in the surgically induced OA model (37). Further evidence for the degradative role of MMP13 was provided using murine models which demonstrated that conditional expression of MMP13 induced spontaneous cartilage degradation (38). The exact role of MMP-1 in OA has proved more difficult to elucidate given the differences between murine MMP-1 and it's human counterpart (39).

1.1.3 Immunometabolism in Osteoarthritis

All cells rely on anabolic or catabolic reactions in order to produce biosynthetic precursors and energy for cell survival and function (summarised in Figure 1.3). Catabolic pathways convert carbohydrates, lipids and proteins into energy, usually in the form of ATP. Complex carbohydrates are broken down into simple sugars such as glucose which can be shuttled into the cell via glucose transporters such as Glut1. Once in the cytosol, glucose is metabolised by an anaerobic pathway known as glycolysis. This converts glucose to pyruvate and generates 2 ATP and 2 NADH molecules. Pyruvate is then further processed via conversion to lactate, which is excreted by the cell, or is transported into the mitochondria to undergo oxidative phosphorylation. In this case, pyruvate is converted to acetyl-coA and enters the tricarboxylic acid (TCA) (or Kreb's) cycle where it is catabolised to generate 3 molecules of NADH and 1 molecule of FADH2. NADH and FADH2 act as a source of electrons for the electron transport chain (ETC), which in the presence of oxygen, creates a proton gradient across the mitochondrial inner membrane. This proton gradient is coupled to the enzyme ATP synthase which

converts ADP to ATP using the energy generated by allowing protons to travel back across the mitochondrial membrane. Each molecule of glucose can generate an additional 34 molecules of ATP during oxidative phosphorylation, making it a much more energy efficient process than glycolysis alone (40). In addition to glucose, cells can also use lipids and proteins as substrates for oxidative phosphorylation, while certain amino acids can be used as precursors for fatty acid synthesis and metabolism, or to produce intermediates of the TCA cycle (41).

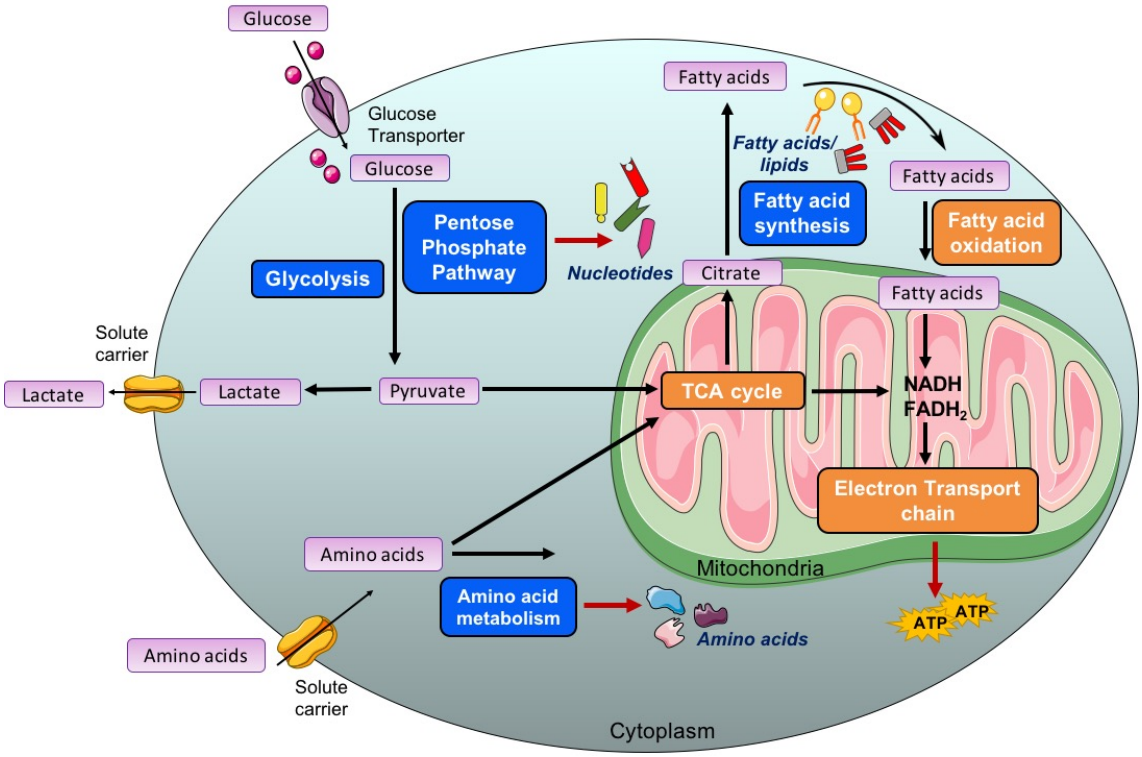

Figure 1.3 Overview of the catabolic and anabolic metabolic pathways. Glucose is transported through a glucose transporter and once inside the cell glucose is converted to pyruvate through glycolysis. This pyruvate can either enter the tricarboxylic acid (TCA) cycle where NADH and $FADH_2$ are generated, feed into the electron transport chain (ETC) which culminates in the production of ATP. Alternatively, pyruvate can be converted to lactate and be secreted by the cell. Glycolysis can feed into the pentose phosphate pathway which generates nucleotides for fatty acid synthesis, which uses citrate generated from the TCA cycle. These fatty acids can also undergo oxidation, generating NADH and $FADH_2$ which drive the production of ATP from the ETC. Amino acid metabolism can also feed into the TCA cycle. Pathways that are dependent on oxygen are coloured in orange, while oxygen independent pathways are coloured in blue.

Anabolic metabolism generates biosynthetic precursors necessary to build cellular components and energy stores. Fatty acid synthesis uses intermediates from catabolic pathways including glycolysis and the TCA cycle to create de novo fatty acids and lipids that are important for cell membrane and organelle structures (41, 42). The pentose phosphate pathway utilises intermediates of glycolysis to synthesise nucleotides and amino acids while also generating nicotinamide adenine dinucleotide phosphate-oxidase (NADPH), a cofactor required for the activity of numerous enzymes (41, 43).

Multiple signals are required to drive appropriate metabolic responses in order to meet the demands of the cell when nutrient availability is altered or when cellular growth, proliferation and protein production is required. Master sensors, such as mechanistic target of rapamycin (mTOR), which is comprised of two complexes, mTOR Complex 1 (mTORC1) and 2 (mTORC2) is a key regulator of cellular metabolism. Growth factors and mitogens activate signalling pathways which eventually converge to activate mTOR, which then promotes synthesis of proteins, lipids and nucleotides via upregulation of their respective anabolic pathways (44). The increased expression of glycolytic genes by mTOR is mediated via upregulation/activation of the transcription factor, hypoxia inducible factor 1α (HIF1α) (45), which also acts as an oxygen sensor, allowing for upregulation of anaerobic glycolysis when oxygen is limiting (46). Additionally, the activation of anabolic metabolism is coupled to nutrient availability, therefore, mTOR is also positively regulated by nutrients such as glucose and amino acids (47, 48).

Immunometabolism, the term coined for a relatively new area of immunology research, is heavily focused on characterising the metabolic pathways utilised by different immune cell populations and a number of studies have demonstrated that altering metabolic circuits impacts significantly on effector function (41). Indeed, the specific metabolic pathways utilised by immune cells upon engagement with different stimuli appears to underpin the type of immune response produced by that cell. For example, recent studies have demonstrated a direct link between macrophage polarization and metabolic reprogramming (49), although it should be noted that fundamental studies examining the metabolism of macrophages and their activation state are primarily limited to murine bone-marrow derived macrophages (BMDM). Such studies have

demonstrated that resting, non-activated macrophages tend to utilise oxidative phosphorylation, as it is the most energy efficient metabolic pathway and allows the cell to prioritise energy production over the generation of biosynthetic precursors. Activation of BMDM with a pro-inflammatory stimulus such as LPS (which promotes an M1 phenotype), drives a metabolic switch favouring glycolysis while at the same time downregulating oxidative phosphorylation causing the cells to rely almost exclusively on glycolysis to meet their metabolic demands (50). This switch to aerobic glycolysis, termed Warburg metabolism, is dependent on upregulation of HIF1α via mTOR activation. HIF1α in turn promotes the expression of genes encoding proteins required for glycolysis in addition to pro-inflammatory cytokines such as pro-IL-1β (51). While, glycolysis produces less ATP than oxidative phosphorylation, this switch is advantageous to activated immune cells as it allows them to rapidly produce additional ATP and biosynthetic precursors, even in inflammatory environments where oxygen is often limiting (52, 53). It is unclear whether human macrophages can engage in Warburg metabolism like their murine counterparts, given the difference in expression of inducible nitric oxide synthase (iNOS) (54, 55). Nitric oxide (NO) produced by iNOS is an important regulator of Warburg metabolism, as it has been shown to mediate the downregulation of oxidative phosphorylation seen in pro- inflammatory BMDM and BMDC (56, 57). Indeed, it has recently been reported that LPS stimulation of human macrophages resulted in increases in both glycolysis and mitochondrial respiration (58). Conversely, in alternatively activated BMDM (M2), which are generally considered to be anti-inflammatory, oxidative phosphorylation is the dominant metabolic pathway. IL-4, the cytokine which mediates alternative activation of macrophages, upregulates fatty acid oxidation and oxidative phosphorylation alongside anti-inflammatory immune pathways in BMDM (59–62).

Not surprisingly, dysregulated immune cell metabolism has been linked to a number of inflammatory diseases including psoriasis, rheumatoid arthritis and Type 2 diabetes (41). In the case of rheumatoid arthritis, altered metabolism was first proposed when elevated levels of various metabolites such as glucose, lactate and lipid metabolites were observed in the serum of RA patients (63) while increased glycolytic metabolites have been observed in RA synovial (64). Further studies have since demonstrated that a

metabolic shift from a resting regulatory state to a highly metabolically active state occurs in RA, with RA patient samples displaying higher expression of GAPDH, PKM2 and GLUT1 (65, 66). Furthermore, it is well established that a highly hypoxic environment persists in the RA joint microenvironment, and this is accompanied by increased synovial inflammation (65). It is now accepted that this hypoxic environment drives a cellular switch in mitochondrial respiration in favour of glycolysis. Binieka *et al* cultured rheumatoid arthritis synovial fibroblasts (RASF) in the synthetic α-ketoglutarate analogue, Dimethyloxallyl Glycine (DMOG), which acts to stabilise HIF1α and therefore drives glycolysis. These cells displayed enhanced glycolytic activity accompanied by altered mitochondrial morphology and a concomitant decrease of mitochondrial respiration. Furthermore, a higher frequency of mitochondrial DNA mutations and ROS production was observed in these cells. This shift to glycolytic metabolism was accompanied by enhanced lactic acid secretion which induced RASF invasion and secretion of bFGF which can induce dysfunctional angiogenesis, a key characteristic of the inflamed synovium in RA (65). Targeting of glycolysis using the glycolytic inhibitor, 3PO, was shown to reduce RASF cell migration and invasion in addition to pro-inflammatory cytokine production, demonstrating a major role for altered metabolism in RA pathogenesis (66).

The role of metabolism in the pathogenesis of OA is less well characterised, however recent studies suggest that a metabolic shift, like that described for RA, occurs in the articular cartilage, subchondral bone and synovium of OA joints positioning OA as a potential metabolic disorder (67). Furthermore, mitochondrial dysfunction is a hallmark of OA and previous studies have shown increased mitochondrial DNA damage in OA chondrocytes compared to healthy controls suggesting that cartilage degradation during OA and normal cartilage aging may be metabolically different processes (68). Finally, lactate levels are elevated in OA and are frequently co-associated with crystal arthropathy comorbidities (69, 70). The drivers of metabolic reprogramming in OA have not yet been identified and, given that the environment is less hypoxic than the RA joint, different mechanisms may be at play.

1.2 Damage Associated Molecular Patterns (DAMPS) in Osteoarthritis

DAMPS are endogenous molecules released from stressed, injured or necrotic cells to signal tissue or cell damage. Pattern Recognition Receptors (PRRs) on both immune and non-immune cells recognise DAMPS, and their prolonged presence can exacerbate inflammation and cause further damage as PRRs typically activate signalling pathways associated with the production of pro-inflammatory mediators (71, 72). In the context of OA, various DAMPS have been shown to initiate and maintain inflammation during disease, particularly at the later stage which is associated with significant tissue destruction. Elevated levels of HMGB1, ATP, HSPs, basic calcium phosphate (BCP) crystals and S100 proteins have been observed in synovial fluid retrieved from OA patients (1, 73–75). Interestingly, OA patients displayed elevated levels of HMGB1 in synovial fluid, which correlated with disease severity, while direct addition of HMGB1 to osteoarthritic synoviocytes drove production of pro-inflammatory cytokines (76, 77). HSP60, HSP70 and HSP90 have all been found to be increased in the OA joint (78, 79) with HSP90 capable of directly driving cartilage degradation (80). Two of the well-studied DAMPS in the context of OA are S100 family members and BCP crystals which are discussed in detail below.

1.2.1 S100 Proteins as DAMPs in Osteoarthritis

S100A8, and its binding partner S100A9, are calcium-binding proteins that regulate various calcium-dependent processes inside the cell (81). Extracellular S100A8/A9, which is released during tissue damage, has been shown to interact with the pattern recognition receptors, TLR4 and RAGE (82). The destructive effects of the protein complex were first identified in the context of RA, where they were shown to be elevated in both the serum and synovial fluid of patients and their concentration was found to correlate positively with disease severity (83). Furthermore, reduced proteoglycan depletion, joint swelling and cartilage destruction has been observed in S100A9-deficient mice (lacking a function S100A8/A9 complex) in the antigen-induced RA model (84). More recently, it was reported that high levels of S100A8 and S100A9 were detected in the synovium of diseased joints in mice after collagenase induced OA,

while S100A8 was found to be highly expressed in the synovium of early and late-stage OA patients (85). Further, support for the pathogenic role of S100A8/A9 was provided by Van lent *et al*, who demonstrated that the presence of S100A8/A9 aggravated osteocyte formation in the collagenase-induced model of OA, while osteophyte size was reduced in S100A9 deficient mice. Furthermore, serum levels of S100A8/A9 were shown to be predictive of osteophyte progression in a human cohort of early symptomatic OA (86).

It has been demonstrated that these proteins can directly influence cartilage degradation through induction of MMPs. Van Lent *et al* demonstrated that in vitro stimulation of macrophages with the heterodimer S100A8/A9 or S100A8 alone induced elevated mRNA levels of MMP-3, -9, and 13 (84), while enhanced expression of MMP-1, -3, -9 and -13 was observed in human chondrocytes directly stimulated with S100A8 and S100A9 (87, 88). In addition to promoting pro-catabolic processes in cartilage, S100A8/9 can also down-regulate expression of anabolic molecules such as aggrecan and type II collagen, further exacerbating cartilage destruction (89).

1.2.2 Basic calcium phosphate crystals as DAMPs in Osteoarthritis

Basic calcium phosphate (BCP) crystals consist of carbonate-substitute hydroxyapatite (HA), octacalcium phosphate (OCP) and tricalcium phosphate (90). HA crystals are the most prevalent form of BCP crystals and are found in 70% of total OA cases where their concentration closely correlates with the extent of cartilage degradation and lesion severity (91, 92). They are thought to form as a result of dysregulated ossification processes (93) and, given that crystal deposition does not occur in healthy cartilage, it is becoming more widely accepted that cartilage calcification plays a pathogenic role in OA (94). BCP crystals are now considered a 'danger signal' as they can activate a number of cell types and contribute to joint degeneration through the production of cartilage-degrading proteases and pro-inflammatory mediators (summarised in Figure 1.4). Early studies demonstrated that BCP crystals drive MMP and inflammatory gene expression in fibroblasts (95, 96), while more recent studies have focused on their effects in

macrophages, chondrocytes, and osteoclasts (97–100). In addition, BCP crystals have been shown to directly upregulate the expression of S100A8 (99).

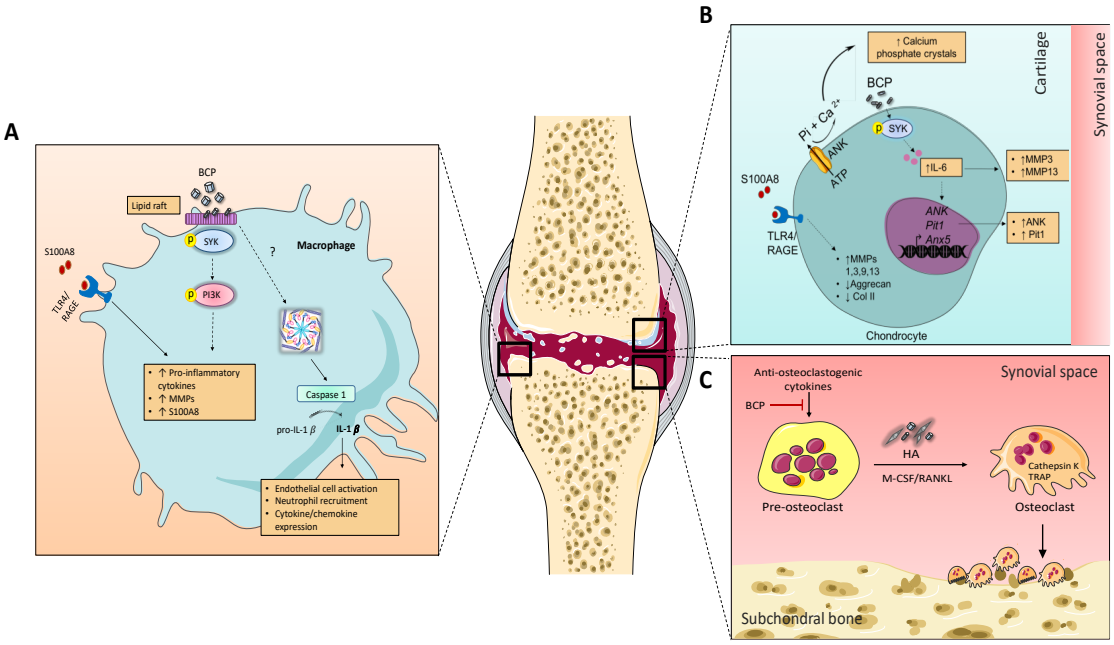

Figure 1.4 Cellular mechanism leading to crystal-induced tissue damage in the joint. A. In macrophages, the direct binding of basic calcium phosphate (BCP) crystals to the cell membrane can activate the membrane-proximal tyrosine-protein kinase Syk and PI3K, resulting in the upregulation of pro-inflammatory cytokines, matrix metalloproteinases (MMPs) and damage-associated molecular patterns (DAMPs) such as protein S100A8. Furthermore, release of S100A8 can function in a feedback manner and bind to TLR4 and/or RAGE expressed on the cell surface to directly upregulate inflammatory mediators. BCP crystals may also activate the NLRP3 inflammasome and drive IL-1β production and secretion. **B.** BCP crystals drive the production of IL-6 from chondrocytes which can directly induce the upregulation of calcification genes ANK, PIT1 and Anx5). S100A8 induces upregulation of the cartilage-degrading enzymes MMP1, MMP3, MMP9 and MMP13 in chondrocytes while downregulating expression of aggrecan and type II collagen. **C.** HA crystals can increase RANKL–M-CSF-mediated osteoclastogenesis, whereas BCP crystals can directly inhibit anti-osteoclastogenic cytokine signalling, which might result in increased osteoclast differentiation and bone resorption of the underlying subchondral bone.

Early signalling events involved in BCP-inflammation have recently been elucidated. It has been demonstrated that BCP crystals can bind to the cell membrane and induce activation of the membrane-proximal kinase Syk and its downstream interacting partner, PI3K, in primary human and murine macrophages. Pharmacological inhibition of these kinases was found to attenuate BCP-induced MMP expression and pro-inflammatory cytokine production (99, 100). While BCP crystals induce potent IL-1β

production in vitro via activation of the pattern recognition receptor, NLRP3, reports from in vivo studies have been conflicting. (101, 102). Indeed, Nasi *et al* recently demonstrated that neither IL-1α nor IL-1β mediate the pathology seen in the murine menisectomy model of OA (103), while synovial inflammation in murine joints post crystal injection appeared to occur independently of Inflammasome components and IL-1β (102). These findings may explain the lack of efficacy of IL-1 inhibitors in human OA. Based on these studies, focus has shifted to other potential targets including IL-6. Recent studies have demonstrated that IL-6 is produced by chondrocytes in response to BCP stimulation in a Syk and PI3K dependent manner. Furthermore, IL-6 can act in an autocrine manner to promote calcium-containing crystal formation and upregulation of genes involved in the calcification process such as ANK, Pit1 and Anx5 (97). In addition to macrophages and chondrocytes, BCP crystals may directly affect osteoclasts and contribute to bone erosion via inhibition of anti-osteoclastogenic cytokine signalling (104). Therefore, targeting synovial inflammation induced by crystal deposition may suppress early destructive processes, while targeting the osteoclastogenic effects of crystals may suppress excessive bone remodelling. Indeed, preventing the actual intra-articular deposition of calcium crystals, as recently demonstrated by Nasi *et al* using sodium thiosulphate, could limit inflammatory responses at the outset (105).

1.3 Current Treatments for OA

The aetiology of OA is poorly understood and as of yet there are no disease-modifying osteoarthritic drugs (DMOADs) available (106). Current treatment strategies are focused on providing symptomatic relief to alleviate pain and improve joint function rather than halting disease progression. Exercise and weight loss are initially recommended to OA patients in order to reduce mechanical load on the joint along with strengthening surrounding muscle. Pharmacological agents such as analgesics, non-steroidal anti-inflammatory drugs (NSAIDs) including COX (cyclooxygenase)-2 selective inhibitors are often prescribed alongside injections of glucocorticoids and delivery of hyaluronic acid (106, 107). As mentioned previously, while inhibition of TNFα has proved effective in the treatment of RA, clinical trials with Infliximab or Adalimumab (monoclonal antibodies

against TNFα) in OA patients have shown no significant radiographic changes or lesion improvements compared to placebo treatment. Thus, while many of the current treatments offer relief from pain in mild to moderate OA, these treatments are ineffective in late-stage OA (108–110). Moreover, deterioration of the joint and disease progression is not halted by current therapeutics. End-stage OA patients often have advanced cartilage damage and the underlying exposed subchondral bone can become extensively compromised which propagates the destructive process in the joint. Ultimately for these patients the only function-restoring option available is surgical arthroplasty (4, 107).

1.3.1 Total Joint Arthroplasty

Total Joint Arthroplasty (TJA) is considered a highly effective surgical procedure used to alleviate pain and restore function in individuals suffering from end-stage joint disease. The procedure involves removing some, or all, of the damaged arthritic joint, and replacing it with a custom made prosthesis which replicates the movement of a normal, healthy joint (111). Prosthesis are composed of a variety of materials which can be grouped into two categories; metals and non-metals (Table 1). For several decades, metals were used as the biomaterials of choice for orthopaedic applications, and are particularly successful for hip and knee prostheses, given that these areas are regarded as weight-bearing joints. However, more recently, non-metals including ceramics, polymers and composites such as polymethylmethacrylate (PMMA) have become popular.

The existing definition of a biomaterial is ‘a non-viable material used in a medical device intended to interact with biological systems’ (112). In order for a biomaterial to fulfil its criteria as an adequate orthopaedic device it must possess several primary characteristics: it must be biologically stable, compatible with the biologics of the host and resilient to wear that would otherwise result in subsequent loosening of the implant. These qualities ensure that it will not cause any adverse effects to the host environment. Typically, the bulk material of the prosthesis (metal like titanium or non-metal like UHMWPE) are coated in a synthetic bioceramic such as hydroxyapatite (HA).

The use of this biomimetic bone substitute aims to improve biocompatibility and promote incorporation of the prosthesis into the surrounding bone and enhance osteointegration, which is classified as the formation of an interface between living bone and the artificial implant (113). The implant is then typically fixed into place with PMMA bone cement.

Table 1: Commonly used biomaterials for TJA.

Metals	Abbreviation
Titanium and titanium base alloys	CP-Ti, Ti-6Al-4A
Cobalt alloys	Co-Cr-Mo
Low Carbon grade stainless steel	316L
Non metals	
Polymers: ultrahigh molecular weight polyethylene	UHMWPE
Ceramics: Alumina, Zirconia, Hydroxyapatite	Al_2O_3, ZrO_2, $Ca_{10}(PO_4)_6(OH)_2$
Composites: Polymethylmethacrylate	PMMA

The current 10 year success rate of total joint replacement is 90%, with 10% of patients requiring revision surgery (114). Various complications post-surgery can occur that lead to implant failure including infection (7%), dislocation (6%), periprosthetic fracture (5%) and surgical error (3%) (115). Aseptic loosening remains the leading complication post-surgery in the medium to long term, accounting for 75% of joint replacement failures (116). It occurs due to the gradual wear and tear of implants over time and results in the continuous generation of wear-debris particles from the articulating surface of the prosthesis (117). Due to their insoluble nature, most wear particles are resistant to digestion and thus, a chronic inflammatory state persists in the joint (118, 119). This then culminates in a process known as periprosthetic osteolysis (PO), which is characterised by the osteoclastic resorption and degradation of bone surrounding the implant that ultimately leads to aseptic implant loosening (116, 119, 120). The subsequent failure of implants results in individuals requiring multiple joint

replacements throughout their lifetime, with each revision surgery adding more risk to the patient and a shorter duration of implant survival which represents a major clinical problem.

1.3.2 Wear debris particles and periprosthetic osteolysis

Periprosthetic osteolysis (PO) is characterised by prosthesis loosening due to the loss of the surrounding bone and is initiated by the formation of wear debris which is recognised as foreign by host immune cells (116). Over time, particles are generated by wear between the various components of modular implants, by abrasion between prosthesis-bearing surfaces or, as in the case of titanium particles, via release from the osteoconductive porous bone-prosthesis interface (121). Furthermore, the HA coating surrounding the prosthesis can undergo dissolution creating a build-up of HA particles in the peri-implant space. A number of studies have reported the presence of wear debris particles in the interfacial tissue and also intracellularly in patients undergoing revision replacement surgeries (118, 122–124). Due to their insoluble nature, most particles are resistant to digestion by macrophages and thus, a chronically activated macrophage population persists in the joint. Furthermore, the flow of joint fluid has been suggested to allow for dissemination of the wear debris particles resulting in a greater area of cell activation and bone resorption (118). This then culminates in periprosthetic osteolysis, which is the osteoclastic resorption and degradation of bone surrounding the implant that ultimately leads to loosening of the prosthesis (116, 119, 125). The progression of tissue destruction is subtle but cumulative and can often remain subclinical with few or no signs even in the very late stages of aggressive osteolysis however, by this time, acute macroscopic bone defects are likely to have developed (116).

A number of cell types including macrophages, osteoclasts, fibroblasts, and neutrophils have been implicated in wear-debris induced osteolysis (126, 127) (Figure 1.5). Uptake of wear debris particles by macrophages initiates a cascade of signalling events that culminates in a chronic inflammatory state mediated by cytokines such as IL-1, IL-6, TNFα and Receptor activator of NF-κB ligand (RANKL) (128). As well as these cytokines

being pro-inflammatory in nature, they can also act as osteoclastogenic cytokines to induce differentiation of bone resorbing cells (osteoclasts). This cellular response favours osteoclast differentiation and procatabolic osteoclast activity which exacerbates bone resorption and thus enhances osteolysis (115). Furthermore, several particulates have been shown to increase chromatin decondensation and neutrophil NET formation (129–133).

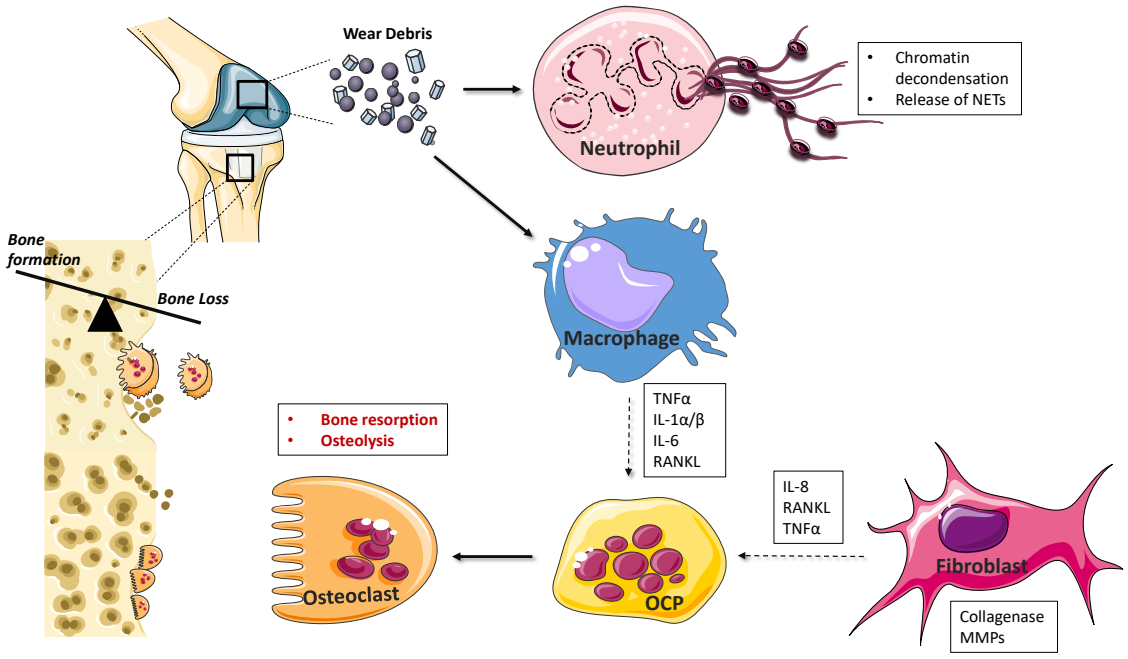

Figure 1.5 Cellular mediators of periprosthetic osteolysis. Wear debris generated from implanted prosthesis activate resident or infiltrating fibroblasts, macrophages and neutrophils at the site of implantation. Neutrophil recognition of biomaterials drives neutrophil extracellular trap (NET) formation while macrophage and fibroblast-induced chemokine production facilitates further leucocyte recruitment to the implant interface. Cytokines, such as tumour necrosis factor (TNF)-α and IL-1 drive inflammation and, together with RANKL, can induce the differentiation of osteoclast precursor cells (OCPs) into activated bone resorbing cells. Matric metalloproteases (MMPs) and collagenases contribute further to catabolic processes and aseptic implant loosening.

1.3.3 Macrophages and periprosthetic osteolysis

A wealth of compelling evidence implicates macrophages as the protagonist in wear debris mediated osteolysis. Several studies have demonstrated that patients undergoing implant revision surgeries have increased macrophage numbers at the interfacial membrane where extensive osteolysis has taken place (126, 134). Blaine *et al*

demonstrated that direct culture of macrophages with titanium particles enhances IL-1β, PGE2, IL-6 and TNFα cytokine production in a particle size, shape and composition dependent manner (135). Several mouse models of osteolysis induced by wear particles have been generated including the murine air pouch model of osteolysis and the murine calvarial model. The murine air pouch model is generated by subcutaneously injecting sterilized air into the back of a mouse, followed by implantation of a section of calvaria (skullcap) from a donor mouse. Particles can then be injected into the pouch and osteolysis of the calvarial bone can be observed (136, 137). In the calvaria model, particles are directly injected to the top of the calvaria leading to inflammation and bone resorption after 1 week (138). Studies using these models have demonstrated that macrophage infiltration and proinflammatory cytokine production is augmented upon PMMA, metal and polyethylene implantation (137). In vivo studies using the murine air pouch model have also demonstrated that UHMWPE, PMMA, Co-Cr and Ti-6Al-4V particles increase IL-1β production and macrophage numbers at the site of injection (137). Along with titanium and PMMA, UHMWPE also induces aggressive osteolysis, and the volume of UHMWPE wear particles appears to correlate with the number of active macrophages present in osteolytic tissues (139).

As expected, M1 macrophages are implicated in the destructive periprosthetic osteolysis process and synovial tissues from patients undergoing revision surgery exhibit a higher ratio of M1 to M2 macrophages compared to tissues from patients undergoing primary TJA (140). Furthermore, several studies have demonstrated that wear-particles directly activate M1 macrophages leading to a sustained inflammatory response characterised by the production of chemokines and pro-inflammatory cytokines such as TNFα, IL-1 and IL-6 (140, 141).

1.3.4 Fibroblasts and periprosthetic osteolysis

Synovial fibroblasts have been suggested to play a role in the osteolytic process as they are abundant in the interfacial membranes of osteolytic joints and exhibit enhanced RANKL expression (126, 142). It has been reported that fibroblasts isolated from the interfacial membranes of patients undergoing revision surgeries have enhanced

collagenase and stromelysin expression levels, further supporting the hypothesis that they can directly contribute to matrix degradation (143). Studies using murine embryonic fibroblasts challenged with titanium particles demonstrated a dose-dependent increase in RANKL gene and protein expression, however this was abrogated in the presence of the COX-2 inhibitor, celecoxib (144). Furthermore, titanium particles were shown to enhance IL-6, collagenase and gelatinase expression as well as PGE2 production in human fibroblasts (145). Recently, Sabokbar *et al* attempted to elucidate whether fibroblasts isolated from periprosthetic tissue, and therefore previously exposed to wear debris particles in vivo, are capable of enhancing osteoclastogenesis. Co-culture of these cells with undifferentiated monocytes resulted in enhanced bone resorption in an in vitro model of osteolysis. Furthermore, in the presence osteoprotegerin (OPG), the natural decoy receptor of RANK, the surface area of resorption was decreased compared to controls without the decoy receptor suggesting that these cells are indeed capable of supporting the differentiation of osteoclasts from monocytes in vivo (142). Finally, in addition to enhancing osteoclast formation and bone resorption, fibroblasts stimulated with wear debris particles were found to upregulate the chemokine IL-8 which may recruit additional osteoclasts to the site of implantation and further propagate the destructive process (145, 146).

1.3.5 Osteoclasts and periprosthetic osteolysis

While macrophages have been reported to exhibit bone-resorbing capabilities (147, 148), the predominant cells that drive bone erosion in periprosthetic osteolysis are osteoclasts. During osteolysis the balance between bone erosion by osteoclasts and de novo bone formation by osteoblasts is skewed towards excessive osteoclast activity. Osteoclast precursors, (OCPs), which are recruited from blood or are already present in the periprosthetic tissue, develop into mature, tartrate-resistant acid phosphatase (TRAP) positive osteoclasts by a process known as osteoclastogenesis (Figure 1.6). RANK, RANKL and the decoy receptor for RANKL, OPG, together play a large role in osteoclast formation and function. RANKL is normally expressed by osteoblasts and their precursors under normal physiological conditions, however in inflammatory conditions it has been reported to be expressed by macrophages (149). RANKL can interact with

RANK on the surface of OCPs though direct cell-cell contact but in some circumstances, RANKL may be cleaved from the membrane and become a soluble ligand (150). Counteracting the effect of the RANK/RANKL pathway is the soluble decoy receptor OPG. Primarily produced by osteoblasts, OPG blocks RANKL from binding to RANK and therefore the regulation and rate of bone resorption is dependent on the ratio between RANKL and OPG (151).

Veigl *et al* reported a positive correlation between RANKL expression and the extent of radiological presence of osteolysis in aseptically loosened hip replacements and periprosthetic tissues, demonstrating a disruption in the balance between RANKL and OPG (150, 151). Furthermore, murine in vivo models have demonstrated the importance of the RANKL/OPG ratio in bone resorption. Disruption of RANK signalling via genetic deletion or through enhancing OPG activity via gene therapy resulted in elimination of osteoclast cells and significantly reduced bone resorption in a model of osteolysis (152–154).

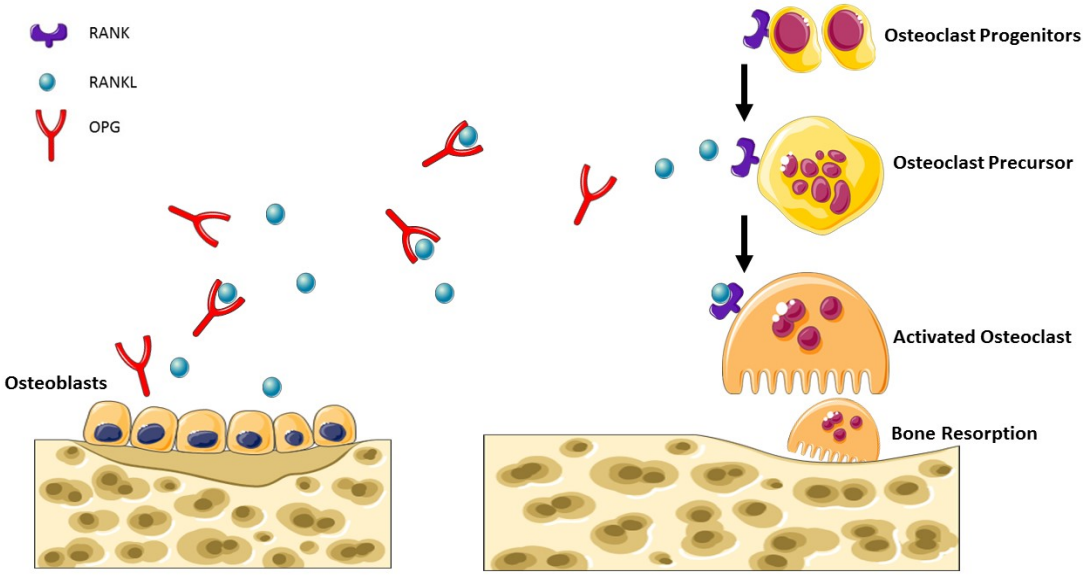

Figure 1.6 The RANK-RANKL-OPG regulatory pathway. Osteoclast maturation is mediated by interaction of RANKL with the osteoclast precursor cell receptor, RANK. RANKL is expressed by osteoblasts and upon binding to RANK results in activation of osteoclasts. This increases the rate of bone resorption. OPG is the soluble decoy receptor for RANKL, preventing RANKL binding to RANK and thereby inhibiting osteoclastic bone resorption. The ratio of RANKL: OPG determines the rate of bone resorption and bone formation.

It has been demonstrated that osteoclastogenesis can be mediated through indirect or direct mechanisms by wear debris particles. In the case of indirect osteoclastogenesis, macrophages phagocytose the particles and secrete pro-inflammatory and pro-osteoclastogenic cytokines such as TNFα, IL-6, IL-1 and RANKL (150). More recently it has been demonstrated that wear debris particles may directly act on osteoclast precursors to enhance osteoclast maturation in a MAP kinase dependent manner, as demonstrated by Clohisy *et al* who reported direct activation of ERK, JNK and p38 MAP kinases by PMMA particles in murine BMDMs (155, 156). The same authors also demonstrated that blockade of NFκB activation, which is required for osteoclast formation, ameliorated PMMA-induced osteolysis and reduced osteoclast cell numbers to control levels in the calvarial model of osteolysis (157).

1.3.6 Current therapies for periprosthetic osteolysis.

Modulation of macrophage phenotype has been suggested as a potential therapeutic avenue for periprosthetic osteolysis. Administration of the M2 polarizing cytokine, IL-4, or the anti-inflammatory cytokine, IL-10, have shown some efficacy, at least in murine models (149, 158, 159). There are, however, no drugs specifically approved for the prevention of periprosthetic osteolysis. As the biological cascades activated by wear particles are now better understood, two main approaches have been suggested and involve modulating osteoclast formation/function and inhibiting periprosthetic inflammation. Bisphosphonates have been shown to inhibit enzymes in the mevalonate pathway which results in apoptosis of osteoclasts (127). They are commonly used for metabolic bone diseases (160) and several experimental studies have demonstrated a significant decrease in osteolysis/bone resorption after treatment with these compounds (161, 162). For example, pamidronate has been shown to reduce particle induced osteolysis in vitro (163) while alendronate was found to inhibit wear-particle induced osteolysis in a murine and rat calvarial model (138, 164). Statins such as HMG-CoA reductase inhibitors are another class of osteoclast inhibitor and can act in a similar manner to bisphosphonates by targeting the mevalonate pathway. In this case, simvastatin has been shown to inhibit UHMWPE induced osteolysis in the murine

calvarial model (165). RANKL is another attractive therapeutic target due to the central role it plays in osteoclastogenesis. As mentioned previously, OPG is a naturally occurring decoy receptor and inhibits the interaction between RANK and RANKL. In a UHMWPE-induced murine air pouch model of osteolysis, OPG gene therapy was shown to diminish mRNA expression of osteoclast markers and reduce bone loss (153). This has also been demonstrated in the murine calvarial model (166). While bisphosphonates and statins have proved effective in murine models of particle-induced osteolysis, it remains to be determined if these agents are efficacious in osteolysis patients.

Modulating pro-inflammatory cytokine production may also prove beneficial for osteolysis patients assuming inflammation is targeted prior to extensive bone damage. Etanercept, a TNFα antagonist, has been shown to reduce titanium-mediated inflammation in murine osteolysis models (152), however a clinical study of osteolysis patients treated with anti-TNF over the course of a year proved inconclusive (167). More recently, inhibition of TNFα secretion by the phosphodiesterase inhibitor pentoxifylline, was shown to reduce wear debris induced inflammation in healthy monocytes, however its efficacy is yet to be tested in vivo (168). Bortezomib (Bzb) is a reversible 26S proteasome inhibitor currently approved for the treatment of relapsed/refractory multiple myeloma (108). As well as anti-tumour effects, it has been shown to limit inflammation and bone resorption in arthritis models (169, 170). Bzb inhibits NF-kB, a master regulator of inflammation, by blocking degradation of the NF-kB inhibitor, IκB. Mao *et al* recently demonstrated that Bzb can inhibit titanium particle induced inflammation in murine macrophages, a finding that warrants further *in vivo* study as it may have implications for the treatment of periprosthetic inflammation.

1.4 Novel approaches for osteochondral defect repair

Articular cartilage is a soft hydrated tissue lining the bones in synovial joints which functions to distribute the high loads passing through these joints. It has unique viscoelastic, compressive, tensile and frictional properties (6) which enable smooth, pain free articulation between bones. The lack of an extended vascular network in hyaline cartilage does not allow for typical scar tissue remodelling events which include

bleeding, inflammation, cell proliferation and remodelling. As a consequence, damaged cartilage loses its protective function, ultimately compromising the integrity of the underlying subchondral bone. As mentioned previously, this results in an osteochondral defect which has poor long-term endogenous regeneration capacity. Because of this, new avenues of research have focused on methods to repair and regenerate tissue around small osteochondral defects before damage progresses. The current standard treatments used to promote tissue regeneration for cartilage defects are outlined below.

Microfracture: This procedure involves the creation of surgical perforations in the subchondral bone around the defect. This facilitates migration of progenitor stem cells from the bone marrow cavity into the defect through the resulting small osteochondral openings (171). Apart from their regenerative capacity, bone marrow stem cells have immunomodulatory properties and thus also provide pain relief. Although microfracture is still considered the gold standard by the FDA, it often results in the generation of fibrocartilage (172). This tissue is inferior to healthy hyaline cartilage, both biochemically and biomechanically, and makes microfracture a short-term solution (5-10 years).

Mosaicplasty: Mosaicplasty grafting involves harvesting a cylindrical plug of hyaline cartilage and underlying subchondral bone from an unaffected, non-load bearing area. This is then implanted into the cartilage defect area (173). This procedure is required when patients have deep defects that extend into the subchondral bone, and long-term studies have shown comparable outcomes to that of microfracture (174).

Autologous chondrocyte implantation (ACI): This two-step procedure consists of chondrocyte isolation from a low-weight-bearing area of the knee joint during a first arthroscopic operation and expansion *in vitro* before transplantation into the lesion in a second surgery. This technique has two major advantages: using host cells avoids potential immune-related complications and the small biopsy size minimizes donor site morbidity.

Matrix-induced autologous chondrocyte implantation (MACI): This is currently the most common scaffold plus cell-based cartilage repair technique in clinical practice. Similar to ACI, MACI requires two surgical procedures. In the first surgery, chondrocytes are harvested from an autologous tissue biopsy and then seeded onto an absorbable porcine-derived collagen scaffold. During the second surgery an arthrotomy procedure debrides the lesion to allow for construct implantation which is secured using fibrin glue. MACI has been shown to have similar functional outcomes to either ACI or microfracture. However, the expense of the technique and the fact that integration with the defect site has not been confirmed in long-term follow up clinical studies warrants further investigation.

The above-mentioned procedures have limited long-term success and eventually severe joint damage necessitates the need for total joint replacement. Repair of complex osteochondral lesions, therefore, remains a significant clinical problem (175, 176). This has, however, motivated the development of innovative tissue engineering strategies to regenerate osteochondral tissues and some of these approaches are outlined below.

1.4.1 Tissue engineering

Tissue engineering utilises a combination of scaffolds, cells and biologically active molecules which can differentiate into functional tissues and has been regarded as a revolution in medical sciences (Figure 1.7). It has been developed for almost every existing human tissue or organ and over the years there has been a particular interest in “soft” tissues such as skin, liver and muscle. Additionally, bone and cartilage tissue engineering to fabricate biological substitutes for the treatment of osteochondral defects has become an active area of research. As mentioned above, articular cartilage lacks any self-healing ability due to its avascular nature. In other tissues, the vascular system delivers specific cells which remove necrotic material and synthesize new matrix as well as creating the appropriate biochemical environment for healing (177). In addition to lacking a vascular system, chondrocytes in the neighbouring healthy cartilage are trapped in a mesh of collagen and proteoglycan which prevents cell migration to damaged sites. Much focus has now been placed on developing and improving research

into mesenchymal stem/stromal cells (MSCs), bioceramics and ECM 3D scaffolds in order to overcome these limitations.

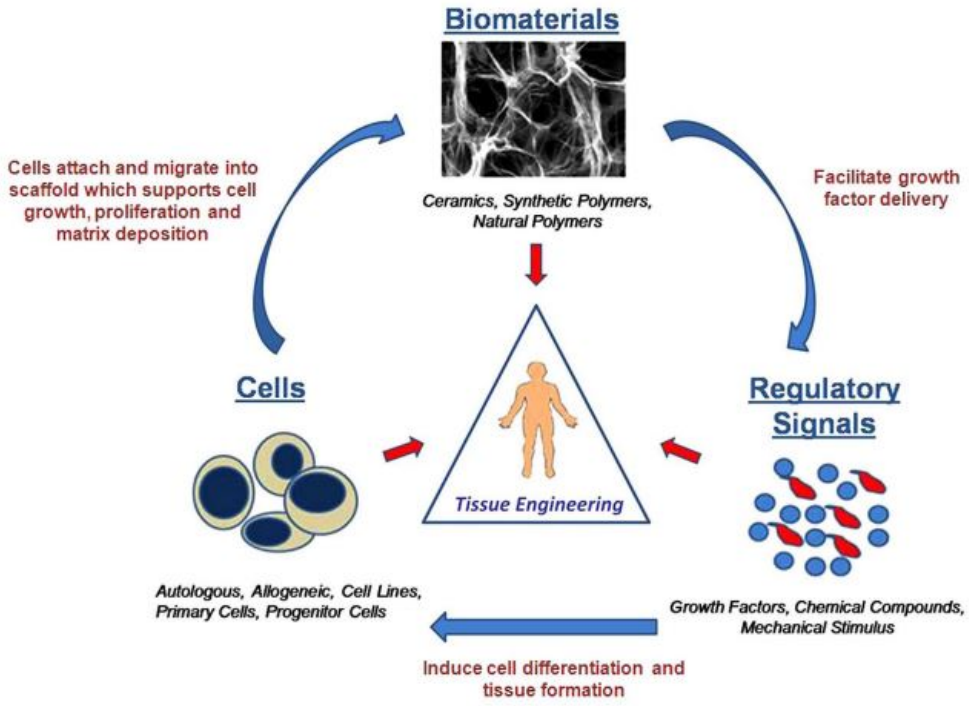

Figure 1.7 The three essential components that make up the tissue-engineering triad. Cells are required to facilitate tissue formation and matrix deposition, growth factors or biophysical stimuli can direct growth and differentiation of cells, while biomaterial scaffolds provide structure and substrate for tissue growth and development (178).

1.4.2 Cell-based approaches: exploiting the pleiotropic nature of MSCs

MSCs were originally discovered in the 1950s and were found to readily proliferate in vitro (179). They exist in almost all tissues and can be obtained from both adult and foetal sources. MSCs have become an attractive cell source for biological applications due to their relative ease of isolation and expansion as well as their ability to differentiate into canonical cells of the mesenchyme (Figure 1.8) (180). Indeed, their characteristics make them ideal for working in osteochondral tissue engineering. In vitro, osteogenic differentiation of MSCs (i.e. differentiation into osteoblasts) has been demonstrated with dexamethasone, β-glycerolphosphate and ascorbic acid, while culture in chondrogenic media (dexamethasone, ascorbic acid and TGFβ3) can enhance chondrogenic differentiation of MSCs into cartilage forming cells (181, 182).

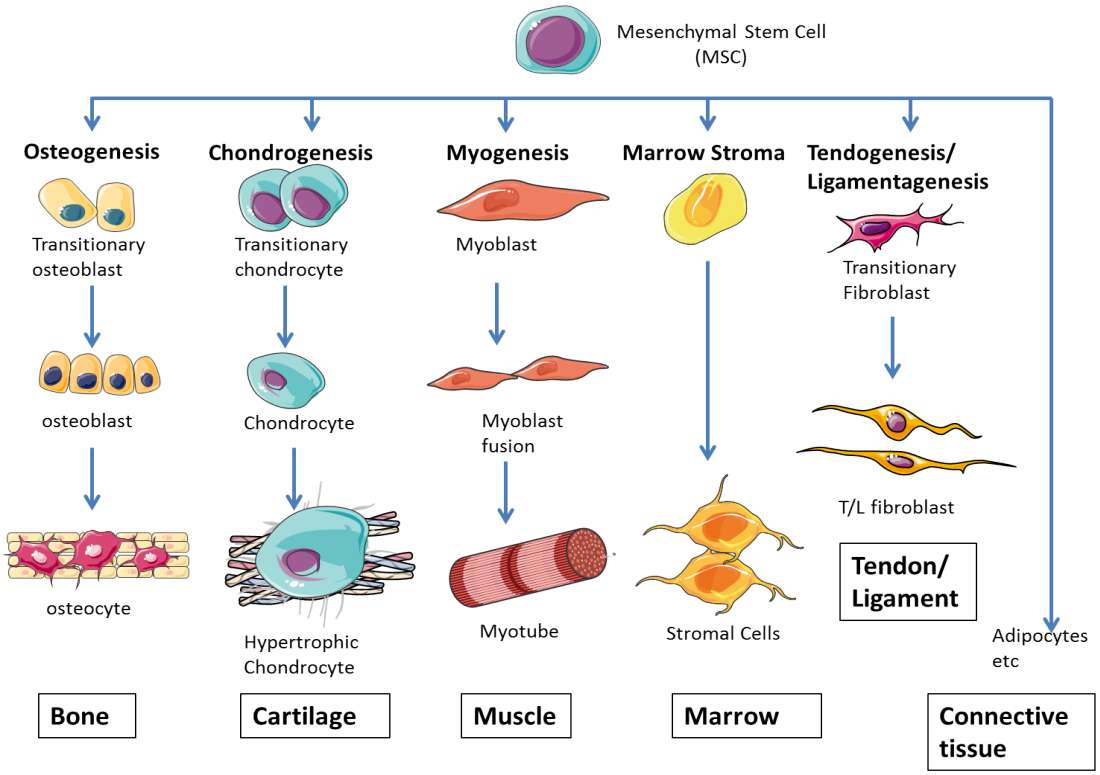

Figure 1.8 Differentiation of mesenchymal stem cells. MSCs are a population of stromal cells present in the bone marrow and most connective tissues. They are capable of differentiation into mesenchymal tissues such as bone, cartilage, muscle, marrow, ligament and connective tissue. Diagram generated using Servier medical Art, adapted from (183).

In addition to the capacity of MSCs to regenerate damaged tissue, MSCs also possess the ability to home to the site of injury or insult and modulate disease through the release of trophic factors that can modulate the immune system or promote intrinsic repair (184, 185).

MSCs have been utilised for various tissue engineering applications. Gao *et al* implanted murine MSCs into a murine skeletal defect model and observed enhanced osteointegration and osteogenic responses (186). It has also been demonstrated that MSCs seeded into hydrogel scaffolds promote cartilage integration into defects created in cartilage explants, further supporting their chondrogenic differentiation potential (187). Finally, it has been demonstrated that direct intra-articular injection of MSCs can promote cartilage regeneration and improve physical function in rats with focal cartilage

defects (188). Overall, the use of MSCs in tissue engineering strategies is a promising approach to enhance tissue repair and regeneration.

1.4.3 Bioceramics for bone tissue engineering

Ceramics that show biocompatible behaviour are known as bioceramics. One of the most common groups of bioceramics are calcium phosphate ceramics which include tricalcium phosphate (TCP, either α or β), tetracalcium phosphate (TTCP), octacalcium phosphate (OCP) and hydroxyapatite (HA). These derivatives are obvious choices of biomaterials as calcium phosphate is found naturally in the body and is the major inorganic constituent of bone. HA is chemically very similar to the inorganic minerals in bone and therefore is extremely osteoconductive and osteoinductive (189). In addition, HA is biocompatible and can be modified by bone resorbing osteoclasts. Due to these characteristics, HA has gained much attention in tissue engineering and several studies have demonstrated its efficiency in the induction of bone formation in vivo and osteogenic differentiation of MSCs *in vitro.* Early studies demonstrated that implantation of HA ceramics subcutaneously in the abdomen of dogs resulted in deposition of new bone around the ceramics after 3 months (190). A later study by Klein *et al* reported similar results for dense and porous HA ceramics implanted intramuscularly in dogs, with new bone being formed in the porous constructs only (191). However, HA is limited in its capacity to repair large bone defects due to its brittleness. Nanophase ceramics, especially nanoHA are popular bone substitutes, coatings and other filler materials due to their documented ability to promote mineralization. The nanometre grain sizes and high surface friction of grain boundaries in nanoceramics increase osteoblast functions (such as adhesion, proliferation and differentiation) (192). The highest adsorption of vitronectin (a protein well known to promote osteoblast adhesion) was observed on nanophase ceramics, which may explain the subsequent enhanced osteoblast adhesion on these materials (193). More recently nanophase ceramics, in particular nanoHA, have been used as a method of non-viral gene delivery with the view that the combination of gene therapeutics with osteogenic biomaterials will promote prolonged, sustained and localized *in situ* delivery of a protein of interest (194).

1.4.4 Natural Biomaterials: Extracellular Matrix-Derived Scaffolds

3D scaffolds are often used in tissue engineering where stem cells and bioactive molecules such as HA are incorporated or loaded prior to implantation. As tissues such as bone and articular cartilage have a very intricate biological and biochemical structure, development of a scaffold using conventional synthetic biomaterials fails to recapitulate this complexity. Additionally, there is a lack of biological interaction with synthetic materials which does not allow for proper integration into surrounding tissues. Natural biomaterial scaffolds such as ECM derived scaffolds essentially represent a natural scaffold that can provide cells with the complex microenvironment of a natural tissue. They act as a source of promotional cues and therefore encourage constructive remodelling, i.e., supporting specific tissue formation at the implantation site rather than forming inferior and less functional scar tissue. Mammalian ECM consists of secreted proteins and biomolecules of the resident cells of each unique tissue (195, 196). Processing of ECM involves decellularisation procedures that remove whole cells and nuclear material in order to eliminate adverse immunogenic effects of xenogeneic cellular antigens. It uses combinations of mechanical and chemical treatments (197) while at the same time attempting to maintain both the structural (collagen), and functional cues (growth factors) that drive differentiation of recruited cells or cells that are seeded onto the constructs prior to implantation (198, 199). Given the multiple roles that ECM plays, and the complex nature of tissue regeneration in a defect, ECMs are superior to synthetic compounds and several ECM derived scaffolds have been shown to facilitate the repair of many tissues in preclinical studies and in human clinical applications including repair of trachea, tendons, muscle, heart valves and abdominal walls (195).

1.4.5 The immune system in tissue engineering

Although vast progress has been made in the last decade, several challenges have hampered the clinical application of tissue engineering technologies. It is now becoming increasingly apparent that, as with traditional implant materials, an understanding of the immune response to novel biologicals scaffolds for tissue repair is of paramount importance. Upon implantation of a biomaterial scaffold or foreign body, the immune

system is the first to respond. This biomaterial can regulate immune cell behaviour and the resulting immune cell secretome can regulate cells within the scaffold microenvironment and downstream mediators of the regeneration process (200). The role of the immune system in response to wound healing and regeneration post-biomaterial implantation involves a complex yet choreographed spatiotemporal host response that directs successful tissue repair and development (Figure 1.9).

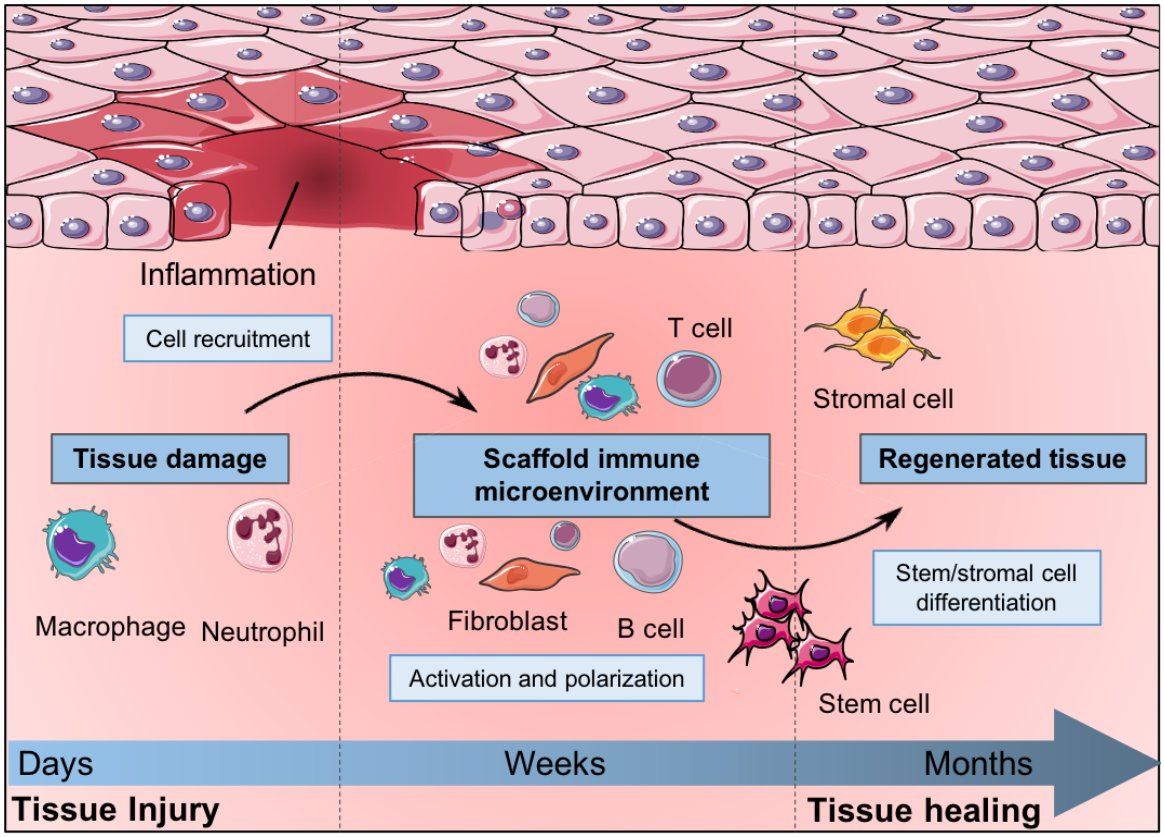

Figure 1.9 The immune system in repair and regeneration upon biomaterial implantation. Signals associated with injury or scaffold implantation recruit innate immune cells to the site of implantation, a process that is followed by activation and polarization of immune cells. These cells can then interact with other cell types in the scaffold microenvironment including stem and stromal cells. This will either result in tissue formation resembling the original host tissue or a more fibrous scar tissue depending on the cues provided and the immune microenvironment. Diagram generated using Servier medical Art, adapted from (200).

While it is well accepted that an early inflammatory response is required to initiate pro-regenerative responses post-injury, a shift from pro-inflammatory to anti-inflammatory function is required to maximize the regenerative capacity of progenitor cells and

minimize the destructive effects of prolonged inflammation. The temporal nature of the inflammatory responses is largely attributed to the transition of macrophages from a classically activated 'M1' state to alternatively activated 'M2' macrophages. While M1 macrophages play a role in early angiogenesis, a prolonged M1 presence can propagate tissue destruction and lead to fibrous scar formation and inferior tissue regeneration (201, 202). M2 macrophages, on the other hand, promote ECM synthesis, vessel formation and osteogenic differentiation (203, 204).

1.4.6 Innate immunity in tissue regeneration

Evidence supporting a central role for macrophages in the normal regeneration process comes from studies demonstrating that depletion of macrophages using clodronate liposomes results in impaired limb regeneration in salamander studies (205). Macrophage phenotype has also been shown to correlate with extent of host tissue repair with higher ratios of M2/M1 polarized macrophages associated with reduced fibrosis and scarring following injury (201, 204). In one particular study, biologically derived mesh materials were implanted into an abdominal wall defect model for 14 or 25 days and in situ macrophage polarization was examined. Histomorphological analysis revealed that an organised and appropriate tissue remodelling response was associated with the presence of M2 macrophages. Moreover, conditioned media from M2 polarised macrophages was shown to have higher chemotactic activity than that of M1 polarised macrophages, suggesting that the enhanced remodelling could be due to the enhanced cellular recruitment (206). ECM based materials have also been shown to have intrinsic M2 macrophage polarisation capabilities, and their degradation products have been reported to directly promote constructive macrophage polarisation in vitro which was associated with enhanced migration and myogenesis of skeletal muscle progenitor cells (207). Certainly, it is clear that M2:M1 ratio and the phenotypic profile of macrophages at early time points are important predictors of implant success, therefore understanding how to control/modulate this will be a key step in the design of next generation immune-informed biomaterials to enhance positive tissue remodelling, integration and regeneration.

1.4.7 Adaptive immunity in tissue regeneration

There is a growing body of literature highlighting the role of T cells in tissue repair and regeneration (208). Seminal work by Sadtler *et al* explored the role of the adaptive immune system on tissue regeneration. In the context of bone, both CD4+ and CD8+ have been associated with poor tissue regeneration (209, 210) and a negative correlation between the presence of differentiated CD8+ T cells in bone regeneration in humans has been reported (209). Furthermore, selected depletion of CD8+ T cells, or complete depletion of functional T and B cells using $Rag1^{-/-}$ mice, results in accelerated bone fracture repair (208, 211). Specific mediators of this inhibitory process have yet to be identified, however T cell derived IFNγ and TNFα have been shown to inhibit bone formation by MSCs (210), while delayed osteogenesis was observed in the presence of IFNγ and TNFα from memory CD8+ T cells (209). Conversely, a positive role for CD4+ Tregs in the context of skin, kidney and skeletal muscle repair and regeneration has been reported (212–215).

While the majority of research into the role of T cells in tissue repair and regeneration has focused on αβT cells, more recently preliminary work has demonstrated that γδT cells have a more pro-regenerative role (216, 217) as the absence of γδT cells results in loss of effective skin healing in both mice and humans (218). This subset of T cells appears 2-7 days post bone injury in murine models and they secret IL-17, which has been shown to enhance osteoblast function (217).

Taken together, much evidence points to a significant role for the immune system in tissue regeneration post biomaterial implantation. Immune cells appear to have distinct roles depending on the tissue type and characteristics of the implanted material, which can, in turn, influence the recruitment and differentiation of stem or progenitor cells to the injury site. This can ultimately determine the regenerative outcome in a process now coined ‘biomaterial-directed regenerative immunology’. As such, controlling immune responses is becoming an attractive approach in regenerative medicine and holds great promise for the treatment of conditions such as OA and osteochondral defects.

1.5 Research Question

The identification of drugs that effectively halt the destructive events in OA are lacking and much sought after. While several pathological mechanisms and OA-associated DAMPs have been identified, studies examining the effects of BCP crystals in humans are limited and characterization of the metabolic pathways induced by BCP crystals has not yet been examined. Therefore, the elucidation of macrophage phenotype and immune cell metabolism induced by BCP crystals is of considerable interest and may provide insights into new therapeutic targets for OA. Similarly, an extensive understanding of the immune response and cellular pathways activated by wear debris generated from orthopaedic implants is of interest in order to identify novel therapeutic targets for periprosthetic osteolysis.

Finally, there is now ample evidence to suggest that manipulation of the immune system is a very plausible therapeutic strategy to drive and induce tissue regeneration after biomaterial implantation. A key challenge here is to develop biomaterials that can control immune mediated responses and tissue healing in situ. Therefore, the final goal of this study is to explore the immunomodulatory properties of commercial and in-house generated biomaterials and immunomodulatory scaffolds for the purpose of enhancing bone tissue repair *in vivo.*

1.5.1 Specific Aims

- To determine if BCP crystals alter macrophage phenotype and the metabolic profile of primary human macrophages.
- To examine human immune cell activation and macrophage polarization following exposure to orthopaedic wear particles.
- To compare macrophage responses to micron and nano sized HA particles in primary human macrophage and to determine whether HA/nHA driven macrophage phenotype can influence MSC osteogenic differentiation in vitro.
- To examine the immune and tissue healing response to HA/nHA functionalised scaffolds using a rat femoral defect model.

Chapter 2:
Materials and Methods

2.1 Materials

All laboratory materials were purchased from Sigma-Aldrich (St. Louis, Missouri) unless otherwise stated.

2.1.1 Cell culture

Lymphoprep was purchased from Axis-Shield poC. MagniSort Human CD14 Positive Selection Kit and Human CD4 Positive Selection Kit were purchased from eBioscience. The following were all purchased from Sigma-Aldrich: Dulbecco's Phosphate-Buffered Saline (PBS), Roswell Park Memorial Institute (RPMI)-1640 Medium, Dulbecco's Modified Eagle's Media (DMEM), L-Glutamine, Penicillin-Streptomycin solution, Foetal Bovine Serum (FBS), Ethylenediaminetetraacetic Acid (EDTA), Trypsin-EDTA solution, Trypan Blue solution, L-ascorbic acid-2-phosphate, dexamethasone, β-Glycerolphosphate and Dimethyl Sulfoxide (DMSO). Human recombinant Monocyte Colony-Stimulating Factor (M-CSF), IL-4 and IFNy were purchased from Miltenyi Biotec.

2.1.2 Inhibitors and Reagents

BCP crystals in the form of hydroxyapatite, synthesised by alkaline hydrolysis of brushite as described in (219), were kindly provided by Professor Geraldine McCarthy (Mater Misericordiae University Hospital, Dublin). Ultrapure lipopolysaccharide (LPS) from E. Coli O111:B4 was purchased from Enzo Life Sciences. Piceatannol (Syk inhibitor) and methyl-B-cyclodextrin (M-βCD), Cytochalasin D, Cytochalasin B, Dynasore and 2DG were purchased from Sigma Aldrich (St. Louis, Missouri). R788/Fostamatinib (Syk inhibitor) was obtained from AdooQ Bioscience (Irvine, CA). MCC950 (NLRP3 inhibitor) was provided by Professor Luke O'Neill (TCD). SB203580 (p38 inhibitor) and PD98095 (ERK inhibitor) were purchased from Invivogen (San Diego, CA). Piceatannol and R788 were made up in ethanol, 2DG, MCC950, M-βCD, Cytochalasin D, Cytochalasin B and Dynasore were all made up in water and PD98095 and SB203580 were made up in DMSO. Inhibitor alone and vehicle alone control treatments were included to ensure no effect on pro-inflammatory macrophage profile (Figure app. 2). The IL-10 neutralizing antibody was obtained from eBioscience (San Diego, CA). Poly (methyl methacrylate) (PMMA) Microspheres were purchased from Polysciences Inc. (Warrington, PA) and hydroxyapatite particles (HA) were purchased from Sigma Aldrich (St. Louis, Missouri).

2.1.3 Western blotting

All chemicals used were purchased from Sigma-Aldrich unless otherwise stated. Acrylamide was purchased from Fisher. SeeBlue Plus2 Pre-Stained Protein Standard was purchased from Invitrogen. Immobilon polyvinylidene difluoride (PVDF) membrane and Enhanced Chemiluminescent (ECL) Horseradish-Peroxidase (HRP) Substrate were purchased from Merck Millipore.

2.1.4 Primary antibodies

Anti-phospho-Syk, anti-Syk, anti-phospho-p38, anti-p38, anti-phospho-ERK (1/2) and anti-ERK (1/2) were all purchased from Cell Signalling 38 Technology. Anti-CD206, anti-CD163, anti-phospho-STAT3, anti-C-Maf, Glut1, HIF1α and HK2 were purchased from Abcam. Anti-β-actin-peroxidase was purchased from Sigma-Aldrich.

2.1.5 Secondary antibodies

Anti-rabbit IgG (whole molecule)-peroxidase, anti-mouse IgG (whole molecule)-peroxidase and anti-goat IgG (whole molecule)-peroxidase were purchased from Sigma-Aldrich.

2.1.6 Flow cytometry

Anti-mouse Ig CompBeads were purchased from BD. FITC-conjugated DQ Ovalbumin, MitoSox Red and Mitotracker Red TM were purchased from Invitrogen. Fixable Viability Dye eFluor506 were all purchased from eBioscience. The following fluorochrome conjugated antibodies were purchased from eBioscience or BioLegend as specified in Tables 2.1 and 2.2.

Table 2.1 Antibodies for flow cytometry of *in vitro* macrophage studies

Specificity	Fluorochrome	Clone	Supplier
CD14	FITC	61/D3	eBioscience (San Diego, CA)
CD11b	APC	M1/70	eBioscience (San Diego, CA)
CD163	BV421	GHI/61	BioLegend (San Diego, CA)
CD206	APC	19.2	eBioscience (San Diego, CA)
CD86	PerCP-Cy5	IT2.2	eBioscience (San Diego, CA)
CD80	PerCP-Cy7	2D10.4	eBioscience (San Diego, CA)
CD40	eFluor450	5C3	eBioscience(San Diego, CA)

Table 2.2. Antibodies for flow cytometry for *in vivo* studies

Specificity	Fluorochrome	Clone	Supplier
CD14	FITC	HCD14	eBioscience (San Diego, CA)
CD86	PerCP-e710	IT2.2	BioLegend (san Diego, CA)
CD206	APC	19.2	eBioscience (San Diego,CA)
CD11b	APC-Cy7	GHI/61	eBioscience (San Diego, CA)
CD45	BV785	30-F11	BioLegend (san Diego, CA)
CD3	PE	17-A2	eBioscience (San Diego, CA)
Ly6G	Pacific Blue	1A8	eBioscience (San Diego, CA)
CCR2	PE-Cy7	SA203G11	BioLegend (san Diego, CA)
CX3CR1	BV650	SA011F11	BioLegend (san Diego, CA)
Ly6C	FITC	AL-21	eBioscience (San Diego, CA)
Siglec F	PE-Dazzle	E50-2440	eBioscience (San Diego, CA)
MHCII	APC	M5144.15.2	BioLegend (san Diego, CA)
CD19	PE-Dazzle	1D3	eBioscience (San Diego, CA)
F4/80	PerCP-CY5.5	BM8	eBioscience (San Diego, CA)

2.1.7 Seahorse extracellular flux analysis

Seahorse XF/XFe 96 well cell culture microplates, extracellular flux assay kits, XF calibrant and XF assay media was purchased from Agilent Technologies. Oligomycin A was purchased from Cayman Chemicals. Carbonyl cyanide-p-trifluoromethoxyphenylhydrazone (FCCP) was purchased from Santa Cruz Biotechnology. Rotenone, antimycin A and 2-deoxy-D-glucose (2-DG) were purchased from Sigma-Aldrich.

2.1.8 Confocal microscopy

Light-protective cell culture microplates were purchased from iBidi. Anti-CD80, anti-CD206, anti-vWF and anti-αSMA were all purchased from Abcam. Fluorochrome-conjugated secondary anti-rabbit Alexa Fluor 488 and anti-rabbit Alexa Fluor 647 antibodies were was purchased from Abcam. 4',6-diamidino-2-phenylindole (DAPI) was purchased from VWR.

2.1.9 Polymerase Chain Reaction (PCR)

High pure RNA Isolation Kit was purchased from Roche (Basel, Switzerland). Applied Biosystems High capacity cDNA transcription kit, TaqMan fast universal PCR Master Mix and TaqMan probes for eukaryotic 18S rRNA, human CCL19, CXCL9, CXCL10, CXCL11, MRC1, CCL13 and S100A8 were purchased from Life Technologies (Calsbad, CA). iTaq Universal SYBR Green Supermix was purchased from Bio-Rad Laboratories (Hercules, California). Forward and reverse oligonucleotide primers for GAPDH, BMP2, ALP, OPN, OCN, Runx2, Osx, VEGF, bFGF, ANG1, HK2, Glut1, HIF1α, HIF2α and PFKβ3 were purchased from Sigma-Aldrich (St. Louis, Missouri). The primer sequences are detailed in Table 2.3.

Table 2.3 Primer sequences

Gene	Forward	Reverse
GAPDH	ACAGTTGCCATGTAGACC	TTTTTGGTTGAGCACAGG
BMP2	TCCACCATGAAGAATCTTTG	TAATTCGGTGATGGAAACTG
ALP	TCTTCACATTTGGTGGATAC	ATGGAGACATTCTCTCGTTC
OPN	GACCAAGGAAAACTCACTAC	CTGTTTAACTGGTATGGCAC
OCN	TTCTTTCCTCTTCCCCTTG	CCTCTTCTGGAGTTTATTTGG
Runx2	AAGCTTGATGACTCTAAACC	TCTGTAATCTGACTCTGTCC
Osx	TGAGGAGGAAGTTCACTATG	CATTAGTGCTTGTAAAGGGG
VEGF	GCAGAATCATCACGAAGTGGTG	TCTCGATTGGATGGCAGTAGCT
bFGF	AAGAGCGACCCTCACATCAAG	ACACTCCTTTGATAGACACAACTC
ANG1	TACTCAGTGGCTGCAAAAACTTGA	ATCTCCGACTTCATGTTTTCCACA
HIF1α	GAAACTTCTGGATGCTGGTGATTT	GCAATTCATCTGTGCTTTCATGTCA
HIF2α	AAGCTCCTCTCCTCAGTTTGCT	GTACAAGTTGTCCATCTGCTGG
HK2	TTCTTGTCTCAGATTGAGAGTGAC	TTGCAGGATGGCTCGGACTTG
Glut1	GAACTCTTCAGCCAGGGTCC	ACCACACAGTTGCTCCACAT
PFKβ3	CCATGAAAGTCCGGAAGCAATG	GCTTTTGACATCTCTCAAGGCAG

2.2 Methods

2.2.1 Cell Culture

Cells were cultured at 37°C with an atmosphere of 95% humidity and 5% CO2. RPMI and DMEM cell culture media were supplemented with 10% FBS, 2 mM L-Glutamine, 100 U/ml penicillin and 100 µg/ml streptomycin unless stated otherwise. Cell numbers and viability were determined by performing cell counts in trypan blue. Cells were diluted in trypan blue and 10 µl was loaded onto a Hycor KOVA Glastic cell counter slide and viewed under a light microscope. Cell viability was assessed by dye exclusion. The number of viable cells was determined using the following formula:

$$Number\ of cells/ml = \#\ cells\ counted \times dilution\ factor \times 10^4$$

2.2.2 Isolation of PBMCs from human venous blood

This study was approved by the research ethics committee of the School of Biochemistry and Immunology, Trinity College Dublin and is in accordance with the Declaration of Helsinki. PBMC were isolated from leukocyte-enriched buffy coat packs (the plasma depleted fraction of anti-coagulated blood) obtained from anonymous healthy donors with consent from the Irish Blood Transfusion Service, St James' Hospital, Dublin. Blood was diluted in sterile PBS and centrifuged at 1250 g for 10 minutes at room temperature, with the brake off. The buffy coat layer containing leucocytes was removed (Figure 2.1 A), and diluted in sterile PBS. 25 ml of diluted buffy coat was layered over 20 ml LymphoPrep and PBMC were isolated by density-gradient centrifugation at 800 g for 20 minutes at room temperature, with the brake off. The PBMC layer was removed from the interface of the gradient (Figure 2.1 B) and washed twice in sterile PBS by centrifugation at 650 g for 10 minutes at room temperature. Isolated PBMC were re-suspended and cultured in RPMI.

2.2.3 Isolation of CD14+ monocytes

CD14+ monocytes were isolated from PBMC by magnetic-activated cell sorting (MACS), using the Magnisort CD14 positive selection kit (eBioscience). PBMC were washed in MACS buffer (PBS supplemented with 2% FBS and 2 mM EDTA) and pelleted by centrifugation at 300 g for 5 minutes. PBMC were re-suspended in MACS buffer at 1 x 10^8 cells/ml in a 12 x 75 mm 5ml tube and incubated with anti-CD14 biotin (10 µl per 100 µl cells) for 10 minutes at room temperature. Cells were then washed in 4 ml MACS buffer and pelleted by centrifugation at 300 g for 5 minutes. Supernatant was discarded, cells were re-suspended in their original volume of MACS buffer and incubated with MagniSort positive selection beads (15 µl per 100 µl cells) for 10 minutes at room temperature. The volume was then adjusted to 2.5 ml and the tube placed inside the magnetic field of a Magnisort magnet for 5 minutes. The negative fraction was then poured off by inverting the tube while held inside the Magnisort magnet, and the remaining cells were re- suspended in 2.5 ml MACS buffer. This step was repeated three times and then the positive fraction containing the CD14+ monocytes was re-suspended in RPMI and counted, CD14+ monocyte purity was confirmed by flow cytometry and was routinely greater than 90%.

2.2.4 Culture of monocyte derived macrophages

Primary human macrophages were cultured from CD14+ monocytes isolated from healthy human PBMCs. Purified CD14+ monocytes were cultured at 1 x 10^6 cells/ml in RPMI supplemented with human recombinant M-CSF (50 ng/ml). On the third day of culture half the media was carefully removed from the wells and replaced with fresh media containing M-CSF. On the sixth day of culture the purity of macrophages was determined by expression of CD14 and CD11b by flow cytometry; CD14+ CD11b+ cells were defined as fully differentiated macrophages and were routinely greater than 95% (Figure 2.2).

2.2.5 Culture of adult human bone marrow-derived mesenchymal stem cells (MSCs)

Bone marrow aspirates, obtained from anonymous donors (Lonza), were washed in PBS and centrifuged at 900 x g for 10 minutes. Supernatant was gently aspirated and cells were plated at 4000-5000 MSCs/cm2 in complete media (DMEM, 10% FBS, 1% P/S, 5ng/ml bFGF2). Cells were cultured for up to two weeks (until colonies form and cells proliferate), with media being replenished every 3-4 days. Cells were washed with PBS in between feedings to dislodge red blood cells. Adherent cells were expanded up to P2 and were characterized by their plastic adherence and fibroblastic nature. Colony Forming Unit assays were used to quantify proliferation, and Trilineage Potential assays were used to determine pluripotency. For in vitro assays, MSCs were seeded at 5 x 104 cells/ml in standard culture media, high glucose Dulbecco's modified Eagle's medium (4.5 mg/mL D-glucose and 200 mM L-glutamine; hgDMEM) supplemented with 10% foetal bovine serum (FBS) and penicillin (100 U/mL) – streptomycin (100 g/mL) and expanded in a humidified atmosphere at 37 °C, 5% CO_2, and 20% pO_2.

2.2.6 HUVEC Tube Formation

Matrigel (100 µl; BD Biosciences, San Jose, CA, USA) was plated in 48-well culture plates after thawing on ice and allowed to polymerise for 45 min at 37°C in humidified air with 5% CO2. HUVECs (2 × 10^4) were plated in serum-free Microvascular Endothelial Cell Growth Medium-2 (Lonza) without or with VEGF (10 ng/ml) as negative and positive controls respectively. Alternatively, cells were seeded in 50% supplemented serum-free

conditioned media from micron or nano particle treated macrophages. Cells were imaged using phase-contrast microscopy every 2 hours to assess endothelial cell tubule formation. Average branch length, average number of branches and average number of junctions were quantified using ImageJ.

2.2.7 Macrophage Conditioned media experiment

Primary human macrophages were cultured with 250 μg/ml of micron or nano particles for 24 hours. Conditioned media (CM) was harvested and centrifuged at 300 x g for 10 minutes to deplete media of any residual particles. A calcium assay of the CM pre and post centrifugation confirmed that media post centrifugation had comparable levels of calcium to that of media alone that had no Hydroxyapatite particle treatment indicating that this CM was Calcium phosphate free and no particles remained. Human MSCs were cultured in the CM for 48 hours and then cultured for a further 7 days in osteogenic media (DMEM + GlutaMAX media supplemented with 100mM dexamethasone, 10mM β-Glycerolphosphate, and 0.05mM L-ascorbic acid-2-phosphate).

2.2.8 Wound Scratch Assay

MSCs were seeded onto 6 well plates and grown to confluence prior to being serum starved for 16 hours. A single scratch wound was induced through the middle of each well with a sterile pipette tip, cells were washed with media to remove lifted cells and media was replaced fresh serum free media. Cells were subsequently either left in serum free control media or cultured in serum free media from untreated, micron or nanoparticle treated macrophages for 24 hours. MSC migration across the wound margins from 24 hours was assessed and photographed using a phase-contrast microscope (Olympus 1X83). Semi-quantitative analysis of cell repopulation of the wound was assessed by three blinded observers. Tiff images of the scratch wound assays were taken at × 20 magnification at 0 and 24 hours. The mean number of cells that migrated back into the wound was calculated from six individual measurements for each wound at each time point. This process was carried out for all biological repeats. Total numbers of cells were also counted in each group to assess for proliferation.

2.2.9 Flow cytometry

2.2.9.1 Cell surface marker staining

$CD14^+$ monocytes post positive MACS sorting were stained with a fluorochrome-conjugated antibody specific for CD14 for 15 minutes at room temperature. Primary human macrophages were plated at a concentration of 1 x 10^6 cells/ml in a 48-well plate and stimulated with particulates for 6 or 24 hours. Cells were Fc blocked for 15 minutes prior to staining for surface markers. Cells were stained with fluorochrome conjugated antibodies specific for CD14, CD11b, CD80/86, CD40, CD206 and CD163 fixed with 4% paraformaldehyde (PFA) washed and acquired on a FACSCantoTM II or LSRFortessa™ (both BD Biosciences). Compensation beads singly stained with every fluor channel utilised were acquired to adjust for spectral overlap. An unstained sample was also run as a control.

2.2.9.2 DQ-Ovalbumin

For assessment of phagocytosis or antigen uptake, DQ-Ova was prepared to a stock concentration of 1 mg/ml. Cells were incubated with fresh media containing 500 ng/ml DQ-Ova for 20 minutes at 37°C, followed by an incubation at 4°C for 10 minutes. Cells were then washed in PBS, centrifuged at 300 x g for 5 minutes, re-suspended in PBS and immediately acquired. Cells treated with media containing no DQ-Ova were used as a gating control for DQ-Ova positive cells. Gating strategy provided in Appendix 1.1.1

2.2.9.3 Mitosox Red labelling

In order to analyse mitochondrial superoxide production (mitochondrial ROS), cells were stained with MitoSox Red. Cells were washed in warm PBS and centrifuged at 300 g for 5 minutes. Supernatants were removed and cells were stained with MitoSox Red at a final concentration of 20 nM in PBS. Cells were incubated for 15 minutes at 37 °C. Cells were washed in FACS buffer and centrifuged at 300 x g for 5 minutes. Supernatants were removed and cells were acquired immediately.

2.2.9.4 Mitotracker Red labelling

In order to analyse mitochondrial mass, cells were stained with Mitotracker Red. Cells were washed in warm PBS and centrifuged at 300 g for 5 minutes. Supernatants were removed and cells were stained with Mitotracker Red at a final concentration of 4 nM in PBS. Cells were incubated for 15 minutes at 37°C. Cells were washed in FACS buffer and centrifuged at 300 x g for 5 minutes. Supernatants were removed and cells were acquired immediately.

2.2.9.5 Acquisition, compensation and analysis

Where flow cytometry experiments contained more than one fluorochrome, single-stained controls were prepared for each fluorochrome using BD CompBeads in order to calculate spectral compensation. Samples were acquired on either a BD FACSCanto II or LSRFortessa flow cytometer. All flow cytometry data analysis was performed using FlowJo v10 (Treestar Inc) software. Cells were gated on according to the gating strategies presented in Figure app. 1.

2.2.10 Fluorescence lifetime image microscopy

Two-photon excited NAD(P)H-FLIM imaging was used to measure levels of free and protein-bound NADH within treated and untreated macrophages. This was performed using a custom upright (Olympus BX61WI) laser multiphoton microscopy system equipped with Titanium:sapphire laser (Chameleon Ultra, Coherent®, USA) and water-immersion 25x objective (Olympus, 1.05NA) with a temperature controlled stage. Two-photon excitation of NAD(P)H was performed at excitation wavelengths of 760 nm. A 455/90 nm bandpass filter was used to isolate the NAD(P)H fluorescence emission. 512 × 512 pixel images were acquired with a pixel dwell time of 3.81 µs and 30-second collection time. A PicoHarp 300 TCSPC system operating in the time-tagged mode coupled with a photomultiplier detector assembly (PMA) hybrid detector (PicoQuanT GmbH, Germany) was used for fluorescence decay measurements yielding 256-time bins per pixel.

Fluorescence lifetime images with their associated decay curves for NAD(P)H were obtained. The overall decay curve was generated by the contribution of all pixels and was fitted with a double exponential decay curve for NAD(P)H from the equation below.

$$I(t) = \alpha_1 e^{-\frac{t}{\tau_1}} + \alpha_2 e^{-\frac{t}{\tau_2}} + c$$

I(t) corresponds to the fluorescence intensity measured at time (t) after laser excitation; α_1 and α_2 represents the fraction of the overall signal proportion of a short and long component lifetime component, respectively. τ_1 and τ_2 are the short and long lifetime components, respectively; C corresponds to background light. χ^2 represents the goodness of multi-exponential fit to the raw fluorescence decay data. In this study all the values with $\chi^2 < 1.3$ were considered 'good' fits.

For NAD(P)H, a two-component fitting was also used to differentiate between the free (τ_1) and protein-bound (τ_2) NAD(P)H: the average lifetime (τ_{avg}) of NAD(P)H for each pixel was calculated by a weighted average of both free and bound lifetime contributions (Eq. 2), with fraction α_1 relating to free NAD(P)H, and fraction α_2 correspond to protein-bound NAD(P)H.

$$\tau_{avg} = \frac{(\alpha_1 \times \tau_1) + (\alpha_2 \times \tau_2)}{(\alpha_1 + \alpha_2)}$$

2.2.11 SDS-PAGE, Gel staining and Western Blot

2.2.11.1 Sample preparation

Primary human macrophages were plated at a concentration of 1 x 10^6 cells/ml in a 6-well plate and stimulated with particles for the appropriate time points. Cells were lysed by the addition of high stringency lysis buffer (50 mM HEPES, 100 mM NaCl, 1 mM EDTA, 10% Glycerol, 1% NP-40, pH 7.5) containing 1% phosphatase inhibitor cocktail 3. Samples were centrifuged at 13,000 rpm for 5 minutes and lysates were transferred to a new microcentrifuge tube for determination of protein concentration.

2.2.11.2 SDS-PAGE

Samples were prepared by the addition of 5x Laemmli buffer (containing 25% β-mercaptoethanol) in a ratio of 1:4 prior to boiling at 100°C for 5 minutes. Depending on the size of the target protein, either 7.5% or 12% polyacrylamide gels were used (see Table 2.4 for composition of gels). Samples and a pre-stained protein standard were loaded and resolved through the gel at 120 volts (V) for 90 minutes.

Table 2.4 Composition of SDS-Polyacrylamide Gels

	7.5 % Resolving Gel	12% Resolving Gel	15% Resolving Gel	Stacking Gel
30% Acrylamide	3.75 ml	6 ml	7.5 ml	0.67 ml
H_2O	7.15 ml	4.9 ml	3.4 ml	2.7 ml
1.5M Tris-HCl	3.8 ml	3.8 ml	3.8 ml	-.
1 M Tris -HCl	-	-	-	0.5 ml
10% SDS	0.15 ml	0.15 ml	0.15 ml	40 µl
10% APS	0.15 ml	0.15 ml	0.15 ml	40 µl
Temed	6 µl	6 µl	6 µl	6 µl

2.2.11.3 Transfer of proteins onto PVDF membrane

A wet transfer sandwich was prepared in the following order: sponge, filter paper, gel, PVDF membrane, filter paper, sponge. PVDF membrane was first activated by submersion in methanol. All other components of the transfer sandwich were first submerged in transfer buffer. The transfer sandwich was placed into the transfer system with the gel on the cathode side and the membrane on the anode side. After ensuring that there were no air bubbles in the system, the proteins were transferred at 200 milliamperes (mA) for 75-90 minutes depending on the size of the protein.

2.2.11.4 Immunodetection of proteins

Following the transfer, the membrane was incubated in blocking buffer under agitation for 2 hours at room temperature. For detection of phospho-proteins, the blocking buffer

and diluent for antibodies was 3% (w/v) BSA in 1 X TBST. For detection of all other proteins, the blocking buffer and diluent was 5% (w/v) milk in 1 X TBST. The membrane was incubated in primary antibody (see Table 2.5 for dilutions) with agitation, overnight at 4°C. The membrane was washed 5 times for 5 minutes each with 1X TBST prior to incubation in secondary antibody (See Table 2.5) for 2 hours at room temperature. The membrane was washed a further 5 times for 5 minutes each and then developed with freshly prepared ECL using Chemi-Luminescent gel documentation system (Alpha-Innotech). The intensity of protein bands was quantified densitometrically, using ImageJ software.

Table 2.5 Immunoblotting antibody dilutions

Primary Antibody	Dilution	Secondary Antibody	Dilution
Anti-phospho-Syk	1:1000	Anti-Rabbit	1:1000
Anti-Syk	1:1000	Anti-Mouse	1:1000
Anti-phospho-p38	1:1000	Anti-Rabbit	1:8000
Anti-p38	1:1000	Anti-Rabbit	1:8000
Anti-phospho-ERK (1/2)	1:2500	Anti-Rabbit	1:5000
Anti-ERK (1/2)	1:5000	Anti-Rabbit	1:5000
Anti-Hexokinase 2	1:1000	Anti-mouse	1:3000
Anti-Glut1	1:1000	Anti-rabbit	1:2000
Anti-HIF1α	1:1000	Anti-mouse	1:2000
Anti-phospho-Stat-3	1:500	Anti-Rabbit	1:2000
Anti-CD206	1:1000	Anti-Rabbit	1:3000
Anti-CD163	1:1000	Anti-Rabbit	1:8000
Anti-cMaf	1:1000	Anti-Rabbit	1:1000
Anti-β-actin-peroxidase	1:50,000	-	-

2.2.12 Polymerase Chain reaction (PCR)

2.2.12.1 Cell treatments

Human macrophages were plated at a concentration of 1 x 10^6 cells/ml in a 24-well plate and stimulated with particles for the appropriate time points. Human MSCs were plated at a concentration of 1 x 10^5 cells/ml in a 6-well plate and cultured in media alone or conditioned media from untreated, HA or nanoHA treated macrophages for 48 hours and lysed at this point, alternatively cells were cultured in osteogenic induction media for a further 7 days.

Following treatments, RNA was extracted using the high pure RNA Isolation Kit as described below.

2.2.12.2 RNA extraction

Supernatants were removed and cells were washed once with PBS before the addition of 400 µl of lysis/-binding buffer and 200 µl of PBS per well. The lysates were transferred to a High Pure Filter Tube that was inserted into a collection tube. Samples were centrifuged at 8,000 x g for 15 seconds (Spectrafuge 24 D). The flowthrough liquid was discarded and 90 µl of DNase incubation buffer with 10 µl DNase I were added to each Filter Tube and incubated for 15 minutes at room temperature. 500 µl of Wash Buffer I was then added to the Filter Tubes which were centrifuged at 8,000 x g for 15 seconds. The flow-through liquid was discarded and 500 µl of Wash Buffer II was added to the Filter Tubes which were centrifuged again at 8,000 x g for 15 seconds. The flow-through liquid was discarded and a further 200 µl of Wash Buffer II was added to Filter Tubes and centrifuged at 13,000 x g for 2 minutes. The Collection Tubes were discarded and the Filter Tubes were placed into sterile, RNase-free 1.5 ml microcentrifuge tubes. 60 µl of Elution Buffer was added to the filter tubes and centrifuged at 8,000 x g for 1 minute. The concentration of eluted RNA in each sample was determined using a NanoDrop 2000c UV-Vis Spectrophotometer and then equalised by the addition of Elution Buffer, where necessary.

2.2.12.3 cDNA synthesis

cDNA synthesis was then carried out using the High capacity cDNA reverse transcription kit (Applied Biosystems). A 2X Reverse Transcription (RT) master mix was prepared with the components in Table 2.6.

Table 2.6 Components and volumes required for the 2X RT Master Mix

Component	Volume added (per sample)
10X RT Buffer	2 µl
25X dNTP Mix (100mM)	0.8 µl
10X RT Random Primers	2 µl
Multiscribe Reverse Transcriptase	1 µl
Total added (per sample)	5.8 µl

14.2 µl of RNA and 5.8 µl of the 2X RT master mix were added to RNase-free PCR tubes and the reverse transcription (see Table 2.7) was performed using the PTC-200 Peltier Thermal Cycler.

Table 2.7 cDNA Reverse Transcription Reaction

	Step 1	Step 2	Step 3	Step 4
Temperature (°C)	23	37	85	4
Time (Minutes)	10	120	5	Indefinitely

2.2.12.4 Real-time Polymerase Chain reaction (PCR)

Two protocols were used for analysis of gene expression by real-time PCR.

TaqMan protocol:

Real-time PCR was carried out on transcripts using the TaqMan fast universal PCR Master Mix (Applied Biosystems) and predesigned TaqMan gene expression primers. Samples were made up as detailed in Table 2.8, into a 96-well PCR microplate. The PCR reaction is detailed in Table 2.9.

Table 2.8 Components and volumes required for qPCR reaction

Component	Volume added (per sample)
18S rRNA Probe	0.5 µl
Target Probe	0.5 µl
TaqMan Universal PCR Master Mix	4.5 µl
cDNA sample	4.5 µl
Total Volume	10 µl

Table 2.9 Thermal cycling parameters for iTaq Universal SYBR Green real-time PCR

	Step 1	Step 2	Step 3	Step 4	Step 5
Temperature (°C)	95	95	60	Plate Read	Go to Step 2
Time (Seconds)	20	3	30	-	X 39

iTaq Universal SYBR Green protocol:

Real-time PCR was carried out on human Mesenchymal Stem cell cDNA transcripts using the iTaq Universal SYBR Green Supermix and oligonucleotide primers. Reactions were made up, as detailed in Table 2.10, into a 96-well PCR microplate. The PCR reaction is detailed in Table 2-11.

Table 2.10 Components and volumes required for iTaq Universal SYBR Green reaction

Component	Volume added (per sample)
Forward primer	0.8 µl
Reverse primer	0.8 µl
RNase free water	7.4 µl
iTaq Universal SYBR Green	9.5 µl
cDNA sample	1.5 µl
Total Volume	20 µl

Table 2.11 Thermal cycling parameters for iTaq Universal SYBR Green real-time PCR

	Step 1	Step 2	Step 3	Step 4	Step 5	Step 6
Temperature (°C)	95	95	60	Plate Read	72	Go to Step 2
Time (Seconds)	10 (mins)	15	30	-	30	X 40

The real-time PCR reactions (detailed in Table 2.9 and Table 2.11) were performed using the BioRad CFX Touch Real-Time PCR detection system. For each sample, mRNA concentration was normalised using the crossing threshold of the housekeeping genes 18s ribosomal RNA or GAPDH. Gene expression, relative to untreated samples, was determined using the $2^{-\Delta\Delta CT}$ algorithm.

2.2.13 Measurement of cytokine production by ELISA

The concentrations of human IL-1β, IL-1α, TNFα, IL-6, IL-8 and IL-10 or IFNγ and IL-10 in serum from cardiac punctures of rats were quantified by ELISA, according to the manufacturer's protocol. 50-75 µl of capture antibody diluted in coating buffer was applied to high-binding 96-well plates (Greiner Bio-one). Plates were incubated overnight at 4°C, capture antibody was removed and non-specific binding sites were blocked with appropriate blocking solution (1% (w/v) BSA) for 1 hour at room temperature. After blocking, plates were washed in PBS-tween solution, dried and supernatant samples were loaded into wells in triplicates either neat or diluted appropriately with assay diluent. A standard curve of serially diluted recombinant cytokine standard was also loaded onto the plates in triplicate. Blank wells, containing assay diluents only, were included on each plate to allow the subtraction of background from each sample. Samples were incubated overnight at 4°C. After washing, biotinylated detection antibody was added to each well and incubated for 2 hours at room temperature. Plates were washed and horseradish-peroxidase (HRP) conjugated to streptavidin was applied to wells for 30 minutes in the dark. Wells were thoroughly washed and the substrate, TMB or OPD, was added as required by manufacturer. The enzyme-mediated colour reaction was protected from light while developing and

stopped with the addition of 2N H_2SO_4. The optical density of the colour was determined by measuring the absorbance at 450 nm using a microtiter plate reader. A standard curve was generated using serial diluted protein standards and used to determine the concentration of cytokine in the supernatant.

2.2.14 Seahorse XF/XFe 96 Analyser

2.2.14.1 Macrophage Seahorse experiments

The Seahorse XF/XFe 96 analyser simultaneously measures in real time the oxygen consumption rate (OCR), a measure of the rate of oxidative phosphorylation, and extracellular acidification rate (ECAR), a measure of the rate of glycolysis, in the medium directly surrounding a single layer of cells.

Macrophages were cultured at 1 x 10^6 cells/ml for 6 days prior to re-seeding at 2 × 10^5 cells/well in a Seahorse 96-well microplate and allowed to rest for 5 hours prior to BCP or LPS stimulation. The Seahorse cartridge plate was hydrated with XF calibrant fluid and incubated in a non-CO_2 incubator at 37°C for a minimum of 8 h prior to use. To determine the effect of particles, macrophages were incubated with particles (50 µg/ml for BCP, 250 µg/ml for HA and nanoHA) for 6 or 24 hours, prior to analysis using a Seahorse XFe96 analyser. 30 min prior to placement into the XF/XFe analyser, cell culture medium was replaced with complete XF assay medium (Seahorse Biosciences; supplemented with 10 mM glucose, 1 mM sodium pyruvate, 2 mM L-glutamine, and pH adjusted to 7.4) and incubated in a non-CO2 incubator at 37°C. Blank wells (XF assay medium only) were prepared without cells for subtracting the background oxygen consumption rate (OCR) and extracellular acidification rate (ECAR) during analysis.

Oligomycin (1µM; Cayman Chemicals), carbonyl cyanide-p trifluoromethoxyphenylhydrazone (FCCP) (1µM; Santa Cruz biotechnology), rotenone (500 nM), and antimycin A (500 nM) and 2-deoxy-D-glucose (2-DG) (25mM; all Sigma-Aldrich) were prepared in XF assay medium and loaded into the appropriate injection ports on the cartridge plate and incubated for 10 min in a non-CO_2 incubator at 37°C. OCR and ECAR were measured over time with sequential injections of oligomycin, FCCP, rotenone and antimycin A and 2-DG.

Table 2.12. Seahorse protocol

Step	Action
1	Equilibrate
2	Mix (3 mins)
3	Wait (2 mins)
4	Measure (3 mins)
5	Repeat steps 2-4 x2
6	Inject Port A
7	Repeat steps 2-4 x3
8	Inject Port B
9	Repeat steps 2-4 x3
10	Inject Port C
11	Repeat steps 2-4 x3
12	Inject Port D
13	Repeat steps 2-4 x3
14	End protocol

2.2.14.2 Seahorse analysis

Analysis of results was performed using Wave software (Agilent Technologies). The rates of basal glycolysis, max glycolysis, glycolytic reserve, basal respiration, max respiration, ATP production and respiratory reserve were calculated as detailed in Table 2.13:

Table 2.13. Seahorse calculations

Rate	Calculation
Non-glycolytic ECAR	Average ECAR values after 2-DG treatment.
Basal glycolysis	Average ECAR values prior to oligomycin treatment – non-glycolytic ECAR
Max glycolysis	Average ECAR values after oligomycin & before FCCP treatment
Glycolytic reserve	Max glycolysis – basal glycolysis
Non-mitochondrial OCR	Average OCR values after rotenone/antimycin A & before 2-DG treatment
Basal respiration	Average OCR values prior to oligomycin treatment – non-mitochondrial OCR
Max respiration	Average OCR values after FCCP & before rotenone/antimycin A treatment
Non-ATP respiration	Average of OCR values after oligomycin & before FCCP treatment
ATP production	Basal respiration – non-ATP respiration
Respiratory reserve	Max respiration – basal respiration
Mitochondrial ATP production rate	OCRATP (pmol O2/min) *2 (pmol O/pmol O2) *P/O (pmol ATP/pmol O)
Glyco ATP Production Rate	Equivalent to glycoPER (pmol H+/min)
ATP Production Rate	GlycoATP Production Rate + mitoATP Production Rate

2.2.15 Cell Staining

2.2.15.1 Alizarin Red staining

To evaluate calcium deposition, MSCs in monolayer culture at day 7 or 14 were stained with alizarin red (AR). Cell culture supernatants were removed and cells were rinsed with PBS prior to being fixed in 100% ethanol for 10 minutes at room temperature. This was removed and cells were rinsed again with PBS prior to the addition of 1% AR. AR was

removed after 2 minutes, cells were washed with deionised water and fixed again with 100 % ethanol. Stained samples were air dried and images were captured using phase transmission microscope (Olympus, UK). Semi-quantitative analysis of AR staining was done through extraction of the dye using 10% cetylpyridinium chloride and measuring the absorbance at 540 nm.

2.2.15.2 Immunocytochemistry

For immunocytochemical analysis of macrophage phenotype, particle-treated macrophages were fixed with 4% PFA, incubated in Block and Perm solution (3% BSA with 0.1% Triton X) for 1 hour at room temperature. Cells were then incubated in primary antibodies against CD206 or CD80 (1:1000 and 1:500 dilutions respectively) overnight at 4°C. Cells were washed and incubated in secondary antibodies for 1 hour at room temperature (anti-rabbit Alexa Fluor 488 and anti-rabbit Alexa Fluor 647 for CD206 and CD80 respectively; both 1:1000). Cells were washed and counterstained with DAPI (1 µg/ml) for 15 minutes and imaged using a Leica SP8 scanning confocal microscope.

2.2.16 Preparation of micron and nanoparticle suspensions

2.2.16.1 Synthesis of nanoHydroxyapatite particles

Bone mimetic nano-sized Hydroxyapatite particles were prepared following a previously described protocol (220). Briefly, a solution of 20 mM calcium chloride was added to a solution of 12 mM sodium phosphate, containing 0.017% DARVAN 821A (RT Vanderbilt) as the dispersant, and nanoHydroxyapatite particles were precipitated. This solution was centrifuged, reconstituted in endotoxin-free water and filtered through a 0.2 µm filter to remove aggregated particles.

2.2.16.2 Preparation of micron Hydroxyapatite particle suspension

Commercial micron HA particles ($Ca_5(OH)(PO_4)3$ 18-20were purchased from Sigma Aldrich (Cat# 04238), weighed out and resuspended at a concentration of 5 mg/ml in endotoxin-free water, sonicated for 10 min and stored at 4°C.

2.2.16.3 Particle sized determination

Particle size distributions of micron sized HA particles and nanoHA particles were measured using dynamic light scattering (DLS) (ZetaSizer 3000 HS, Malvern instruments, UK). Measurements were carried out under monochromatic, coherent He-Ne laser light of fixed wavelength (633nm) at room temperature with each size determination yielding an average particle size expressed as the mean diameter (Zave) together with a graph of the size range.

2.2.16.4 Structural and Physical characterization of Particles

Powder X-ray diffraction (XRD) analysis was performed in a Bruker D8 Discover diffractometer operating in the reflection mode at CuKα radiation of wavelength 0.154 nm and 2Θ values from 10° to 60°, using a step scan of 0.02°/step and held for 2s/step. The Fourier-transform infrared (FTIR) spectroscopy experiments from powdered samples were conducted with a SpectrumOne (Perkin–Elmer) spectrometer in attenuated total reflection (ATR) mode. The spectra were recorded by accumulating 16 scans in the range of 650–4000 cm-1 at a resolution of 4 cm-1. The solid-state Nuclear Magnetic Resonance (NMR) spectroscopy experiments were conducted on a Bruker 400 MHz Avance-III spectrometer running TopSpin software. Powdered samples were packed into 4.0 mm (o.d.) zirconia rotors and spun at 20 kHz in a 4 mm Bruker MAS probe. 1H chemical shifts were referenced to TetraMethylSilane (TMS) at δ1H = 0.0 ppm, while 31P chemical shifts were referenced to H3PO4 (85% w/w aqueous solution) at δ31P = 0.0 ppm. To allow full relaxation of the magnetization, 1H recycle delays were set to 2s and 20s for nano and micron HA, respectively; whereas 31P recycle delays were set to 240s and 300s for nano and micron particles, respectively. In the two-dimensional (2D) {1H}31P Heteronuclear Correlation (HetCor) MAS NMR spectra, the 1H relaxation

delays were set to 2s and 4s for nano and micron particles, respectively; the contact time (tCP) was set to 1ms for both particle sizes; and 128 scans were accumulated for each 256 t1 increments.

Micron particle size and morphology was characterized using scanning electron microscopy. Scanning Electron Microscopy (SEM) was carried out on an ULTRA Plus microscope (Zeiss,

Oberkochen, Germany) operating at 5 kV acceleration voltage. The micron HA sample was deposited on an aluminum stud using conductive carbon adhesive stickers and was subsequently coated with approximately 5 nm of Au/Pd prior to imaging. Nanoparticle size and morphology was characterized by transmission electron microscopy (TEM). Samples were prepared by placing approximately 5 µl onto a lacey carbon film Cu TEM grid (Agar Scientific, UK) and allowed to air dry overnight. Samples were imaged using a Titan TEM (ThermoFisher Scientific, Eindhoven, The Netherlands) at 300 kV.

2.2.16.5 Assessment of endotoxin contamination

In-house synthesized nanoparticles and micron HA particles (Sigma Aldrich (Cat# 04238)) were first tested for lipopolysaccharide (LPS) contamination using the HEK-BlueTM hTLR4 assay system (Invivogen). HEK-blue cells (5 x 105 cells/ml) expressing TLR4 were stimulated with LPS (10–100 ng/ml; positive control), micron or nano HA particles (250 mg/ml) for 24 h. The expression of SEAP which is under the control of NF-κB and AP-1 was tested by incubating cell supernatants with HEK-blue detection medium for 30 min at 37 °C and absorbance was read at 650 nm. Data provided in Figure app. 3.

2.2.16.6 Determination of particle uptake

Micron and nano particles were fluorescently stained with fluorescein-5-maleimide to visualize uptake and cellular internalization. One milligram of each particle type was suspended in 1 ml of PBS and sonicated for 5 min before adding 4 ml of fluorescein-5-maleimide stock solution (5 mg/ml). The particle–fluorescein mixture was left to react at 4 °C at 1400 rpm for 12 h and the stained particles were washed five times with PBS

to remove unbound fluorescein. Cells were incubated with tagged particles for 1 or 3 hours fixed with 4% PFA for 10 mins, permeabilised in 0.5% Triton in PBS for 15 minutes and stained with Rhodamine red (1:2000) for 1 hour and finally stained with DAPI (1:1000) for 15 minutes. Cells were imaged using a Leica SP8 scanning confocal microscope. FITC fluorescence intensity from images was quantified using Image J and is displayed as corrected total cell fluorescence (CTCF). Alternatively, cells were pre-treated with the actin polymerization inhibitor, Latrunculin B (1µM), for 45 minutes prior to treatment with particles for 24 hours. RNA was extracted as previously described and M1 and M2 associated genes (CXCL9, CXCL10, MRC1 and CCL13) were assessed by Real-Time PCR.

2.2.17 Scaffold Fabrication

Articular cartilage (AC) and growth plate (GP) used in the fabrication of ECM-derived scaffolds were harvested, in aseptic conditions, from the femoral condyles of female pigs (4 months old) shortly after sacrifice. The cartilage was obtained using a biopsy punch (8 mm) to remove articular cartilage from the head of the femur. Following this, the head of the bone was sawed in half and hammered through the epiphyseal line to gain access to the growth plate, which was scraped with a scalpel (Figure 2.3).

2.2.17.1 Collagen solubilisation

AC or GP were harvested from porcine chondyles as previously described and Collagen type II and X were isolated from the tissues respectively. 1000 mg of wet tissue was pre-treated with sterile filtered 0.2 M NaOH at a ratio of 1ml: 50 mg wet tissue and incubated at 4°C for 24 hours with gentle rotation. The tissue was then centrifuged at 2500 x g for 10 minutes at 4°C. The supernatant was discarded and the pellet was resuspended in sterile ultra-pure water (UPW) at a ratio of 1ml: 50 mg wet tissue. This was centrifuged again at 2500 x g for 10 minutes, supernatant was discarded and this wash step was repeated a further time. The pellet was then resuspended in activated pepsin solution, 1ml: 50 mg tissue, agitated and vortexed vigorously to dissolve the pellet and incubated for 24 hours at < 20°C with rotation at a speed of 4 rpm. Tissue was then centrifuged at

2500 x g for 1 hour at 4 °C, and supernatant was transferred to a new tube for salt precipitation. Appropriate volumes of sterile filtered 5M NaCl were added to supernatants in order to get a final concentration of 0.9 M NaCl or 2.5 M NaCl for Collagen II or Collagen X salt precipitation respectively. Tubes were mixed by inverting several times and the mixture was allowed to equilibrate overnight at 4°C. Tubes were centrifuged at 2500 x g for 2 hour at 4°C, and the supernatant was discarded. The pellet was resuspended in sterile filtered 1.5 N acetic acid and allowed to dissolve overnight at < 20°C with rotation at 4 rpm. This salt precipitation was repeated a further time. The acid solubilised collagens were then transferred to a dialysis membrane (MWCO 10 kDa) which had been soaked in diH2O for at least 30 minutes. This was dialyzed against 0.02 Na_2HPO_4 (pH 9.4) for 24 hours at 4°C. The dialysate was removed after 2 hours and new dialyzing solution added. The outside of the dialysis tubing was then rinsed in PBS, and the dialyzed collagen was transferred to Petri dishes and freeze dried using a drying temperature of -10°C for 20 hours. Once freeze drying is complete, lyophilized collagen can be stored in Petri dishes closed with IMS-sprayed parafilm at -20°C for short term use.

2.2.17.2 Scaffold cross-linking

Collagen scaffolds were first chemically cross-linked with Glyoxal solution. Lyophilized ECM was resuspended in high glucose DMEM+Glutamax (DMEM - Gibco) to give a final concentration of 10 mg/ml. This ECM slurry was mixed with either micron particles or nanoparticles at a ratio of 1:1. Appropriate volume of 1.5 N acetic acid was added to the collagen solution to give a final concentration of 0.06 N acetic acid, this was mixed well and a colour change of pink to slightly yellow was observed as the pH changes. The solution was then neutralised by the addition of 0.1 M NaOH, accompanied with a colour change back to pink until the solution matches that of control media with no collagen, indicating that the solution has a reached a neutral pH. 100 mM Glyoxal solution was added to the collagen solutions to give a final concentration of 10 mM Glyoxal; this was mixed well and incubated for 30 minutes at 37°C to allow crosslinking to occur. After 30 minutes, the solution was mixed and the collagen gel was transferred to the custom made moulds (containing wells 7mm in diameter and 4mm in height) and freeze dried

for 28 hours. AC or GP scaffolds then underwent DHT cross linking and sterilizing in a vacuum oven (VD23, Binder, Germany), at 115°C, in 2 mbar for 24 hours. Scaffold Biochemical analysis

2.2.17.3 Determination of scaffold pore size and porosity

SEM images were obtained using a Zeiss Ultra Plus (Zeiss, Germany) with an acceleration voltage of 5 kV and working distance of 5 mm. To quantify the mean pore size of the various scaffolds, 5 images (containing a minimum of 100 pores) from 3 different scaffolds were measured using the analyse particle function of ImageJ following thresholding of the images. Scaffold porosity was determined by gravimetry, where scaffolds were weighed using a digital mass balance and dimensions obtained using vernier callipers to calculate density value. Total porosity is measured by gravimetry according to the equation (1– ρ scaffold/ρ material), where ρ=density.

2.2.18 Rat femoral defect model

2.2.18.1 Surgical procedure

Critically-sized (5 mm) femoral defects were created in immune-competent adult Fischer rats (>12 weeks old) following an established procedure (221). Constructs were press-fit into the defect site, and repair tissue was harvested for analysis at 1 and 4 weeks post-implantation. One defect was created per animal and n = 5-8 constructs were implanted per time point. Briefly, anaesthesia was induced and maintained by isoflurane-oxygen throughout the surgery. The rats were also injected with buprenorphine (0.03 mg/ml) to provide pain relief during and after surgery. The shaft of the left femur was exposed by dissections and the periosteum was scraped back to allow access to the bone. A custom-made weight-bearing polyetheretherketone (PEEK) internal fixation plate was secured to the exposed femur with four screws into pre-drilled holes. A 5 mm mid-diaphyseal defect was then created using a dental drill fitted with 2 small circular parallel saw blades welded to a narrow straight rod separated with a 5 mm spacer. The defect site was thoroughly irrigated with saline to remove bone

debris before it was treated with a construct. The wounds were closed with sutures and the rats were allowed to recover. On dates of scheduled explant retrieval, rats were sacrificed by CO_2 asphyxiation. The repaired femur, with the PEEK plate fixator intact, was carefully separated from the adjacent hip and knee joints for analysis.

2.2.18.2 Characterization of immune cell subsets

Punch biopsies (4 mm) of the defect site were performed 1 week post-surgery and cells were recovered by digestion in a Collagenase digestion cocktail (Collagenase VI (2 mg/ml), DNAse I (0.1 mg/ml) and Hyaluronidase (0.5 mg/ml) at 37°C under agitation on an orbital shaker at 7 x g for 45 minutes . Cells were blocked by incubating in Fcγ blocker (BD Pharmingen; 1 µg/ml) for 10 min. To discriminate live from dead cells, cells were stained with LIVE/DEAD Aqua for an additional 30 min. Staining was performed with fluorescent antibodies specific for CD11b (M1/70), CD3 (17A2), Ly6G (1A8), CCR2 (SA203G11), CX3CR1 (SA011F11), Ly6C (AL-21), CD19 (1D3), F4/80 (BM8), Siglec F (E50-2440), CD45 (30-F11), MHCII (M5144.15.2), and CD86 (GL-1) (Supplementary Table 3). Cells were acquired using FACS Canto II (BD), or LSRFortessa (BD). Analysis was completed using FlowJo version 9.2 (Tree Star). Gating strategies utilised in all experiments are detailed in Figure app.1.2 and 1.3.
In order to assess circulating cytokines 1 week post-surgery, cardiac punctures were performed and blood samples were centrifuged at 300 x g for 20 minutes and serum was collected. IL-10 and IFNγ cytokine concentrations were quantified by ELISA (R&D systems).

2.2.18.3 In vivo µCT analysis

µCT scans were performed on constructs using a Scanco Medical vivaCT 80 system (Scanco Medical, Bassersdorf, Switzerland). Rats (n = 8) were scanned at 4 weeks post-surgery to assess defect bridging and bone formation within the defect. First, anaesthesia was induced in an induction chamber. Next, the rats were placed inside the vivaCT scanner and anaesthesia was maintained by isoflurane-oxygen throughout the scan. Next, a radiographic scan of the whole animal was used to isolate the rat femur.

The animal's femur was aligned parallel to the scanning field-of view to simplify the bone volume assessments. Scans were performed using a voltage of 70 kVp, and a current of 114 mA. A Gaussian filter (sigma = 0.8, support = 1) was used to suppress noise and a global threshold of 210 corresponding to a density of 399.5 mg hydroxyapatite/cm3 was applied. A voxel resolution of 35 mm was used throughout. 3D evaluation was carried out on the segmented images to determine bone volume and density and to reconstruct a 3D image. Bone volume and bone density in the defects was quantified by measuring the total quantity of mineral in the central 130 slices of the defect. The variance of bone density with depth through the constructs was analysed qualitatively by examining sections at a depth of 25%, 50% and 75% from the top of the construct (one quarter, mid and three-quarter sections). The bone volume and densities were then quantified using scripts provided by Scanco.

2.2.18.4 Histological and immunohistochemical analysis

Constructs were fixed in 4% paraformaldehyde, dehydrated in a graded series of ethanols, embedded in paraffin wax, sectioned at 10 μm and affixed to microscope slides. Post-implantation constructs were decalcified in EDTA for 1 week. The sections were stained with haematoxylin and eosin (H&E) to assess tissue architecture and cell infiltration. Von Willibrand (vWF) and alpha smooth muscle actin (α-SMA) staining was performed as follows: Antigen retrieval was performed using enzymatic digestion with proteinase K solution (20 minutes at 37° C) in a humidified chamber. Slides were washed with PBS-Tween 0.5% v/v and blocked (3% donkey serum, 1% BSA in PBS) for 1 hour at room temperature. Slides were incubated in primary antibody overnight (1:250 and 1:200 dilution for α-SMA and vWF respectively), washed with 1% BSA prior to incubation with secondary antibody (both 1:200) for 1 hour. Slides were washed with 1% BSA, mounted with fluoroshield mounting media, dried and imaged using a Leica SP8 scanning confocal microscope.

2.2.19 Statistical Analysis

A one-way ANOVA or Kruskal-Wallis test were used for the comparison of more than two groups for parametric and non-parametric analysis respectively, with the Tukey or Dunn's post-test (where applicable). A paired Student's t-test was used when there were only two groups for analysis and the data was normally distributed and a Two-tailed paired Wilcoxon Signed rank test was used for normally distributed data. All statistical analysis was performed on GraphPad Prism 7.00 (GraphPad Software). P values of <0.05 were considered significant and denoted with an asterisk. Normality tests were carried out to ensure that the data was normally distributed for parametric statistical tests.

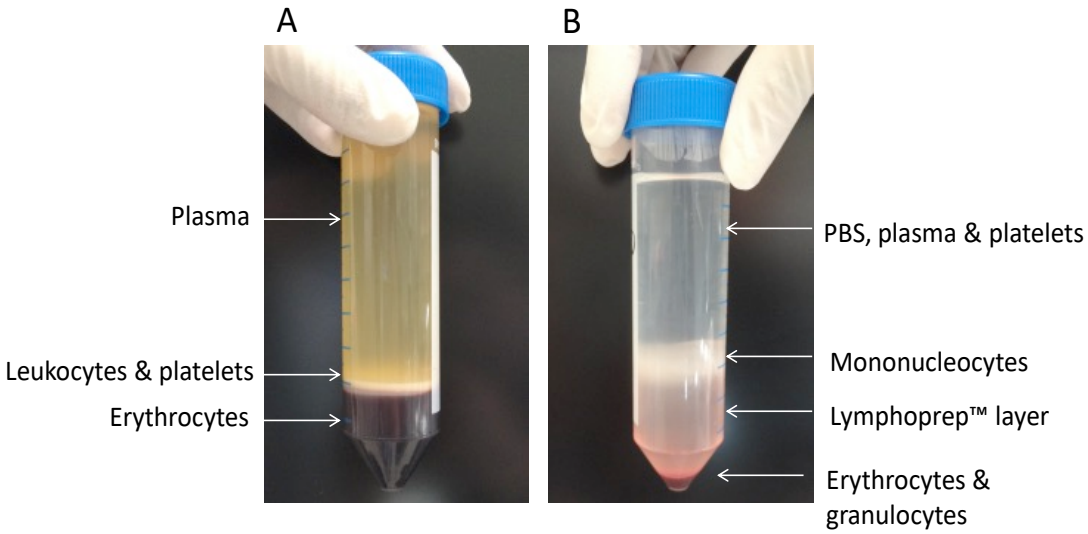

Figure 2.1: Isolation of PBMC from buffy coat blood packs. Blood was diluted 1 in 2 with sterile PBS and centrifuged at 1250 g for 10 minutes at room temperature with the brake off. The blood separates into its constituent parts (A). The buffy coat layer containing leukocytes was removed, diluted in sterile PBS, layered over Lymphoprep and centrifuged at 800 g for 20 minutes at 20oC, with the brake off. The desired mononucleocyte-enriched layer is the cloudy interface between the PBS-containing layer and the Lymphoprep™ layer (B).

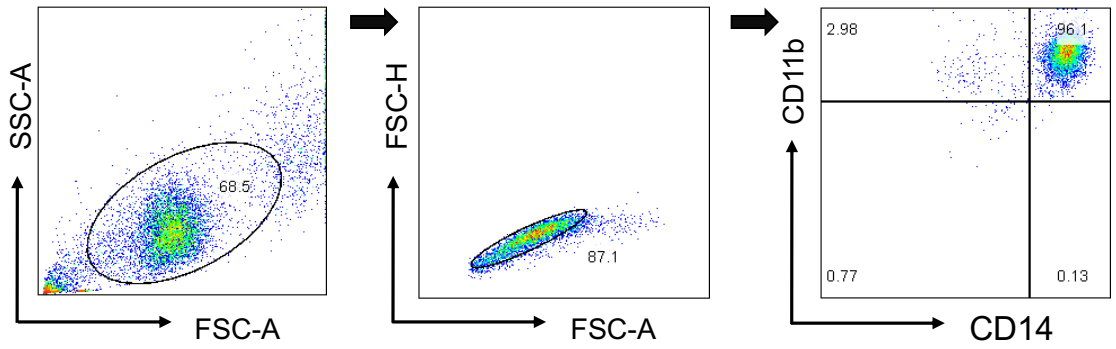

Figure 2.2: Analysis of macrophage purity by flow cytometry. Human monocyte-derived macrophages were identified as CD14+/CD11b+ by flow cytometry. (A) Dead cells and cellular debris were excluded on the basis of size (FSC) and granularity (SSC). Single cells were then gated for based on FSC-H and FSC-A. FMO defined CD14 vs CD11b gate was then applied to macrophage sample to determine purity of the macrophage population.

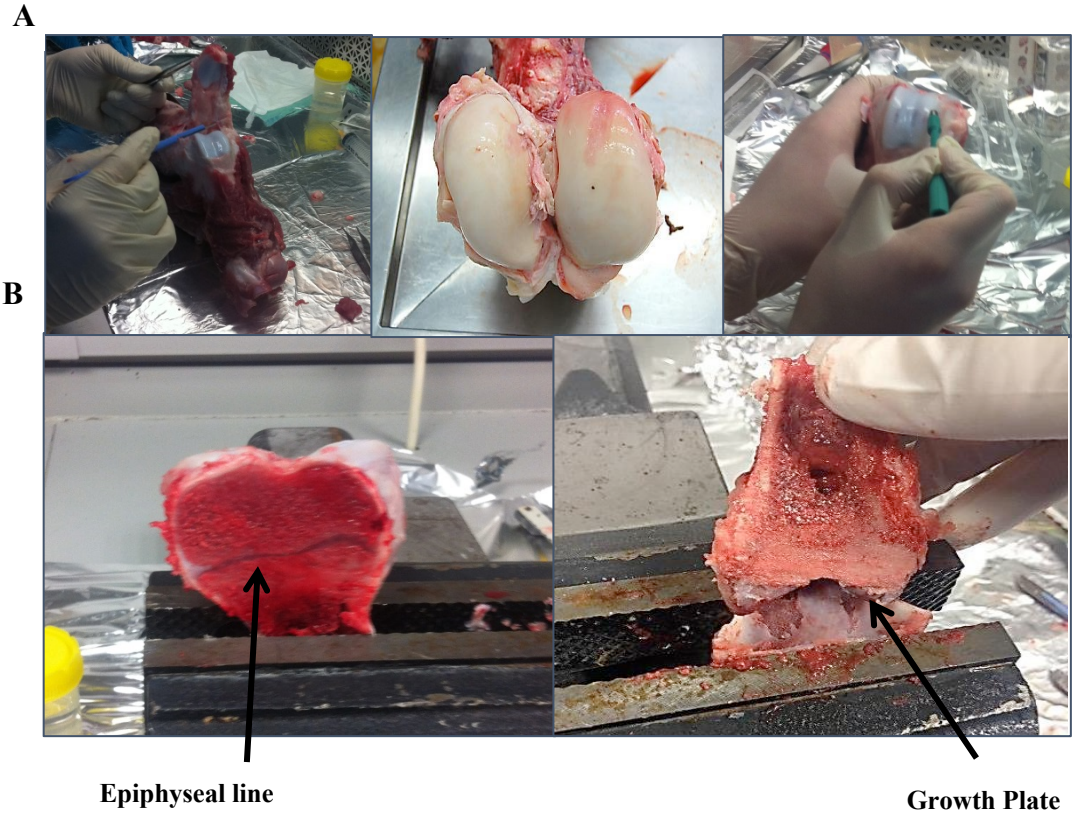

Figure 2.3: Isolation of articular cartilage (AC) and growth plate (GP). Harvested AC (A) and GP (B) from the femoral condyle of four month old pigs. AC was harvested by biopsy punch and GP was scraped away after breaking the bone at the epiphyseal line.

Chapter 3: Investigation of osteoarthritis-associated basic calcium phosphate crystal-induced alterations in immune cell metabolism and M1 macrophage polarization

3.1 Introduction

Osteoarthritis (OA) is the most common form of chronic arthropathy and a leading cause of disability worldwide. It affects 10% of males and 18% of females over the age of 45, a figure that is set to rise as life expectancy increases (222, 223). In addition, the current obesity epidemic has resulted in an increased incidence of OA in younger individuals, many of whom will undergo multiple joint replacements due to the limited lifespan of artificial joints. Extensive research has highlighted a complex interplay between chondrocytes, synovial fibroblasts and the innate immune network, and while much progress has been made in elucidating the cellular and molecular events contributing to OA, the complex nature of the disease has hampered the development of a successful disease-modifying drug. Current therapies are focused on providing symptomatic relief rather than halting or reversing disease progression, hence, there is a clear need to identify specific orchestrators that initiate and/or contribute to eventual joint destruction.

Immunometabolism is an emerging field of research that focuses on changes in intracellular metabolic pathways in immune cells and how these alterations impact on cell fate and function (41, 224, 225). It is now recognised that a metabolic shift from oxidative phosphorylation to a highly metabolically active glycolytic state (designed to maintain energy homeostasis under conditions of low oxygen and acute stress) can lead to an accumulation of reactive oxygen species (ROS) and metabolic intermediates that promote the synthesis of degradative enzymes and inflammatory mediators (226). Increased glycolytic rates and glucose consumption are associated with enhanced expression of the glucose transporter, GLUT1, as well as elevated lactate production (227). Furthermore, activated immune cells exhibit Warburg metabolism and HIF-1α induction even under normoxic conditions (228, 229). Recent studies have also demonstrated that macrophage activation and phenotype is intricately linked to cellular metabolic status. For example, lipopolysaccharide (LPS)-activated M1 macrophages exhibit an enhanced glycolytic profile characterised by increased expression of glucose transporters, glycolytic enzymes and rapid production of ATP (41, 49, 230). While this metabolic switch is required to meet the energy demands of the cell during infection

and provide biosynthetic components required to carry out effector functions, dysregulated immune-cell metabolism which results in sustained inflammatory responses, has been linked to a number of debilitating diseases and it has been strongly suggested that strategies to modulate metabolic reprogramming represents a novel approach to regulate disease pathology (231–234). Furthermore, a number of metabolites have been shown to alter macrophage polarization and there is now a host of studies demonstrating how inhibitors of metabolism (e.g. glycolysis, fatty acid synthesis and fatty acid oxidation) can regulate immune responses providing potential new avenues to manipulate immune cell activation (234).

Altered immunometabolism has been recognised as a component of a number of inflammatory and autoimmune conditions (65, 66, 232–234) and while it is well established that glycolysis is important for energy production in chondrocytes, there is now also evidence for increased glycolysis and deregulated cellular metabolism in OA (67, 235–237). Indeed, mitochondrial dysfunction is a hallmark of OA and previous studies have shown increased mitochondrial DNA damage in OA chondrocytes compared to healthy controls suggesting that cartilage degradation during OA and normal cartilage aging may be metabolically different processes (68). Furthermore, lactate levels are elevated in OA and are frequently co-associated with crystal arthropathy comorbidities (69, 70). One notable link between mechanical and inflammatory mechanisms in OA pathogenesis is calcium crystal deposition. As mentioned previously, basic calcium phosphate (BCP) crystals are uniquely associated with OA. While several pathological cellular mechanisms have been identified, studies examining the effects of BCP crystals in humans are lacking, as are drugs that prevent crystal deposition, permit crystal dissolution or specifically target the pathogenic effects that result in clinical manifestations. Furthermore, characterization of the metabolic pathways induced by BCP crystals has not yet been examined and may provide insights into new therapeutic targets for crystal related arthropathies. Therefore, the purpose of this chapter is to determine if BCP crystals impact on macrophage phenotype and immune cell metabolism.

3.2 Specific Aims:

- To determine if BCP crystals alter macrophage phenotype and the metabolic profile of primary human macrophages.
- To determine if blockade of metabolic pathways affects BCP induced responses in primary human macrophages.

3.3 Results

3.3.1 BCP crystals do not affect macrophage viability.

Prior to carrying out assays in primary human macrophages, BCP crystals were imaged by scanning electron microscopy (SEM) to investigate their size and morphology. The crystals appear to range in diameter from 1 μm to 5 μm and are irregular in shape. High magnification images also reveal that they have a rough surface topography (Figure 3.1 A & B). The effect of BCP crystals on the viability of purified macrophages was next assessed. Primary human macrophages were treated with BCP crystals at 50 μg/ml (BCP crystal concentration detected in OA joints ranges between 20-120 μg/ml (91, 238)) for 24 hours and stained with a fixable viability dye before assessing cell viability by flow cytometry. The viability of BCP-treated macrophages was comparable to untreated control cells and typically in the range of 90-95% (Figure 3.1 C).

3.3.2 BCP crystals are not contaminated with endotoxin.

In order to first verify that BCP crystal preparations were endotoxin free, crystals were tested for lipopolysaccharide (LPS) contamination using the HEK-BlueTM hTLR4 assay system. HEK-blue cells expressing TLR4 were stimulated with LPS (1, 10 and 100 ng/ml; positive control), or BCP crystals (25, 50 and 100 μg/ml) for 24 hours. The expression of SEAP which is under the control of NF-κB and AP-1 was tested by incubating cell supernatants with HEK-blue detection medium for 30 min at 37 °C and absorbance was read at 650 nm. Results demonstrate that the concentration of endotoxin (LPS) was below the threshold level for TLR4 activation as determined using the HEK-Blue LPS detection kit and particle preparations were therefore deemed suitable for further in vitro assays (Figure 3.2).

3.3.3 BCP crystals induce foreign body giant cell formation in human macrophages.

It has previously been demonstrated that endogenous particles such as MSU crystals can drive formation of foreign body giant cells (FBGCs) (239–241) which form due to the fusion of phagocytic cells (242). This process is part of the foreign body response and is associated with a pro-inflammatory phenotype. In order to determine whether BCP crystals also induce these morphological changes, primary human macrophages were treated with BCP crystals for 24 hours. Immunofluorescent staining for actin demonstrated that treatment of cells with BCP crystals induced a 'sheet-like' cell morphology with some cells appearing to fuse with one another to form multinucleated cells (Figure 3.3 B) compared to untreated control cells which had a more elongate morphology (Figure 3.3 A). Semi quantitative analysis of the cell shape parameters revealed that BCP crystals induced a significant increase in cell area and cell circularity (Figure 3.4 C & E), while cell perimeter was significantly decreased (Figure 3.4 D).

3.3.4 BCP crystals drive IL-8 but not TNFα or IL-6 cytokine expression in primary human macrophages.

In order to determine the cytokine profile induced by BCP crystals in primary human macrophages, cells were stimulated with BCP crystals for 24 hours and cytokine expression was analysed by ELISA. In line with previous findings (100), BCP-crystals did not induce secretion of the cytokines TNFα or IL-6 in primary human macrophages (Figure 3.5 A & B), however, BCP-treated macrophages significantly enhanced secretion of the chemokine IL-8 (Figure 3.4 C). While this data, together with results from the HEK-BlueTM hTLR4 assay system (Figure 3.2), confirms a lack of endotoxin contamination in our BCP crystal preparation, it also demonstrates that these crystals are capable of directly driving IL-8 chemokine production. This is in agreement with a previous study by Nadra *et al,* which also demonstrates significant IL-8 release from primary human macrophages upon stimulation with BCP crystals (243).

3.3.5 BCP crystals upregulate CD86, CD80 and CD40 maturation markers in primary human macrophages.

In addition to CXCL9/10 expression, M1-like macrophages also upregulate surface maturation markers such as CD80, CD86 and CD40 (244). These markers are involved in antigen presentation to the adaptive immune system and act as co-stimulatory molecules during the antigen presentation process, interacting with CD28 and CD40L receptors on T cells. In order to determine if BCP crystals impact on M1 surface marker expression, macrophages were stimulated with BCP crystals for 24 hours and surface marker expression was assessed by flow cytometry. BCP crystal stimulation induced a significant increase in the expression of CD86 and CD40, and although not significant, a trend towards increased CD80 surface marker expression was also observed (p=0.0874) (Figure 3.5). This data further supports the hypothesis that BCP treatment can directly promote macrophage maturation and an M1-like phenotype.

3.3.6 BCP crystals promote M1 macrophage polarization.

It has been reported that an imbalance between M1 and M2 macrophages occurs in osteoarthritic knees with a higher M1:M2 ratio correlating with OA severity (245). Furthermore, it has recently been reported that calcium oxalate crystals can promote M1 macrophage polarization (246). In order to determine if BCP crystals directly impact on macrophage polarization, primary human macrophages were treated with BCP crystals (50 μg/ml) for 24 hours and expression of established genes associated with M1 and M2 macrophage polarization was assessed by real-time PCR. BCP-stimulated macrophages exhibited significantly enhanced mRNA expression of the M1 associated markers, CXCL9 and CXCL10, compared to control cells (Fig 3.6 A & B). Conversely, treatment of macrophages with the crystals led to a significant decrease in basal levels of the M2 macrophage markers, MRC1 and CCL13 (Figure 3.6 C & D), suggesting that BCP is primarily driving an M1-like phenotype in primary human macrophages.

3.3.7 BCP induced M1 macrophage polarization occurs in an ERK and p38 MAP kinase dependent manner.

It has been reported that endogenous crystals such as MSU crystals are capable of driving membrane affinity-triggered signaling (MATS) and the downstream activation of the membrane-proximal tyrosine kinase, Syk (247). Furthermore, it has previously been demonstrated by the Dunne laboratory that BCP crystals activate MAPKs including ERK and p38, downstream of Syk activation in a receptor independent manner (100, 248). Therefore, it was of interest to next assess whether BCP induced changes in macrophage phenotype was dependent on ERK and p38 MAP kinases. Macrophages were pre-treated with either SB203580 or PD98059 (both 20 μM) to inhibit p38 and ERK, respectively, prior to stimulation with BCP for 24 hours. Pre-treatment with both MAP kinase inhibitors significantly inhibited BCP-induced IL-8, CXCL9 and CXCL10 mRNA expression (Figure 3.7 A-C), demonstrating that MAPK activation is also involved in BCP crystal-induced macrophage polarization. Of note, inhibition of MAPKs had no effect on MRC1 or CCL13 mRNA expression in BCP crystal treated macrophages (Figure 3.7 D & E).

3.3.8 BCP crystals decrease the phagocytic capacity of primary human macrophages.

Upon maturation, antigen presenting cells, such as macrophages, reduce their phagocytic capacity as their role switches from tissue surveillance to antigen presentation (249). The phagocytic capacity of M1 or activated macrophages has been shown to be much lower than that of resting or M2 macrophages (250–252). Having established that BCP crystals can induce the upregulation of M1 associated macrophage markers, it was of interest to also assess the functionality and the phagocytic capacity of BCP treated macrophages. Primary human macrophages were treated with BCP crystals for 6 hours and then incubated with FITC-conjugated DQ-Ovalbumin (DQ-Ova) at 500 ng/ml and analysed for antigen uptake by flow cytometry. As expected, unstimulated macrophages displayed high DQ-Ova uptake, however, this was significantly reduced upon stimulation of cells with BCP crystals (Figure 3.8 A & B) demonstrating that the macrophages are becoming more activated and losing their phagocytic capacity after BCP treatment. This data provides further evidence that BCP crystals induce macrophage polarization towards an M1-like state.

3.3.9 BCP crystals upregulate surrogate markers of glycolysis

A number of studies have demonstrated that activated macrophages exhibit an enhanced glycolytic profile characterized by increased expression of glucose transporters and glycolytic enzymes (253). In order to determine whether BCP crystal-induced macrophage polarization coincided with a metabolic switch favouring glycolysis, macrophages were treated with BCP crystals and established markers of glycolysis were assessed by real-time PCR and immunoblotting. BCP crystals significantly upregulated mRNA expression of the glycolytic enzyme, hexokinase 2 (HK2), the glucose transporter, GLUT 1 and the transcription factor, HIF1α. There was also a trend towards increased expression of glyceraldehyde-3-phosphate dehydrogenase (GAPDH) ($p=0.0634$). Interestingly there was no change in mRNA expression of PFKFB3, the first enzyme in the glycolysis pathway or in mRNA expression of HIF2α (Figure 3.9 A). The upregulation of glycolytic markers was also confirmed at the protein level, with both HK2 and GLUT1 exhibiting increased expression at 24 hours post BCP crystal treatment, while increased expression of HIF1α was observed at 3, 6 and 24 hours post stimulation (Figure 3.9 B). Densitometric analysis revealed a time dependent upregulation of HK2 and Glut 1 proteins at 3, 6 and 24 hours with maximal and significant upregulation occurring at 24 hours for both proteins (Figure 3.9 C). Therefore, it appears that BCP crystal treatment upregulates proteins and transcription factors associated with a metabolic switch favouring glycolysis.

3.3.10 Human macrophages temporally increase glycolysis and oxidative phosphorylation after LPS stimulation.

Having demonstrated that BCP crystals alter the expression of glycolytic enzymes in primary human macrophages, experiments were next carried out to examine the rates of glycolysis and oxidative phosphorylation in treated cells in order to provide an in-depth understanding of metabolic pathways. To this end, the Agilent Seahorse XF Cell Mito and Glycolysis Stress Test assays were used to measure glycolytic and mitochondrial functions (oxidative phosphorylation), respectively. Glycolysis involves the conversion of glucose to lactate which is accompanied by extrusion of H+ protons into the extracellular medium and thus acidification of the medium. This acidification

rate can be measured by the instrument and is reported as extracellular acidification rate (ECAR). This then provides a method to assess the key parameters of glycolytic flux such as glycolysis, glycolytic capacity, and glycolytic reserve. Additionally, oxidative phosphorylation consumes oxygen and this can be directly measured and reported as the oxygen consumption rate (OCR). It was necessary in the present study to first optimize the conditions for this technique for primary human macrophages. Therefore, the metabolic changes in primary human macrophages were characterised using the well-known TLR agonist, LPS. Human macrophages were seeded into a Seahorse microplate and stimulated with LPS for 3, 6 or 24 hours prior to placement into a Seahorse XF96 analyser. The rates of glycolysis and oxidative phosphorylation were determined by the measured ECAR and OCR respectively, after treatment with metabolic inhibitors oligomycin, FCCP, Rotenone and Antimycin A and 2-DG (as described in Section 2.2.13). The ECAR of LPS stimulated macrophages was high at all timepoints compared to unstimulated control cells, with the highest glycolytic rate observed at 3 and 6 hours (Figure 3.10 A). This was reflected in the calculated glycolytic profile with the basal rate of glycolysis being significantly increased after 3 hours of LPS stimulation (Figure 3.10 B). Furthermore, the calculated max glycolysis, which is used as an indication of the cellular maximum glycolytic capacity, of LPS-stimulated cells, was greatest at 3 and 6 hours post-stimulation and was lowest at 24 hours post-stimulation (Figure 3.10 C). Interestingly, the glycolytic reserve, of LPS-treated cells was significantly higher than that of untreated macrophages at all timepoints (Figure 3.10 D). Therefore, while stimulation of human macrophages with LPS transiently increases the basal glycolytic and max glycolytic rate, peaking at 3-6 hours post-activation, the glycolytic potential of LPS-stimulated macrophages is significantly enhanced and appears to be sustained over 3, 6 and 24 hours.

The respiratory profiles of macrophages appeared to mirror their observed glycolytic activity. LPS stimulated macrophages displayed an enhanced OCR compared to untreated cells (Figure 3.11 A). The calculated basal respiratory rate of LPS stimulated macrophages was higher than that of unstimulated at all timepoints, peaking at 6 hours (Figure 3.11 B). Interestingly the max respiration, which gives an indication of the maximal rate of respiration that the cell can achieve, was increased at 3 and 6 hours,

whereas at 24 hours post-LPS stimulation, macrophages displayed a max respiration similar to unstimulated cells (Figure 3.11 C). Furthermore, the capability of the cell to utilize oxidative phosphorylation, as measured by the respiratory reserve, was enhanced at 3 and 6 hours returning to basal levels at 24 hour post-stimulation (Figure 3.11 D). Taken together, these data indicate that, human macrophages temporally upregulate both glycolytic metabolism and oxidative phosphorylation upon LPS stimulation. This differs from reports of metabolism in murine macrophages, which strongly upregulate aerobic glycolysis and downregulate oxidative phosphorylation upon TLR stimulation (254). However, human monocyte derived macrophages do not readily express iNOS, which is required to produce NO and therefore allows for engagement of Warburg metabolism (57). Therefore, human macrophages likely produce a different metabolic response when activated compared to their murine counterparts.

3.3.11 Human macrophages alter their metabolism in response to BCP crystal stimulation.

Having observed an upregulation of surrogate markers of glycolysis upon BCP stimulation and having optimized the parameters for Seahorse analysis in section 3.3.11, it was of interest to next assess the metabolic profile of BCP crystal-stimulated cells. Macrophages were seeded into a Seahorse microplate and stimulated with BCP crystals for 3, 6 or 24 hrs. The rate of glycolysis was determined by the measurement of ECAR (extracellular acidification rate), before and after injections of metabolic inhibitors, as described above. Overall, stimulation of cells with BCP crystals resulted in a temporal increase in glycolytic metabolism. The ECAR was increased at all time-points tested, peaking at 3 hours post -stimulation and was lowest at 24 hours post-BCP crystal treatment (Figure 3.12 A). The calculated basal rate of glycolysis was increased at all timepoints, with a significant enhancement at 3 hours (Figure 3.12 B). The maximum rate of glycolysis was also enhanced in cells stimulated with BCP crystals for 3 hours, and although not significant, there was a trend toward increased max glycolytic capacity at the 6 and 24 hour time-point (Figure 3.12 C). The glycolytic reserve of BCP treated cells was also higher than that of untreated control cells (Figure 3.12 D). Taken together these

data suggest that BCP crystals enhance the cells capacity and capability to utilize glucose for their metabolic needs.

The respiratory profile of BCP crystal stimulated macrophages was also assessed by measuring the OCR. The OCR of cells treated with BCP crystals for 3 and 6 hours was enhanced compared to that of unstimulated cells, while at 24 hours there was a marginally reduced OCR (Figure 3. 13 A). Moderate changes in the basal respiration rate were observed at each timepoint tested with a slight enhancement at 3 hours and a decrease at 6 and 24 hours post stimulation (Figure 3.13 B). Maximal respiration peaked at 3 hours but decreased at 6 and 24 hour post BCP treatment (Figure 3.13 C). Furthermore, the capability of the cells to utilize oxidative phosphorylation, as measured by the respiratory reserve, was enhanced at 3 and 6 hour post BCP treatment but returned to basal levels at 24 hours and was comparable to that of untreated cells (Figure 3.13 D).

As a greater effect was observed on the glycolytic vs respiratory profile of macrophages treated with BCP crystals, the overall preference for glycolysis or oxidative phosphorylation in these cells was determined via calculation of the basal ECAR:OCR ratio. Interestingly, the ECAR:OCR ratio of BCP-treated macrophages was significantly increased at 3 and 6 hour post-BCP stimulation compared to control cells (Figure 3.14 A). These results indicate that BCP-stimulated macrophages are more glycolytic than untreated cells, and that BCP treated cells upregulate glycolysis to a greater degree than oxidative phosphorylation. We also compared the metabolic profile of BCP crystal-treated cells to LPS-treated cells. While both treatments enhanced glycolysis as well as oxidative phosphorylation, overall the ECAR:OCR ratio was higher for BCP crystal-treated macrophages compared to LPS stimulated macrophages, suggesting that the crystals may be more potent inducers of glycolysis overall (Figure 3.14 B).

3.3.12 BCP treated cells primarily derive their ATP from glycolysis.

Having observed that BCP crystal-treated macrophages preferentially utilize glycolytic metabolism, it was of interest to further verify this metabolic switch by assessing the

rate and cellular source of ATP production which is a highly informative parameter used to assess cellular metabolism and bioenergetics (255). Using obtained ECAR and OCR values at 3, 6 and 24 hr post BCP crystal stimulation, the glycoATP production rate, i.e. the rate of ATP production associated with the conversion of glucose to lactate in the glycolytic pathway and the mitoATP production rate, i.e. the rate of ATP production associated with oxidative phosphorylation in the mitochondria, was determined using a series of calculations described in Section 2.2.13. Results demonstrate a significant increase of total cellular ATP at 3 and 6 hour post BCP crystal stimulation. The percentage of glycoATP was increased to 51% (3 hr), 48 % (6 hr) and 66% (24 hr) following BCP crystal stimulation, compared to that of untreated control cells (19%). Furthermore, the mitoATP production rate was decreased from 81 % in untreated cells to 41%, 52% and 34 % at 3, 6 and 24 hour post BCP crystal stimulation (Figure 3.15). Taken together, this data indicates that the majority of ATP produced by these cells is derived from glycolysis rather than mitochondrial oxidative phosphorylation, further verifying that human macrophages utilize glycolytic metabolism upon BCP crystal stimulation.

3.3.13 Macrophage polarization and metabolic reprogramming by BCP crystals is dependent on particle uptake.

Having established that BCP crystals can induce a metabolic and phenotypic switch in human macrophages, it was of interest to determine if these responses are dependent on particle uptake. Particle internalization requires orchestration of a number of processes including actin cytoskeleton rearrangement, the extension of the plasma membrane, and fusion to form a phagolysosome (256). Latrunculin B, a commonly used phagocytosis inhibitor, can bind actin monomers and subsequently prevent F-actin assembly. Therefore, macrophages were pre-treated with Latrunculin B (1 μM) for 45 minutes prior to stimulation with BCP crystals in order to inhibit particle uptake. BCP induced CXCL9 and CXCL10 mRNA expression was significantly reduced in the presence of latrunculin B (Figure 3.16 A & B) as was BCP crystal induced IL-8 production (Figure 3.16 C). Furthermore, mRNA expression of the glycolytic markers, HK2, Glut1 and HIF1α was reduced upon inhibition of particle uptake (Figure 3.16 D-F). For further validation

of these results, cells were pre-treated with alternative phagocytosis inhibitors to ensure that the observed were not due to loss of membrane integrity. Cells were pre-treated with Cytochalasin D or B (5 μM), which both inhibit polymerization/depolymerization of F-actin (257), or Dynasore (80 μM), which inhibits dynamin (258), prior to stimulation with BCP crystals. Similar trends were observed with all three inhibitors of phagocytosis, with a reduction in BCP-induced M1 and glycolytic markers (Figure 3.17 A-E). Taken together, this indicates that particle uptake by phagocytosis is essential for BCP crystal mediated activation of macrophages and glycolytic gene expression.

3.3.14 BCP crystal-induced M1 macrophage polarization is reduced in the presence of the glycolytic inhibitor 2-DG.

Having established that BCP crystals directly alter macrophage metabolism and promote polarization towards an M1 phenotype, it was next of interest to elucidate if direct inhibition of glycolysis abrogates BCP crystal induced macrophage polarization. Cells were stimulated with BCP crystals as described, in the presence or absence of the glycolytic inhibitor, 2-DG (25 mM). Pre-treatment of cells with 2-DG resulted in a significant decrease of BCP induced CXCL9 and CXCL10 mRNA expression (Figure 3.18 A & B). Moreover, inhibition of glycolysis with 2-DG resulted in a trend towards decreased surface maker expression of CD40, CD80 and CD86 in BCP treated macrophages (Figure 3.19 A-F). Taken together, these results suggest that BCP crystals induce metabolic reprogramming and that glycolytic blockade inhibits BCP-induced macrophage polarization.

3.3.15 Inhibition of glycolysis abrogates BCP crystal-induced alarmin expression.

Studies have demonstrated that mRNA and protein levels of the alarmin, S100A8, are highly elevated in human OA biopsy samples, and that, together with S100A9, S100A8 is heavily implicated in driving catabolic processes in OA (82, 85, 89). It has also previously been demonstrated that BCP crystals strongly upregulate expression of

S100A8 in human macrophages and fibroblasts (100, 248). Furthermore, pharmacological targeting of membrane proximal kinases and MAP kinases has been shown to prevent induction of BCP crystal-induced S100A8 expression (248), therefore, it was of interest to determine whether inhibition of glycolysis also prevents S100A8 upregulation in primary human macrophages. To test this, macrophages were treated with BCP crystals for 24 hours in the presence or absence of the glycolytic inhibitor, 2-DG and S100A8 mRNA expression was measured by real-time PCR. Results demonstrate that S100A8 expression is significantly inhibited in the presence of 2-DG (Figure 3.20), suggesting that inhibition of macrophage metabolic reprogramming may impact on the ability of BCP crystals to induce expression of this highly catabolic alarmin.

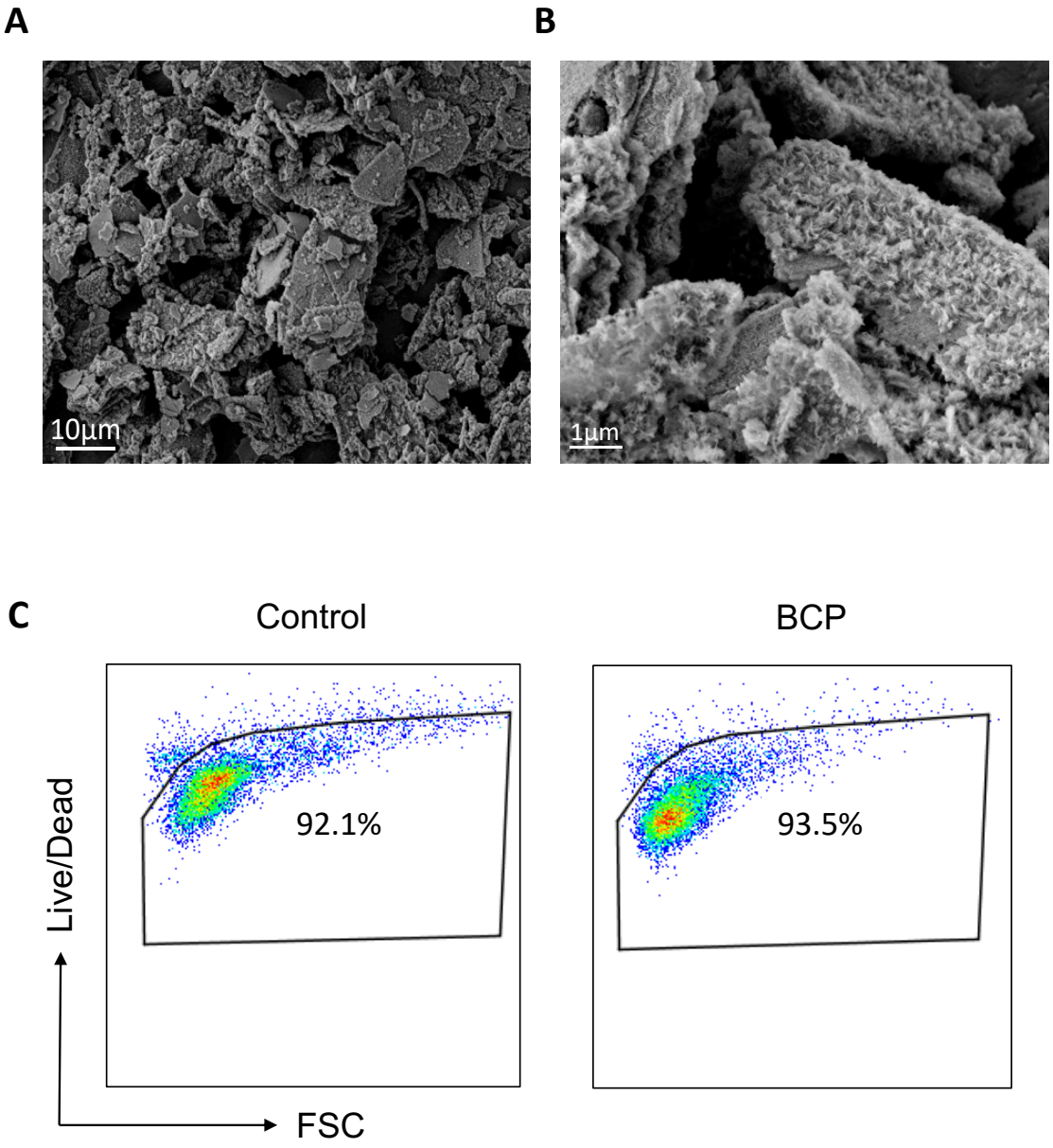

Figure 3.1: BCP crystals do not effect macrophage viability. (A) Low magnification and **(B)** high magnification scanning electron micrographs of BCP crystals. **(C)** Primary human macrophages (1 x 106 cells/ml) were left untreated or stimulated with BCP crystals (50 µg/ml). After 24 hours cells were stained with a live/dead viability stain and assessed by flow cytometry. Results shown are from one healthy donor and are representative of data from 3 independent experiments.

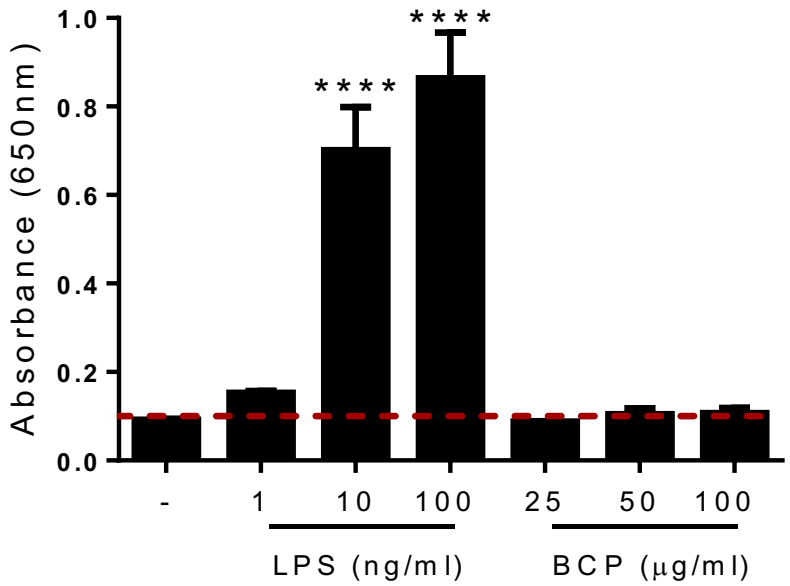

Figure 3.2: BCP crystals are not contaminated with endotoxin. BCP crystal preparations were shown to be endotoxin free, using the HEK-BlueTM hTLR4 assay system (Invivogen). HEK TLR4 cells were treated with 25, 50 or 100 μg/ml of BCP crystals, or cells were treated with LPS (1 ng/ml, 10 ng/ml or 100 ng/ml) as a positive control. The expression of SEAP was measured by absorbance at 650nm. Data was analysed using one-way ANOVA with Tukey post-test and is represented as mean ± SEM of 3 independent experiments (****P≤0.0001).

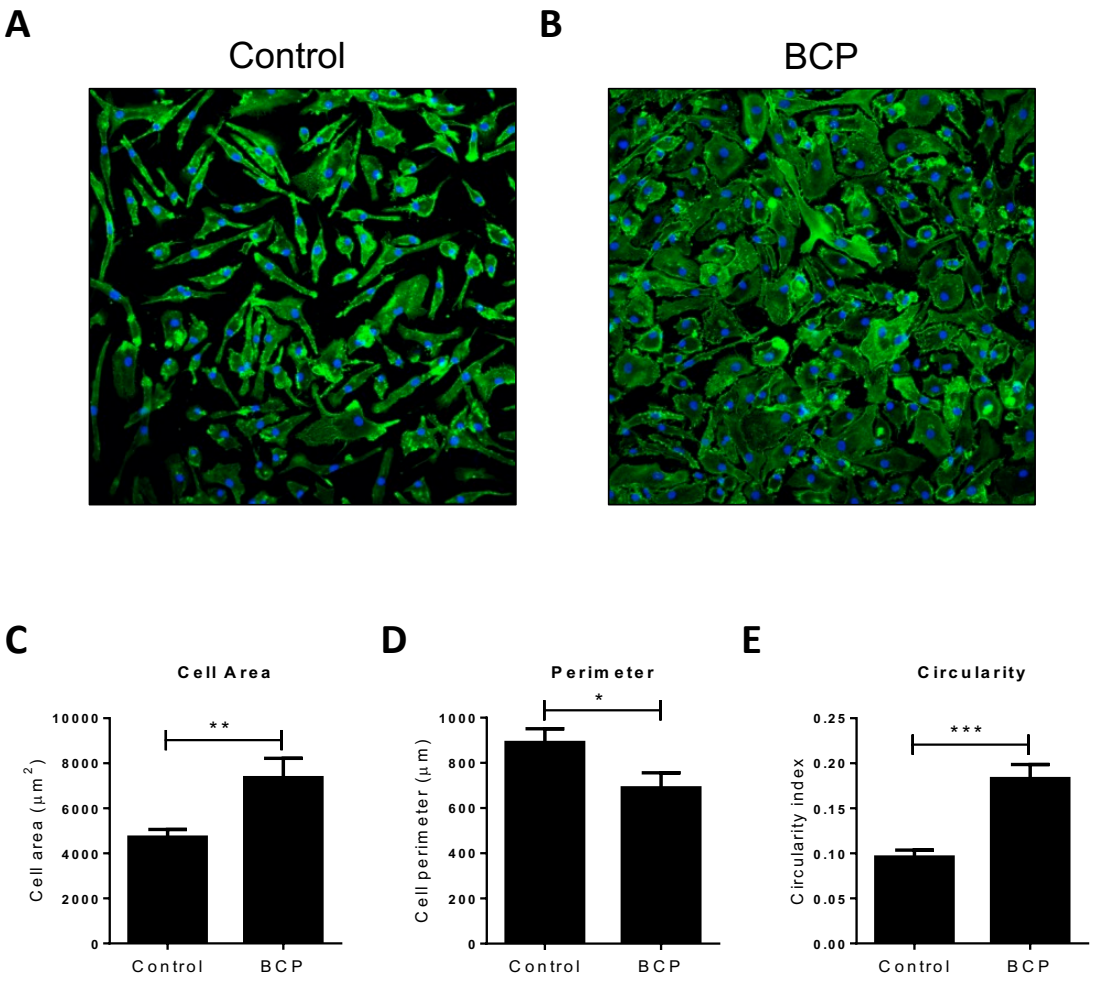

Figure 3.3: BCP crystals induce foreign body giant cell formation in human macrophages. (A & B) Primary human macrophages were seeded at 0.5 x 106cells/ml and treated with 50µg/ml BCP crystals for 24 hours. Cells were fixed with 4% paraformaldehyde for 10min, washed with PBS and permeabilised with 0.5% Triton X-100 for 10 min. Cells were then stained with Rhodamine-Phalloidin (for actin) for 2 hours at room temperature and counterstained with DAPI (for nuclei). Subsequently, stained cells were imaged using a fluorescent microscope (Leica SP8 scanning confocal). Shape parameters including **(C)** area, **(D)** perimeter and **(E)** circularity, of 50-100 individual imaged cells per condition were quantified using Image J software. Data was analysed using one-way ANOVA with Tukey post-test and is representative of 2 independent experiments (*P≤0.05, **P≤0.01, ***P≤0.001).

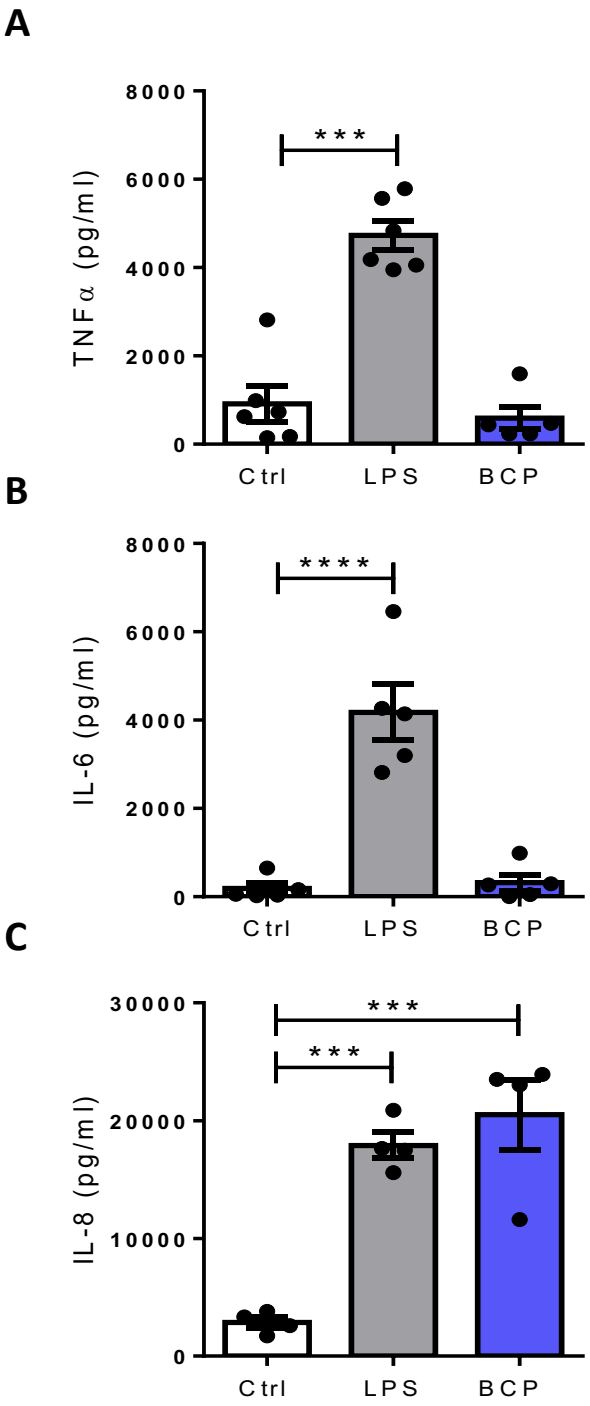

Figure 3.4: BCP crystals drive IL-8 but not TNFα or IL-6 cytokine expression in primary human macrophages. Primary human macrophages (1 x 10^6 cells/ml) were treated with BCP crystals (50 μg/ml) or LPS (100 ng/ml) as a positive control for 24 hours. Cytokine levels of **(A)** TNFα, **(B)** IL-6 and **(C)** IL-8 in cell supernatants were measured by ELISA. Pooled data (n=4-5) is represented as mean ± SEM was analysed using Kruskal Wallis with Dunn's post-test (*P≤0.05, **P≤0.01, ***P≤0.001).

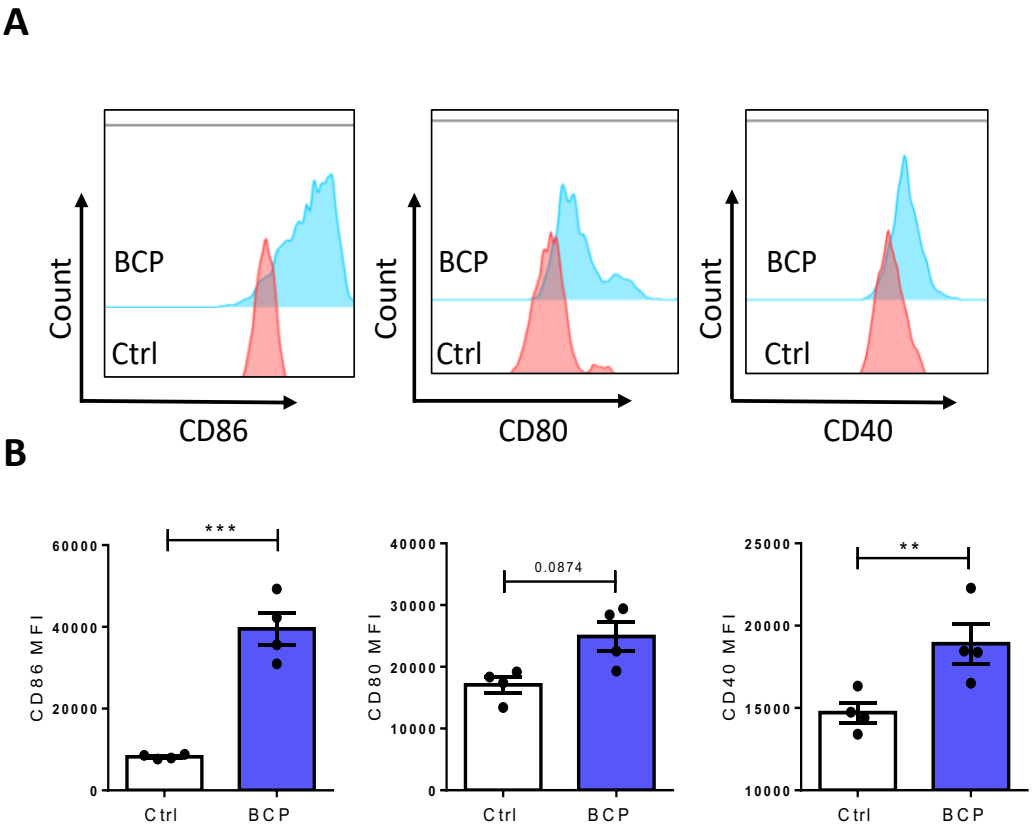

Figure 3.5: BCP crystals upregulate CD86, CD80 and CD40 maturation surface markers in primary human macrophages. Primary human macrophages (1 x 10^6 cells/ml) were stimulated with BCP crystals (50 µg/ml) for 24 hours. **(A)** Representative histograms from one experiment of the macrophage maturation markers CD86, CD80 and CD40 were determined by flow cytometry. **(B)** Pooled data (n=5) depicts Mean Fluorescence Intensity (MFI) of surface marker expression. Data is represented as mean ± SEM and was analysed using Wilcoxon Signed Rank test (**P≤0.01, ***P≤0.001).

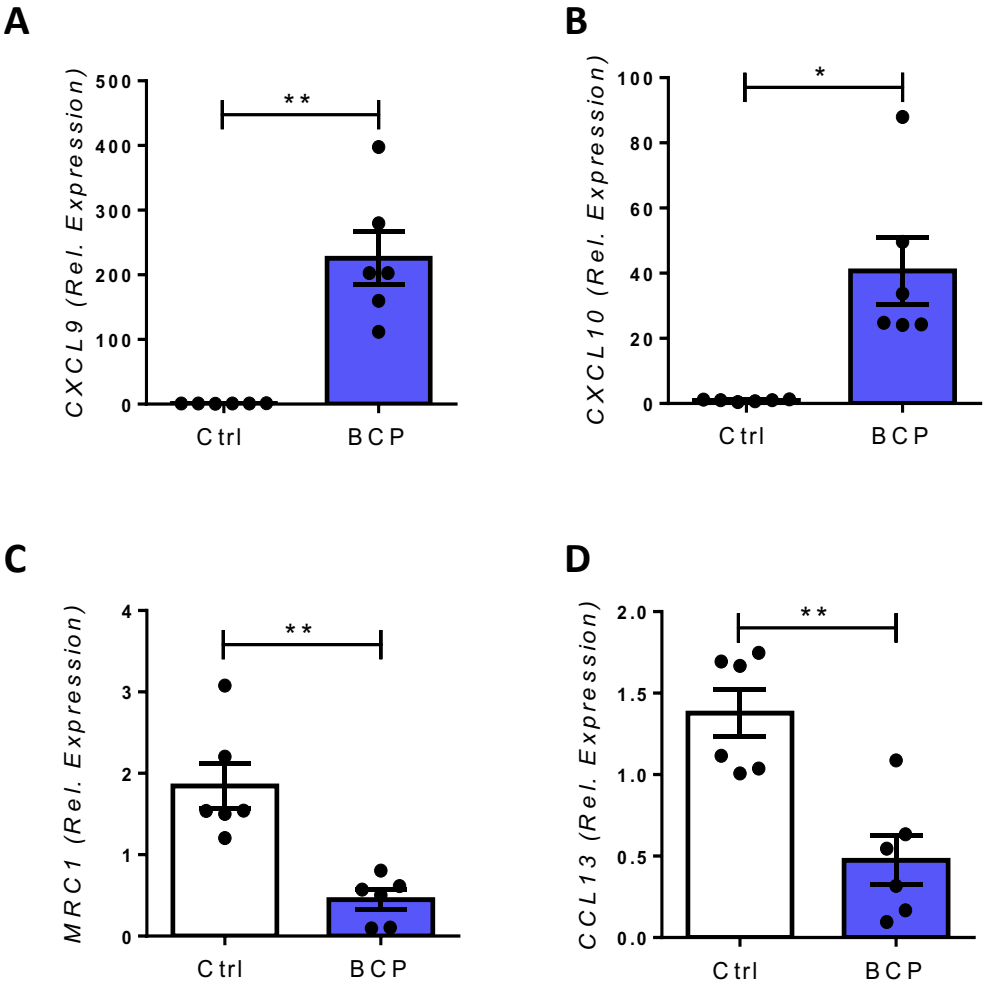

Figure 3.6: BCP crystals promote M1 macrophage polarization. Primary human macrophages (1 x 10^6 cells/ml) were stimulated with BCP crystals (50 µg/ml) for 24 hours. mRNA expression of **(A)** CXCL9, **(B)** CXCL10, **(C)** MRC1 and **(D)** CCL13 was analysed by real-time PCR. For each sample, mRNA concentration was normalised using the crossing threshold of the housekeeping gene 18s ribosomal RNA. Gene expression, relative to untreated control cells, was determined using the $2^{-\Delta\Delta CT}$ algorithm. Pooled data (n=6) is represented as mean ± SEM was analysed using Kruskal Wallis with Dunn's post-test for cytokine assays and one-way ANOVA with Tukey post-test (*P≤0.05, **P≤0.01).

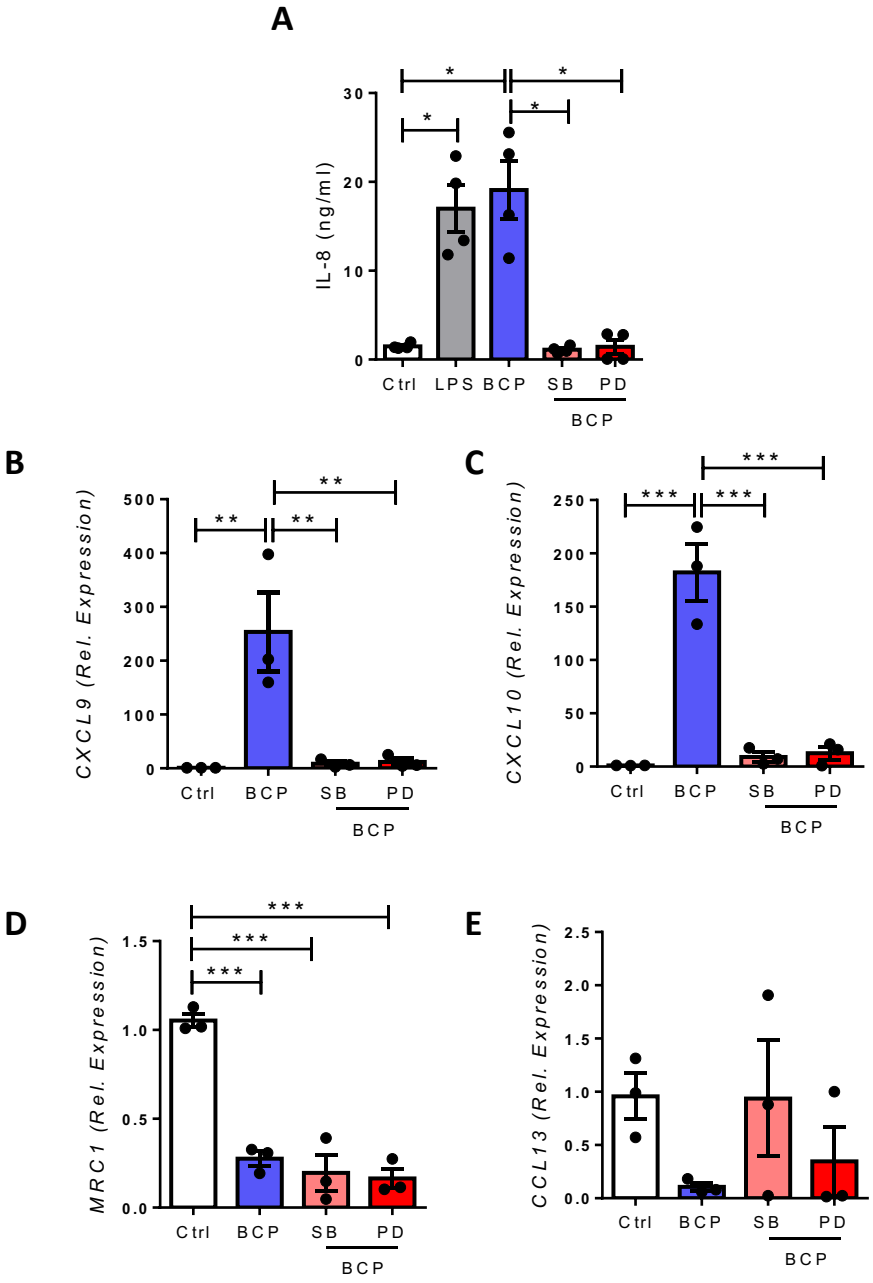

Figure 3.7: BCP induced M1 macrophage polarization occurs in an ERK and p38 MAP kinase dependent manner. Primary human macrophages (1 x 10^6 cells/ml) were pre-treated with the p38 and ERK MAP kinase inhibitors (SB203580; 20 µM, PD98059; 20 µM) for 45 min prior to stimulation with BCP crystals (50 µg/ml) for 24 hours. **(A)** IL-8 cytokine production in cell supernatants was analysed by ELISA. mRNA levels of **(B)** CXCL9, **(C)** CXCL10, **(D)** MRC1 and **(E)** CCL13 were analysed by real-time PCR. mRNA concentration was normalised to the housekeeping gene 18s ribosomal RNA. Gene expression, relative to untreated control cells, was determined using the $2^{-\Delta\Delta CT}$ algorithm. Pooled data (n=3-4) is represented as mean ± SEM. Data was analysed using Kruskal Wallis with Dunn's post-test for cytokine assays and one-way ANOVA with Tukey post-test for real-time PCR assays (*P≤0.05, **P≤0.01, ***P≤0.001).

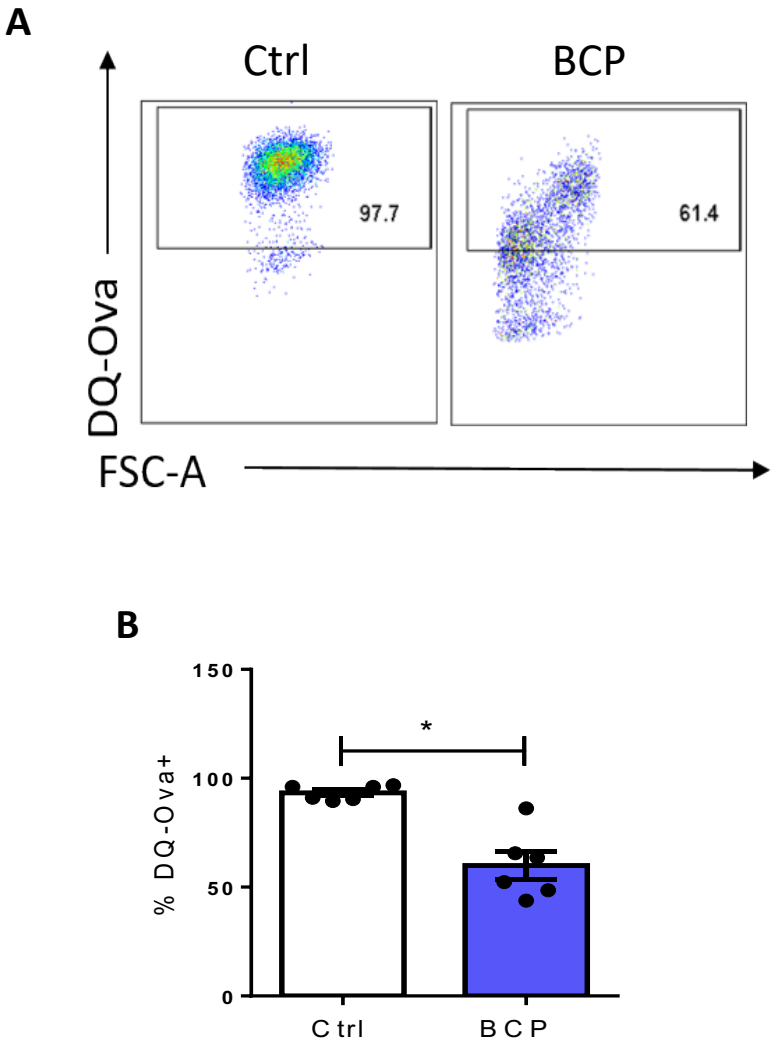

Figure 3.8: BCP crystals decrease the phagocytic capacity of primary human macrophages. Primary human macrophages (1 x 10^6 cells/ml) were stimulated with BCP crystals (50 µg/ml) for 24 hours and then incubated with FITC-conjugated DQ-ovalbumin (DQ-Ova; 500 ng/ml) for 20 min prior to analysis by flow cytometry. **(A)** Representative dot plots depicting DQ-Ova uptake by BCP treated macrophages. **(B)** Pooled data (n=6) depicts percentage DQ-Ova uptake. Data is represented as mean ± SEM and was analysed using Wilcoxon Signed Rank test (*P≤0.05).

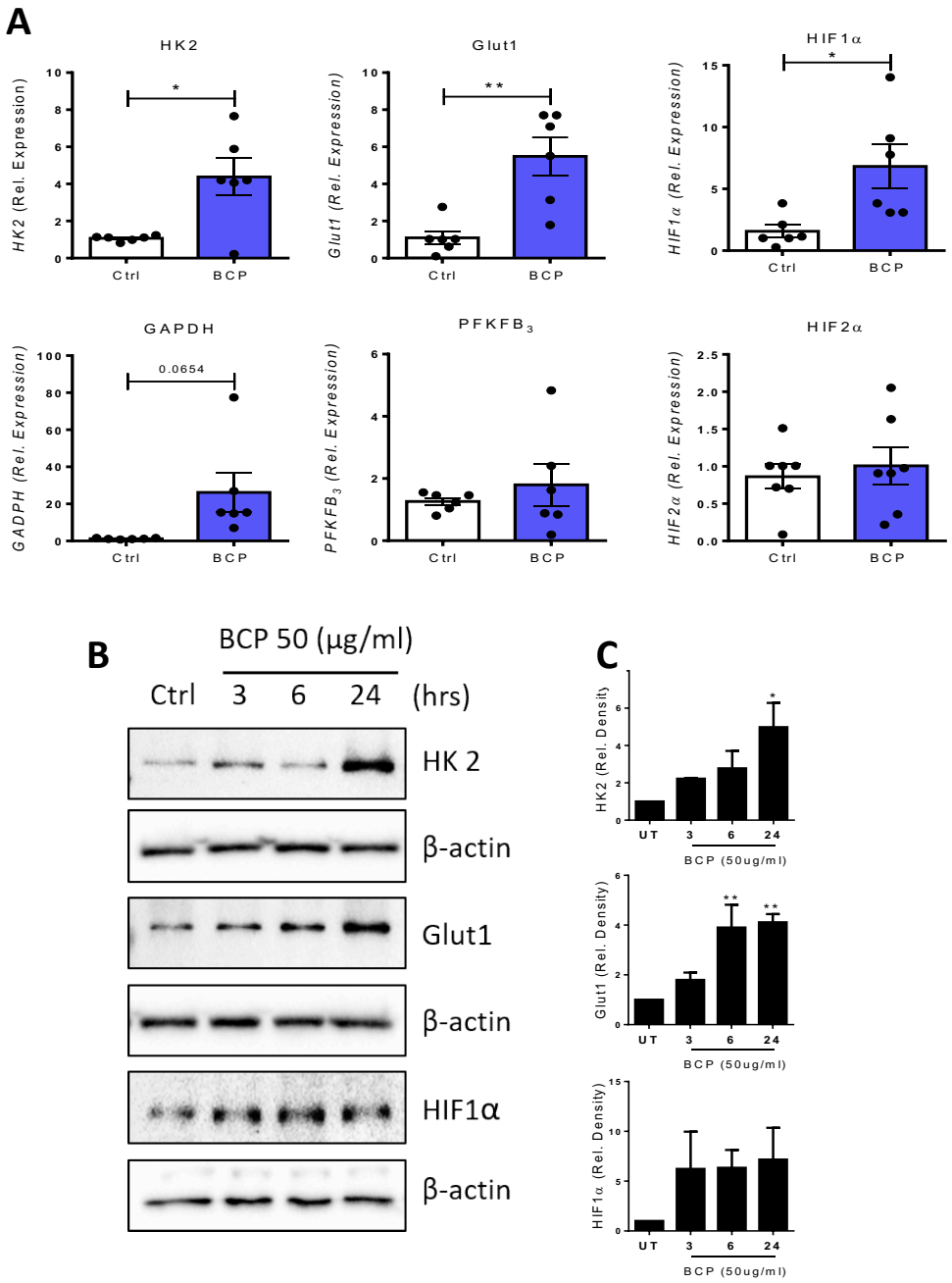

Figure 3.9: BCP crystals upregulate surrogate markers of glycolysis. Primary human macrophages (1 x 10^6 cells/ml) were stimulated with BCP crystals (50 µg/ml) for 24 hours. **(A)** mRNA expression of glycolytic markers HK2, GLUT1, HIF1α, GAPDH, PFKB3, and HIF2α were analysed by real-time PCR (n=6). mRNA concentration was normalised to the housekeeping gene RPLPO ribosomal RNA and gene expression, relative to untreated control cells, was determined using the $2^{-\Delta\Delta CT}$ algorithm. **(B)** Representative western blots demonstrating expression of HK2, Glut 1 and HIF1α in whole cell lysates in response to BCP crystals post 3, 6 or 24 hour stimulation. **(C)** Pooled data (n=3) depicting densitometric analysis of immunoblots using ImageJ software. Bar graphs illustrate the mean ± SEM increase in protein expression relative to untreated control and normalised to β-actin housekeeping protein. Data was analysed using Student's t test for real-time PCR and one-way ANOVA with Tukey post-test for western blotting (*P≤0.05, **P≤0.01).

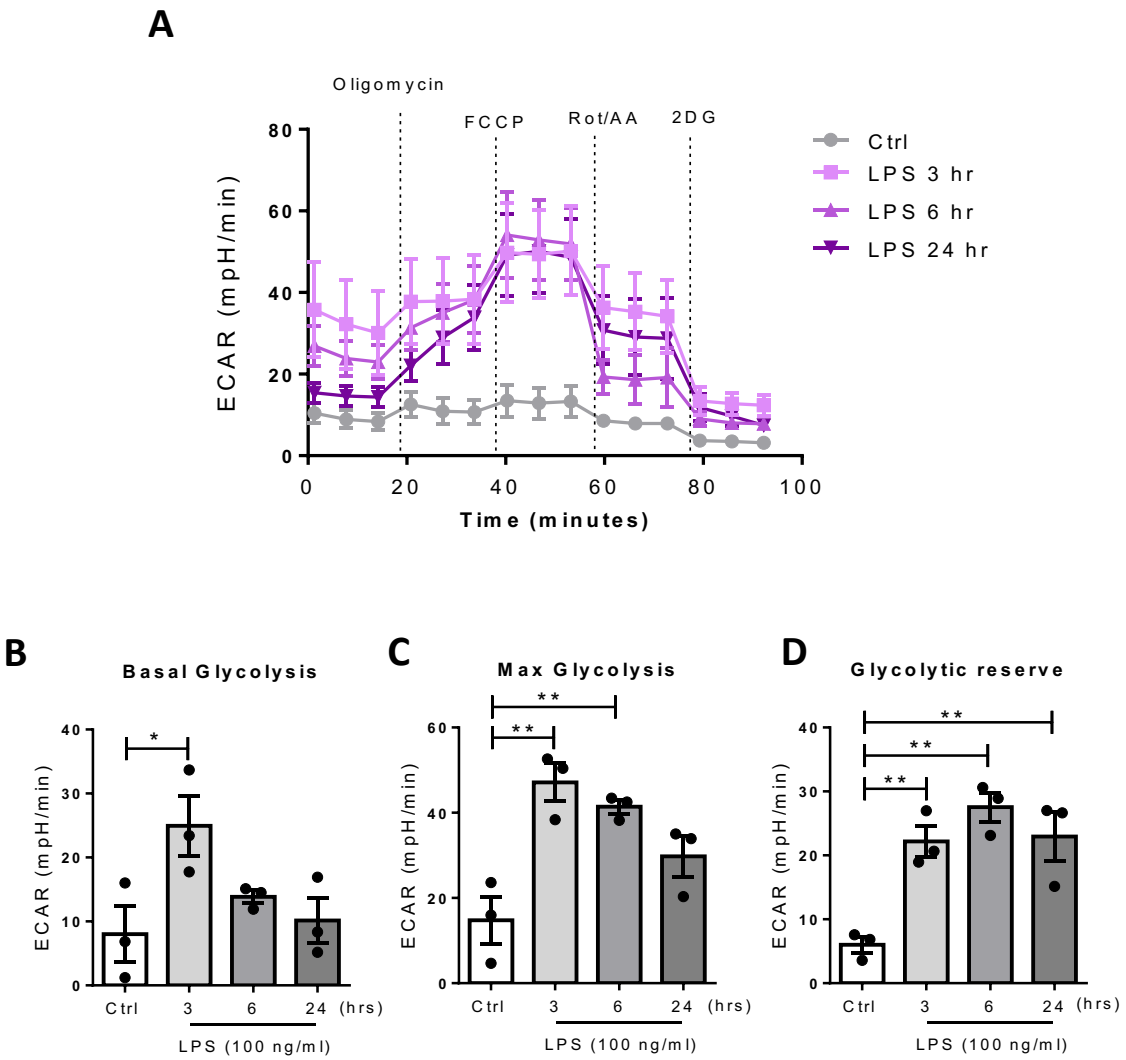

Figure 3.10: Human macrophages temporally increase glycolytic metabolism after LPS stimulation. Primary human macrophages (1 x 10^6 cells/ml) were stimulated with LPS (100 ng/ml) for 3, 6 or 24 hours prior to placement in a Seahorse XF96 analyser. The extracellular acidification rate (ECAR) was measured before and after injections of oligomycin (1 µM), FCCP (1 µM), antimycin A (500 nM)/Rotenone (500 nM), and 2-DG (25mM). **(A)** Representative glycolysis (ECAR) measurements over time for each LPS stimulation time-point. Data depicts one representative experiment. **(B-D)** Pooled data (n=3) depicting the calculated mean basal glycolytic rate, max glycolytic rate and glycolytic reserve for each LPS stimulation time-point. All data is represented as mean ± SEM and was analysed using was analysed using Kruskal Wallis with Dunn's post-test (*P≤0.05, **P≤0.01).

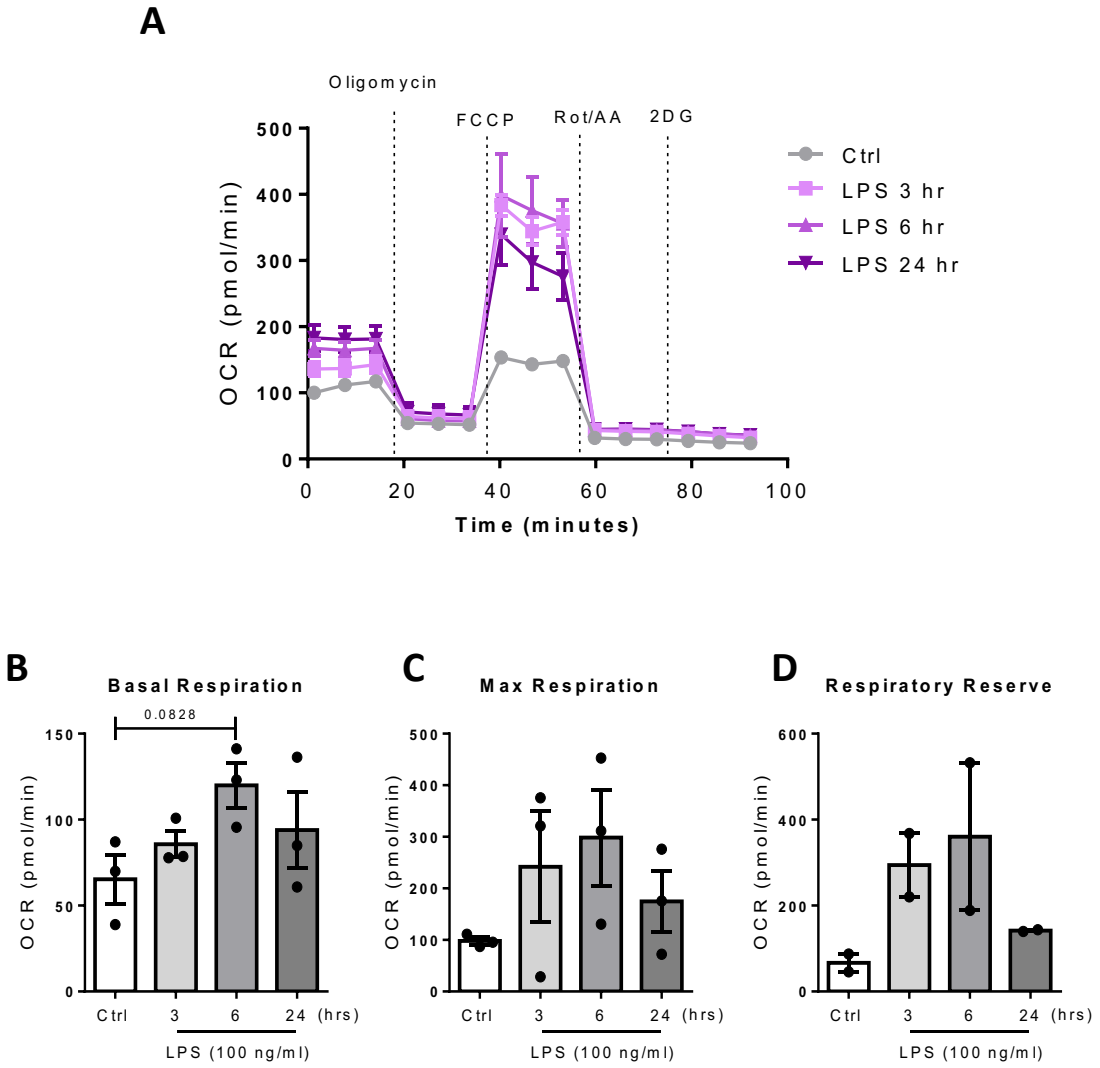

Figure 3.11: Human macrophages temporally increase oxidative phosphorylation after LPS stimulation. Primary human macrophages (1 x 10^6 cells/ml) were stimulated with LPS (100 ng/ml) for 3, 6 or 24 hours prior to placement in a Seahorse XF96 analyser. The oxygen consumption rate (OCR) was measured before and after injection of oligomycin (1 µM), FCCP (1 µM), antimycin A (500 nM)/Rotenone (500 nM), and 2-DG (25mM). **(A)** Representative OCR measurements over time for each LPS stimulation time-point. Data depicts one representative experiment. **(B-D)** Pooled data (n=3) depicting the calculated mean basal respiratory rate, max respiratory rate and respiratory reserve for each LPS stimulation time-point. All data is represented as mean ± SEM and was analysed using was analysed using Kruskal Wallis with Dunn's post-test.

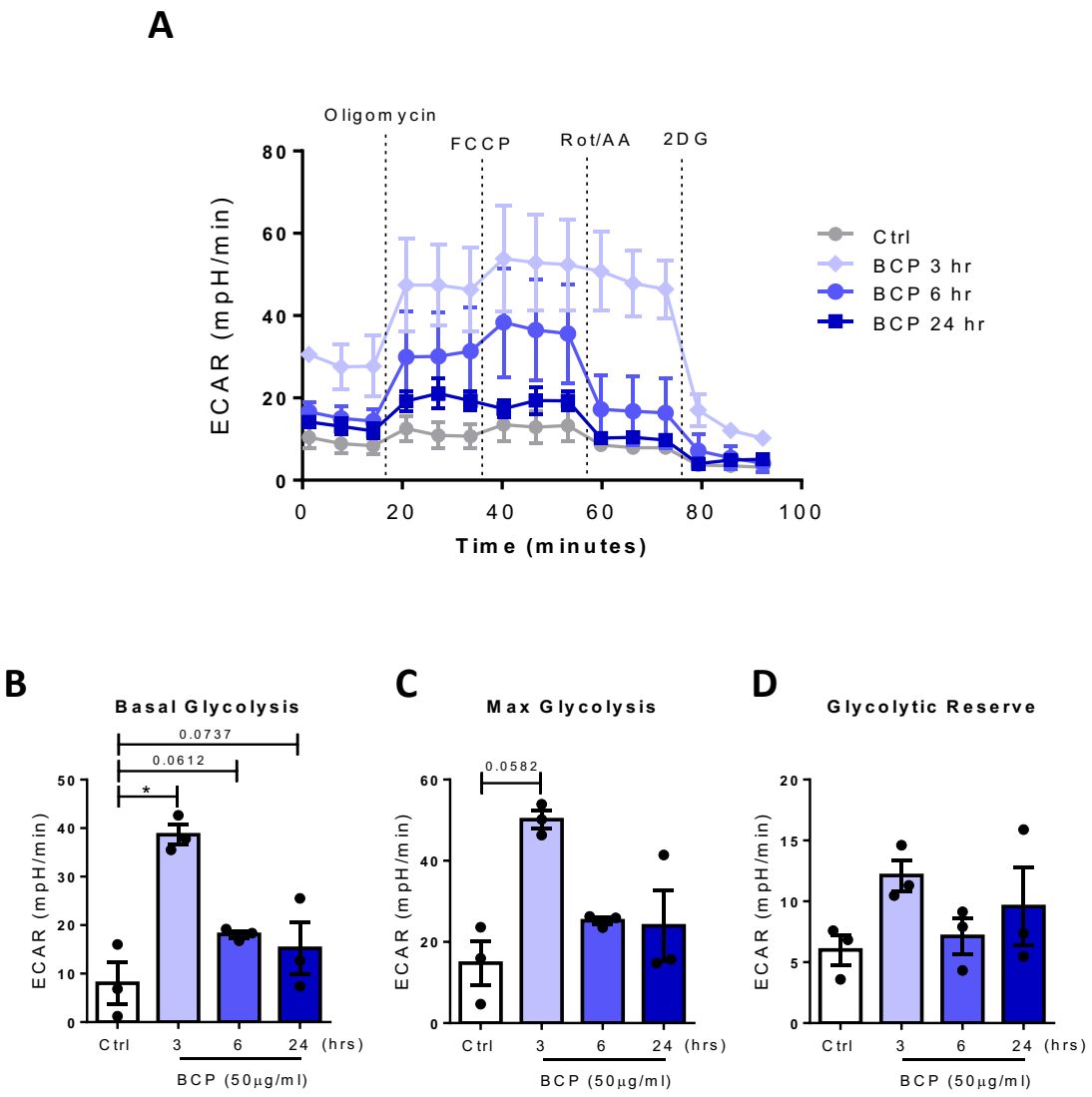

Figure 3.12: Human macrophages temporally increase glycolytic metabolism in response to BCP crystal stimulation. Primary human macrophages (1 x 10^6 cells/ml) were stimulated with BCP crystals (50 µg/ml) for 3, 6 or 24 hours prior to placement in a Seahorse XF96 analyser. The extracellular acidification rate (ECAR) was measured before and after before and after injection of oligomycin (1 µM), FCCP (1 µM), antimycin A (500 nM)/Rotenone (500 nM), and 2-DG (25 mM). **(A)** Representative glycolysis (ECAR) measurements over time for each LPS stimulation time-point. Data depicts one representative experiment. **(B-D)** Pooled data (n=3) depicting the calculated mean basal glycolytic rate, max glycolytic rate and glycolytic reserve for each LPS stimulation time-point. All data is represented as mean ± SEM and was analysed using was analysed using Kruskal Wallis with Dunn's post-test (*P≤0.05, **P≤0.01).

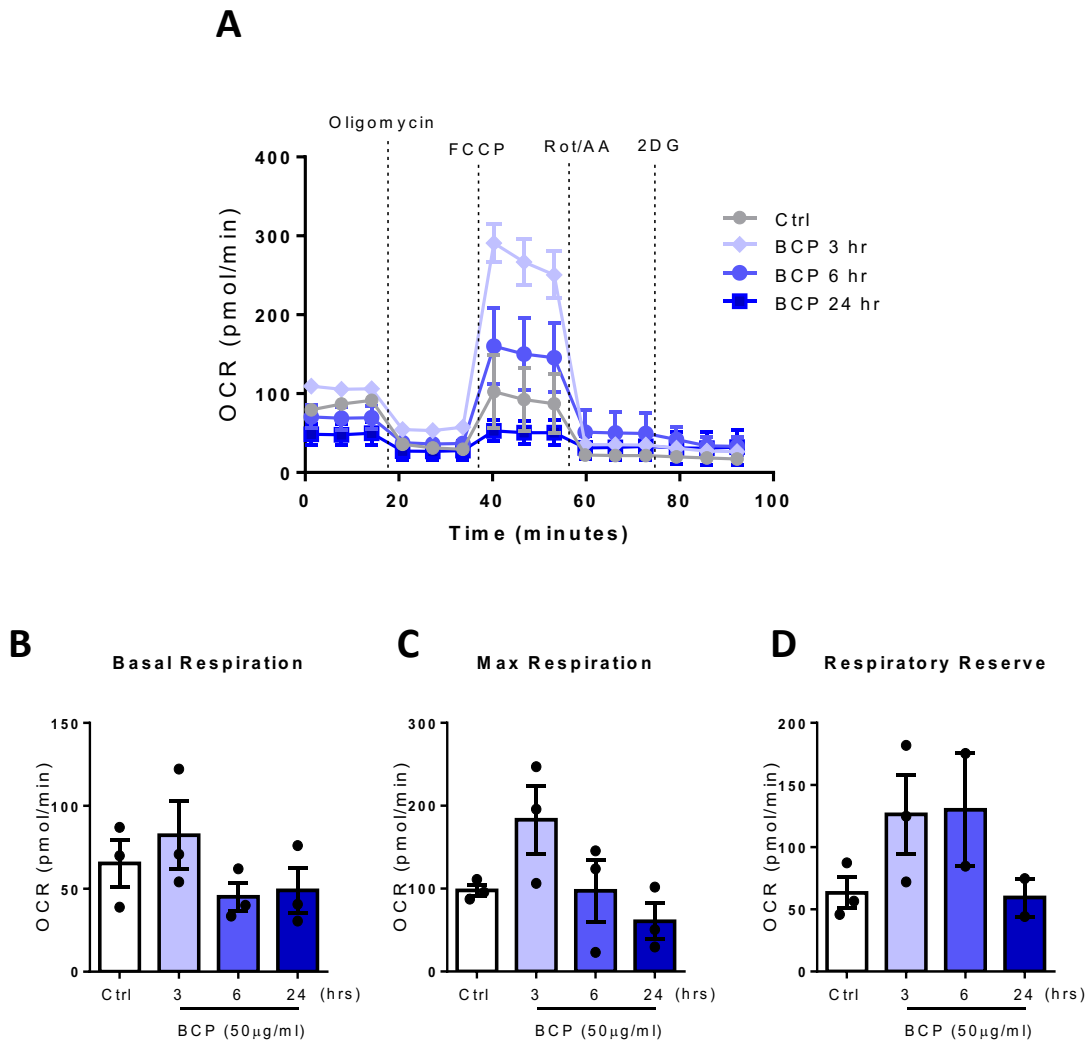

Figure 3.13: Human macrophages temporally increase oxidative phosphorylation in response to BCP crystal stimulation. Primary human macrophages (1 x 10^6 cells/ml) were stimulated with BCP crystals (50 µg/ml) for 3, 6 or 24 hours prior to placement in a Seahorse XF96 analyser. The oxygen consumption rate (OCR) was measured before and after injection of oligomycin (1 µM), FCCP (1 µM), antimycin A (500 nM)/Rotenone (500 nM), and 2-DG (25 mM). **(A)** Representative OCR measurements over time for each LPS stimulation time-point. Data depicts one representative experiment. **(B-D)** Pooled data (n=3) depicting the calculated mean basal respiratory rate, max respiratory rate and respiratory reserve for each LPS stimulation time-point. All data is represented as mean ± SEM and was analysed using was analysed using Kruskal Wallis with Dunn's post-test.

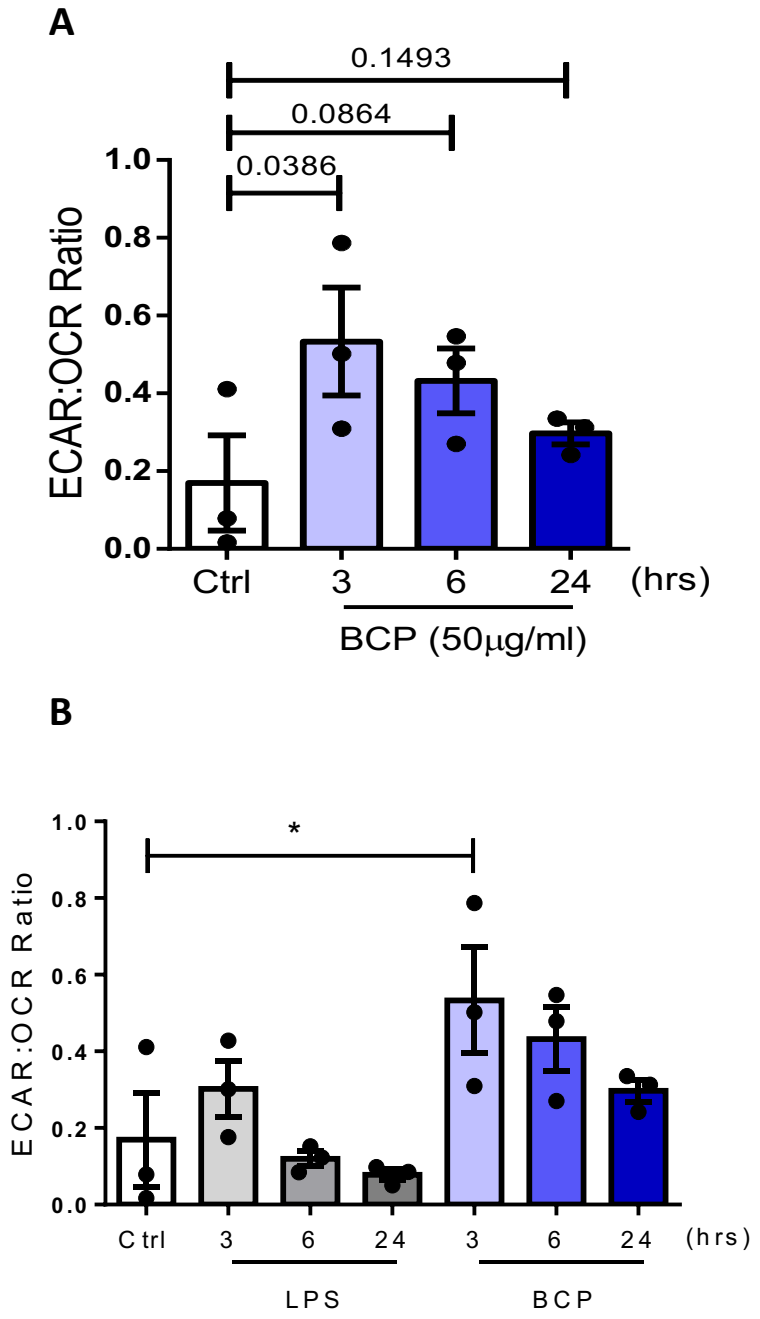

Figure 3.14: BCP crystal stimulated macrophages favour glycolytic metabolism compared to LPS stimulated macrophages. Primary human macrophages (1 x 10^6 cells/ml) were stimulated with BCP crystals (50 μg/ml) or LPS (100 ng/ml) for 3, 6 or 24 hours prior to placement in a Seahorse XF96 analyser. Basal rates of glycolysis and oxidative phosphorylation were measured by ECAR and OCR respectively. **(A)** Pooled data (n=3) the calculated mean ratio of ECAR:OCR for each BCP stimulation time-point. **(B)** Pooled data (n=3) the calculated mean ratio of ECAR:OCR for each BCP and LPS stimulation time-point. All data is represented as mean ± SEM and was analysed using Kruskal Wallis with Dunn's post-test (*P≤0.05).

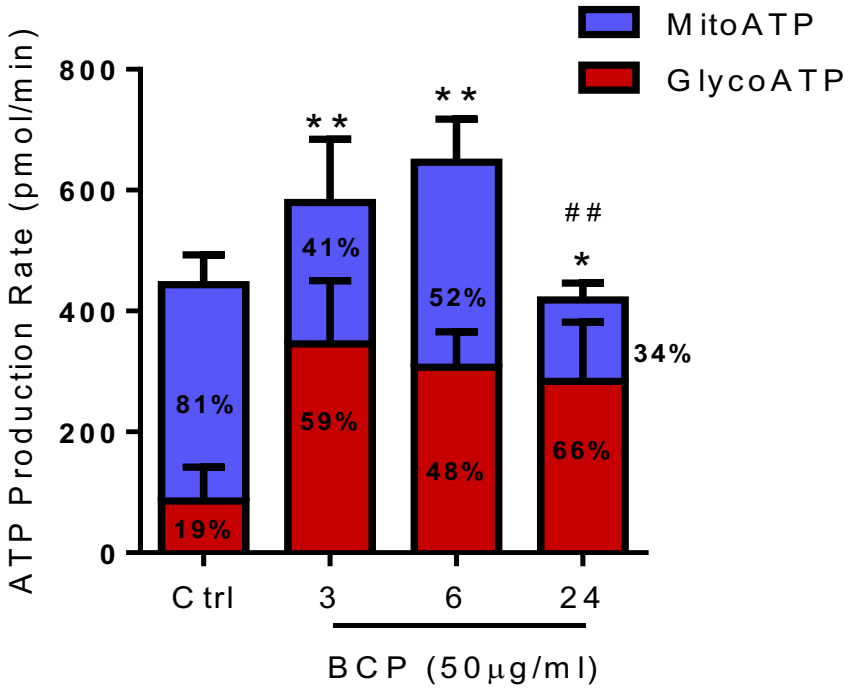

Figure 3.15: BCP crystal treated cells primarily derive their ATP from glycolysis. Primary human macrophages (1 x 10^6 cells/ml) were stimulated with BCP crystals (50 µg/ml) for 3, 6 or 24 hours prior to placement in a. Seahorse XF96 analyser. The extracellular acidification rate (ECAR) and oxygen consumption rate (OCR) was measured before and after injection of oligomycin (1 µM) and antimycin A (500 nM)/Rotenone (500 nM). Pooled data (n=3) depicting ATP production rate in response to BCP crystal stimulation. All data is represented as mean ± SEM and was analysed using Kruskal Wallis with Dunn's post-test was used for all Seahorse calculations. (** denotes statistical significance for changes in GlycoATP vs untreated control, ## denotes statistical significance for changes in MitoATP vs untreated control).

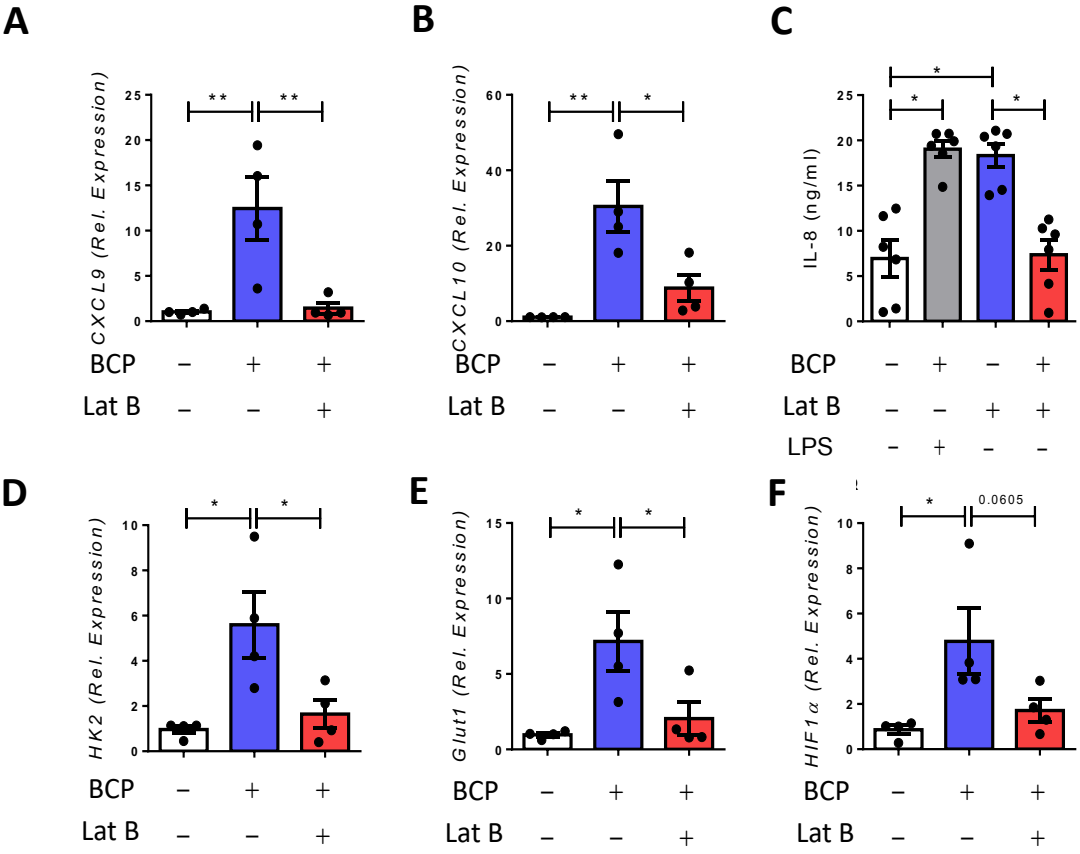

Figure 3.16: Macrophage polarization and metabolic reprogramming by BCP crystals is dependent on particle uptake. Primary human macrophages (1 x 10^6 cells/ml) were treated with BCP crystals (50 µg/ml) alone or were pre-treated with the actin polymerization inhibitor, Latrunculin B (1 µM), prior to treatment with BCP (50 µg/ml). Graphs demonstrating mRNA expression levels of (A) CXCL9 and (B) CXCL10 (n=4). (C) Cytokine levels of IL-8 in cell supernatants (n=6). mRNA expression of the glycolytic markers (D) HK2, (E) Glut1 and (F) HIF1α (n=4). mRNA concentration was normalised to the housekeeping genes 18s (A-C) or RPLPO (D-F) ribosomal RNA. Gene expression, relative to untreated control cells, was determined using the $2^{-\Delta\Delta CT}$ algorithm. Data is represented as mean ± SEM and analysed using Kruskal Wallis with Dunn's post-test for cytokine assays and one-way ANOVA with Tukey post-test (*P≤0.05, **P≤0.01).

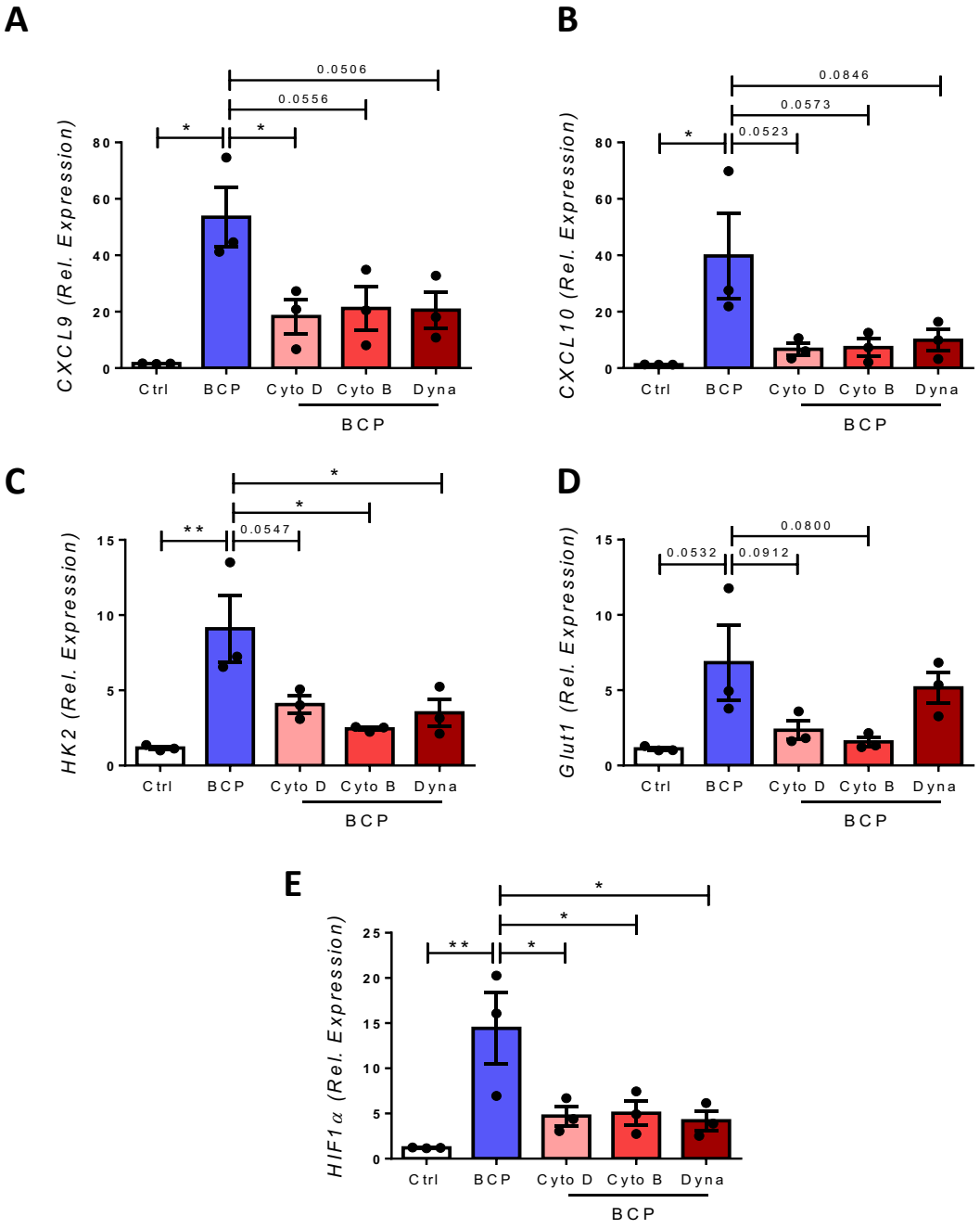

Figure 3.17: Macrophage polarization and metabolic reprogramming by BCP crystals is dependent on particle uptake. Primary human macrophages (1 x 10^6 cells/ml) were treated with BCP crystals (50 µg/ml) alone or were pre-treated with the actin polymerization inhibitors, Cytochalasin D (5 µM), Cytochalasin B (5 µM) or the Dynamin inhibitor, Dynasore (80 µM) prior to treatment with BCP crystals (50 µg/ml). Graphs demonstrating mRNA expression levels of **(A)** CXCL9, **(B)** CXCL10, the glycolytic markers **(C)** HK2, **(D)** Glut1 and **(E)** HIF1α (n=3). mRNA concentration was normalised to the housekeeping genes 18s (A & B) or RPLPO (C-E) ribosomal RNA. Gene expression, relative to untreated control cells, was determined using the $2^{-\Delta\Delta CT}$ algorithm. Data is represented as mean ± SEM and analysed using one-way ANOVA with Tukey post-test (*P≤0.05, **P≤0.01).

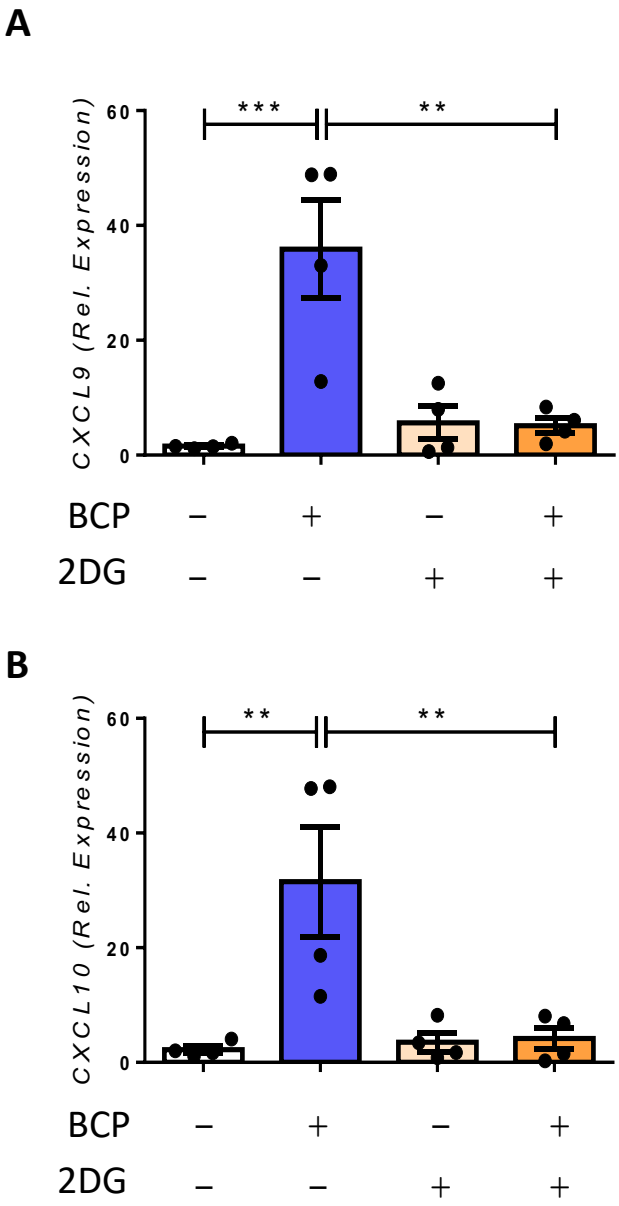

Figure 3.18: BCP crystal-induced M1 macrophage polarization is reduced in the presence of the glycolytic inhibitor 2-DG. Primary human macrophages (1 x 10^6 cells/ml) were stimulated with BCP crystals (50 µg/ml) in the presence or absence of the glycolytic inhibitor 2-DG (25 mM) for 24 hours. Cells were lyzed and mRNA expression of **(A)** CXCL9 or **(B)** CXCL10 was assessed by real-time PCR. mRNA concentration was normalised to the housekeeping gene 18s ribosomal RNA. Gene expression, relative to untreated control cells, was determined using the $2^{-\Delta\Delta CT}$ algorithm. Data is represented as mean ± SEM (n=4) and analysed using one-way ANOVA with Tukey post-test (**P≤0.01, ***P≤0.001).

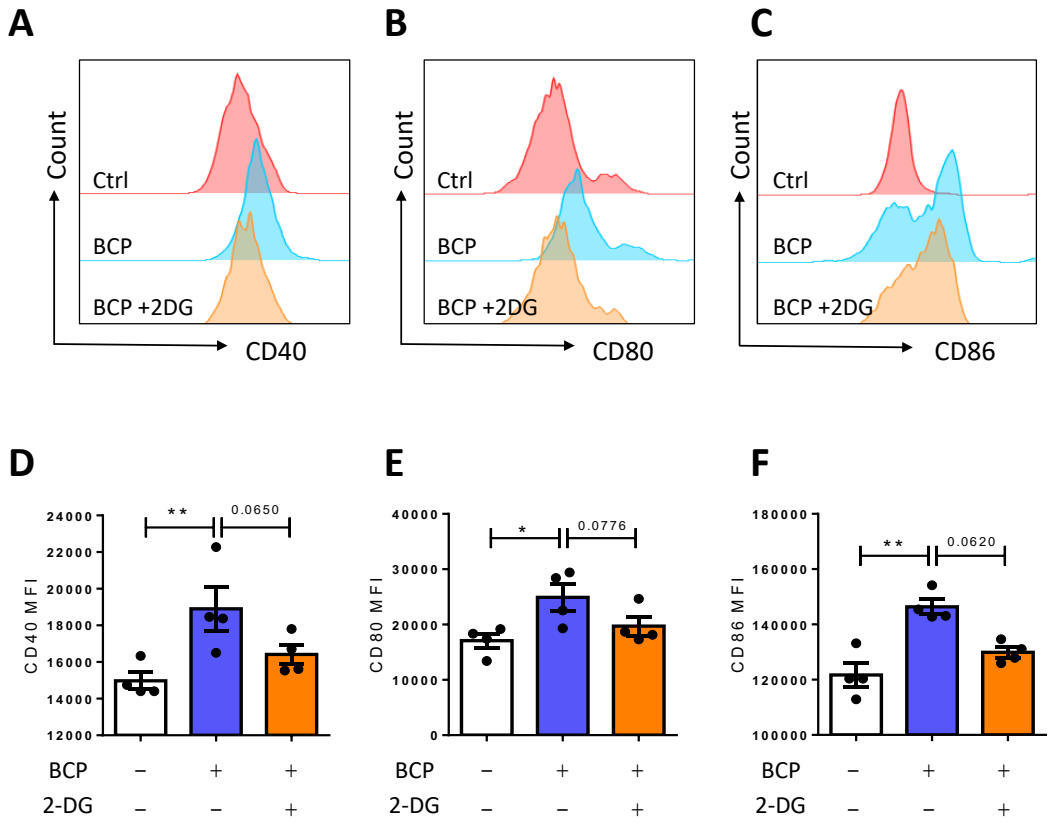

Figure 3.19: There is a trend towards a reduction in BCP crystal-induced maturation marker expression in the presence of the glycolytic inhibitor, 2-DG. Primary human macrophages (1 x 10^6 cells/ml) were stimulated with BCP crystals (50 µg/ml) in the presence or absence of 2-DG (25 mM) for 24 hours. Representative histograms from one experiment demonstrating **(A)** CD40, **(B)** CD80 and **(C)** CD86 surface marker expression. (D-F) Graphs of pooled data (n=4) depicts Mean Fluorescence Intensity (MFI) of surface marker expression. Data is represented as mean ± SEM Data and was analysed using Kruskal Wallis with Dunn's post-test (*P≤0.05, **P≤0.01).

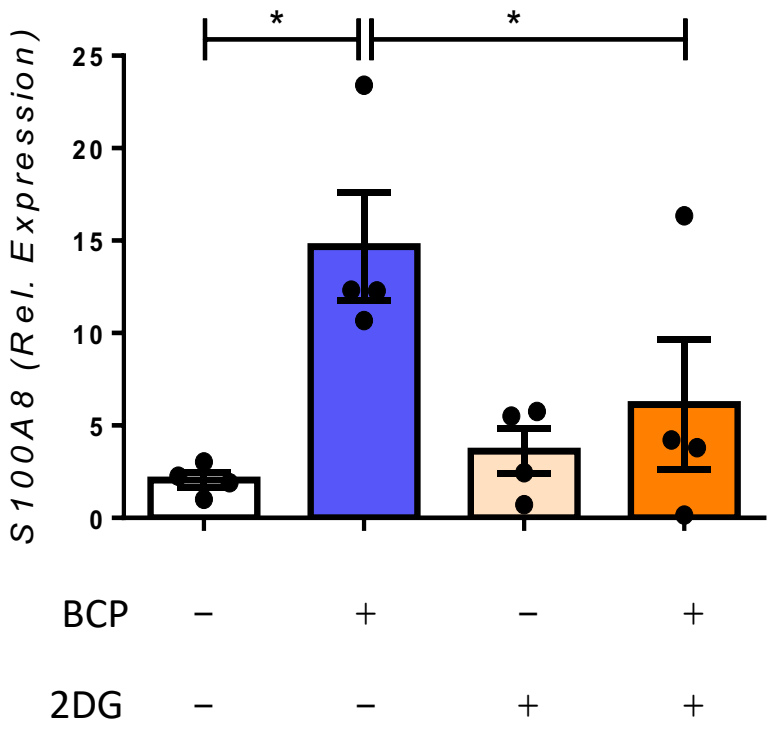

Figure 3.20: BCP crystal induced-S100A8 expression is dependent on glycolysis. Primary human macrophages (1 x 10^6 cells/ml) were stimulated with BCP crystals (50 µg/ml) in the presence or absence of 2-DG (25 mM) for 24 hours. Cells were lysed and mRNA expression of S100A8 was assessed by real-time PCR. mRNA concentration was normalised to the housekeeping gene 18s ribosomal RNA. Gene expression, relative to untreated control cells, was determined using the $2^{-\Delta\Delta CT}$ algorithm. Data is represented as mean ± SEM (n=4) and analysed using one-way ANOVA with Tukey post-test (*P≤0.05).

3.4 Discussion

While several studies have demonstrated that impaired mitochondrial dysfunction contributes to pro-catabolic processes in OA chondrocytes, the factors contributing to this phenomenon have not been fully characterized (67). Furthermore, there have been few studies examining metabolic reprogramming in OA synovial fibroblasts or macrophages. During infection, stimulation of pattern recognition receptors (PRRs) leads to enhanced glycolysis which enables immune cells to generate sufficient ATP and pro-inflammatory mediators required to carry out effector functions (41). It is now well accepted that sterile tissue injury can provoke an immune response analogous to that seen during infection and that endogenous molecules generated upon tissue damage are capable of exerting similar effects on cellular processes. Hence, while the switch to a highly active metabolic state is necessary for immune cell activation during infection, metabolic reprogramming by DAMPs/alarmins in the absence of infection has the potential to exacerbate existing inflammation. The data presented in this chapter demonstrates that BCP crystals, which are OA-associated DAMPs, polarize primary human macrophages towards an M1-like phenotype, enhancing expression of M1-macrophage associated markers and elevating expression of surface maturation markers. Furthermore, BCP crystal stimulation promotes a bioenergetic switch favouring glycolysis and this is accompanied by increased expression of HIF1α, GLUT1 and hexokinase 2, all of which are surrogate markers of glycolysis. Finally, BCP-induced expression of M1 markers and the alarmin, S100A8, was inhibited in the presence of glycolytic inhibitor, 2DG, suggesting that BCP-induced macrophage polarization and inflammation may be dependent on metabolic reprogramming.

Particulates such as calcium oxalate crystals have previously been reported to promote M1 macrophage polarization (246) and, while a number of studies have investigated metabolic reprogramming in human immune cells in response to exogenous pathogen associated molecules (i.e. PAMPs), there have been no studies to date examining the impact of endogenous particulates on immune cell metabolism. In this chapter, it was demonstrated that human macrophages stimulated with BCP crystals upregulate both glycolysis and oxidative phosphorylation within hours of activation, however, the overall

glycolytic and ATP production rate is higher. LPS stimulation also resulted in enhanced glycolysis and oxidative phosphorylation in human macrophages however, BCP crystals promoted a higher ECAR:OCR ratio than LPS which is considered a potent PAMP. The observed effects of LPS on ECAR and OCR rates differs from reports in murine DC demonstrating that LPS strongly upregulates aerobic glycolysis whilst simultaneously downregulating oxidative phosphorylation via the action of iNOS-derived NO (259, 260). There is, however, controversy regarding the expression/activity of iNOS in human immune cells (55, 57) and the data presented in this chapter is in agreement with a recent study by Malinarich *et al* who reported that, while mature human DC are more glycolytic than immature DC, they do not entirely downregulate oxidative phosphorylation, and instead display a more "balanced" switch to glycolysis whereby glycolysis and oxidative phosphorylation are both upregulated (261).

BCP crystals have previously been reported to upregulate the expression of inflammatory and catabolic mediators in a number of cell types implicated in OA (70, 262–264). The data presented here demonstrates that, in addition to cytokines, chemokines and MMPs, BCP crystals can also upregulate expression of the key glycolytic enzymes, hexokinase 2, GLUT1 and HIF1α, an effect, which was attenuated in the presence of phagocytosis inhibitors. Furthermore, when glycolysis was inhibited with the glucose analog, 2-DG, a notable decrease in M1-macrophage marker expression was observed, in addition to S100A8, which is a key OA-associated DAMP. Further study is required to determine if metabolic targeting impacts on downstream targets of S100A8 which include cytokines such as IL-6 and IL-8, as well as MMPs 1, 9 and 13 (100, 248). Of note, paquinimod, a quinoline-3-carboxamide derivative that binds to S100A9 and prevents interaction with TLR/RAGE, is currently under investigation as a potential treatment for OA (265). Prophylactic treatment with paquinimod reduced osteophyte size, synovial thickening, and cartilage damage in the collagenase-induced OA model (266). It has also been demonstrated that ex vivo treatment of human OA synovium with paquinimod prior to S100A9 stimulation reduced IL-6, IL-8, TNFα, MMP1 and MMP2 secretion. Furthermore, clinical scores of RA patients was improved by 50 % upon treatment with an anti-S100A9 (267). A phase Ib clinical trial has reported paquinimod

to be well-tolerated in SLE (268), therefore, this molecule may also be a promising DMOAD for OA patients given their high synovial concentrations of S100A8/9.

Interestingly, results presented in this chapter demonstrate that BCP crystals themselves were potent drivers of IL-8 expression, whose primary role is to act as chemoattractant for neutrophils. While OA is not necessarily considered a neutrophil mediated disease, elevated levels of IL-8 have been observed in the serum, synovial fluid and synovium of OA patients, where enhanced IL-8 levels were found to be positively correlated with radiographic score and joint pain (269, 270). Furthermore, IL-8 expression was found to be 37-fold higher in chondrocytes from OA knee tissue compared to that of non-OA control tissue (271) Additionally, neutrophils themselves can actively perpetuate cartilage damage through secretion of elastase, a protease capable of degrading collagens, elastin and proteoglycans (272). Furthermore, neutrophils have been implicated in driving angiogenesis, which in turn can promote hypertrophy of chondrocytes, propagating joint damage (273). Therefore, IL-8 may play a significant role in OA pathogenesis and indeed, neutralization of IL-8 was found to attenuate clinical symptoms in a mouse model of OA (274). While the specific factors involved in the upregulation of IL-8 have not yet been elucidated, data presented in this chapter demonstrate that BCP crystals can directly drive IL-8 secretion in macrophages. This is in line with Nadra *et al*, which demonstrated enhanced IL-8 release from BCP crystal treated macrophages (243). Furthermore, calcium pyrophosphate dihydrate (CPPD) crystals, associated with pseudogout have also been shown to induce expression of IL-8 in monocytes and macrophages (273). As S100A8 is known to stimulate the synovial membrane to generate pro-inflammatory mediators, including IL-8 in OA (275), BCP-induced IL-8 observed in this chapter may represent a feed forward mechanism whereby BCP-induced S100A8 drives expression of IL-8. Further study is required to fully elucidate the relationship between BCP crystals, IL-8 and the downstream effects of S100A8 production. It will also be necessary to determine whether the effects observed here are heightened in synoviocytes from OA patient samples and whether glycolytic inhibitors impact on inflammatory/catabolic processes. Indeed, upregulation of glucose transport and an increase in glycolytic metabolism has been demonstrated in OA and particularly in chondrocytes where accumulation of lactic acid contributes to matrix

acidification and impaired ECM synthetic function (276–279). Less is known regarding metabolic disturbances in OA-synoviocytes, however an increase in the glycolysis/OXPHOS ratio has been observed in OA-FLS (67). Silencing of PHD2, one of several PHDs that when active, are involved in the targeted proteasomal degradation of HIF-1α, resulted in decreased expression of angiogenic genes (273). Furthermore, high glucose levels were shown to induce ROS and VEGF in OA-FLS further implicating a metabolic switch and increased glucose transport in synovial joint cells in OA (274).

In summary, the results presented in this chapter contribute to our current understanding of the pathogenic role of BCP crystals and their pro-inflammatory properties. The data presented herein supports a model whereby BCP crystals can drive metabolic reprogramming to a glycolytic state resulting in the production of ATP via glycolysis rather than oxidative phosphorylation in primary human macrophages. It also provides evidence of polarization of macrophages to an M1 state upon crystal stimulation (Figure 3.21). While the field of immunometabolism is still in its infancy and much remains to be learned regarding the impact of metabolic reprogramming on disease pathogenesis, ultimately the data presented in this chapter supports the idea that the it may be possible to modulate metabolic changes in polarized macrophages by specifically targeting key glycolytic enzymes. However, extreme caution is required given the strong potential for off target effects. This is of particular importance in OA given that chondrocytes, in particular, exist in a hypoxic environment and rely on HIF1α and glycolysis to maintain homeostasis. Currently, there are no drugs available to target BCP crystal deposition in the OA joint and subsequent inflammatory responses, however, based on the above findings, it is possible that targeting BCP-and DAMP-induced metabolic reprogramming represents a novel avenue that requires further consideration and exploration.

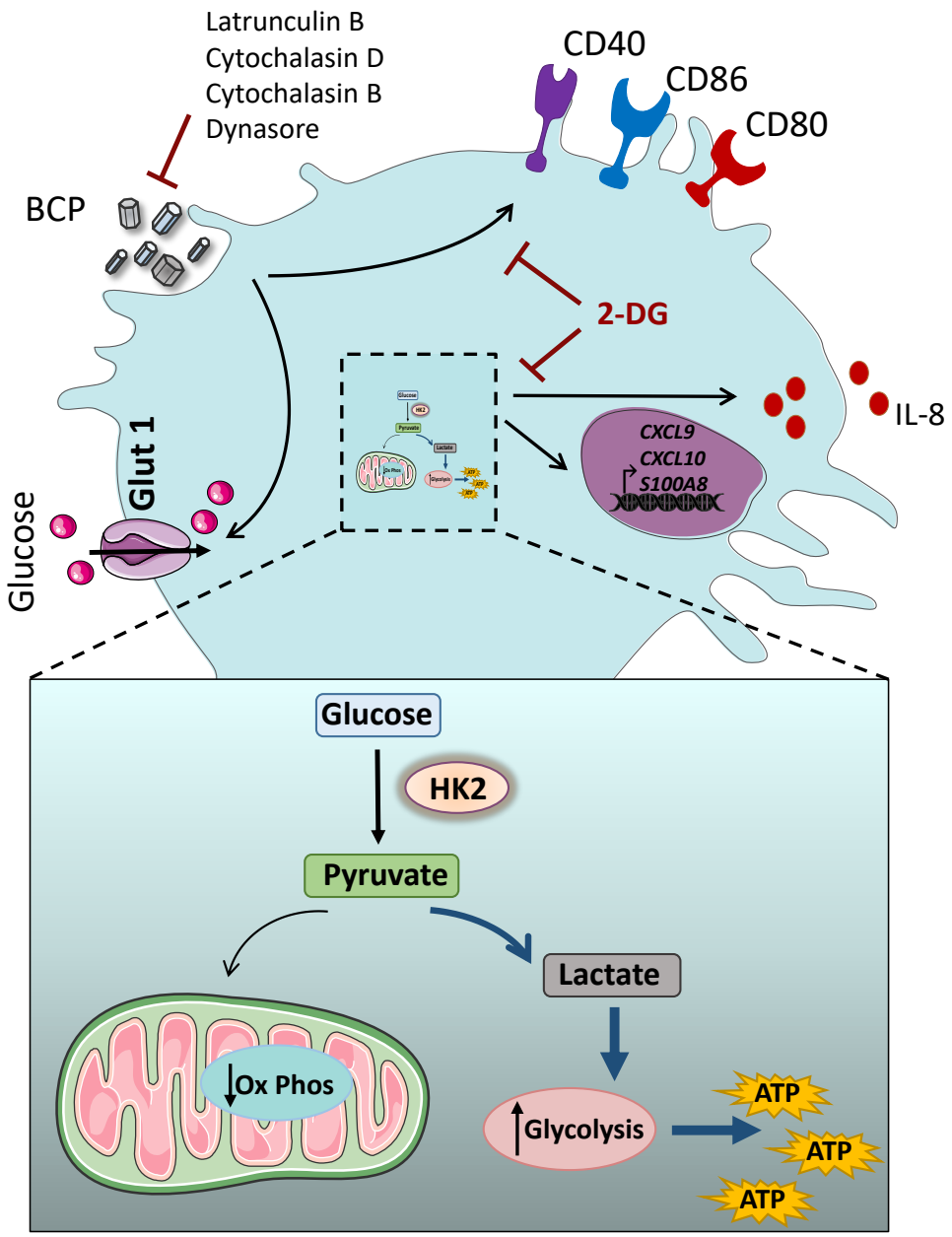

Figure 3.21: Model of BCP crystal mediated macrophage metabolic reprogramming and M1 polarization. BCP crystals are internalized via phagocytosis and mediate direct upregulation of M1 surface markers including CD40, CD80 and CD86 and the M1 associated genes, CXCL9 and CXCL10. Additionally, BCP crystals promote a metabolic switch favouring glycolysis and this is accompanied by increased expression of the glycolytic enzymes HK2, Glut1 and HIF1α. Inhibition of glycolysis in turn abrogates BCP crystal induced M1 marker and alarmin expression.

Chapter 4: Investigation of the signalling pathways activated by orthopaedic implant particulates and their involvement in macrophage polarization

4.1 Introduction

Total joint replacements (TJR) are costly procedures required to alleviate pain and improve ambulation in patients with end stage osteoarthritis (OA) and rheumatoid arthritis. While many advances have been made in implant technology, revision surgeries are often required due to the limited lifespan of orthopaedic devices. The predominant factor contributing to implant failure is aseptic loosening which arises due to progressive inflammation at the bone-implant interface. Several studies have shown that synthetic materials currently marketed for orthopaedic applications drive potent host immune responses during the early post-implantation period and contribute significantly to local bone loss or osteolysis (282). Specifically, 'wear debris' from ceramic and metal based prostheses can drive macrophage-mediated inflammatory responses leading to chronic synovitis, osteoclast activation and eventual implant loosening. In fact, periprosthetic osteolysis accounts for 75% of implant failures, and as a result, individuals must undergo revision surgery which, in itself, is associated with shorter duration of implant survival and higher patient risk (114).

A number of studies have demonstrated that macrophages play an integral role in the initiation of periprosthetic osteolysis (283–285). These cells can undergo phenotypic polarization to pro-inflammatory M1 macrophages, which promote pathogen killing and are associated with chronic inflammation, or anti-inflammatory M2 macrophages, which are associated with immunoregulation, tissue repair and remodelling. In the case of TJR, classically activated M1 macrophages are required to initiate the foreign body response necessary for early post-implantation wound healing, while their eventual transition to alternatively activated M2 macrophages is required to prevent fibrous capsule formation and chronic inflammation (203). However, it has been demonstrated that synovial tissues from patients undergoing revision surgery exhibit higher ratios of M1 versus M2 macrophages compared to tissues from patients undergoing primary TJR and that PMMA particles can enhance the expression of the M1 macrophage marker, iNOS (140). Furthermore, several studies have demonstrated that wear-particles directly activate M1 macrophages leading to a sustained inflammatory response characterised by the production of chemokines and pro-inflammatory cytokines such as TNFα, IL-1 and

IL-6 (286–290). As well as causing tissue damage, this increased production of pro-inflammatory mediators contributes to an imbalance in the levels the key osteoclastogenesis regulators, RANKL and OPG, and facilitates the formation and activation of bone-resorbing osteoclasts (139, 150, 291, 292). As a result, efforts are underway to develop strategies to modulate periprosthetic inflammatory responses using selective small molecule inhibitors or anti-cytokine therapies. For example, studies have demonstrated that the COX-2 inhibitor, Celecoxib, suppresses wear-debris induced osteolysis in both the murine calvarial model and rabbit prosthesis model (293, 294). Furthermore, Etanercept, the decoy receptor for TNF-α, has been shown to reduce bone resorption and osteoclastogenesis in mice (138), as has gene delivery of the anti-inflammatory cytokine, IL-10 (159). In addition to specific targeting, efforts are also being made to manipulate the interplay between the implant material itself and the host immune system, and recent evidence suggests that promoting specific interactions between the two can boost immune tolerance and positive healing outcomes (201).

Despite these efforts, many aspects of macrophage mediated responses to particulate wear debris remain poorly characterised. Furthermore, most studies to date have focused on murine macrophages. Therefore the aim of this chapter is to carry out a detailed analysis of the effects of two commonly used biomaterials in primary human macrophages. This study will focus on hydroxyapatite (HA), which is widely used to coat orthopaedic implants given it's biocompatible and osteogenic capabilities (295, 296) PMMA particles, known to be generated from PMMA bone cement (the fixative used to hold implants in place), will also be examined as they have been shown to induce inflammatory responses in murine macrophages and *ex vivo* patient samples (140, 141, 297).

While micron sized HA is routinely used in orthopaedic devices, more recently, nanoHA has been explored for use in orthopaedic applications due to its high surface area and superior cell adhesive properties (220). Commercial HA particles are available in a range of shapes and sizes and it has been well documented that the immune response induced by HA particles depends heavily on their size and morphology. For example, it has been demonstrated that needle shaped HA particles of approximately 0-25 µm in size

enhance both IL-1β and IL-18 production in LPS primed murine macrophages and dendritic cells, compared to their spherical counterparts of the same size. Furthermore, HA particles larger than 100 μM do not drive production of either cytokine (101, 298). While, the use of nano-HA coatings is becoming more common, the effects of these particles on macrophage activation/phenotype has not yet been examined. Therefore, the final aim of this chapter is to assess macrophage responses to nano sized HA particles and to determine if there are differences in responses when compared to micro-sized HA particles.

4.2 Specific Aims

- To examine human immune cell activation and macrophage polarization following exposure to orthopaedic wear particles in primary human macrophages.
- To compare macrophage responses to micron and nano sized HA particles in primary human macrophages.

4.3 Results

4.3.1 Physical characterisation of PMMA and HA particles.

Prior to assessing cellular responses to hydroxyapatite (HA) and PMMA particulates, it was first of interest to characterise the size and morphology of the individual particles. HA and PMMA particles were imaged using scanning electron microscopy (SEM) and, as expected, the PMMA particles are microspheres ranging in diameter from approximately 1µm to 10µm, with a smooth even surface (Figure 4.1 A). HA particles were found to be very irregular in shape with a rough surface and range in size from 1µm to 5µm (Figure 4.1 A). Unlike the PMMA particles, HA particles are prone to aggregation and as result their actual size is difficult to determine by imaging analysis alone. Therefore, dynamic light scattering was performed to accurately determine their size range. Using this method, the mean particle size was found to be approximately 1.3 µm (Figure 4.1 B). The zeta potential of the HA particles was also assessed using electrophoretic light scattering and was determined to be -10.13 mV. This small value obtained for zeta potential is indicative of the tendency of the particles to aggregate.

Prior to undertaking biological assays, it was necessary to first verify that the particles were endotoxin free. Particles were tested for lipopolysaccharide (LPS) contamination using the HEK-BlueTM hTLR4 assay system. HEK-blue cells expressing TLR4 were stimulated with LPS (1, 10 and 100 ng/ml; positive control), PMMA particles (500 µg/ml) or HA particles (250 µg/ml) for 24 hours. The expression of SEAP, which is under the control of NF-κB and AP-1 was measured by incubating cell supernatants with HEK-blue detection medium for 30 min at 37 °C and absorbance was read at 650 nm. Results demonstrate that the concentration of endotoxin (LPS) was below the threshold level for TLR4 activation as determined using the HEK-Blue LPS detection kit and particle preparations were therefore deemed suitable for further in vitro assays (Figure 4.1 C).

4.3.2 PMMA and HA particles directly promote M1 macrophage polarization.

It has previously been demonstrated that periprosthetic tissues exhibit increased M1/M2 macrophage ratios compared to non-operated osteoarthritic synovial tissues,

and that PMMA particles can enhance the expression of the M1 macrophage marker, iNOS (140). In order to examine the direct impact of HA and PMMA particles on macrophage polarization, primary human macrophages were treated with previously published doses of PMMA particles (500 μg/ml) or HA (250 μg/ml) for 24 hours and expression of established M1 associated genes was assessed by real-time PCR. PMMA significantly enhanced the mRNA expression of the M1 markers, CXCL9, CXCL10 and CXCL11 compared to control samples (Figure 4.2 A, C & E). HA particles also significantly enhanced the expression of CXCL9, CXCL10 and CXCL11 (Figure 4.2 B, D & F). Interestingly the relative fold increase in mRNA of these M1 associated genes was higher in HA treated macrophages (200-550) than PMMA treated macrophages (20-100) indicating that HA particles may be a more potent inflammatory particulate than PMMA particles.

4.3.3 PMMA and HA particles decrease M2 macrophage marker expression and phagocytic capacity.

Having assessed the impact of HA and PMMA particles on M1 macrophage associated gene expression, their impact on M2 associated genes was next assessed. Primary human macrophages were stimulated with HA or PMMA particles for 24 hours and mRNA expression of MRC1 and CCL13 was analysed by real-time PCR. In contrast to the observed induction of M1 markers upon HA or PMMA treatment, there was a significant decrease in the basal level of M2 macrophage marker gene expression upon particle treatment (Figure 4.3 A-D).

It has been reported that the phagocytic capacity of M1 activated macrophages is much lower than that of non-activated or M2 polarized macrophages which retain a high phagocytic capacity (250–252, 299). Having established that PMMA and HA particles enhance M1 macrophage marker but decrease M2 marker gene expression, it was next of interest to assess the phagocytic capacity of macrophages following stimulation with wear particles as an indication of their functionality. Primary human macrophages were treated with PMMA or HA (250 μg/ml) for 6 hours. Cells were then incubated with FITC-conjugated DQ-Ovalbumin (DQ-Ova) at 500 ng/ml and analysed for antigen uptake by

flow cytometry. Unstimulated macrophages had high basal DQ-Ova uptake (66.4%), however upon HA particle stimulation, antigen uptake was reduced to 17%. Similar results were observed with PMMA particle treatment with a reduction to 57.8% (Figure 4.3 E) demonstrating that both particles reduce macrophage phagocytic capacity which is associated with a more mature and activated phenotype. Taken together this indicates that both particle types promote macrophage activation and polarization to an M1-like state.

4.3.4 PMMA and HA particles activate the membrane-associated tyrosine kinase, Syk in primary human macrophages.

Having established that HA and PMMA particles preferentially polarize macrophages towards an M1-like phenotype, the signalling events involved in this transition were next examined. The Dunne laboratory has previously reported that BCP and cholesterol crystals activate the membrane proximal kinase, Syk, in a receptor-independent manner and by a process known as membrane affinity-triggered signalling (MATS) which involves lipid raft formation (99, 300). Syk inhibition has also been reported to inhibit HA-induced IL-6 production in murine chondrocytes (97) and PMMA induced IL-1β production and cell binding in murine macrophages (297). Therefore, in order determine if HA and PMMA particles can directly activate Syk, primary human macrophages cells were stimulated with PMMA particles (500µg/ml) or HA (250 µg/ml) over the course of 30 min and activation of Syk, as indicated by phosphorylation, was examined by immunoblotting. Phosphorylation of Syk was detected within 10-15 min of PMMA particle treatment (Figure 4.4 A) and within 5 min of HA stimulation (Figure 4.4 B). Densitometric analysis of western blots from three individual donors revealed that maximal phosphorylation occurs at 30 minutes post-stimulation with both particle types inducing an approximate 15-30 fold increase in Syk phosphorylation compared to control cells (Figure 4.4 C & D).

4.3.5 PMMA and HA particles drive pro-inflammatory cytokine production in a Syk dependent manner in human macrophages.

In order to investigate if Syk is involved in PMMA and HA-induced pro-inflammatory cytokine production in primary human macrophages, cells were pre-treated with previously published doses of either piceatannol (25 μM) or the orally available Syk inhibitor, R788 (25 μM), for 1 hour, prior to stimulation with HA or PMMA for 24 hours. In the case of PMMA, pre-treatment with both inhibitors resulted in a significant reduction in IL-6 production (Figure 4.5 A) with R788 also significantly reducing TNFα production (Figure 4.5 C). HA-induced IL-6 and TNFα was significantly reduced upon Syk inhibition with piceatannol while the alternative Syk inhibitor, R788, also abrogated HA-induced IL-6 and TNFα (Figure 4.5 B & D). It has been reported that wear particles can drive expression of the chemokine, IL-8 (301), and while IL-8 production was enhanced in PMMA and HA treated cells, pre-treatment with either Syk inhibitor did not significantly alter the levels of this protein suggesting that it is regulated in a distinct manner (Figure 4.5 E & F).

4.3.6 PMMA and HA particles induce IL-1β production in an NLRP3 dependent manner in human macrophages.

In addition to IL-6, TNFα and IL-8, PMMA and HA particles are known to drive the production of IL-1β which contributes significantly to periprosthetic inflammation (302). In an in vitro setting, PMMA and HA driven IL-1β production has been shown to be dependent on activation of the NLRP3 inflammasome in murine macrophages (98, 297), however there is evidence to suggest that this complex may be dispensable for the in vivo production of IL-1β (303, 304). In order to determine whether NLRP3 is required for wear particle-induced IL-1β production in primary human macrophages, cells were primed with LPS (100 ng/ml) for 2 hrs to drive the intracellular expression of pro-IL-1β before being treated with the specific NLRP3 inflammasome inhibitor, MCC950 (1 & 5 μ, for 1 hr prior to exposure to PMMA or HA particles for 24 hours. Both PMMA and HA treatment induced secretion of IL-1β, however, this was significantly reduced upon treatment with MCC950 (Figure 4.6) suggesting that NLRP3 is required for production of this cytokine in human macrophages, at least in an in vitro setting. Syk is reportedly activated upstream of NLRP3 inflammasome assembly (305). In order to determine if Syk is involved in wear particle-induced IL-1β production, primary human macrophages

were primed with LPS (100 ng/ml) for 2 hrs before being treated with the Syk inhibitors piceatannol (25 μM) and R788 (25 μM), for 1 hr prior to exposure to PMMA or HA particles for 24 hours. IL-1β production was attenuated upon treatment with both Syk inhibitors confirming that Syk is also involved in PMMA and HA induced IL-1β production in vitro (Figure 4.7).

4.3.7 PMMA and HA-induced cytokine production occurs via lipid raft formation in primary human macrophages.

As mentioned previously, it has been demonstrated that particulates can activate Syk and drive cytokine production via lipid raft formation in a process known as MATS (100, 104, 248). In order to ascertain whether MATS is involved in wear particle-induced IL-1β production in primary human macrophages, LPS-primed cells were depleted of membrane cholesterol with M-βCD (10 mM) to prevent lipid sorting, prior to stimulation with PMMA or HA. Treatment with M-βCD significantly reduced PMMA-induced IL-1β production (Figure 4.8 A) and there was a trend towards reduced IL-1β in HA treated cells ($p = 0.0889$; Figure 4.8 B). A similar study was performed to establish whether MATS is involved in PMMA and HA-induced TNFα and IL-6 production. There was a significant reduction in HA-induced TNFα and IL-6 (Figure 4.8 C & E), however only a modest reduction was observed with PMMA-induced TNFα and IL-6 upon depletion of membrane cholesterol (Figure 4.8 D & F).

4.3.8 PMMA and HA particles activate ERK and p38 MAP kinases in primary human macrophages.

It is known that MAPKs are activated downstream of Syk activation following Fc receptor engagement (306, 307). In addition, previous work in the Dunne laboratory has demonstrated that BCP and cholesterol crystals activate MAPKs downstream of Syk in a receptor independent manner (99, 300). In order to examine whether wear particles can activate MAPKs, primary human macrophages were stimulated with PMMA and HA over the course of 30 minutes and ERK/p38 activation, as indicated by phosphorylation, was assessed by immunoblotting. Robust phosphorylation of ERK was evident from the 15 minute time point, with maximal phosphorylation evident at 30 minutes post

stimulation for both particle types (Figure 4.9 A & B). Densitometric analysis of western blots from three individual donors revealed that phosphorylation of ERK was significantly increased by PMMA (maximal phosphorylation approx. 80-fold) (Figure 4.9 C) and in the case of HA, an approximate 200-fold increase in ERK phosphorylation was observed (Figure 4.9 D). A similar trend was observed for p38 phosphorylation with phosphorylation occurring at 15 minutes for PMMA simulation (Figure 4.9 E), while phosphorylation was observed as early as 5 minutes upon HA article stimulation (Figure 4.9 F). Similar to ERK phosphorylation, maximal activation was evident at 30 minutes post stimulation with each particle type. Densitometric analysis of three western blots from individual donors revealed that phosphorylation of p38 MAP kinase was significantly increased by approximately 30-fold at 30 minutes post PMMA treatment (Figure 4.9 G) and approximately 80-fold in HA treated macrophages at same time point (Figure 4.9 H).

4.3.9 Pharmacological inhibition of ERK and p38 MAP kinases reduces PMMA and HA-induced TNFα and IL-6 production in primary human macrophages.

Having observed that PMMA and HA activate MAPKs, experiments were carried out to establish whether particle induced cytokine production is dependent on ERK and p38 MAPK activation. Primary human macrophages were pre-treated with SB203580 or PD98059 (20 μM) to inhibit p38 and ERK, respectively, prior to stimulation with PMMA particles or HA for 24 hours. Inhibition of p38 resulted in a significant decrease in PMMA-induced IL-6 and TNFα production while inhibition of ERK also significantly reduced PMMA-induced TNFα. A trend towards inhibition, although not significant, was observed in the case of PMMA-induced IL-6 (Figure 4.10 A & C). In the case of HA, both IL-6 and TNFα were significantly reduced upon p38 inhibition while inhibition of ERK also abrogated HA-induced IL-6 (Figure 4.10 B & D). Taken together this data demonstrates that MAPK activation is directly coupled to PMMA and HA-induced pro-inflammatory cytokine expression. As was the case for Syk inhibition, MAPK inhibition had no effect on particle-induced IL-8, again suggesting an alternative activation pathway (Figure 4.10 E & F).

4.3.10 PMMA and HA particles induce M1 macrophage marker expression in a Syk and MAP kinase dependent manner.

Having observed that PMMA and HA particles drive M1-associated gene expression, and both Syk and ERK/p38 MAP kinases were coupled to HA- and PMMA-induced pro-inflammatory cytokine production, the next step was to establish whether wear particle induced M1 macrophage polarization is dependent on Syk and MAP kinase activation. To test this, primary human macrophages were pre-treated with the MAP kinase inhibitors, SB203580 (p38) and PD98059 (ERK), or the Syk inhibitors, piceatannol and R788, prior to stimulation with PMMA or HA particles and mRNA expression levels of M1-associated genes were measured. Inhibition of p38 resulted in a significant decrease in mRNA expression of CXCL9 and CXCL10 in PMMA particle-treated macrophages, while ERK inhibition also significantly reduced expression of both genes (Figure 4.11 A & B). Inhibition of p38 significantly reduced HA-induced CXCL9 and CXCL10 mRNA expression and, as with PMMA, this was also the case upon ERK inhibition (Figure 4.11 C & D). Similarly, blockade of Syk prior to particle treatment resulted in a significant inhibition of these M1-associated genes (Figure 4.11 A-D).

4.3.11 Chemical and physical characterization of micron and nano-sized Hydroxyapatite particles.

While micron sized HA is routinely used in orthopaedic devices, nanoHA is now being given significant attention due to its high surface area and superior cell adhesive properties (220). However, the immune response induced by different sized HA particles (especially in the nanometre range), has not yet been characterised in primary human macrophages. In order to explore this in more detail, nanoHA particles were produced using the dispersant-aided precipitation method described in section 2.2.5.1. A number of physical characterization techniques were applied to analyse the structural and compositional features of the newly synthesized nanoHA and the commercially available micron-sized HA. Powder X-ray diffraction (XRD) analysis showed that the Bragg diffraction peaks of nanoparticles were largely broadened compared to those of micron particles indicating that the nanoparticles are a “poorly crystalline apatite”, while micron

particles appear as a well crystallized apatite (Figure 4.12 A). Transmission electron microscopy (TEM) revealed nanoparticles were in the form of nanosized rod-like particles whose length and width range from approximately 50 to 100 nm and from 15 to 25 nm, respectively, consistent with previous reports (194, 220). In contrast, scanning electron microscopy (SEM) observations show that micron particles were 1-2μM in size and irregular in shape. (Figure 4.12 B). The size of the nanoparticles was confirmed using dynamic light scattering (Figure 4.12 C). Analysis of the chemical composition, specifically the presence of hydroxyl (OH-) and carbonate (CO_3^{2-}) ions and of water molecules, of both particle types was performed using Fourier-transform infrared (FTIR) spectroscopy. A broad absorption band spreading from approximately 3000 to 3600 cm-1 attributed to water molecules, together with the asymmetric stretching band (v3 mode, from approximately 1360 cm-1 to 1580 cm-1) and the out-of-plane bending band (v2 mode, at around 870 cm-1) of the carbonate ions are clearly visible for nanoparticles but not for micron particles. In contrast, the stretching band at 3570 cm-1 originating from OH- ions is visible for micron but not for nanoparticles (Figure 4.12 D). Solid-state one dimensional (1D) 1H and 31P single-pulse (SP) magic angle spinning (MAS) Nuclear Magnetic Resonance (NMR) was performed to provide further information on compositional and structural features. Spectra of the nano and micron particles differ greatly in their spectral widths (full width at half maximum, FWHM = 2.9 ± 0.1 ppm and 0.9 ± 0.1 ppm for nano and micron particles, respectively), with a broader distribution of chemical environments appearing in nano particles, supporting the earlier XRD analysis data. In addition, the 1H SP MAS NMR spectrum of nanoparticles also display a broad and intense composite signal observable in the range of δ1H = 5-17 ppm. This signal not only shows the presence of structural water molecules observable at δ1H = 5.5 ppm, but also the presence of acidic phosphate species observable in the form of a downfield shoulder up to δ1H = 17.0 ppm (Figure 4.13). These acidic phosphate species, that are also detected in bone hydroxyapatite (308), were recently demonstrated to be HPO_4^{2-} ions based on accurate interatomic distance measurements (309).

To further investigate the chemical environments of these hydrogen-bearing species, two-dimensional (2D) {1H} 31P Heteronuclear Correlation (HetCor) MAS NMR spectra of nano and micron HA particles were recorded (Figure 4.14 A i & ii). These spectra are in

the form of proton-phosphorus correlation maps in which the different signals, named "correlation peaks", reveal the presence of atomic-scale spatial proximities among rigid hydrogen-bearing [displayed along the vertical (F1) dimension] and phosphorus-bearing species [displayed along the horizontal (F2) dimension]. On the one hand, the upper correlation peak observable at δ1H = 0.0 ppm in the vertical (F1) dimension is present both particles and corresponds to OH- ions near PO_4^{3-} ions in hydroxyapatite structure. On the other hand, a lower correlation peak observable in the range of δ1H = 5-17 ppm in the vertical (F1) dimension is only present for the nanoparticles. The molar proportion of HPO_4^{2-} and PO_4^{3-} ions respectively present in the amorphous surface layer and in the apatitic crystalline core were found to be approximately 40/60 for nanoparticles (Figure 4.14 B & C) whereas a value of 50/50 was determined for bone hydroxyapatite from a mature bone tissue sample (309).

4.3.12 HA and nanoHA particles drive differential cytokine expression.

Data presented earlier in this chapter demonstrated that micron-sized HA particles directly drive polarization of human macrophages towards a pro-inflammatory M1 phenotype. The immune response to nano-sized hydroxyapatite particles has not yet been assessed in human immune cells, therefore, experiments were performed to compare the immune modulating properties of nanoHA to the commercially available micron-sized HA particles. As demonstrated, micron-sized HA can activate the NLRP3 inflammasome to drive maturation of IL-1β in human macrophages (Figure 4.6). In order to examine if nanoHA drives IL-1β production, primary human macrophages were primed with LPS for 3 hours prior to treatment with both particle types for 24 hours. As expected, treatment with HA significantly enhanced secretion of both IL-1β and its co-secreted isoform, IL-1α, however cytokine production was not observed upon treatment with nanoHA particles, suggesting that the smaller particles are below the size range required to activate the NLRP3 inflammasome (Figure 4.15 A & B). This is in contrast to findings in murine dendritic cells which demonstrated NLRP3-dependent IL-1β production by hydroxyapatite particles in the 100 nm size range (310). In addition to IL-1, particulate matter has been shown to drive TNFα production (101). In order to ascertain whether HA or nanoHA were capable of driving TNFα production in primary

human macrophages, cells were treated with particles for 24 hrs and TNFα production was measured by ELISA. As previously demonstrated, micron sized HA significantly enhanced production of the pro-inflammatory cytokine, TNFα, and the chemokine, IL-8, when compared with untreated controls, whereas nanoHA treatment failed to induce production of either of these inflammatory mediators (Figure 4.15 C & D). Of note, only micron sized HA particles were capable of inducing the pleiotropic cytokine, IL-6 (Figure 4.16 E). Taken together these results suggest that nano-sized particles are significantly less inflammatory than micron-sized HA particles.

4.3.13 NanoHA activates STAT3 and drives IL-10 production.

In addition to pro-inflammatory cytokines, it has recently been demonstrated that some particles have the capacity to drive anti-inflammatory cytokine production. For example, particles of alum (a common vaccine adjuvant), with an average size of approximately 1-10 μm has recently been reported to drive robust induction of IL-10 in murine macrophages and DC (311). In order to establish whether micron or nano particles are capable of driving IL-10 production in primary human macrophages, cells were treated with both particle types (250 μg/ml) for 24 hrs and IL-10 production was measured by ELISA. While micron HA particles did not appear to significantly drive IL-10 production, significant induction of IL-10 was observed upon treatment of cells with nanoHA particles (Figure 4.16 A). It was next of interest to identify potential factors involved in nanoparticle-induced IL-10 secretion. It has been reported that IL-10 expression is regulated by the transcription factor, c-Maf, which is in turn upregulated by the signaling molecule, STAT3 (312, 313). Treatment of macrophages for 24 hours with micron HA or nanoHA particles revealed that the latter is indeed capable of driving cMaf expression with robust induction of this protein observed in nanoHA treated macrophages compared to untreated controls and micron HA treated macrophages (Figure 4.16 B). Given that STAT3 activation is upstream of c-Maf activation, it was next assessed whether nano HA particles are capable of phosphorylating, and therefore activating, STAT3. To test this, cells were stimulated with nanoHA particles at the indicated time points. Transient activation, as indicated by phosphorylation, was observed upon nanoHA particle treatment, with enhanced phosphorylation of STAT3 occurring at 15

minutes post cell stimulation and maximal phosphorylation occurring at 30 minutes (Figure 4.16 C). Taken together, these results suggest that nano-sized HA particles are significantly less inflammatory than micron-sized HA particles and are capable of driving the production of the anti-inflammatory cytokine IL-10 in a STAT3/cMaf-dependent manner.

4.3.14 NanoHA particles upregulate M2 macrophage associated genes.

Having observed clear differences in cytokine production between the two particle types and having previously established that micron sized HA particles drive M1 macrophage polarization, macrophage phenotype in response to nanoparticles was next assessed by examining the expression of M1 and M2 macrophage-associated markers. Micron sized HA particles were used as a control. Primary human macrophages were stimulated with HA or nanoHA particles (250 μg/ml) for 24 hours and mRNA expression of M1 and M2 associated genes was assessed by real-time PCR. In agreement with our earlier findings, treatment with HA particles lead to robust expression of the M1-associated genes, CXCL11 and CCL19, however the expression of these genes was not affected by nanoHA particles (Figure 4.17 A & B). In contrast, the M2 associated genes, MRC1 and CCL13, were significantly enhanced with nanoHA treatment compared to untreated control and HA-treated macrophages (Figure 4.17 C & D). Taken together this suggests that nano HA particles are capable of driving M2 macrophage polarization.

4.3.15 NanoHA particles alter macrophage surface marker expression.

In order to further validate the results described above, the expression of surface markers associated with polarized M1 and M2 macrophages was next assessed using flow cytometry following treatment of cells with either HA (250 μg/ml) or nanoHA (250 μg/ml) particles. Cells treated with LPS (100 ng/ml) and IFN-γ (10 ng/ml) were included as positive controls for M1 macrophages, while cells treated with IL-4 (10 ng/ml) were included as a positive control M2 macrophages. Flow cytometric analysis revealed that HA particles significantly enhanced surface expression of the M1-associated marker, CD86, above the level of the both positive controls (IFNγ and LPS), however no induction

was observed upon nanoHA particle stimulation (Figure 4.18 A). The M2 surface markers, CD206 and CD163, were also assessed. In this case, HA particle treatment resulted in a modest decrease in CD163 surface expression, while nanoHA particles significantly enhanced surface expression of this marker to a level above that of the positive control, IL-4 (Figure 4.18 B). Similar results were obtained with CD206, with no apparent change upon HA treatment, however a significant increase was observed with the highest dose of nanoHA particles (Figure 4.18 C). This was confirmed at the protein level by immunoblotting for CD163 and CD206 (Figure 4.18 D & E).

To further validate these findings, immunofluorescent staining for CD206 and CD80 was performed. To this end, cells were stimulated with HA or nanoHA particles (250 μg/ml) for 24 hours. Cells were fixed and stained overnight with primary antibodies specific for CD206 and CD80, then stained with fluorescently conjugated secondary antibodies and imaged under a confocal microscope. HA treated cells exhibited intense fluorescence for CD80 compared to untreated control cells. This was comparable to the M1 positive control, IFNy. Conversely, and in line with the immunoblotting data, cells stimulated with nanoHA particles stained highly positive for CD206, to a comparable level of that of the M2 positive control, IL-4 (Figure 4.19 A).

Recent research suggests that M1 and M2 macrophages exhibit differences in cell shape and morphology (314), with M1 macrophages assuming a more elongate and irregular shape compared to M2 macrophages which are circular in appearance (315). In order to determine whether changes in macrophage phenotype upon particle stimulation also results in changes in cell morphology, cell shape parameters were determined from immunofluorescent images. Image J software was utilised to determine cell perimeter and circulatory index from individual cells. Nanoparticle-treated macrophages exhibited a higher circularity index compared to macrophages treated with micron sized HA particles, which appeared to have a decreased circularity index and a large perimeter value. This is in line with suggested changes that occur in cell shape upon macrophage polarization (Figure 4.19 B).

4.3.16 Micron and nano HA particles are internalised by macrophages within 3 hours of stimulation.

Particle internalization can occur by a range of processes including phagocytosis or pinocytosis, among others. Given the observed differences in macrophage phenotype driven by the HA and nano HA particles, it was next of interest to determine whether the particles are taken up by different mechanisms and to compare their level of uptake. To test this, the particles were fluorescently tagged and their uptake by macrophages was assessed using confocal microscopy. Both particle types are internalized within 1 hr of treatment, and while not significant, it would appear that the nano sized HA particles are taken up at a higher level than the micron sized HA particles (Figure 4.20 A & B). Furthermore, both particles are localised to the cytoplasmic space, with some clustering evident at the cell membrane. Pre-treatment of cells with Latrunculin B (a commonly used inhibitor of phagocytosis) significantly reduced microparticle-induced expression of M1 markers, while having no effect on nanoparticle-induced M2 marker expression (Figure 4.20 C). While further study is required, it can be suggested from this data, that the larger particles are taken up by phagocytosis while the nanoparticles may enter the cell via by pinocytosis or endocytosis. Indeed, this has previously been demonstrated for particles in the nanometre range (316).

4.3.17 HA particles potentially drive metabolic reprogramming in primary human macrophages.

As outlined in Section 1.2.1 recent studies have demonstrated a direct link between macrophage polarization and metabolic reprogramming (49). Having observed such striking differences in macrophage phenotype upon particle stimulation, it was of interest to next assess the metabolic profile of particle stimulated cells. In order to do this, an emerging technique called fluorescence lifetime imaging microscopy (FLIM) was utilized. This technique allows for a non-invasive and quantitative live read-out of cellular metabolism based on the excited state lifetime of a fluorophore. It relies on the sensitive detection of endogenously fluorescent NAD(P)H, using a two-photon microscope fitted with time correlated single photon counting (TCSPC) unit enabling the downstream analysis of the fluorescence decay by fitting a multi-exponential equation.

Free NAD(P)H is associated with glycolysis and has a short emission lifetime whereas protein-bound NAD(P)H is associated with oxidative phosphorylation and has a longer emission lifetime. This therefore allows for discrimination between both forms of respiration under a given treatment (317). NAD(P)H exhibits a multi-exponential fluorescence decay, which is fitted using a double-exponential equation:

$$I(t) = \alpha_1 e^{-\frac{t}{\tau_1}} + \alpha_2 e^{-\frac{t}{\tau_2}} + C$$

derived from two different lifetimes and corresponding fractions (τ1-2, α1-2). The short fluorescence lifetime τ1 and fraction α1 relate to free NAD(P)H, while long fluorescence lifetime τ2 and fraction α2 correspond to protein-bound NAD(P)H. Based on the calculation τ avg = (α1. τ 1) + (α2. τ 2)/ (α1 + α2), a ratio of bound: free NADH can be calculated to give indications of the metabolic state of the cell. In order to determine if the particles have any impact on metabolic reprogramming, primary human macrophages were stimulated with HA or nano HA (250 μg/ml) and imaged 24 hours post particle treatment. Macrophages stimulated with micron sized HA particles exhibited a significant decrease in the ratio of bound to free NADH (Figure 4.21) suggesting that micron HA treated cells are more glycolytic compared to untreated cells, while nanoHA treated cells appear to favour oxidative phosphorylation. Further analysis using the Seahorse flux Analyzer is required to fully validate these results.

4.3.18 Micron HA particles upregulate surrogate markers of glycolysis in primary human macrophages.

Given the suggested alteration in cellular metabolism induced by the particles, it was next of interest to determine whether HA particles alter the expression of key glycolytic genes. To test this, macrophages were treated with micron and nano HA particles for 6 and 24 hours, and established markers of glycolysis were assessed by real-time PCR and immunoblotting. Micron sized HA particles significantly upregulated mRNA expression of the glycolytic enzyme, hexokinase 2 (HK2) at the 6 and 24 hour time-point (Figure 4.22 A), while the glucose transporter, GLUT 1 and PFKFβ3, the first enzyme in the glycolysis pathway, were both significantly upregulated at 24 hours post micron HA particle stimulation (Figure 4.22 B & C). Furthermore, there was a significant increase in

mRNA expression the transcription factor, HIF1α and the enzyme, glyceraldehyde-3-phosphate dehydrogenase (GAPDH) at 24 hours post micron HA particle treatment (Figure 4.22 D &E). Interestingly, stimulation with nanoHA particles did not drive any increase in expression of these markers, however, the particles did significantly increase mRNA expression of HIF2α which has been associated with M2 macrophages (318) (Figure 4.22 F).

In order to further confirm the upregulation of glycolytic markers by micron sized HA particles, cells were stimulated over the course of 3, 6 or 24 hours with either micron or nanoHA particles and expression of the proteins, HK2 and Glut1, was examined by immunoblotting. Minimal Glut1 protein was detected upon nanoHA particle treatment, however robust protein expression was evident at 24 hours stimulation with micron HA particles. Upregulation of HK2 was observed at 6 and 24 hour post micron HA particle treatment (Figure 4.22 G). Densitometric analysis of western blots from 5 individual donors revealed maximal and significant upregulation occurring at 24 hours for both proteins (Figure 3.22 H). Therefore, it appears that HA particle treatment upregulates proteins and enzymes associated with a metabolic switch favouring glycolysis.

4.3.19 Micron sized HA particles decrease macrophage mitochondrial mass and drive mitochondrial ROS production.

It has been reported that M1 macrophages utilise glycolysis and therefore exhibit reduced mitochondrial biogenesis (259). This can be assessed by measuring mitochondrial mass using mitochondrial specific dyes such as Mitotracker red or equivalent dyes that stain and accumulate in the mitochondria. In order to determine if HA particle size impacts on mitochondrial biogenesis, primary human macrophages were stimulated with micron or nano HA particles (100 μg/ml) for 6 or 24 hours prior to staining with Mitotracker Red. Mitochondrial mass was then measured by flow cytometry. Macrophages stimulated with nanoHA particles exhibited no discernible difference in mitochondrial mass and displayed similar Mitotracker staining as untreated cells. Interestingly, cells stimulated with micron sized HA particles showed a loss of mitochondrial mass and a significant decrease in Mitotracker staining at both 6 and 24

hours post stimulation (Fig 4.23). Taken together this indicates that reduced mitochondrial expansion, indicative of glycolysis, is occurring following micron particle stimulation, while nanoHA treated cells maintain their mitochondrial mass.

Mitochondrial ROS (mROS) production is linked to activated macrophages and M1 polarization, and it has been postulated that ROS production can promote an M1-like phenotype (259, 319). mROS production can be measured using MitoSox Red reagent which is a fluorogenic dye specifically targeted to mitochondria in live cells. Oxidation of MitoSOX Red reagent by superoxide produces red fluorescence allowing for detection of mROS by flow cytometry. Having observed changes in mitochondrial biogenesis, it was next of interest to assess mROS production in particle treated cells. To test this, cells were incubated with MitoSox Red reagent following treatment of macrophages with HA or nanoHA (100 μg/ml) at 6 or 24 hours. NanoHA treatment did not alter mROS production at either the 6 or 24 hour time-point, however micron HA particles drove mROS production at both 6 and 24 hours, as evidenced by a higher percentage of cells that stained positive for MitoSOX red (Figure 4.24 A and B). Taken together, this suggests that micron sized HA particles, but not nano HA particles, impact on mitochondrial function and ROS production, providing further evidence that the two particle types differentially effect the metabolic status of innate immune cells.

A

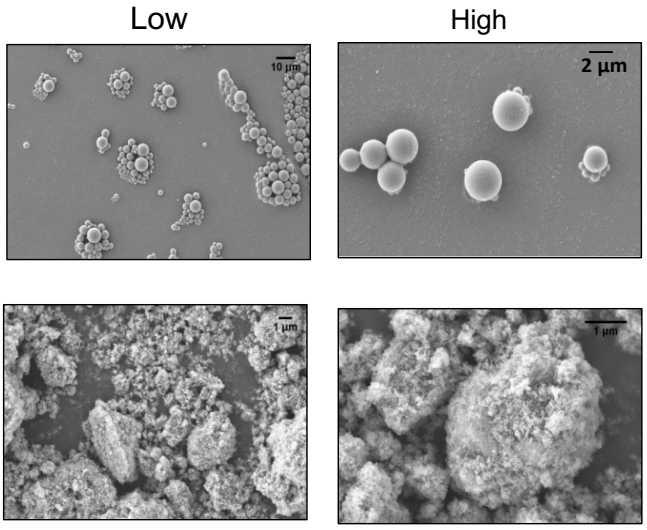

B

Average Zeta potential	Particle size (µm)
-10.13	1.318

C

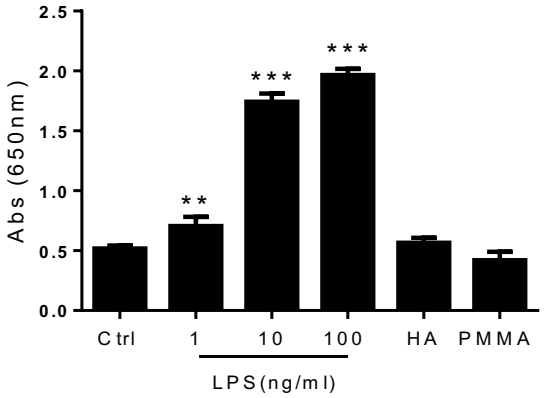

Figure 4.1: Characterization of PMMA and HA particles. (A) Low and high magnification SEM images of PMMA (top) and HA (bottom) particles. **(B)** Zeta potential determination and particle size distribution using Electrophoretic Light Scattering (ELS) and Dynamic Light Scattering (DLS) respectively. **(C)** HA and PMMA particle preparations were shown to be endotoxin free, using the HEK-BlueTM hTLR4 assay system (Invivogen). HEK TLR4 cells (5 x 10^5 cell/ml) were treated with HA particles (250 µg/ml) or PMMA particles (500 µg/ml) or cells were treated with LPS (1 ng/ml, 10 ng/ml or 100 ng/ml) as a positive control. The expression of SEAP was measured by absorbance at 650nm. Results shown are means ± SD for triplicate cultures and are representative of three independent experiments. Data was analysed using one-way ANOVA with Tukey post-test (**P≤0.01, ***P≤0.001).

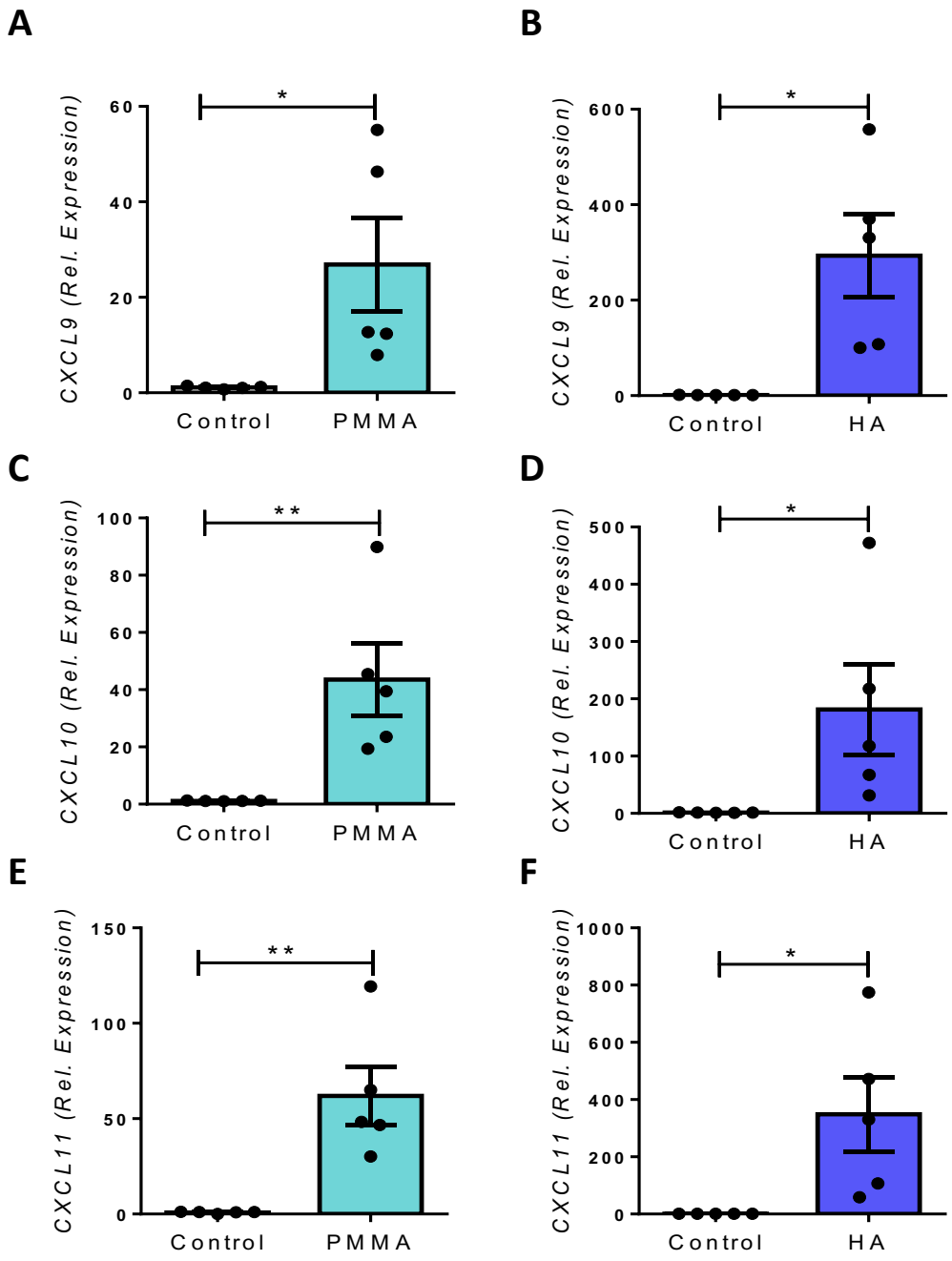

Figure 4.2: PMMA and HA particles promote M1 macrophage polarization. Primary human macrophages (1 x 10^6 cells/ml) were stimulated with PMMA (500 µg/ml) or HA particles (250 µg/ml) for 24 hours. mRNA levels of **(A & B)** CXCL9, **(C & D)** CXCL10 and **(E & F)** CXCL11 were analysed by real-time PCR. mRNA concentration was normalised to the housekeeping gene 18s ribosomal RNA. Gene expression, relative to untreated control cells, was determined using the 2-ΔΔCt algorithm. Pooled data (n=5) is represented as mean ± SEM. Data was analysed using a student's T-test (*P≤0.05, **P≤0.01).

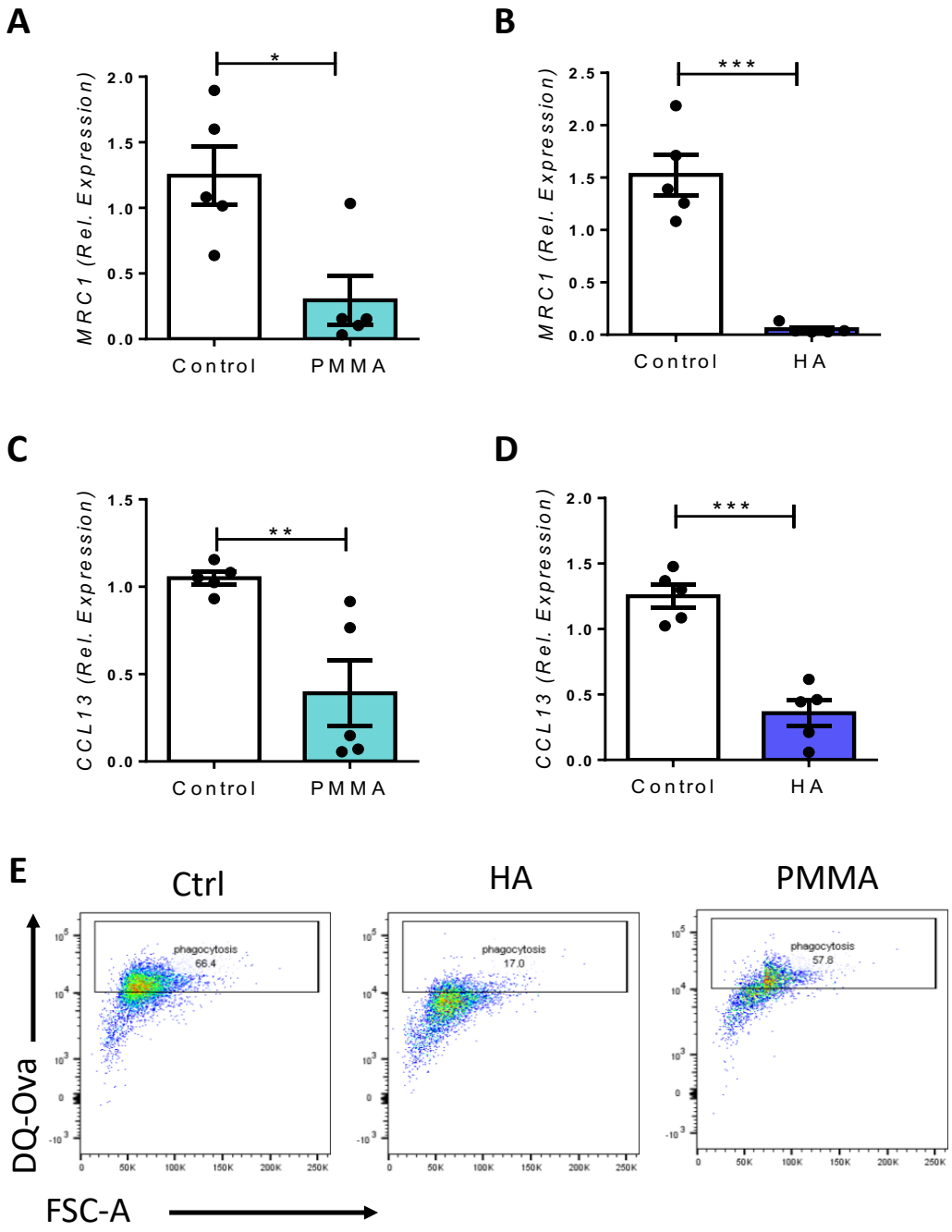

Figure 4.3: PMMA and HA particles decrease expression of M2 associated genes. Primary human macrophages (1 x 10^6 cells/ml) were stimulated with PMMA (500 µg/ml) or HA particles (250 µg/ml) for 24 hours. mRNA levels of **(A & B)** MRC1 and **(C & D)** CCL13 were analysed by real-time PCR. mRNA concentration was normalised to the housekeeping gene 18s ribosomal RNA. Gene expression, relative to untreated control cells, was determined using the $2^{-\Delta\Delta CT}$ algorithm. Pooled data (n=5) is represented as mean ± SEM. Data was analysed using a student's T-test (* P≤ 0.05, ** P≤ 0.01 and *** P≤ 0.001). **(E)** Primary human macrophages were stimulated with PMMA (500 µg/ml) or HA particles (250 µg/ml) for 24 hours and then incubated with FITC-conjugated DQ-ovalbumin (DQ-Ova; 500 ng/ml) for 20 minutes prior to analysis by flow cytometry. Representative dot plots depicting DQ-Ova uptake by HA and PMMA treated macrophages.

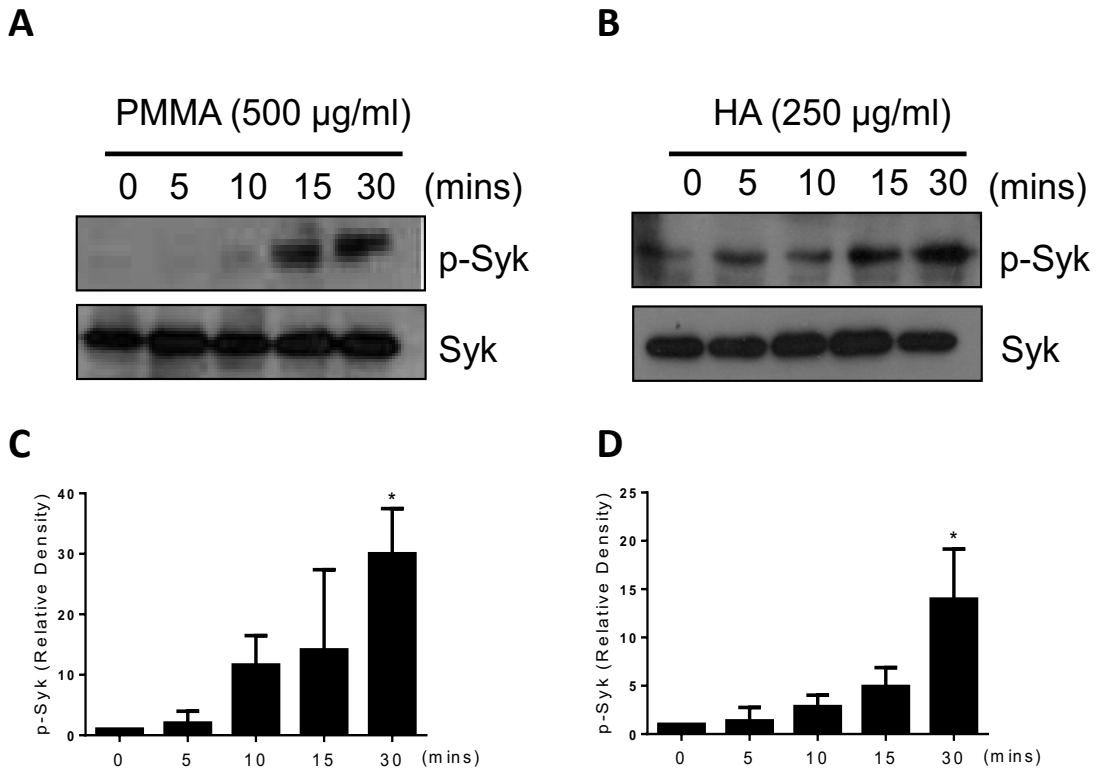

Figure 4.4: PMMA and HA particles phosphorylate Syk tyrosine kinase. Primary human macrophages (1 x 10^6 cells/ml) were stimulated with PMMA (500 µg/ml) or HA particles (250 µg/ml) for the indicated time points. **(A & B)** Phosphorylation of Syk was detected by immunoblotting using phospho-specific antibodies. **(C & D)** Densitometric analysis of 3 immunoblots was performed using ImageJ software. Bar graphs illustrate the mean ± SEM increase in phosphorylation of p-Syk relative to the untreated sample (0) and normalised to total Syk protein. Statistical differences were assessed using one-way ANOVA with Tukey Post-Test. (* P≤ 0.05).

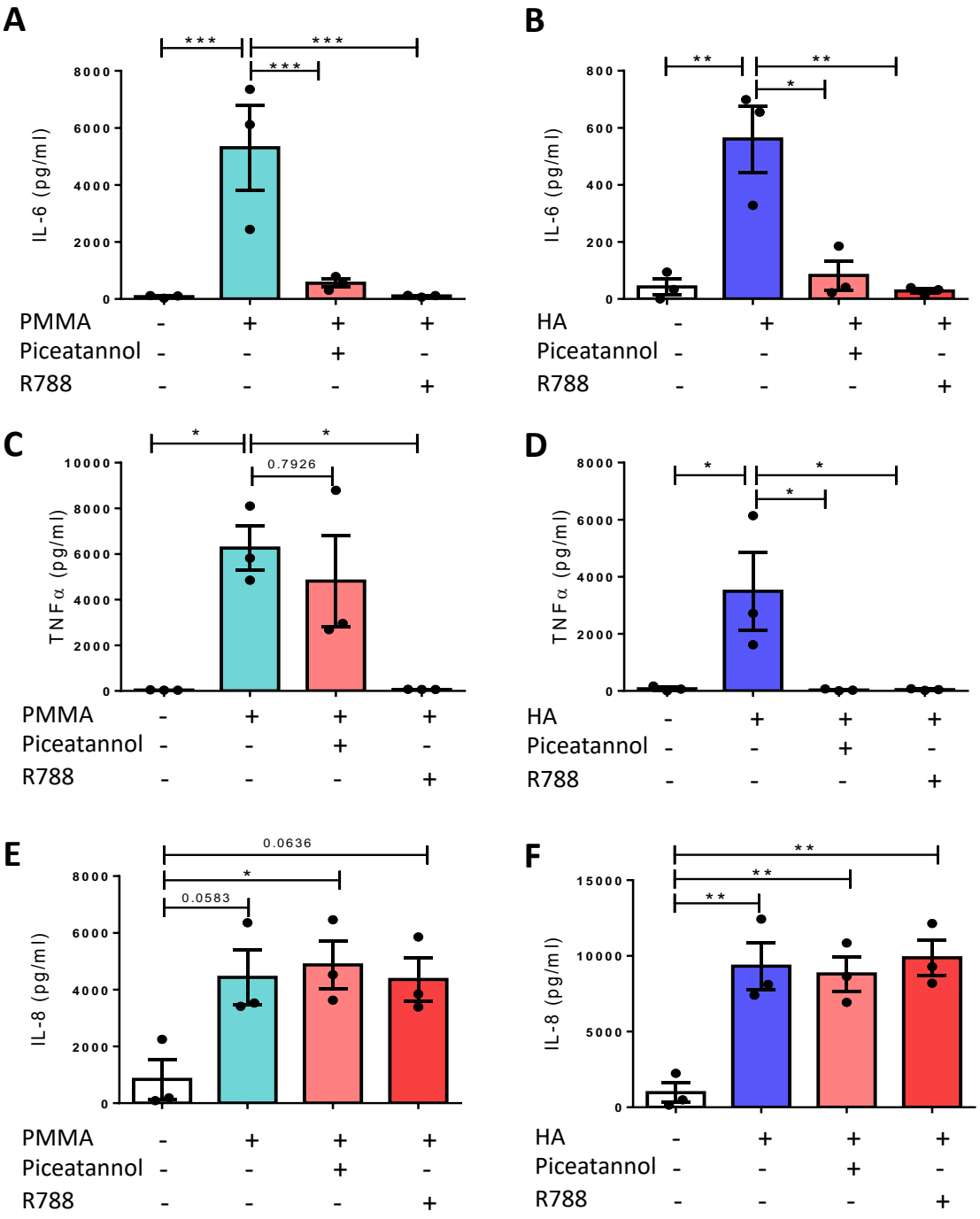

Figure 4.5: PMMA and HA particles drive TNFα and IL-6, but not IL-8 in a Syk dependent manner. Primary human macrophages (1 x 10^6 cells/ml) were treated with the two Syk inhibitors, Piceteannol (20 µM) and R788 (25 µM) for 45 minutes prior to stimulation with PMMA (500 µg/ml) or HA particles (250 µg/ml) for 24 hours. Cytokine production of **(A & B)** IL-6, **(C & D)** TNFα and **(E & F)** IL-8 in cell supernatants was analysed by ELISA. Pooled data (n=3) is represented as mean ± SEM. Data was analysed using Kruskal Wallis with Dunn's post-test (*P≤0.05, **P≤0.01, ***P≤0.001).

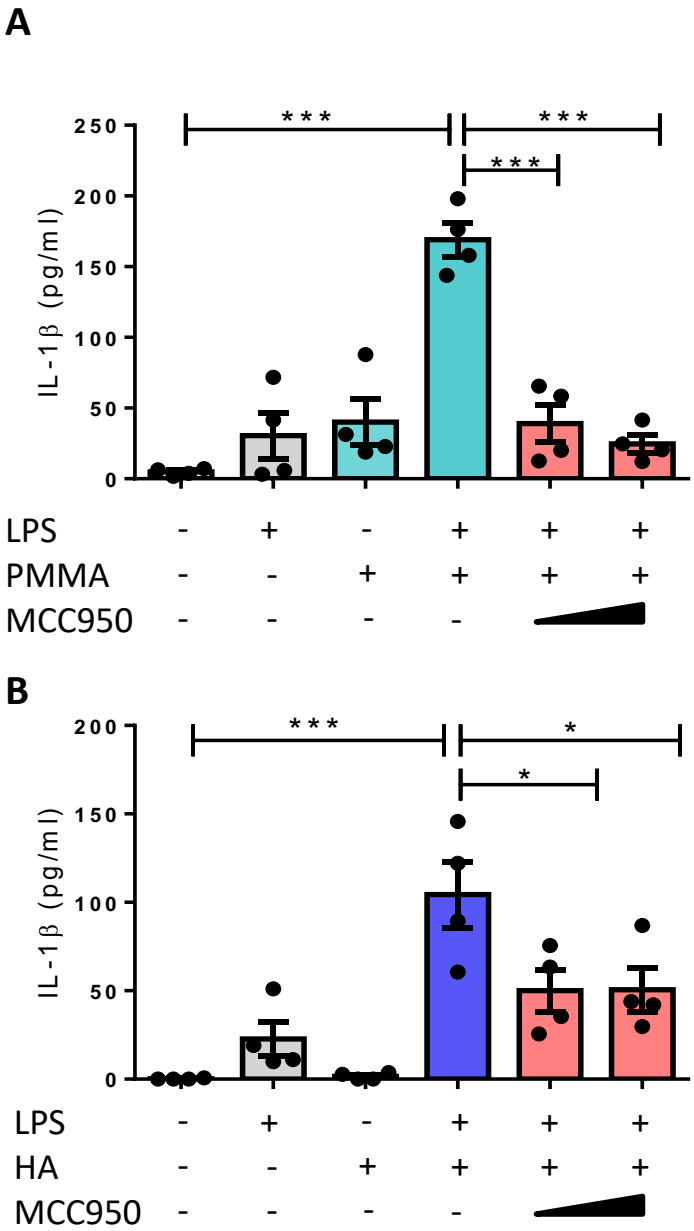

Figure 4.6: PMMA and HA particles drive IL-1 cytokine production in an NLRP3 dependent manner. Primary human macrophages (1 x 10^6 cells/ml) were primed with LPS (100 ng/ml) for 2 hours prior to treatment with an NLRP3 inhibitor, MCC950 (1 & 5µM) for 45 minutes prior to stimulation with **(A)** PMMA (500 µg/ml) or **(B)** HA particles (250 µg/ml) for 24 hours. Cytokine production of IL-1β in cell supernatants was analysed by ELISA. Pooled data (n=4) is represented as mean ± SEM. Data was analysed using Kruskal Wallis with Dunn's post-test (*P≤0.05, **P≤0.01, ***P≤0.001).

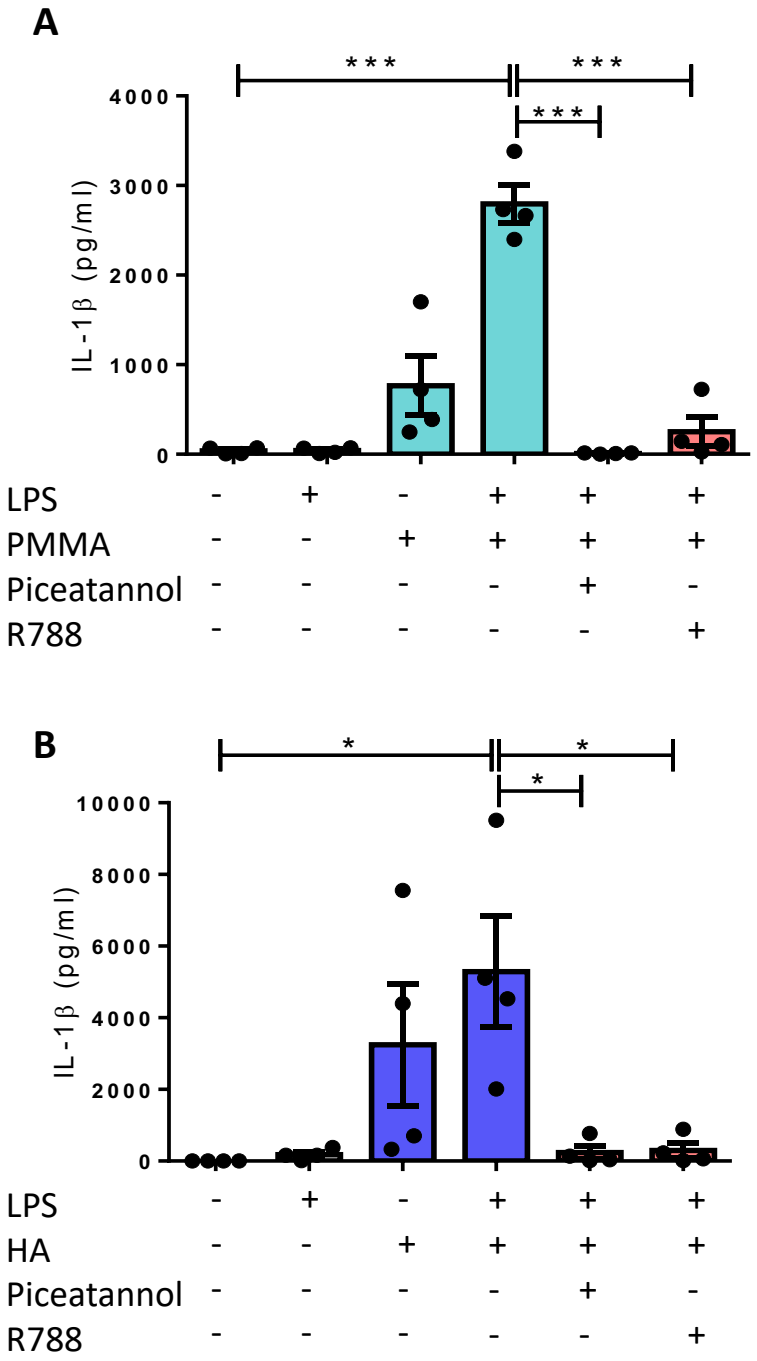

Figure 4.7: PMMA and HA particles drive IL-1 cytokine production in Syk dependent manner. Primary human macrophages (1 x 10^6 cells/ml) were primed with LPS (100 ng/ml) for 2 hours prior to treatment with the Syk inhibitors Piceatannol (20 µM) and R788 (25 µM) for 45 minutes prior to stimulation with **(A)** PMMA (500 µg/ml) or **(B)** HA particles (250 µg/ml) for 24 hours. Cytokine production of IL-1β in cell supernatants was analysed by ELISA. Pooled data (n=4) is represented as mean ± SEM. Data was analysed using Kruskal Wallis with Dunn's post-test (*P≤0.05, **P≤0.01, ***P≤0.001).

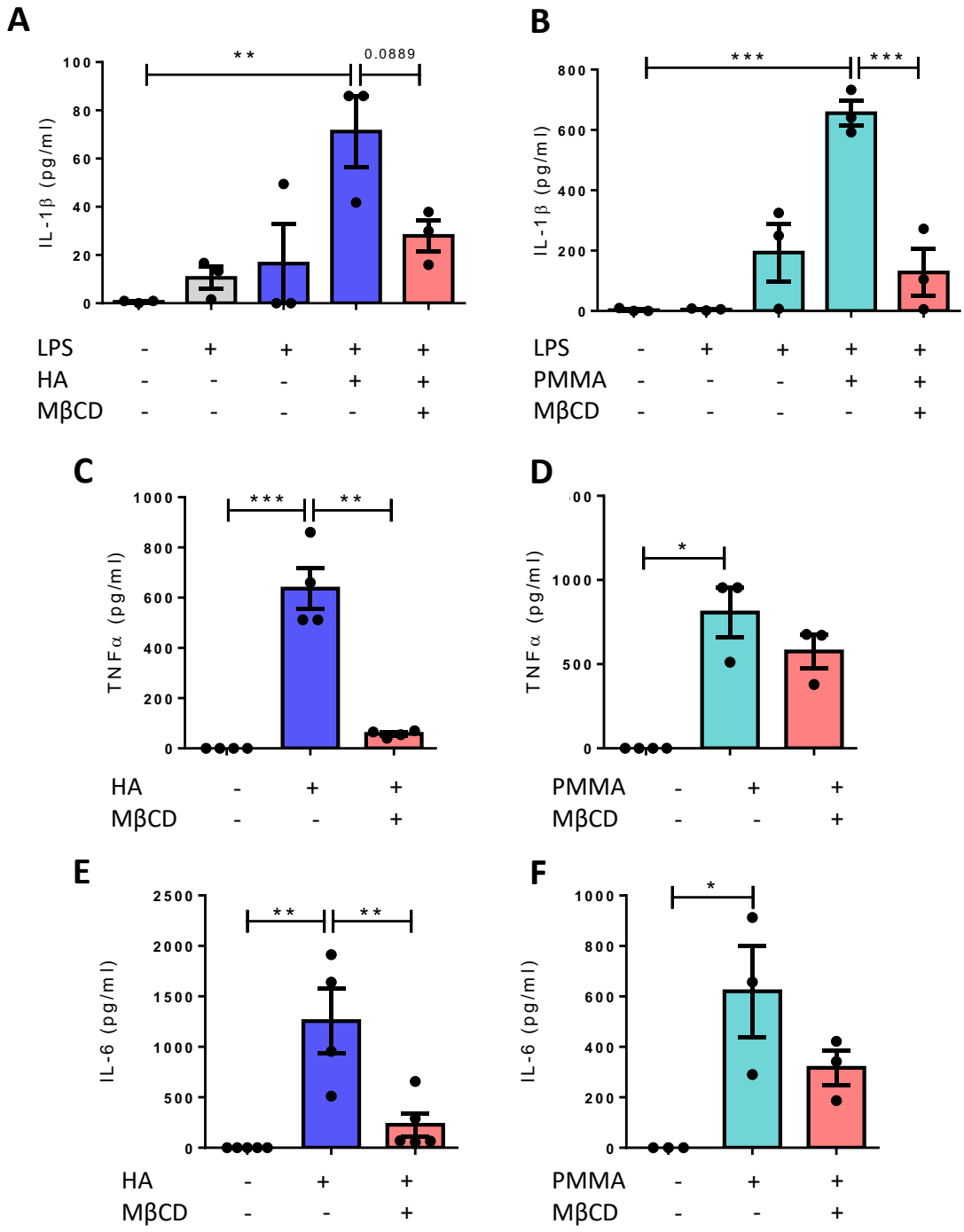

Figure 4.8: PMMA and HA-induced IL-1 production occurs via lipid raft formation in primary macrophages. LPS-primed human macrophages (1 x 10^6 cells/ml) were treated M-βCD (10 mM) for 1 hour prior to stimulation with PMMA or HA particles (250 µg/ml) for 24 hours. Cell supernatants were assessed for IL-β, TNFα and IL-6 by ELISA. Cytokine production of **(A & B)** IL-1β, **(C & D)** TNFα and **(E & F)** IL-6 in cell supernatants was analysed by ELISA. Pooled data (n=3) is represented as mean ± SEM. Data was analysed using Kruskal Wallis with Dunn's post-test (*P≤0.05, **P≤0.01, ***P≤0.001).

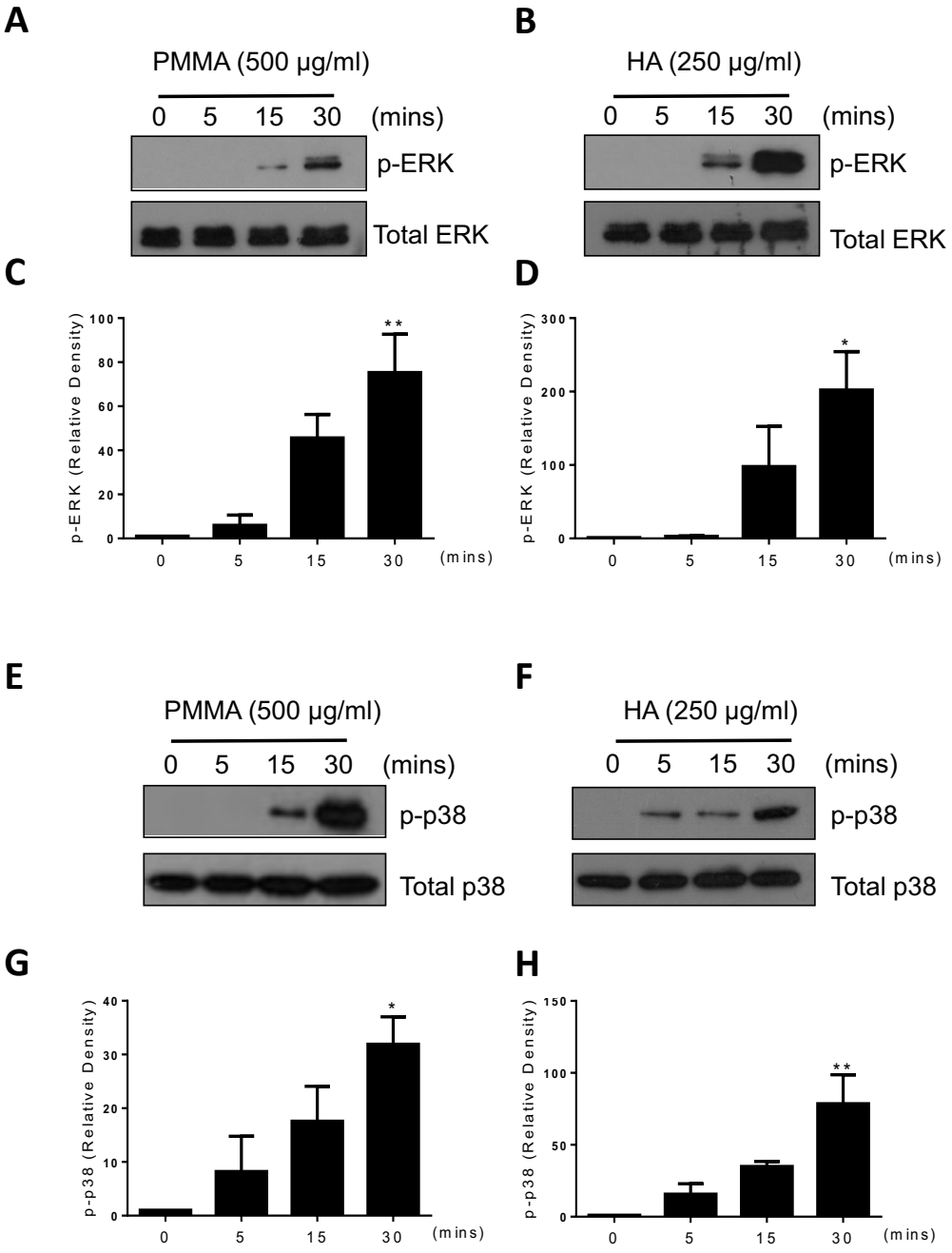

Figure 4.9: PMMA and HA particles activate ERK and p38 MAP kinase. Primary human macrophages (1 x 10^6 cells/ml) were stimulated with PMMA (500 µg/ml) or HA particles (250 µg/ml) for the indicated time points. Phosphorylation of **(A & B)** ERK and **(E & F)** p38 were detected by immunoblotting using phospho-specific antibodies. **(C & D and G & H)** Densitometric analysis of 3 immunoblots for PMMA and HA was performed using ImageJ software. Bar graphs illustrate the mean ± SEM increase in phosphorylation of ERK or p38 relative to the untreated sample (0) and normalised total ERK or p38 protein. Statistical differences were assessed using one-way ANOVA with Tukey Post-Test. (* P≤ 0.05 and ** P≤ 0.01).

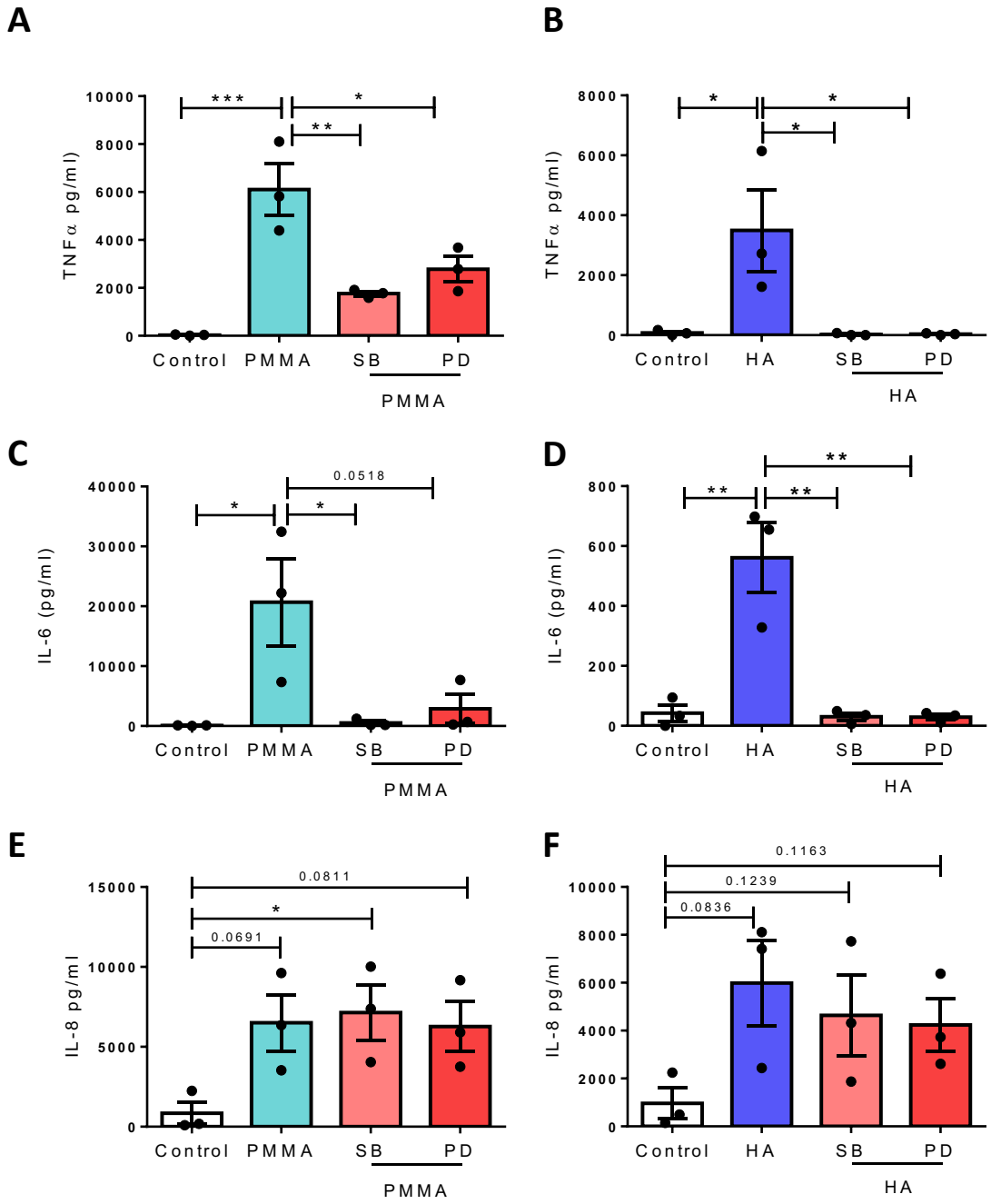

Figure 4.10: PMMA and HA particles drive TNFα and IL-6 production in a MAP kinase dependent manner. Primary human macrophages (1 x 10^6 cells/ml) were treated with the p38 inhibitor, SB203580 (20 µM) or the ERK inhibitor, PD98059 (20 µM) for 45 minutes prior to stimulation with PMMA particles (500 µg/ml) or HA particles (250 µg/ml) for 24 hours. Cytokine production of **(A & B)** TNFα, **(C & D)** IL-6 and **(E & F)** IL-8 in cell supernatants was analysed by ELISA. Pooled data (n=3) is represented as mean ± SEM. Data was analysed using Kruskal Wallis with Dunn's post-test (*P≤0.05, **P≤0.01, ***P≤0.001).

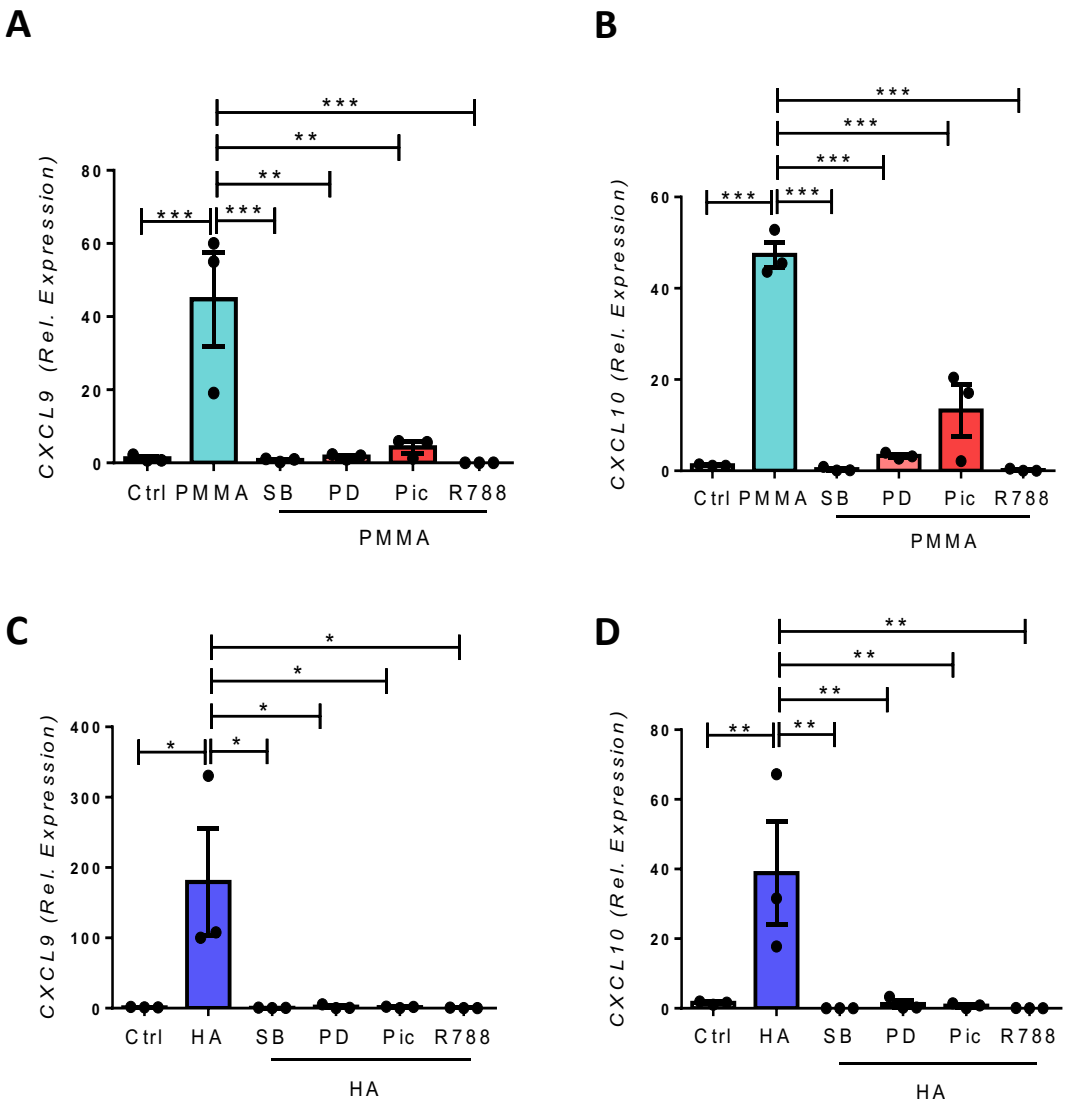

Figure 4.11: PMMA and HA particles induce M1 macrophage marker expression in a Syk and MAP kinase dependent manner. Primary human macrophages (1 x 10^6 cells/ml) were pre-treated with SB203580 (20 µM) or PD98059 (20 µM) in order to inhibit p38 and ERK MAP kinases, respectively, or the Syk inhibitors, Piceatannol (20 µM) and R788 (25 µM) for 45 minutes prior to stimulation with PMMA particles (500 µg/ml) or HA particles (250 µg/ml). mRNA Expression levels of **(A & C)** CXCL9 and **(B & D)** CXCL10 were analysed by real-time PCR. mRNA concentration was normalised to the housekeeping gene 18s ribosomal RNA. Gene expression, relative to untreated control cells, was determined using the $2^{-\Delta\Delta CT}$ algorithm. Pooled data (n=3) is represented as mean ± SEM. Data was analysed using one-way ANOVA with Tukey Post-Test (*P≤0.05, **P≤0.01, ***P≤0.001).

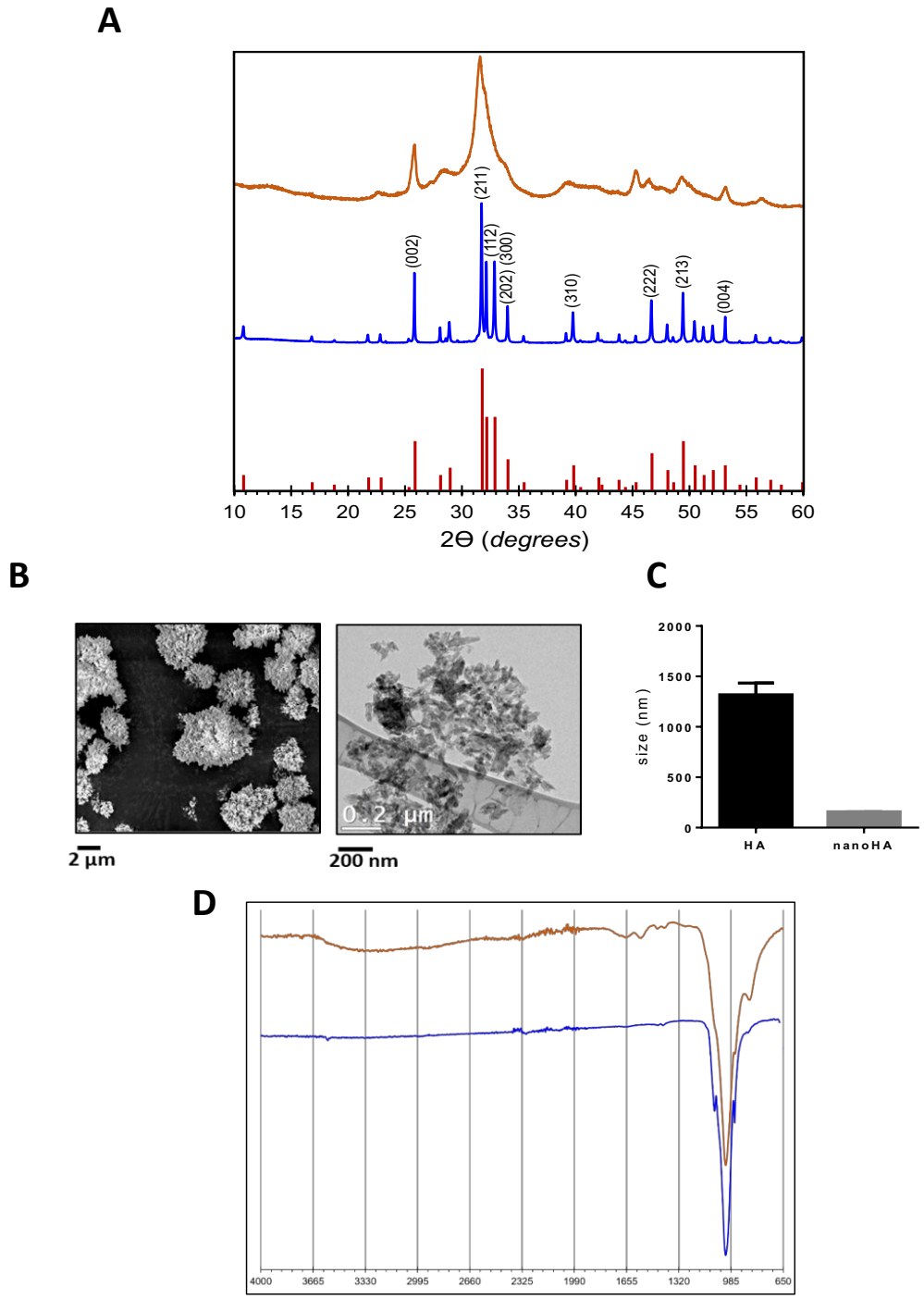

Figure 4.12: Characterisation of structural and compositional features of micron and nano sized hydroxyapatite particles. (A) Powder X-ray diffraction (XRD) patterns of nanoHA (orange line) and micron HA (blue line), together with the theoretical XRD pattern of hydroxyapatite (red lines, JCPDS file No. 9-432). **(B)** A representative scanning electron micrograph (SEM) of the micronHA particles and a representative transmission electron micrograph (TEM) of the nanoHA particles. **(C)** Particle size distribution using Dynamic Light Scattering (DLS) respectively**.** **(D)** Fourier-transform infrared (FTIR) spectra of nano (orange line) and micron (blue line) Hydroxyapatite particles. This experiment was performed with assistance from Dr. Stanislas Von Euw.

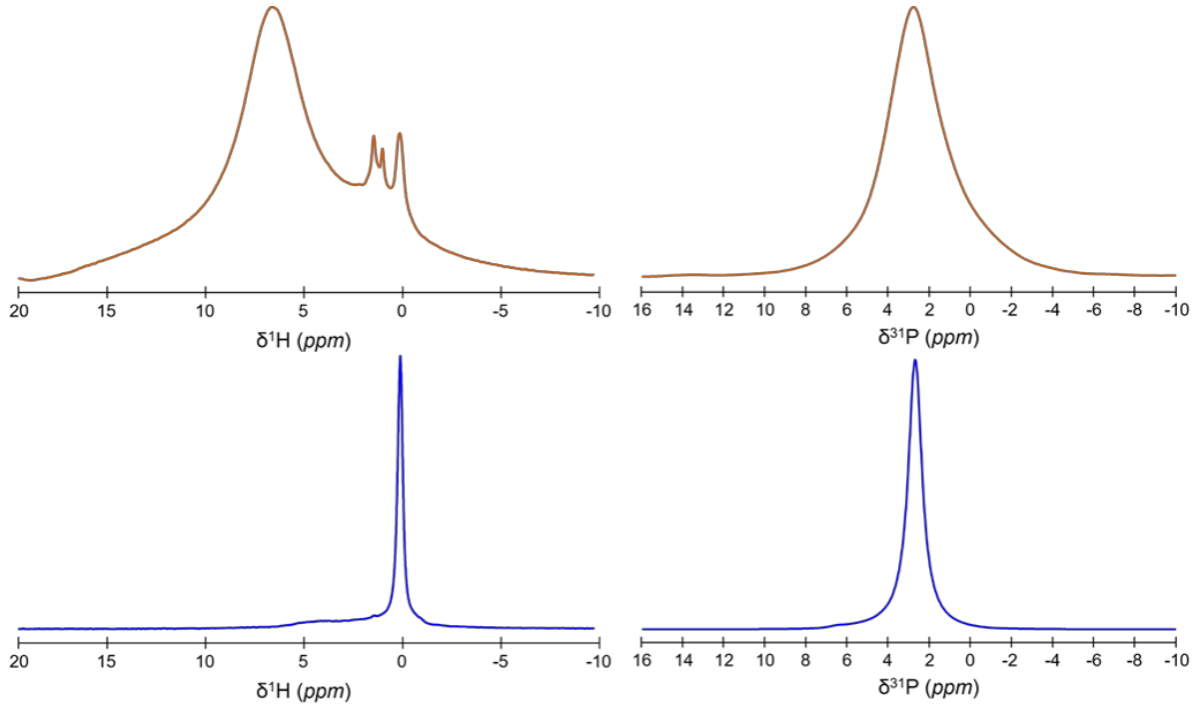

Figure 4.13: Assessment of the chemical composition of nanoHA and micronHA. One dimensional (1D) 1H (left) and 31P (right) single-pulse (SP) magic angle spinning (MAS) solid-state Nuclear Magnetic Resonance (NMR) spectra of nano (orange lines) and micron (blue lines) Hydroxyapatite particles. This experiment was performed with assistance from Dr. Stanislas Von Euw.

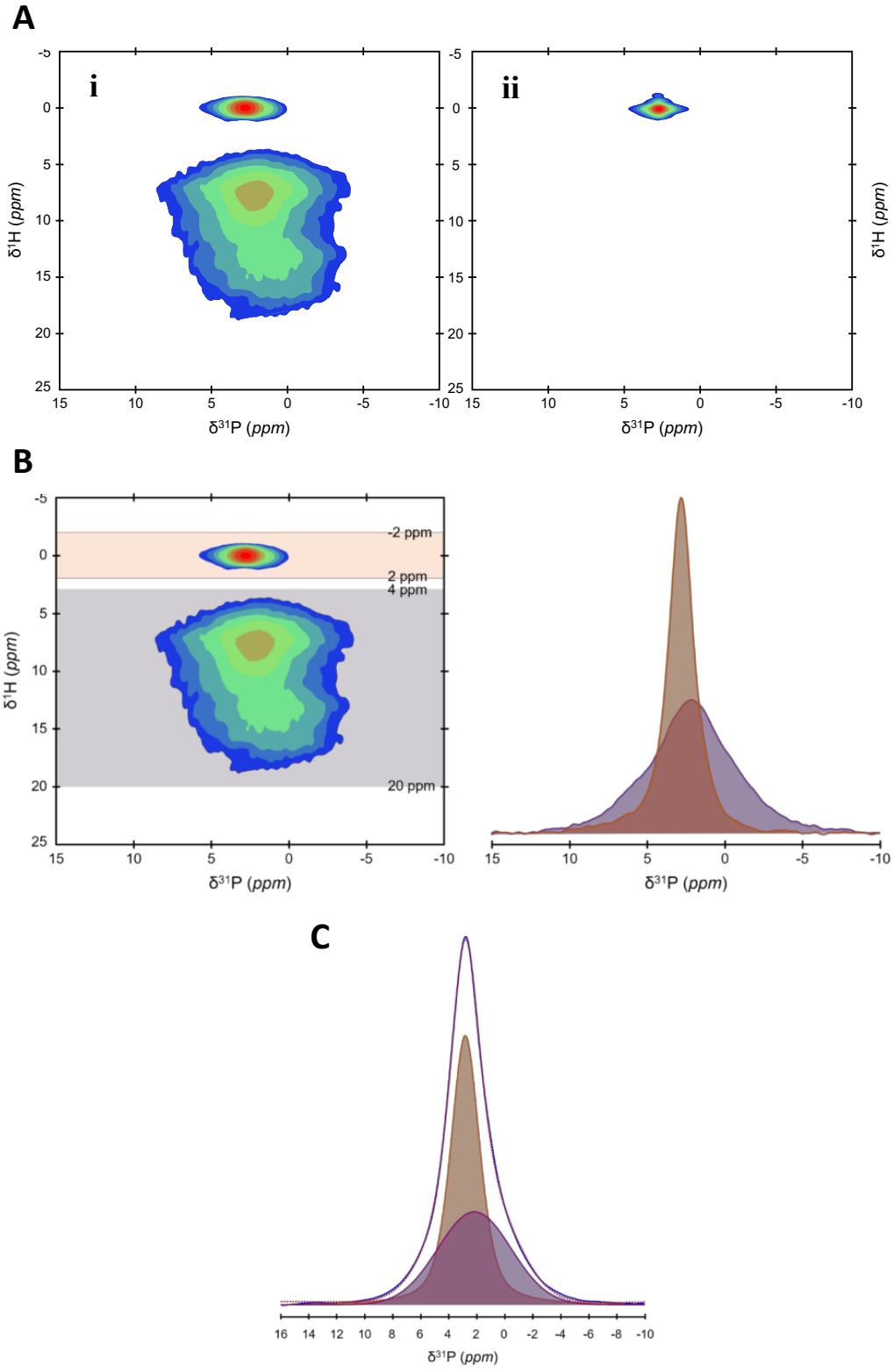
A
i
ii
δ¹H (ppm)
δ³¹P (ppm)
B
-2 ppm
2 ppm
4 ppm
20 ppm
C

Figure 4.14: Assessment of the chemical environments of nanoHA and micronHA. (A) Two-dimensional (2D) {1H} 31P Heteronuclear Correlation (HetCor) NMR spectra of (i) nanoparticles and (ii) micron particles. **(B)** One-dimensional (1D) individual 31P NMR signals of the apatitic crystalline core (orange spectrum) and the amorphous surface layer (violet spectrum) of the nanoparticles. These individual 31P NMR signals were extracted from the two-dimensional (2D) {1H} 31P Heteronuclear Correlation (HetCor) MAS NMR spectrum of nanoparticles that is shown here. To do this, the sums of the F2 slices taken at the OH- ions position (orange area, from δ1H = -2 to 2 ppm) in F1 have been used to generate the individual 31P signal of the crystalline nanoparticle core. In addition, the sums of the F2 slices taken at the structural water molecules together with HPO_4^{2-} ions position (violet area, from δ1H = 4 to 20 ppm) in F1 have been used to generate the individual 31P signal of the amorphous surface layer. **(C)** Quantification of the molar proportion of HPO_4^{2-} and PO_4^{3-} ions respectively present in the amorphous surface layer and in the apatitic crystalline core of the nanoparticles. Quantitative 31P single-pulse (SP) magic angle spinning (MAS) solid-state Nuclear Magnetic Resonance (NMR) spectrum of nanoparticles (blue line) and its corresponding fitting (red dashed line) with two peaks. Those two peaks correspond to the PO43--containing apatitic crystalline core (orange peak) and the HPO_4^{2-}-containing amorphous surface layer (purple peak). This experiment was performed with assistance from Dr. Stanislas Von Euw.

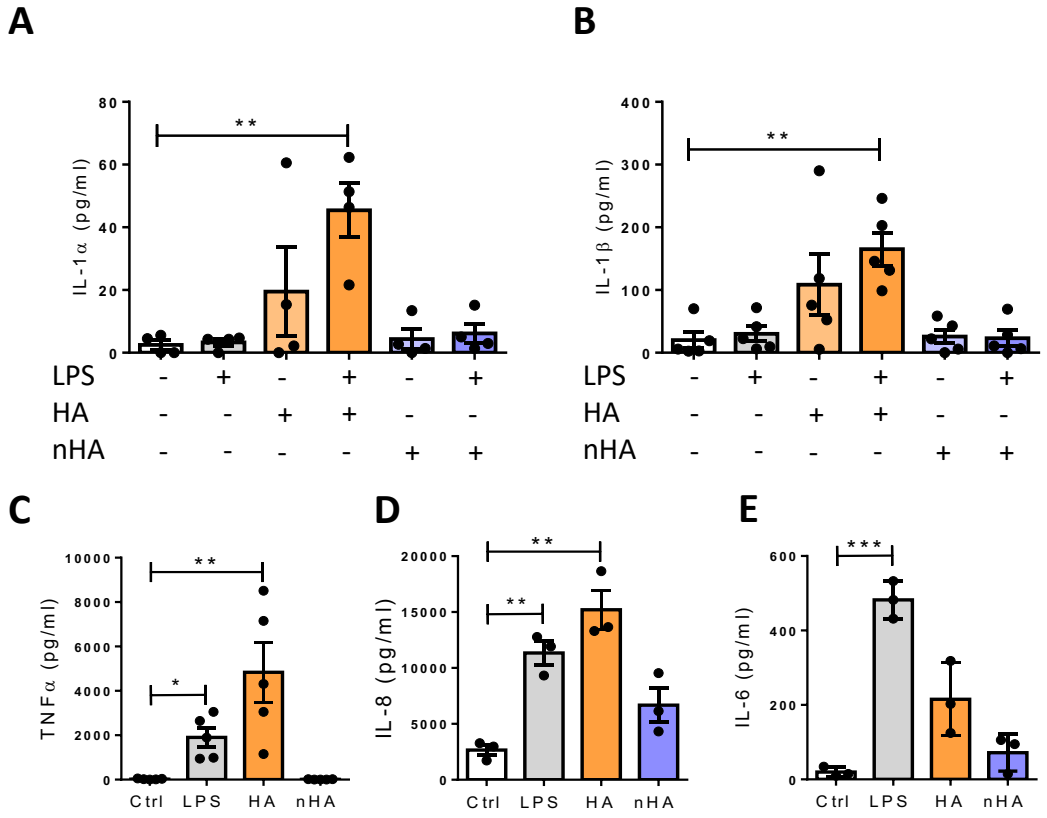

Figure 4.15: Micron sized HA particles but not nanoHA drive pro-inflammatory cytokine production. Primary human macrophages (1 x 10^6 cells/ml) were stimulated with micron HA (250 µg/ml) or nanosized HA particles (250 µg/ml) for 24 hours. Cytokine production of **(A)** IL-1α, **(B)** IL-1β, **(C)** TNFα, **(D)** IL-8 and **(E)** IL-6 in cell supernatants was analysed by ELISA. Pooled data (n=3-5) is represented as mean ± SEM. Data was analysed using Kruskal Wallis with Dunn's post-test (*P≤0.05, **P≤0.01, ***P≤0.001).

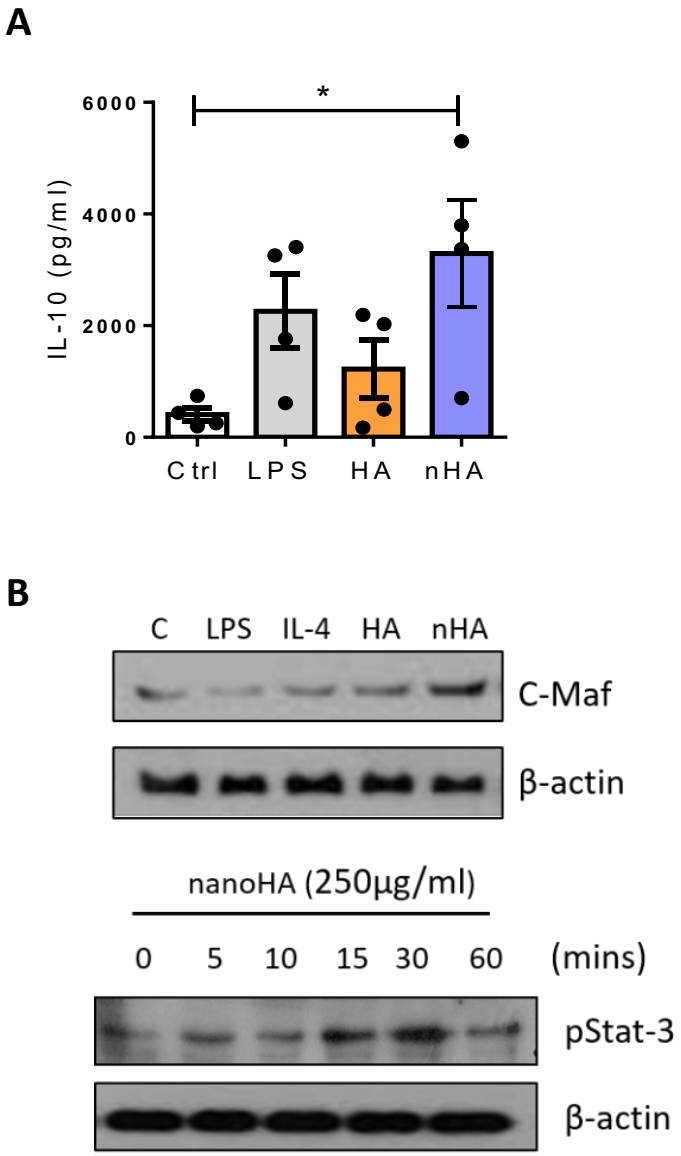

Figure 4.16: Nanoparticles activate the STAT 3 and drive IL-10. (A) Primary human macrophages (1x 10^6 cells/ml) were treated with micron particles or nanoparticles (250 µg/ml) for 24 hours. Cytokine production of IL-10 in cell supernatants was analysed by ELISA. Pooled data (n=4) is represented as mean ± SEM. **(B)** Primary human macrophages (1x 106 cells/ml) were treated with LPS (100 ng/ml), IL-4 (20 ng/ml) or particles (250 µg/ml) for 24 hours, and upregulation of c-Maf protein was detected by immunoblotting. Alternatively, cells were stimulated with nanoparticles (250 µg/ml) over the course of 60 minutes and Stat-3 activation, as indicated by phosphorylation, was detected by immunoblotting using phospho-specific antibodies. Data was analysed using Kruskal Wallis with Dunn's post-test (*P≤0.05, **P≤0.01, ***P≤0.001).

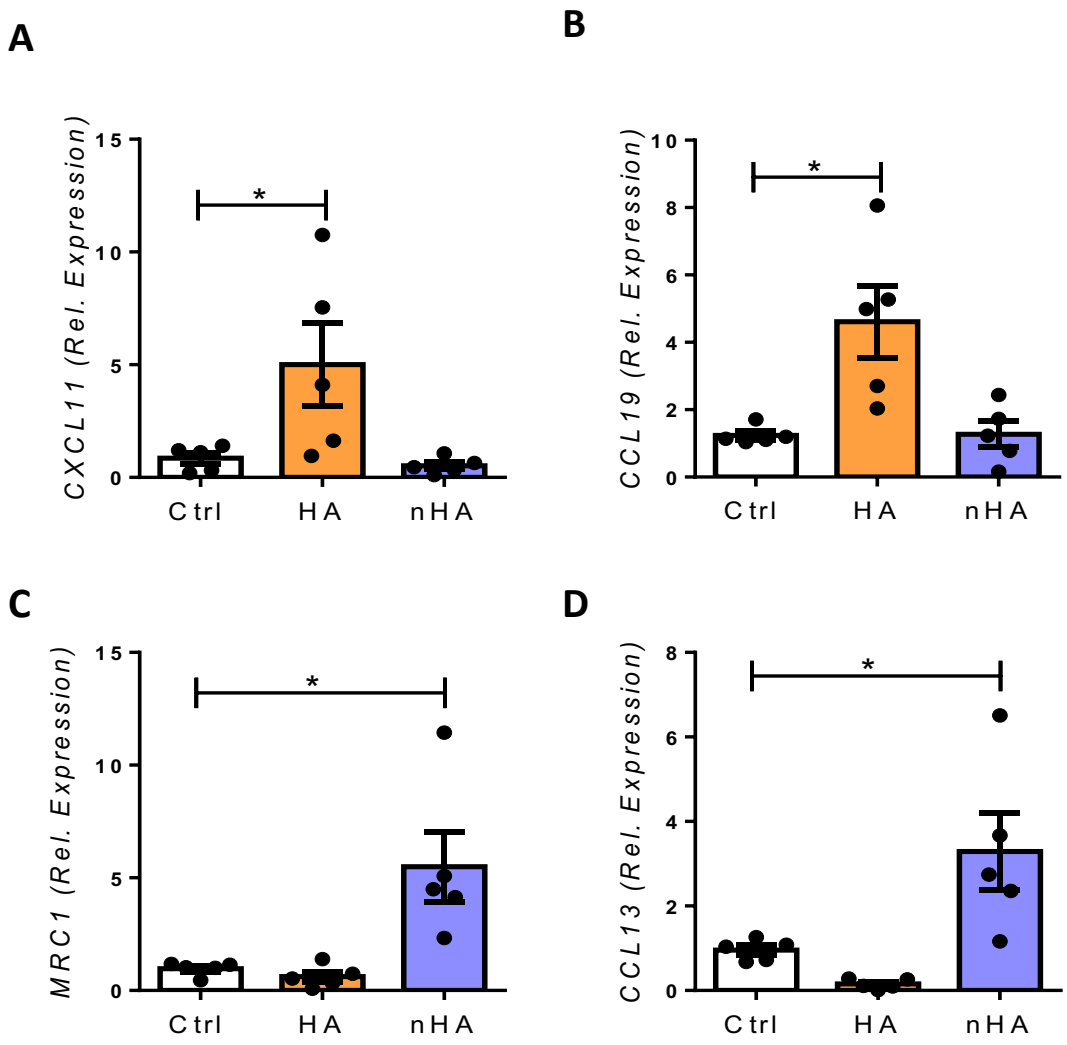

Figure 4.17: Polarization of macrophages is dependent on particle size. Primary human macrophages (1x 10^6 cells/ml) were stimulated with particles (250 µg/ml) for 24 hours. mRNA expression of **(A & B)** CXCL11 and CCL19 and **(C & D)** MRC1 and CCL13 were analysed by real-time PCR. mRNA concentration was normalised to the housekeeping gene 18s ribosomal RNA. Gene expression, relative to untreated control cells, was determined using the $2^{-\Delta\Delta CT}$ algorithm. Pooled data (n=5) is represented as mean ± SEM. Data was analysed using one-way ANOVA with Tukey post-test (*p<0.05).

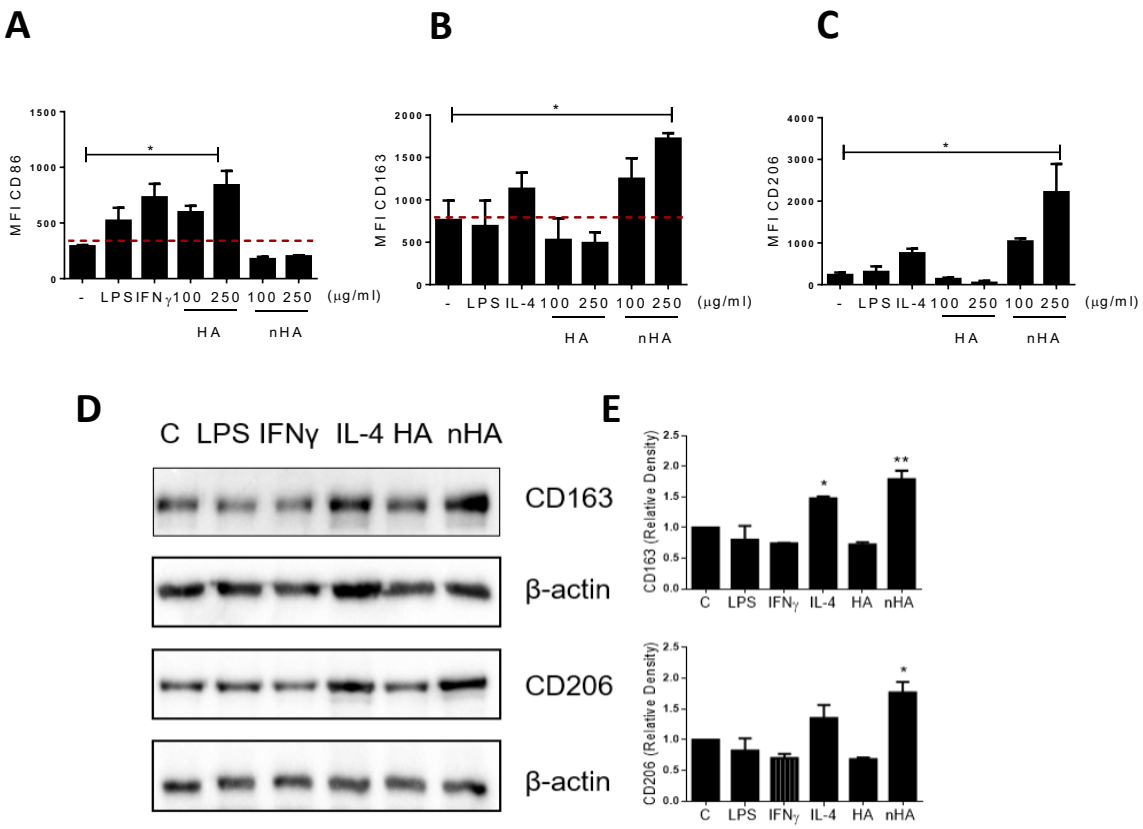

Figure 4.18: Nanoparticles drive M2 macrophage polarization. Primary human macrophages (1x 10^6 cells/ml) were treated with micron particles or nanoparticles (100 or 250 μg/ml) for 6 hours prior to staining with fluorochrome-conjugated antibodies against **(A)** CD86, **(B)** CD163 or **(C)** CD206 and analysed by flow cytometry. Pooled data (n=3) is represented as mean ± SEM. Data was analysed using Kruskal Wallis test with Dunn's post-test. **(D)** Primary human macrophages (1x 10^6 cells/ml) were treated with LPS (100 ng/ml), IFNγ (20 ng/ml), IL-4 (20 ng/ml) or particles (250 μg/ml) for 24 hours. Upregulation of CD206 and CD163 protein was detected by immunoblotting using antibodies specific for CD206 and CD163. **(E)** Densitometric analysis of 2 immunoblots was performed using image J software. Bar graphs illustrate the mean ± SEM increase in protein expression of CD206 or CD163 relative to untreated sample (C) and normalized to β-actin protein. Data was analysed using one-way ANOVA with Tukey post-test (*p<0.05, **p<0.01, ***p<0.001, ****p<0.0001).

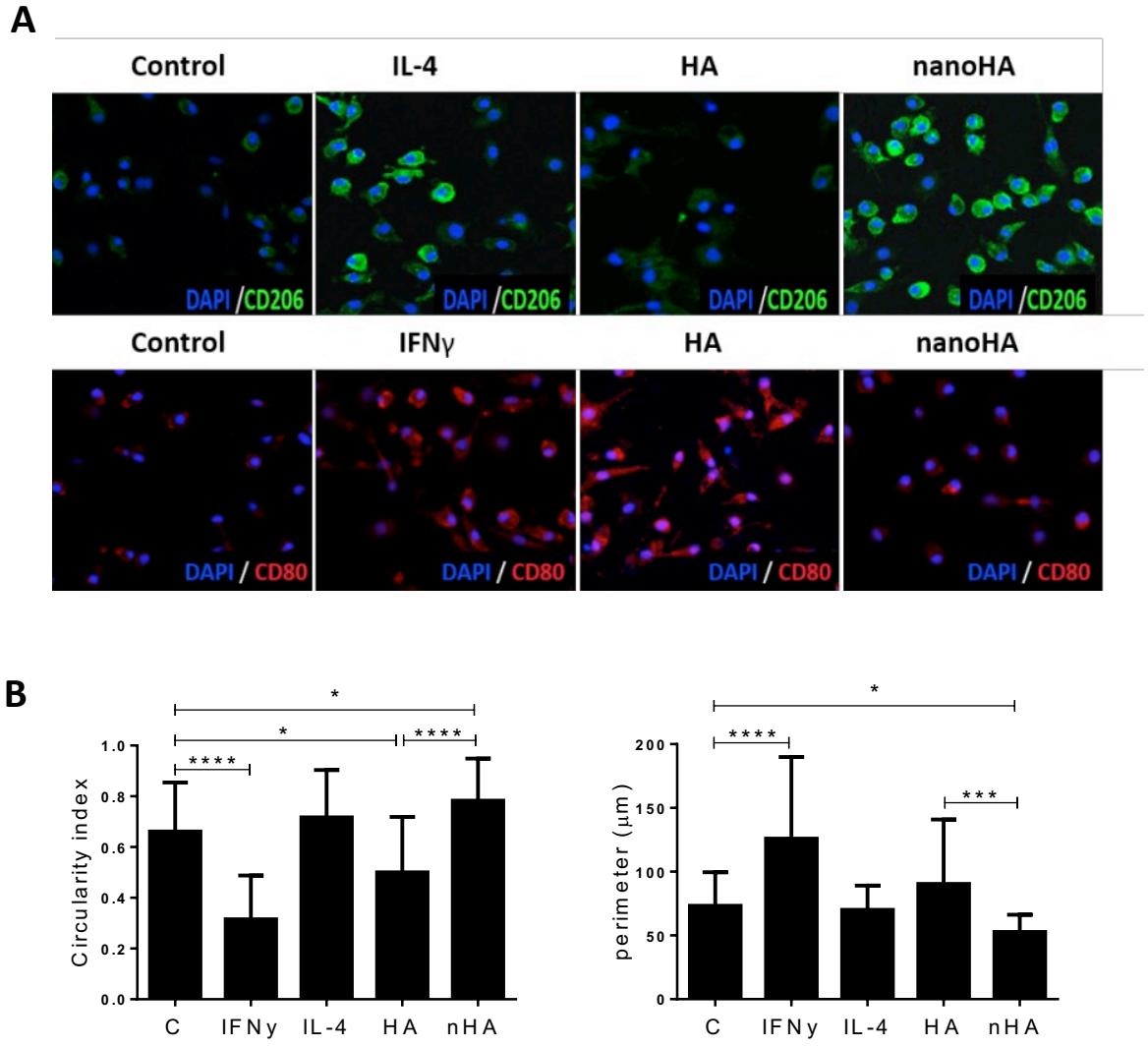

Figure 4.19: Polarization of macrophages by particles alters cell shape. (A) Immunofluorescence staining images of primary human macrophages (0.5 x 10^6 cells/ml) treated with particles (250 µg/ml) for 24 hours or the positive controls IL-4 (20 ng/ml) or IFNγ (20 ng/ml). CD206 (green) and CD80 (red), DAPI in blue. Magnification =20x. Scale bar = 50µm. **(B)** Cell shape parameter analysis using image J software. Data was analysed using one-way ANOVA with Tukey post-test (*p<0.05, ***p<0.001, ****p<0.0001).

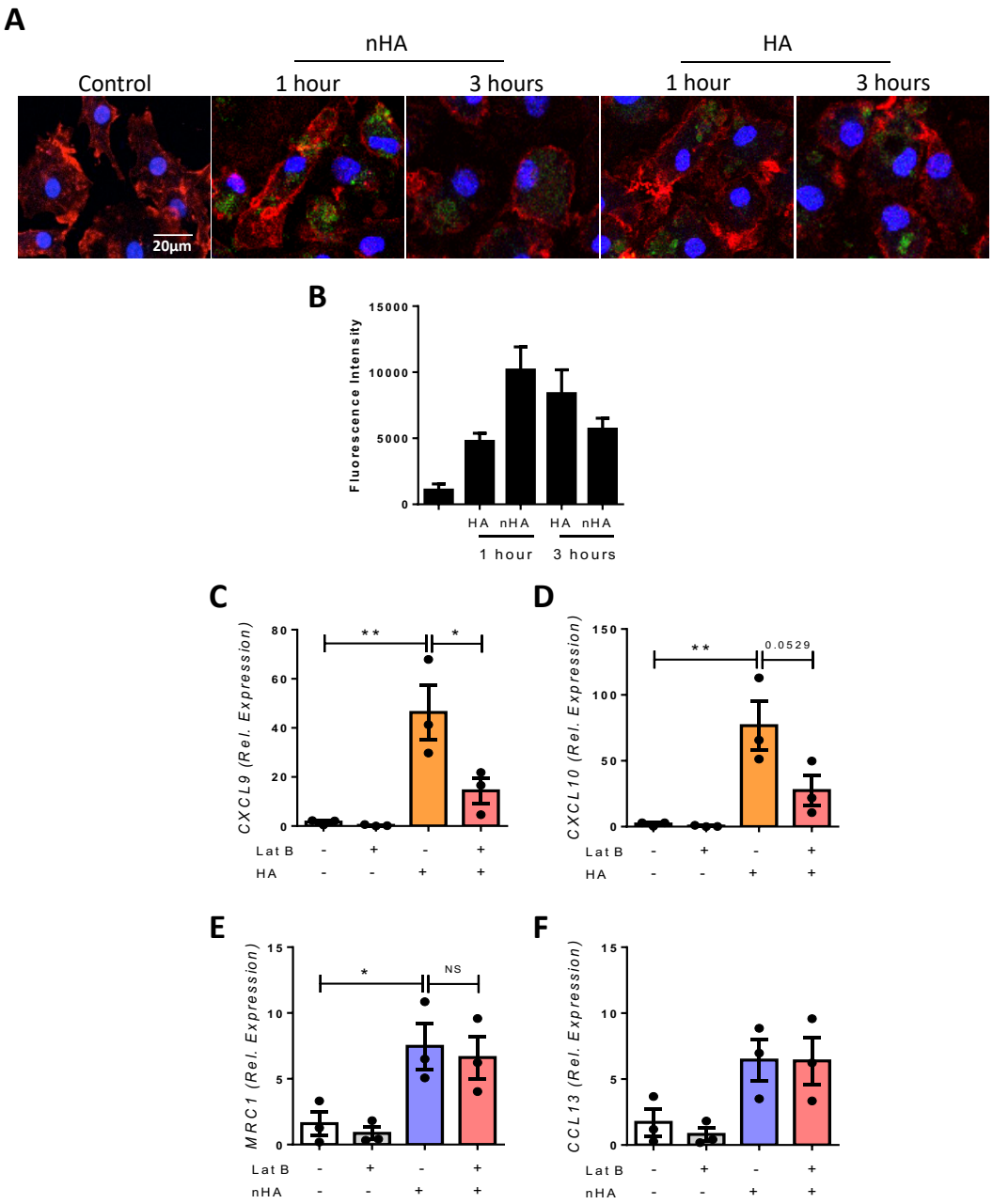

Figure 4.20: Cellular uptake of fluorescently tagged particles by primary human macrophages. (A) Primary human macrophages (1x 10^6 cells/ml) were stimulated with FITC (green) tagged micron or nano particles (250 µg/ml) for 1 or 3 hours. Cells were fixed with PFA, and with rhodamine red to stain F-actin and DAPI to stain nuclei. Magnification =40x Scale bar = 20 µm. **(B)** FITC fluorescence quantification from images was assessed using Image J. **(C-F)** Primary human macrophages (1 x 10^6) were treated with micron or nano particles (250 µg/ml) alone or were pre-treated with the actin polymerization inhibitor, Latrunculin B (1 µM), prior to treatment with micron **(C & D)** or nano particles **(E & F)** for 24 hours. mRNA levels of the M1 genes CXCL9 and CXCL10 **(C & D)**, and the M2 genes **(E & F)** MRC1 and CCL13 were analysed by real-time PCR. mRNA concentration was normalised to the housekeeping gene 18s ribosomal RNA. Gene expression, relative to untreated control cells, was determined using the $2^{-\Delta\Delta CT}$ algorithm. Pooled data (n=3) is represented as ± SEM. Data was analysed using one-way ANOVA with Tukey post-test (*p<0.05, **p<0.01).

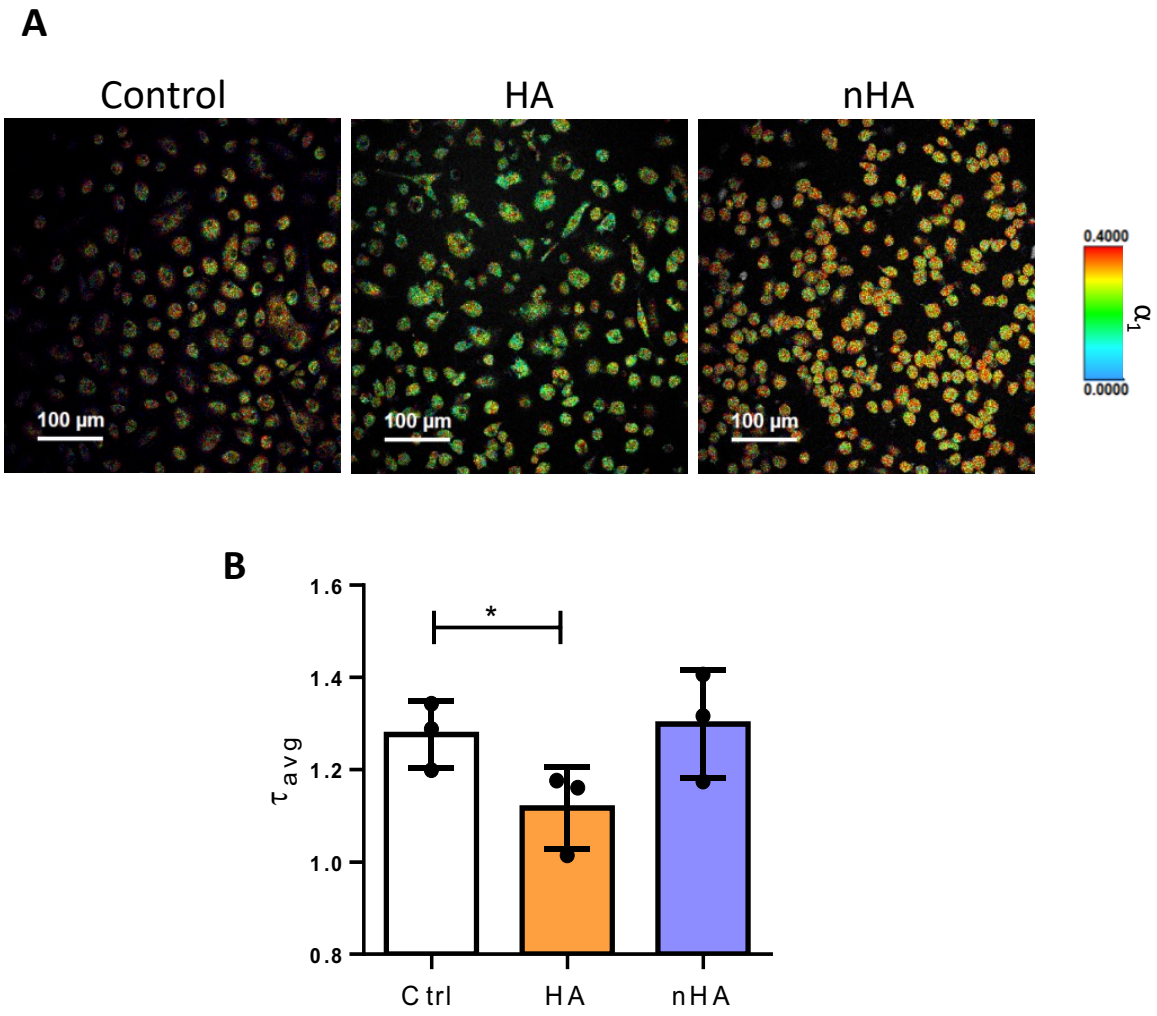

Figure 4.21: Metabolic profile of macrophages is dependent on particle size. Primary human macrophages (1 x 10^6) were stimulated with stimulated with particles (250 µg/ml) for 24 hours. Cells were imaged using Fluorescence lifetime imaging microscopy (FLIM) to assess the endogenously fluorescent metabolic molecule NADH. **(A)** Representative FLIM images from control, micron HA or nano HA treated macrophages. **(B)** Bar graphs the ratio of bound: free NADH (τ avg) Pooled data (n=3) is represented as ± SEM. Data was analysed using one-way ANOVA with Tukey post-test (*p<0.05). This experiment was performed with assistance from Nuno Neto.

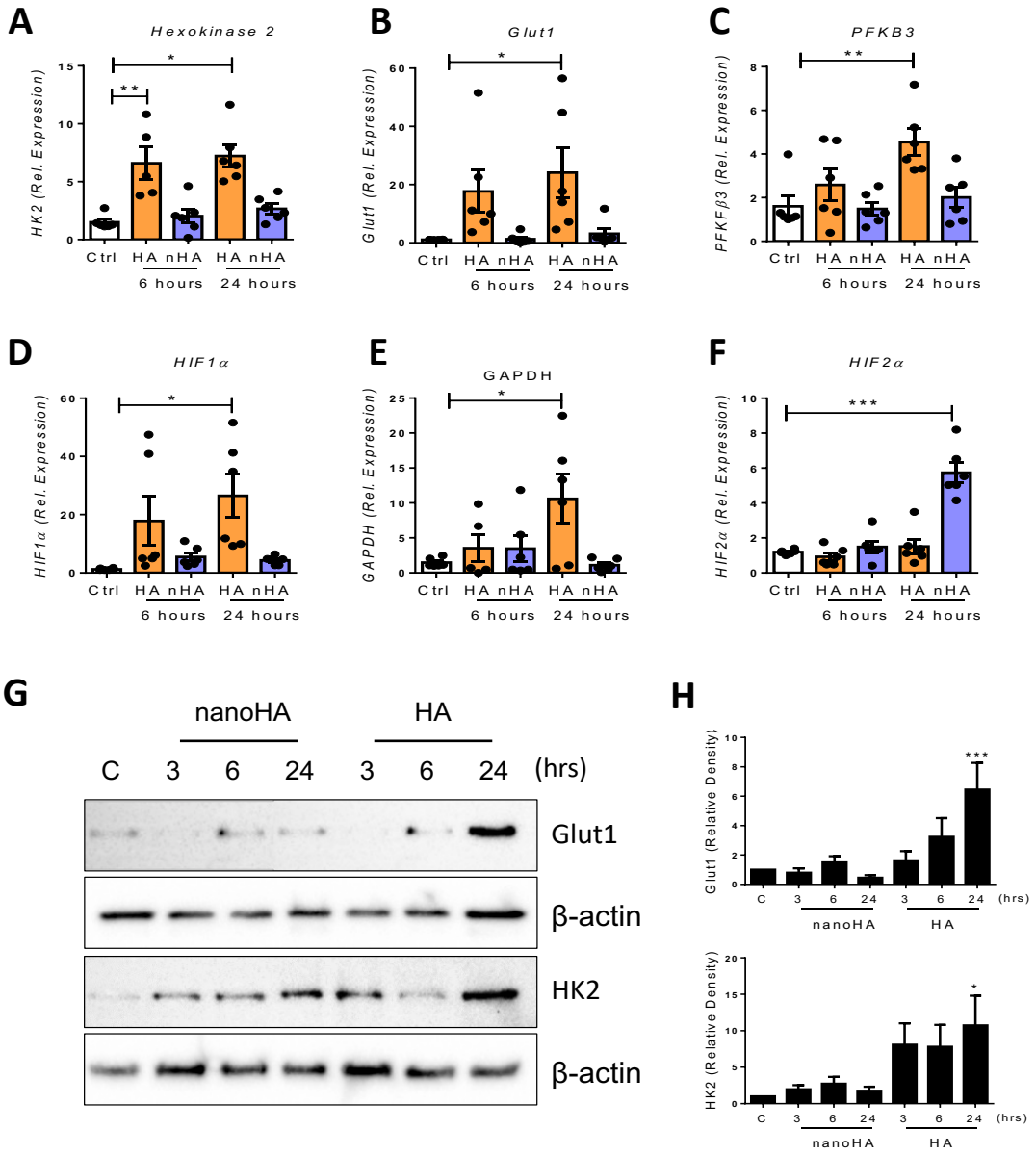

Figure 4.22: Micron but not nano particles upregulate surrogate markers of glycolysis. Primary human macrophages (1 x 10^6 cells/ml) were stimulated with stimulated with particles (250 µg/ml) for 6 or 24 hours. mRNA expression of glycolytic markers **(A)** HK2, **(B)** GLUT1, **(C)** PFKB3, **(D)** HIF1α, **(E)** HIF2α and **(F)** GAPDH were analysed by real-time PCR. mRNA concentration was normalised to the housekeeping gene RPLPO ribosomal RNA. Gene expression, relative to untreated control cells, was determined using the $2^{-\Delta\Delta CT}$ algorithm. Pooled data (n=6) is represented as mean ± SEM. **(G)** Representative western blots demonstrating expression of HK2, Glut 1 and HIF1α in whole cell lysates in response to micron or nanoHA particles post 3, 6 or 24 hour stimulation. **(H)** Pooled data (n=5) depicting densitometric analysis of immunoblots using ImageJ software. Bar graphs illustrate the mean ± SEM increase in protein expression relative to untreated control and normalised to β-actin housekeeping protein. Data was analysed using one-way ANOVA with Tukey post-test for western blotting (*P≤0.05, **P≤0.01, ***p<0.001).

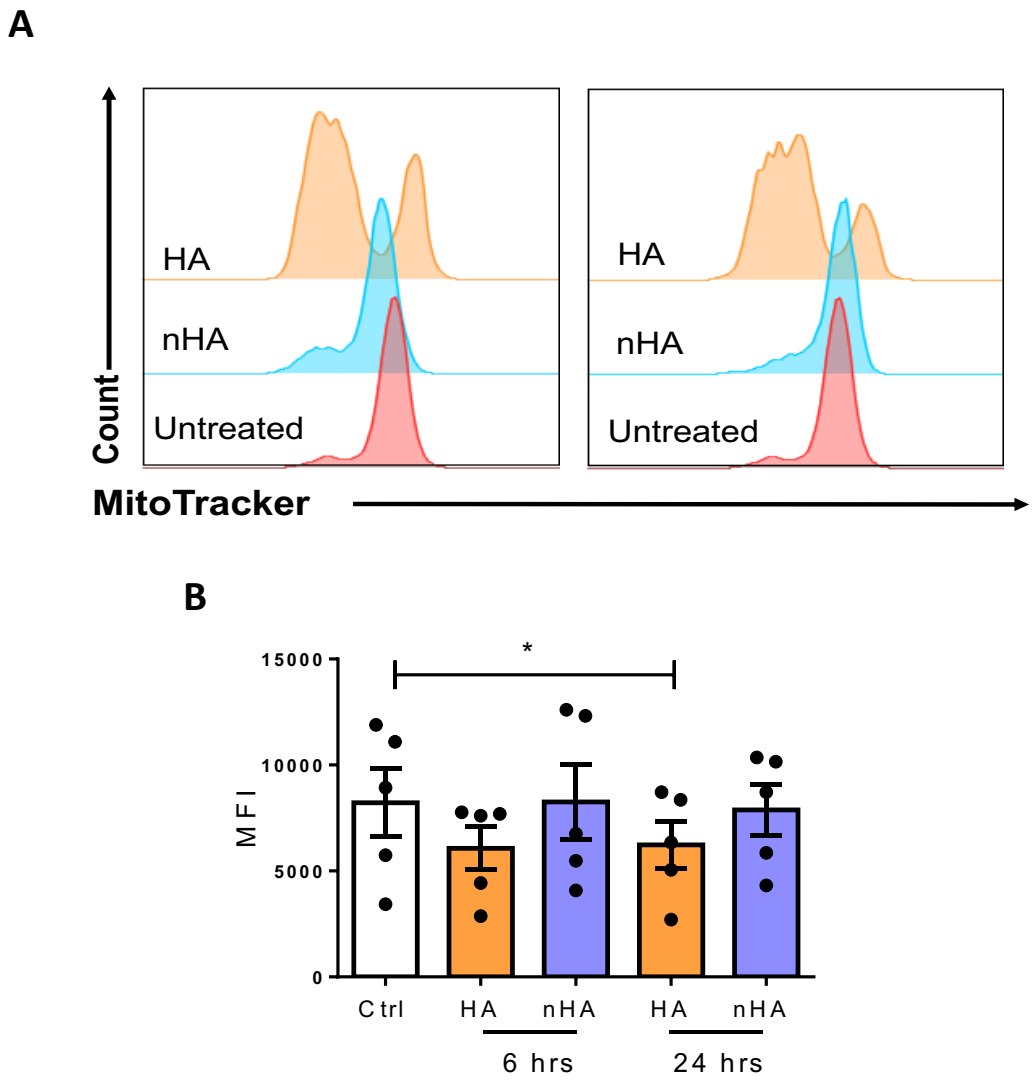

Figure 4.23: Micron HA particles reduce mitochondrial mass in primary human macrophages. Primary human macrophages (1 x 10^6) were stimulated with stimulated with particles (250 µg/ml) for 6 or 24 hours. Cells were then stained with Mitotracker Red and mitochondrial biomass was measured by flow cytometry. **(A)** Histogram depicting Mitotracker Red staining in control-, micron HA- and nanoHA-treated macrophages from one representative experiment. **(B)** Pooled data (n=5) depicting Mitotracker Red staining in control-, micron HA- and nanoHA-treated macrophages. Results shown are mean ± SEM of the measured Mean Fluorescence Intensities (MFI). Data was analysed using Kruskal Wallis with Dunn's post-test (*P≤0.05).

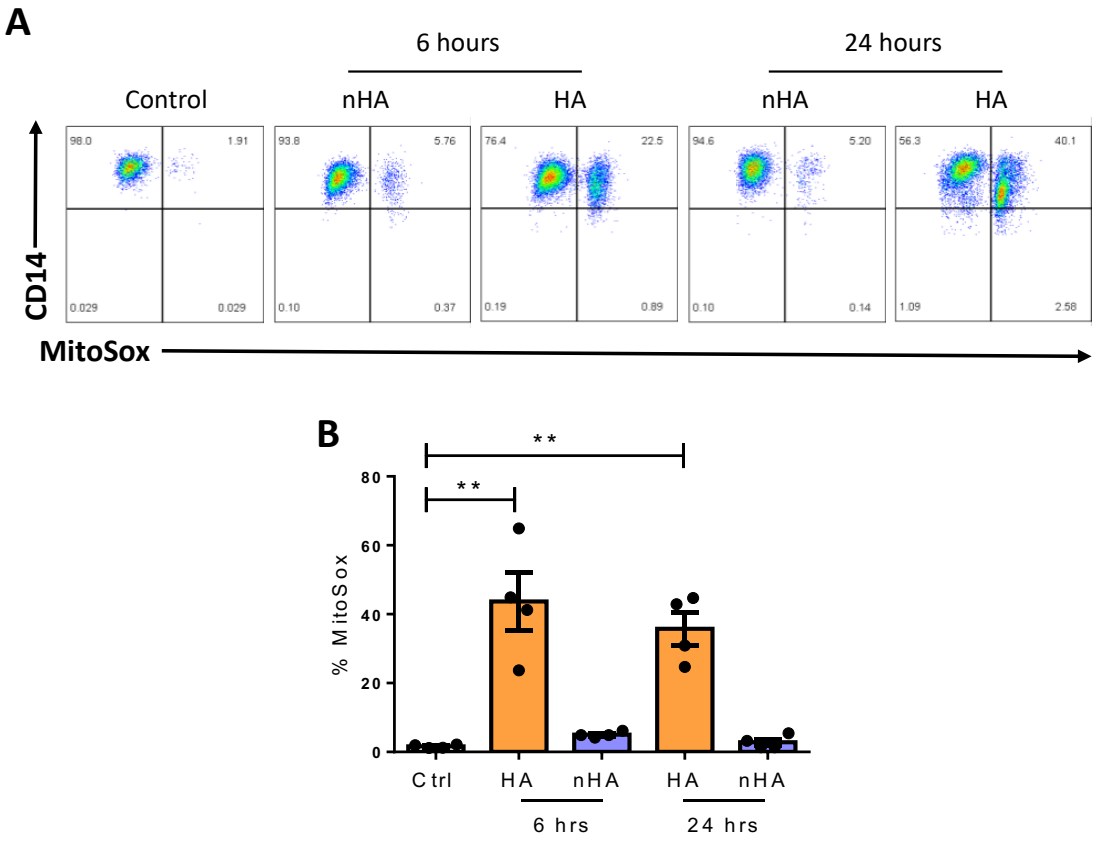

Figure 4.24: Micron particles drive mitochondrial ROS production in primary human macrophages. Primary human macrophages (1 x 10^6 cells/ml) were stimulated with stimulated with particles (250 µg/ml) for 6 or 24 hours. Cells were then stained with MitoSox Red and mitochondrial ROS was measured by flow cytometry. **(A)** Representative dot plots depicting MitoSox Red staining in control-, micron HA- and nanoHA-treated macrophages from one representative experiment. **(B)** Pooled data (n=4) depicting MitoSox Red staining in control-, micron HA- and nanoHA-treated macrophages. Results shown are mean percentages ± SEM of MitoSox positive cells Data was analysed using Kruskal Wallis with Dunn's post-test (**p<0.01).

4.4 Discussion

Due to increased life expectancy and the current obesity crisis, the number of individuals requiring joint replacement surgeries is predicted to rise to 4 million annually by 2030 (320, 321). Several studies have reported that wear particles generated from orthopaedic implants can activate innate immune cells to drive deleterious inflammatory responses and osteolysis leading to aseptic loosening and implant failure. The findings presented in this chapter demonstrate that PMMA and HA particles polarize macrophages towards an M1 phenotype which is associated with pro-inflammatory activity. It is also demonstrated that the binding of these particles to the cell surface likely leads to the formation of lipid rafts and activation of the proximal kinase, Syk. This in turn leads to activation of the downstream signalling molecules, ERK and p38, and, as was the case with Syk inhibition, pharmacological blockade of these molecules prevents M1 macrophage polarization and inflammatory gene expression. Furthermore, this chapter provides evidence that in-house generated nanoHA particles, in contrast to the commercially available micron sized HA particles, preferentially polarize primary human macrophages towards an M2 phenotype and specifically drive the production of the anti-inflammatory cytokine, IL-10. These effects may be coupled to metabolic changes in particle stimulated cells, with micro sized HA particles driving a metabolic switch favouring glycolysis, a phenomenon now recognised as being directly linked to M1 macrophage polarization.

In most circumstances, Syk is activated following Fc receptor engagement on immune cells and upon phagocytosis (322). However, recent studies have reported that Syk is activated by particulates via MATS, a receptor-independent process that involves direct binding of particulates to the cell membrane. This results in lipid raft formation and aggregation of ITAM-containing molecules which mediate the recruitment of Syk, to the plasma membrane and facilitate its subsequent activation (247, 323). Syk been implicated in both the internalisation of gout-associated MSU crystals and subsequent MSU-induced signalling in neutrophils and dendritic cells (247, 324). It has also previously been reported that atherosclerosis-associated cholesterol crystals and osteoarthritis-associated BCP crystals activate Syk via MATS leading to IL-1β processing

and secretion (99, 300). In this chapter, treatment of macrophages with M-βCD, which is used to prevent lipid raft formation, effectively reduced PMMA- and HA-induced IL-1β production which is in agreement with a previous study showing similar effects in PMMA-activated murine macrophages (297). It was also demonstrated that pharmacological inhibition of the NLRP3 inflammasome, which is activated downstream of Syk (305), prevents wear particle induced IL-1β production. This is in agreement with in vitro studies using NLRP3 deficient murine macrophages (98, 297), however there is evidence to suggest that this complex may be dispensable for the in vivo production of IL-1β (303, 304) and further study is required to determine if MCC950 (or derivatives of) represents a viable therapeutic for the treatment of periprosthetic inflammation. Atomic force microscopy should also be performed to confirm that Syk activation is required for high affinity interactions between wear particles and the cell membrane of human macrophages.

Interestingly, while the depletion of membrane cholesterol and prevention of lipid raft formation with M-βCD significantly reduced HA-induced IL-6 and TNFα cytokine production, only partial inhibition of PMMA-induced IL-6 an TNFα was observed in the presence of this inhibitor. It has been demonstrated that lipid rafts, in addition to being involved in MATS, play an important role in the internalization of particles such as HA (325, 326). While this study does not assess the mechanism of particle uptake, previous studies have demonstrated that the degree of particle internalization is very much governed by physicochemical properties such as shape, size and charge (326–328). Given the difference in chemistry, shape, size and presumably charge of HA and PMMA particles, it is tempting to speculate that their internalization may require distinct pathways. Particles may be internalized via a number of endocytic pathways, including clathrin-mediated endocytosis (CME) and clathrin-independent (caveolae-mediated) endocytosis (CIE) pathways (316, 329–331), the latter of which is dependent on the clustering of lipid rafts. As HA-induced inflammatory responses were nearly completely mitigated in the presence of M-βCD, a commonly used inhibitor of caveolae-mediated endocytosis, it is likely that, in addition to blockade of MATS and downstream signalling, this inhibitor also blocked internalisation of this particle and therefore completely abrogated particle-induced cell responses. In contrast, it is possible that PMMA

particles, in addition to uptake via caveolae-mediated endocytosis, may also be internalised via a secondary pathway such as clathrin mediated endocytosis, which does not involve lipid clustering, and therefore only partial inhibition of PMMA internalization and downstream intracellular responses occurred with M-βCD. Studies using specific inhibitors of clathrin mediated endocytosis, such as Dynasore, are required to elucidate the mechanism of PMMA particle uptake and to determine whether it differs to that of HA particle uptake.

PMMA and HA particles were also shown to activate the downstream MAPKs, ERK and p38, in primary human macrophages and, as with Syk inhibition, pharmacological blockade of these molecules prevents M1 macrophage polarization and inflammatory gene expression. It has previously been reported that PMMA particles activate MAPKs in murine osteoclast precursor cells, contributing to osteoclast differentiation (332) hence, MAPK targeting has the potential to modulate the two key processes leading to aseptic implant loosening i.e. periprosthetic inflammation and osteoclast formation. Interestingly, while inhibition of IL-1β, TNFα and IL-6 was observed, wear particle-induced IL-8 production was not affected by Syk or MAPK inhibitors suggesting that this chemokine is regulated in a different manner. The findings that PMMA particles drive M1 macrophage polarization are consistent with previous in vitro/ex vivo studies reporting M1 polarization upon PMMA particle stimulation, however this chapter now demonstrates that HA particles are also capable of directly polarizing macrophage to an M1 phenotype. Efforts to alter M1 polarization by wear debris particulates and mitigate these inflammatory processes are ongoing and primarily involve the use of anti-inflammatory cytokines. Antonios *et al* demonstrated that stimulation of murine macrophages with PMMA particles in combination with IL-4, decreased particle induced TNFα and IL-1β mRNA expression. Furthermore pre-treatment of macrophages with IL-4 decreased particle induced iNOS expression (141). Similarly Rao *et al* demonstrated that co-administration of polyethylene (PE) particles with IL-4 mitigated wear particle induced osteolysis in vivo and this was accompanied by a decreased M1/M2 ratio (140, 149). Additionally administration of the anti-inflammatory cytokine, IL-10, was shown to suppress osteolysis in the calvarial model in response to titanium particles (159). While the use of anti-inflammatories like IL-4 or IL-10 may ameliorate particle induced

osteolysis and prove a beneficial strategy, the results presented in this chapter now position Syk and/or MAPKs as novel therapeutic targets for wear debris induced M1 polarization in periprosthetic osteolysis. Therefore, it will now be of interest to determine whether Syk and/or MAPK inhibitors can alter macrophage phenotype and prevent bone loss in in vivo osteolysis models.

There are currently no drugs specifically approved to prevent or inhibit peri-implant inflammation and subsequent periprosthetic osteolysis. Inhibitors of osteoclastogenesis and osteoclast function are being considered. For example, bisphosphonates are a class of drugs known to have anti-osteoclast activity through the induction of osteoclast apoptosis (127, 138, 333–335). They are commonly used for metabolic bone diseases such as osteoporosis, osteogenesis imperfecta and hypercalcemia (336). Bisphosphonates such as risedronate and zoledronic acid have proven to be particularly potent and, in addition to alendronate, have been shown to reduce wear debris-induced osteolysis in animal models (138, 333–335). Statins such as HMG-CoA reductase inhibitors are another class of osteoclast inhibitors and can act in a similar manner to bisphosphonates by targeting the mevalonate pathway. In this case, simvastatin has been shown to inhibit UHMWPE-induced osteolysis in the murine calvarial model (165). Statins and inhibitors of RANKL and recombinant parathyroid hormone are also reported to show efficacy in animal models, however it remains to be determined if any of these agents are efficacious in osteolysis patients (138, 153, 166, 337).

Given the pathological similarities between periprosthetic osteolysis and arthritis, it has also been suggested that treatments that have been developed for the latter may be applicable for the prevention of aseptic implant loosening (152, 338). Specific targeting of TNFα with etanercept (a decoy receptor for TNFα), has been shown to have anti-resorptive effects in a murine calvarial model. However, in a pilot study of 20 patients with established periprosthetic osteolysis, no significant difference in osteolysis progression was observed between the etanercept-treated group and placebo controls (although the small sample size may have been a factor here) (167). More recently inhibition of TNFα secretion by the phosphodiesterase inhibitor pentoxifylline, was shown to reduce wear debris induced inflammation in healthy monocytes, however its

efficacy is yet to be tested in vivo (168). As mentioned previously, the COX-2 inhibitor, celecoxib has also shown efficacy in murine osteolysis models (294) however, one of the limitations with these existing therapeutics is that they only allow for the targeting of single inflammatory mediators and therefore may not be efficacious in osteolysis patients where a plethora of cytokines contribute to peri-inflammation and osteolysis. Furthermore, while anti-cytokine therapies are indeed promising candidates for periprosthetic osteolysis, preventing cytokine expression rather than inhibiting their activity may prove more efficient. Given the data presented in this chapter, which demonstrates that inhibition of Syk activity reduces the production of pro-inflammatory cytokine production following particle stimulation, it now positions Syk as an attractive target for the treatment of particle-induced inflammation. The orally available Syk inhibitor used in this study (R788) has previously shown efficacy in clinical trials for rheumatoid arthritis, however, reports of side effects during phase III trials led to trial termination (339). Nevertheless, a modification on the current drug or indeed, an alternate method of administration, such as local delivery into the joint, is worthy of consideration given our in vitro results showing dual inhibition of IL-1β and TNFα, both of which are known to promote osteoclastogenesis even when RANKL levels are low (340). It is apparent that an improved understanding of the signalling cascades activated by wear particles may pave the way for new treatments to either prevent or modulate inflammation and periprosthetic osteolysis. Furthermore, the development of early detection methods for osteolysis would aid the prevention of aseptic implant loosening, which continues to represent a major complication of total joint replacement.

The second aim of this chapter focused on elucidating the human macrophage response to nano sized HA particles. In-house generated nanoHA particles were synthesized and their structural, physical and chemical properties were compared to commercially available micron sized HA particles. The results presented demonstrate that micron HA particles appear as a more stoichiometric hydroxyapatite with a formula close to Ca10(PO4)6(OH)2 (308). This is in contrast to the in-house generated nano-sized hydroxyapatite particles, which are very similar to that of natural bone hydroxyapatite, with a crystalline core in the form of hydroxyapatite, coated by a mineral amorphous surface layer (341–343). However, it should be noted that differences in stoichiometry

between the two particles formulations may be attributed to the fabrication process(es). Unlike micron HA particles, these bone mimetic nanoparticles did not promote IL-1, TNFα and IL-8 cytokine secretion. Furthermore, the nanoHA particles used in this study are capable of driving production of IL-10. While there are a number of transcription factors that regulate IL-10 expression, stimulation of human macrophages with nanoHA particles was found to upregulate c-MAF, a well-known IL-10 inducing transcription factor. To our knowledge this is the first time hydroxyapatite nanoparticles have been shown to drive IL-10 production, however this has been demonstrated with other non-biological/polymer particulates. PLGA particles ranging in size from 500 nm-2 μm have been found to promote IL-10 induction in DC, while alum particles, with an average size of around 1-10 μm, are capable of significantly promoting IL-10 secretion in BMDCs in vitro and in vivo at the injection site and in draining lymph nodes (311).

In addition to observing robust IL-10 induction by nanoHA-treated macrophages, which is indicative of a more anti-inflammatory phenotype, data also demonstrated that these particles are capable of preferentially polarizing human macrophages towards an M2 phenotype. These results parallel with a recent study by Schoenenberger *et al* which demonstrated that larger TiO2 particles of 2 μM, but not nano TiO2 particles, significantly enhanced the M1 macrophage markers, TNFα and CD197, in a human monocytic cell line. In contrast to the findings with nanoHA in this chapter, there was no discernible effect on the M2 macrophage markers upon TiO2 nano particle treatment (344). The use of a cell line rather than primary macrophages, and the difference in composition of the two particles may account for the observed differences between the two studies.

It has been reported that different sized particles have different uptake rates in macrophages (345), with PLGA particles of 100 nm taken up more rapidly than larger particles (346). Here it is demonstrated that, while both particle types are taken up within 1 hour of cell treatment, it would appear that the nano sized HA particles are taken up at a higher level than micron sized particles. Internalization of particles by phagocytosis (for particles larger than 0.5 μm) and micropinocytosis (for particles less than 0.5 μm) requires actin machinery and cytoskeletal rearrangement (347, 348). Inhibition of actin polymerization resulted of in a loss of HA-induced M1 responses,

whereas no effect on nanoHA-induced M2 polarization was observed indicating that a non-actin dependent pathway may be involved in the uptake of the nano HA particles. It has been demonstrated that alternative processes such as clathrin-mediated endocytosis (CME) and clathrin-independent endocytosis (CIE) can also mediate nanoparticle uptake (316, 329–331). Further studies involving the use of inhibitors such as Chlorpromazine or Dynasore/Dynoles to inhibit CIE and CME, respectively (349), are required to determine if these processes are involved in the uptake of nanoHA by macrophages. It has also been demonstrated that lipid rafts play a role in the phagocytosis of PS microspheres (325), and data presented earlier in this chapter indeed suggest that disruption of lipid rafts, using M-βCD, abrogates PMMA and HA induced inflammatory responses. Therefore, it would be of interest to determine whether inhibition of this process also affects nanoHA induced cellular responses.

This chapter also provides preliminary evidence of particulate matter-induced metabolic reprogramming. Stimulation of macrophages with different size particulates appeared to drive distinct metabolic profiles with micron HA particles dampening mitochondrial biogenesis and enhancing glycolytic metabolism in macrophages. While alterations in metabolism are known to be intricately linked to differentiation and maturation of immune cells, the molecular links between metabolic signalling and immunological function have yet to be fully elucidated. Further studies using RNA sequencing or metabolomics are required to fully characterise the metabolic profile of macrophages post-particle stimulation. This avenue of research represents a novel aspect of material-induced immune response as it has recently become apparent that intrinsic properties of materials may be utilised to direct cellular metabolism and cell behaviour (350). With this in mind, consideration of how the intracellular metabolic pathways are influenced by material properties is an important aspect of material design, and indeed materials may be designed to specifically alter cellular metabolism and downstream tissue repair responses.

In conclusion, the results presented in this chapter (summarised in Figure 4.25) describe the signalling pathways activated by HA and PMMA particles and implicate Syk tyrosine kinase and ERK/p38 MAPKs in particle-induced M1 macrophage polarization. This now

positions these kinases as novel therapeutic targets for periprosthetic osteolysis. This is an interesting area for future research with the prospects of incorporating small-molecule inhibitors of these targets into coatings of the implants or even direct intra-articular injection of these inhibitors for a targeted approach. Furthermore, this chapter provides evidence that in-house generated nanoHA particles, in contrast to commercially available micron sized HA, are inherently anti-inflammatory, therefore coating implants with HA particles in the nanometre size range could mitigate inflammatory responses in periprosthetic osteolysis and improve implant longevity. Moreover, micron-size HA particles alter the metabolic status of cells and appear to drive a metabolic switch favouring glycolysis. This switch has been linked to macrophage polarization towards an inflammatory phenotype and provides a new avenue for exploration into design of biomaterials that can dictate innate immune responses, which may have important implications for regenerative engineering.

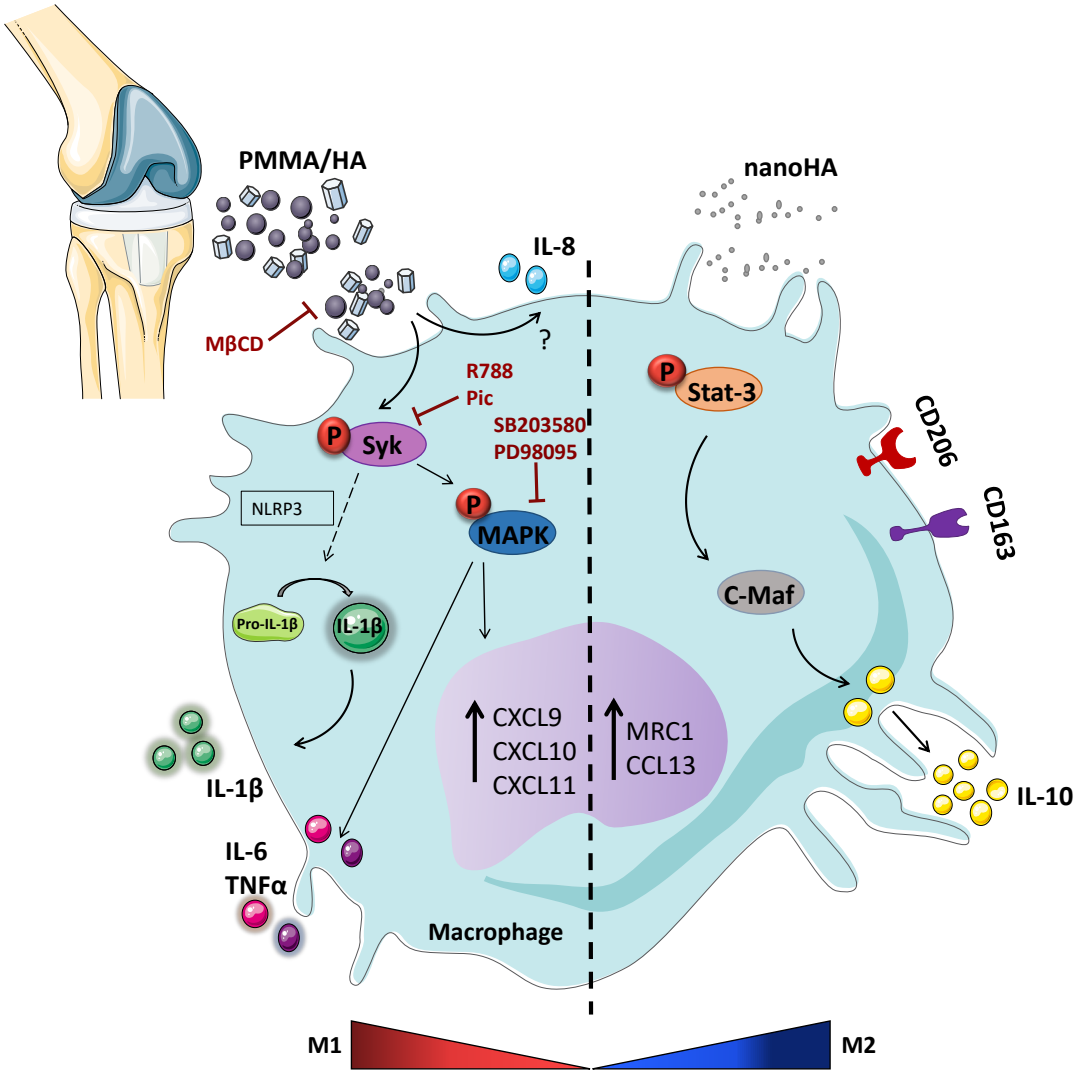

Figure 4.25: Model of particle-induced macrophage polarization and activation of signalling pathways. Micron sized particles, HA and PMMA upregulate M1-associated markers in a Syk tyrosine kinase dependent manner and drive production of pro-inflammatory cytokines, IL-1β, TNFα and IL-6. nanoHA particles polarize macrophages toward an M2-like phenotype and activate STAT3 and the IL-10 transcription factor, c-Maf, culminating in downstream IL-10 cytokine production.

Chapter 5: Investigation of the immunomodulatory capacity of HA/nanoHA functionalised scaffolds for use in bone tissue regeneration

5.1 Introduction

The field of tissue engineering has placed significant focus on designing biomaterial scaffolds capable of directing the fate of tissue-specific progenitor cells. A number of studies have demonstrated that the specific composition of engineered constructs can impact mesenchymal stromal cell (MSC) differentiation and that properties inherent to biomaterials such as topography and stiffness can direct lineage specific cell differentiation and promote successful tissue integration (351–354). In addition to scaffold composition, efforts are being made to manipulate the interplay between MSCs and the host immune system given that innate immune cells, including macrophages, interact will tissue specific progenitor cells to direct tissue regeneration (355). Despite the fact that promoting an appropriate immune response is integral to the success of any implant (208), there has been less focus on the design of scaffolds capable of eliciting immune responses that specifically direct functional tissue regeneration.

While it is well accepted that an early inflammatory response is required to initiate pro-regenerative responses post-injury, a shift from pro-inflammatory to anti-inflammatory function is required to maximize the regenerative capacity of progenitor cells and minimize the destructive effects of prolonged inflammation. In the field of bone regeneration, it has been demonstrated that administration of pro-inflammatory cytokines such as TNFα to fracture sites immediately after injury accelerates fracture repair (356), while prolonged administration inhibits cartilage formation in the early phase of bone induction (357). The temporal nature of the inflammatory responses is largely attributed to the transition of macrophages from a classically activated 'M1' state, to alternatively activated 'M2' macrophages. While M1 macrophages play a role in early angiogenesis, a prolonged M1 presence can propagate tissue destruction and lead to fibrous scar formation and inferior tissue regeneration (201, 202). M2 macrophages promote ECM synthesis, vessel formation and osteogenic differentiation (203, 204). Scaffolds loaded with IFNγ and IL-4 to promote sequential polarization of M1 and M2 macrophages, respectively, have shown promising results in fracture repair models, further attesting to the contribution of innate immune cells in bone reconstitution (358). In the context of biomaterial implantation, the contribution of the

adaptive immune system to bone healing has also been explored using RAG knockout mice and the results indicated that functional T and B cell responses decelerate bone repair (211). Overall, these studies provide compelling evidence that modulation of immune responses may serve as a beneficial strategy to consider when designing scaffolds for efficient osteoinduction.

It was demonstrated in Chapter 4 that micron-sized HA particles promote M1 macrophage polarization in primary human macrophages and the specific signaling pathways involved in driving activation of M1 macrophages were identified. Furthermore, it was demonstrated that nanoHA particles were capable of polarizing macrophages to an M2 phenotype and driving IL-10 production. While this data is highly important from an immunological perspective, the influence of HA-dependent macrophage phenotype on MSC differentiation has not yet been established. Therefore, the first aim of this chapter is to examine whether the impact of HA/nanoHA on macrophage phenotype can influence MSC differentiation and bone tissue formation *in vitro.*

Extracellular matrix derived materials such as collagen are commonly used as 3D biological constructs for bone and cartilage engineering as they can promote chondrogenesis and osteogenesis both *in vitro* and *in vivo* (359, 360). Studies have focused on incorporating HA particles into ECM derived 3D scaffolds for in vivo bone repair given that HA-collagen pairing occurs naturally in bone and such scaffolds have previously shown excellent biocompatibility and osteoinductivity (361). Furthermore, seeding of pre-osteoblast cells onto nanoHA-collagen scaffolds showed superior osteogenic capacity and enhanced mineral deposition compared to those seeded on collagen only scaffolds (361). While much progress has been made in developing osteoinductive scaffolds, the *in vivo* immune response is still poorly understood and remains to be elucidated. Therefore, the final aim of this chapter is to establish the immune response to HA functionalised ECM scaffolds in order to determine whether early immune responses are predictive of downstream bone tissue repair.

5.2 Specific Aims

- To determine whether HA/nanoHA driven macrophage phenotype can influence MSC osteogenic differentiation in vitro.
- To examine the immune and tissue healing response to HA/nanoHA functionalised scaffolds using a rat femoral defect model.

5.3 Results

5.3.1 Conditioned media from nanoparticle treated macrophages upregulates osteogenic genes in human MSCs.

It is well established that macrophages play a significant role in tissue repair and regeneration. Data presented in Chapter 4 demonstrated that, in contrast to micron-sized HA particles, nanoHA particles specifically promote an M2-like phenotype. It was next of interest to determine whether the osteogenic differentiation capacity of MSCs is influenced by macrophage phenotype/secreted factors following exposure to hydroxyapatite particles. To test this, macrophages were treated with HA or nanoHA particles (250 μg/ml) for 24 hours. Media was removed and centrifuged for 1 hour at 1200 x g to remove any residual particles and generate particle free conditioned media. Human MSCs were then cultured for 48 hours in either control media or particle free conditioned media (CM) from macrophages treated with micron or nano-sized HA particles. Quantitative PCR was then carried out to assess the impact of the CM on osteogenic gene expression. Results revealed that CM from nanoparticle treated macrophages significantly enhanced mRNA expression of the osteogenic genes, bone morphogenetic protein 2 (bmp2) and alkaline phosphatase (alp) in MSCs, when compared to CM from untreated macrophages or CM from micron HA particle treated macrophages (Figure 5.1 A & B). While there was a non-significant trend ($p=0.0753$) towards increased osteopontin (OPN) expression with CM from micronHA particle-treated macrophages (Figure 5.1 C), expression of osteocalcin (OCN) was not significantly affected by any treatment (Figure 5.1 D). Furthermore, no discernible difference in mRNA expression of the osteogenic transcription factors, Runx2 and Osterix, which work together to upregulate OPN, was observed (Figure 5.1 E & F). To further support the finding that nanoHA CM may be driving osteogenesis, MSCs were pre-treated with CM from nanoHA/HA treated macrophages for 48 hours. The medium was then removed and the MSCs were cultured for a further 7 days in osteogenic induction media. Assessment of mineralization and calcification by Alizarin Red staining after 7 days revealed an enhanced appearance of calcification granules in the nanoparticle-CM treated MSCs (Figure 5.2 A). This was further verified following dye extraction and quantification demonstrating significantly enhanced mineralization in

the nanoHA CM group compared to control and HA CM (Figure 5.2 B). Importantly, CM was shown to be free of any residual particles (Figure 5.3 A), and while there was a trend towards osteogenic gene expression upon treatment with the particles alone, this was not significant. Furthermore, no difference was observed between the micron HA and nanoHA particle groups under these conditions. (Figure 5.3 B). Furthermore, particles were incubated for 24h in cell-free media to control for any material release and no discernible differences in MSC osteogenic gene expression was observed under these conditions (Figure 5.3 C). Taken together this data suggests that nanoHA macrophage CM, which consists primarily of an M2-like secretome, can enhance early matrix mineralization of MSCs in an *in vitro* setting.

5.3.2 Conditioned media from nanoHA treated macrophages enhances MSC migration.

Infiltration and recruitment of host MSCs into any tissue-engineered construct is an important factor for consideration given their role in ECM deposition. Therefore, in addition to osteogenic differentiation, the migratory capacity of the MSCs was assessed using an in vitro scratch assay as a model of wound healing. To this end, a single scratch was made through a monolayer of MSCs before culture in media alone, or conditioned media from untreated, HA and nanoHA treated macrophages. MSC migration across the wound margins was then assessed visually at 24 hours and cells migrating into the wound site were counted by blinded individuals. Enhanced migration and repopulation of the wound site was apparent by eye in cells cultured in the nanoHA macrophage CM group (Figure 5.4 A). Semi-quantitative analysis of cell repopulation at the wound site within 24 hours revealed a significantly higher number of MSCs migrating back across the wound margin (Figure 5.4 B). Importantly there were no differences in the total cell number in each group, eliminating the possibility that the differences observed were due to cell proliferation (Figure 5.4 C). Taken together, these results suggest that secreted factors from nanoparticle polarized macrophages enhance MSC migratory capacity.

5.3.3 HA and nanoHA particles induce differential angiogenic gene expression in primary human macrophages and endothelial cells.

Vascularization and angiogenesis are crucial processes for functional and efficient bone tissue repair (362). Several growth factors such VEGF and Ang1 have well established roles in vascularization and angiogenesis as well as possessing chemotactic properties (363). While VEGF promotes endothelial cell proliferation, Ang-1 promotes vessel maturation and prevents endothelial cell apoptosis and permeability (364). Due to their complementary functional relationship, it was next of interest to assess the capacity of micron and nano particles to induce these growth factors in primary human macrophages. Cells were stimulated with micron and nano particles for 24 hours and mRNA expression of VEGF and Ang1 were assessed using real-time PCR. Both micron HA and nanoHA particles significantly increased mRNA expression of VEGF compared to untreated control cells (Figure 5.5 A). In contrast, increased expression levels of Ang1 were only observed in nano particle treated cells (Figure 5.5 B). The capacity of macrophage CM to influence endothelial cell angiogenic responses was also assessed. A GFP-tagged human endothelial cell line (HUVEC) was utilized to analyse tubule formation using CM from macrophages treated with micron HA or nanoHA particles, or a positive control, VEGF. Conditioned media from nanoHA particle treated macrophages significantly enhanced tube formation in HUVECs at 2, 4 and 6 hours (Figure 5.6 A). Furthermore, increased branching, branch length and junction formation between cells was significantly increased in nanoHA conditioned media, which was comparable to treatment with the positive control, VEGF (Figure 5.6 B). Taken together, this suggests that the secretome from nanoHA treated macrophages enhances the capacity of endothelial cells to undergo pro-angiogenic processes.

5.3.4 Conditioned media from nanoparticle treated macrophages drives osteogenesis and mineralization of human MSCs in an IL-10 dependent manner.

The role of various cytokines, such as TNFα and IL-1β in osteogenesis has gained much attention (365–367). Given that nanoparticles were capable of driving robust IL-10 expression, it was of interest to determine if this cytokine plays a role in nanoparticle-

driven MSC osteogenic differentiation. To test this, macrophages were pre-treated with an anti-IL-10 neutralizing antibody or an isotype control antibody prior to treatment with micronHA or nanoHA particles for 24 hours. MSC were then cultured for 48 hours in CM from treated macrophages. Consistent with earlier observations, CM from nanoparticle treated macrophages enhanced BMP2 and ALP mRNA expression, however expression of both genes was significantly reduced when MSC were cultured in CM from particle-treated macrophages that were pre-incubated with anti-IL-10 (Figure 5.7 A & B), demonstrating that IL-10 signaling is coupled to BMP2 and ALP induction. Interestingly, OPN expression was enhanced in MSC cultured in CM from micron HA particle-treated macrophages, however, IL-10 neutralization had no effect on gene expression (Figure 5.7 C), suggesting that OPN induction by HA CM is occurring independently of this cytokine. As before, no differences in expression of OCN, Runx2 or Osterix were observed (Figure 5.7 D-F).

To further support the finding that nanoHA CM may be driving osteogenesis in an IL-10 dependent manner, macrophages were pre-treated with an anti-IL-10 neutralizing antibody or an isotype control antibody prior to treatment with micron or nanoparticles for 24 hours. MSC were then cultured for 48 hours in CM from particle treated macrophages. The medium was then removed and the MSCs were cultured for a further 7 days in osteogenic induction media. Downstream mineralization and calcification was analysed by AR staining as before. Consistent with the gene expression findings, calcification and mineralization was not apparent by eye at day 7 in the nanoHA CM group when IL-10 was neutralized (Figure 5.8 A). Moreover, extraction of Alizarin Red and measurement by spectrophotometry indicated a significant decrease in mineralisation in the IL-10 neutralizing antibody treated group (Figure 5.8 B). No differences were observed in cells treated with the IgG isotype control antibody, confirming the role of IL-10 (Figure 5.8 C). Taken together, this data suggests that that the pro-osteogenic effects of nanoparticles may be largely attributed to IL-10.

5.3.5 Neutralization of IL-10 does not affect M2 macrophage polarization.

In order to confirm that neutralization of IL-10 was not inhibiting the polarization of the macrophages towards an M2 phenotype in response to the nanoHA particles, the phenotype of the macrophages after IL-10 neutralization was assessed. Macrophages were stimulated with nanoHA particles, or the M2 polarizing cytokine IL-4, in the presence of the IL-10 neutralizing antibody and M2 gene expression was assessed by real-time PCR. Pre-treatment of macrophages with the IL-10 neutralizing antibody did not appear to affect nanoHA-induced M2 macrophage polarization, based on expression of the M2 markers, MRC1 and CCL13 (Figure 5.9 A & B). This was also the case with the positive control, IL-4, with robust induction of both MRC1 and CCL13 observed even in the presence of the IL-10 neutralizing antibody (Figure 5.9 C & D). This suggests that the effects observed are more likely mediated by IL-10 signaling in the MSCs rather than IL-10-induced macrophage polarization.

5.3.6 IL-10 is a direct driver of osteogenesis in human MSCs.

In order to further validate the role of IL-10 in osteogenic gene expression, recombinant human (Rh) IL-10 was added directly to the MSCs for 48 hr prior to carrying out real-time PCR. Supplementation with 1ng/ml of IL-10 did not appear to drive osteogenic responses, however addition of 10 ng/ml, (a dose close to that produced by the nanoHA-treated macrophages; Figure 5.10) resulted in a significant induction of ALP, OPN and BMP2 but not OCN (Figure 5.11 A-D). Furthermore, supplementation of culture media with Rh IL-10 resulted in significantly more calcification and mineralization of MSCs after 7 days (Figure 5.11 E & F), providing further evidence for a direct role for IL-10 in early osteogenesis and mineralization of MSCs *in vitro*.

5.3.7 Solubilized ECM from differential tissue sources differentially influence macrophage immune response.

In order to translate the in vitro data to a physiologically relevant in vivo system, it was next necessary to characterize the immune response to hydroxyapatite functionalized scaffolds using a rat femoral defect model (221). Extracellular matrix (ECM)-based

scaffolds are commonly used in bone and cartilage tissue engineering and several growth factors or bioceramics, such as HA particles, have been incorporated into these scaffolds in order to enhance osteogenesis (360, 361, 368). In order to develop HA/nanoHA functionalized scaffolds for our in vivo femoral defect model, porcine growth plate (GP) and articular cartilage (AC) tissue was harvested from the femur of skeletally immature pigs and subjected to a collagen solubilization protocol recently established in the Kelly laboratory, as described in Section 2.2.16.1. Mass spectrometry protein analysis of GP and AC ECM provided in Figure app.4.

The inherent immunomodulatory capacity of AC and GP ECM was compared by culturing primary human macrophages in the presence of solubilised ECM for 24 hr before assessing cytokine production. LPS (1–100 ng/ml) was included as a positive control. GP but not AC derived ECM induced IL-6 and TNFα cytokine production (Figure 5.12 A & B). Interestingly, high levels of the chemokine IL-8 were observed in macrophages cultured in the presence of both AC and GP derived ECM (Figure 5.12 C). The precise role of this chemokine in chondrogenesis and osteogenesis has not yet been established, however IL-8, in the presence of bone marrow concentrate, has been shown to upregulate chondrogenic markers in MSCs, while IL-8 alone has also been shown to promote osteoclastogenesis. Neither of the ECM types induced IL-12 or IL-10 cytokine production (Figure 5.12 D & E). Analysis of chemokine expression revealed that GP derived ECM specifically induced expression of the M1 associated chemokines, CXCL9 and CXCL10 (Figure 5.12 F& G). Both AC and GP derived ECM significantly induced expression of the M2 associated chemokine, CCL13 (Figure 5.12 H).

In addition to cytokines and chemokines, the AC and GP derived ECMs enhanced expression of growth factors that are known to be important in the maintenance and regeneration of the source tissue from which they are derived. AC-derived ECM specifically upregulated FGF (Figure 5.13 A) while only GP-derived ECM was found to significantly upregulate mRNA expression of VEGF (Figure 5.13 B). No effect was observed on Ang1 mRNA expression in the presence of LG derived ECM, however both AC-and GP-derived ECMs significantly drove expression of this growth factor (Figure 5.13 C). In order to verify that the macrophage responses were not due to any contaminating

endotoxin, solubilized ECM preparations were tested for lipopolysaccharide (LPS) contamination using the HEK-BlueTM hTLR4 assay system (Invivogen). HEK-blue cells (5 x 10^5 cells/ml) expressing TLR4 were stimulated with LPS (1–100 ng/ml; positive control), or ECM for 24 h. The expression of SEAP which is under the control of NF-κB and AP-1 was tested by incubating cell supernatants with HEK-blue detection medium for 30 min at 37 °C and absorbance was read at 650 nm. Results demonstrate that the concentration of endotoxin (LPS) was below the threshold level for TLR4 activation as determined using the HEK-Blue LPS detection kit (Figure 5.14).

5.3.8 Fabrication of HA and nanoHA functionalised scaffolds.

Given the minimal inflammatory responses to AC-derived ECM, this ECM source was deemed the most appropriate for use as a collagen based scaffold. AC derived scaffolds were functionalized with micron or nano-sized HA particles for use in subsequent in vivo studies. HA and nanoHA particles were incorporated into the scaffolds by mixing with solubilised AC at a 1:1 ratio. Glyoxal was then added to chemically cross-link the collagens before freeze drying. Finally, the freeze-dried scaffolds were physically cross-linked by dehydrothermal (DHT) treatment. This allows for the production of porous and highly elastic ECM derived scaffolds as described previously (369). In order to ensure that HA particles remained in the ECM scaffold post the freeze drying process and that a HA–collagen composite construct was successfully synthesised, SEM imaging with Energy Selective Backscatter (ESB) and Energy Dispersive X-ray (EDX) was performed to analyse compositional contrast and chemical characterisation of the sample, respectively. Imaging of the composite scaffolds revealed particle-like structures at the highest magnification which, when analysed by ESB, revealed phase contrast to the surrounding material, suggesting that there are two different materials in the nHA functionalised scaffold (Figure 5.15 A). This was also the case for the micron HA functionalised scaffolds, where phase contrast using ESB clearly showed the presence of two different materials (Figure 5.15 B). To further confirm the presence of micron and nanoHA particles within the ECM scaffolds, EDX was performed to distinguish individual elements. As calcium and phosphorous are the principal elements of HA, these were chosen for analysis and were found to be almost absent in the ECM scaffolds alone,

however a higher intensity was present in both the HA and nanoHA composite scaffolds (Figure 5.16). Electromagnetic emission spectral analysis to estimate relative abundance revealed peaks (indicated by arrows) for all three elements in the nanoHA composite scaffolds but not the ECM scaffolds alone (Figure 5.17) confirmed the presence of HA particles in the collagen scaffold. Taken together, it was confirmed that HA particle functionalised scaffolds were prepared.

5.3.9 Characterisation of scaffold pore size and mechanical properties.

It has previously been demonstrated by the Kelly lab that porous scaffolds can be fabricated from solubilised articular cartilage ECM which has been cross-linked with glyoxal prior to freeze drying (369). Furthermore, porosity and pore size can be controlled by altering parameters during the freeze-drying process. The freeze-drying process used in this study slowly drops the ambient temperature to -30°C thus forming ice crystals. As the temperature increases slowly to -10°C, the ice crystals melt, creating a porous architecture. As an interconnected pore network is a requirement of a successful scaffold given that it permits cellular infiltration and therefore tissue development, the porosity of the solubilized scaffolds was next assessed. Scanning electron microscopy images demonstrated that both HA and nanoHA functionalised scaffolds retained their internal porous nature after the addition of either HA or nanoHA particles (Figure 5.18 A). Semi-quantitative analysis of SEM imaging revealed that the functionalized scaffolds had an average pore size of 50 µm (Figure 5.18 B) which is in the range suitable for cell infiltration (370, 371). Moreover, the calculated porosity of both scaffold types was in the range of 95-97% (Figure 5.18 C). It was next of interest to mechanically evaluate the various scaffolds to ascertain if incorporation of different particle types can affect the mechanical properties of the resulting scaffolds. Mechanical testing of the scaffolds was performed using uniaxial compression testing and revealed that both scaffold types had comparable mechanical properties, with a Young's modulus of approximately 1.5 kPa for micron HA functionalised scaffolds, while nanoHA functionalised scaffolds had an average value of 2 kPa (Figure 5.18 D). Importantly, incorporation of particles into the scaffolds did not affect their ability to differentially polarize macrophages in vitro, as evidenced by induction of the M1 macrophage marker,

CXCL11, by micron HA functionalized scaffolds and the M2 macrophage marker, MRC1, by nanoHA functionalized scaffolds (Figure 5.19).

5.3.10 Implantation of micron HA but not nanoHA scaffolds drives T cell and neutrophil infiltration in vivo.

In order to translate the in vitro data to a physiologically relevant in vivo system, we characterized the immune response to hydroxyapatite functionalized ECM scaffolds using a rat femoral defect model (221). Functionalized scaffolds were implanted into a 5 mm femoral defect and repair tissue was harvested for analysis 1 week post-implantation. The defect was left empty with no implant as a control. Flow cytometric analysis of immune cell subsets at the defect site revealed no discernible difference in the number of B cells (CD45+ CD19+), but showed significant infiltration of T cells (CD45+CD3+) and neutrophils (CD45+CD11b+Ly6G+), indicative of a more pro-inflammatory microenvironment in tissue samples from rats implanted with micron HA functionalized scaffolds but not nanoHA functionalized scaffolds (Figure 5.20 A-D). There was no significant difference in immune cell infiltration in samples taken outside the defect area (Figure 5.21 A-D). Individual T cell subsets were not assessed as part of this study, however, serum cytokine analysis revealed higher concentrations of the Th1-associated cytokine, IFNy, in the micron HA-treated rats (Figure 5.22 A). Conversely, circulating concentrations of the anti-inflammatory cytokine, IL-10, were higher in the nanoHA group versus the empty defect ($p=0.065$) and significantly higher than the micron HA-treated rats (Figure 5.22 B). Overall, these results indicate that larger micron particles are primarily driving a pro-inflammatory host response.

5.3.11 NanoHA functionalised scaffold promote ant-inflammatory macrophage phenotype in vivo.

Having established immune cell subsets in the response to micron or nanoHA functionalised scaffolds, it was next of interest to determine the macrophage phenotype and functionality at the defect site. Macrophages were gated based on F4/80+/CD11b+ expression and analysis of surface markers associated with M1-like or M2-like macrophage phenotype was assessed. While non-significant, there was a higher

percentage of CCR2+ and CD86+ macrophages in the micron HA functionalised scaffold group compared to both the nanoHA and empty control group, while a significantly higher percentage of cells positive for the anti-inflammatory marker, CX3CR1, was found in the nanoHA scaffold group (Figure 5.23 A). Of note, CX3CR1 is typically expressed by pro-resolution/anti-inflammatory macrophages and is associated with and M2-like phenotype (372, 373). Analysis of the fluorescence intensity of M1/M2 surface markers, as measure by Mean Fluorescence Intensity (MFI), revealed a significant increase in expression of CCR2 and CD86 in macrophages from rats that had been implanted with micron HA functionalized scaffolds, whereas cells from rats implanted with nanoHA-functionalized scaffolds consisted primarily of a large pool of macrophages expressing CX3CR1 (Figure 5.23 B & C). Taken together, this data indicates that micron and nanoHA particles are still capable of polarizing macrophages in vivo, with micron HA driving an M1-like response and nanoHA particles promoting an anti-inflammatory M2-like response.

5.3.12 NanoHA particle functionalised scaffolds promote early vessel formation.

In addition to assessing the immune cell profile 1 week post-scaffold implantation, it was also of interest to assess early tissue repair and tissue architecture. Tissue samples were taken from the defect site and analysed by histology. Haematoxylin and Eosin (H & E) staining at 1 week post implantation demonstrated poor cell infiltration in rats implanted with micron HA functionalized scaffolds, while both empty defect and nanoHA functionalized scaffold groups showed homogenous infiltration of cells into the scaffold and defect site (Figure 5.24 A). Furthermore, we observed a thick fibrous layer consisting of multinucleated cells surrounding the implant in the micron HA scaffold group (Figure 5.24 A (i) and (ii)). This is indicative of fibrous encapsulation which can often occur after construct implantation and prevents infiltrating cells from gaining access to the centre of the defect, ultimately resulting in less extracellular matrix being deposited (201).

Vascularization is also an essential aspect of functional bone tissue regeneration (374). Given the in vitro findings demonstrating enhanced pro-angiogenic responses in

macrophages upon nanoHA stimulation, the capacity of these scaffolds to induce vessel formation was next examined. NanoHA-functionalized scaffolds, but not micron HA-functionalized scaffolds, promoted the formation of vessel-like structures (Figure 5.24 A, lower panel), that stained positively for vWF and α-SMA, indicating the presence of vascular endothelial cells (Figure 5.24 B). This is consistent with previous studies demonstrating that the prolonged presence of inflammatory cytokines impairs angiogenesis (374, 375), while an anti-inflammatory environment can promote angiogenesis and vascularization (376, 377). Furthermore, the presence of vessels in tissue-engineered constructs is particularly important as efficient vascularization in large bone defects still remains a key challenge.

5.3.13 NanoHA but not HA functionalized scaffolds support bone formation following implantation into a rat femoral defect model.

Given the link between inflammation, vascularization and bone regeneration, defect repair and new bone formation was analysed at 4 and 8 weeks post-implantation. µCT analysis was used to assess and quantify new bone formation in the defect site and to determine whether the early differences in inflammatory profile and vessel formation would result in differences in downstream bone formation. At 4 weeks post implantation, the total bone volume in the nanoHA functionalized scaffold group was significantly increased compared to micron HA functionalized scaffolds, which failed to bridge or have any mineral matrix deposition in the defect site (Figure 5.25 A & B). Furthermore, quantitative densitometric analysis revealed a lower bone density (mg HA/cm3) in the micron HA functionalized scaffold group (Figure 5.25 C). A similar profile was observed at 8 weeks, with no bridging observed in the micron HA group, but partial defect repair in the nanoHA scaffold group (Figure 5.25 D). Again, bone volume in the nanoHA group was enhanced, although not significant, while the micron HA group displayed significantly less new bone formation compared to the empty control group (Figure 5.25 E). Similar to the week 4 data, bone density was decreased in the micron HA group (Figure 5.25 F). Taken together, this suggests that nanoHA functionalized scaffolds are capable of supporting mineral matrix deposition in addition to promoting

the formation of vessels at the defect site and are therefore superior to micron HA functionalized scaffolds in the bone regeneration process.

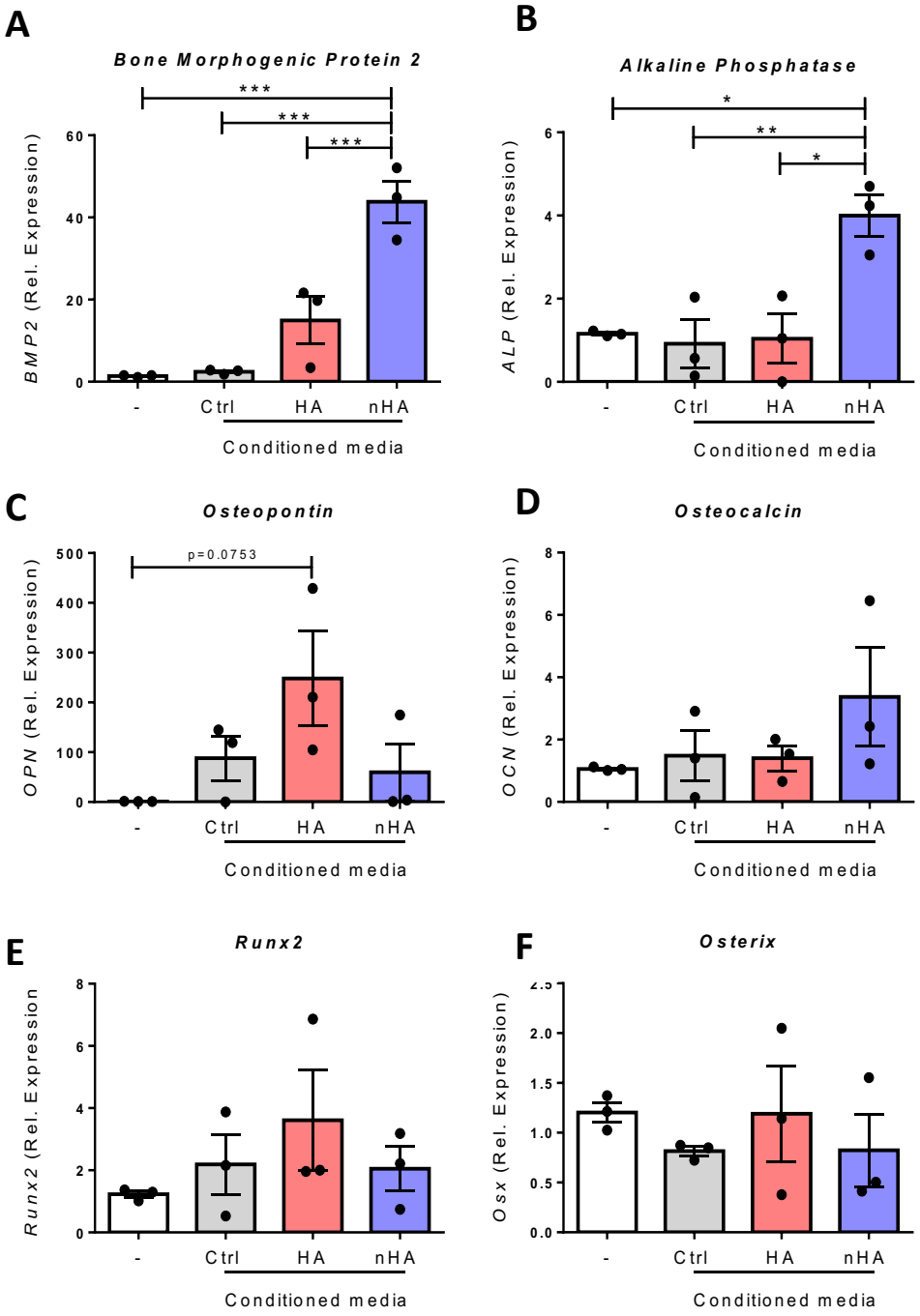

Figure 5.1: Conditioned media from nanoHA treated macrophages upregulates osteogenic genes in human MSCs. Human MSCs (1x 10^5 cells/ml) were cultured in media alone or conditioned media from untreated, micron or nano particle treated macrophages for 48 hours. mRNA levels of **(A)** BMP2, **(B)** ALP, **(C)** Osteopontin, **(D)** Osteocalcin, **(E)** Runx2 and **(F)** Osterix were analysed by real-time PCR. mRNA concentration was normalised to the housekeeping gene GAPDH. Gene expression, relative to media alone (-) control cells, was determined using the $2^{-\Delta\Delta CT}$ algorithm. Pooled data (n=3) is represented as mean ± SEM was analysed using one-way ANOVA with Tukey Post-Test (*p<0.05, **p<0.01, ***p<0.001).

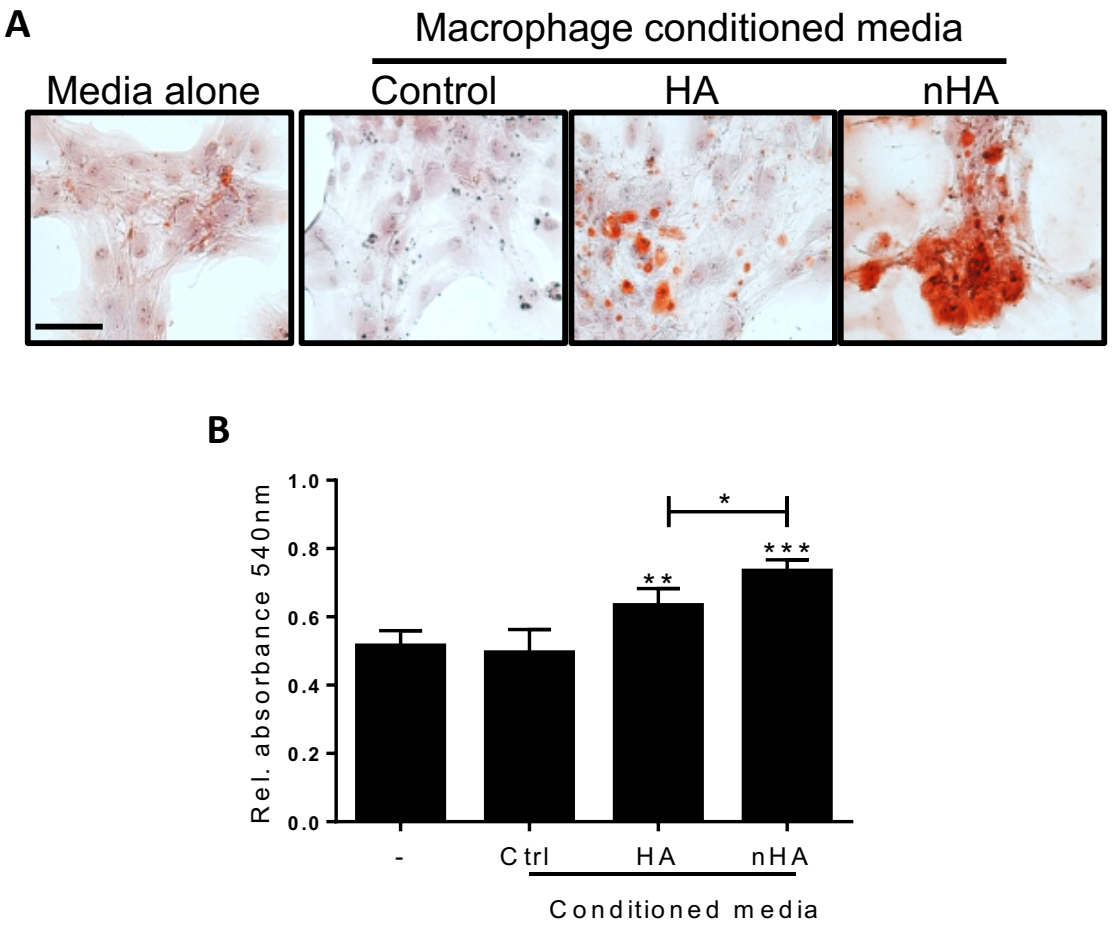

Figure 5.2: Conditioned media from nanoHA (nHA) treated macrophages enhances matrix mineralization of human MSCs. Human MSCs (1 x 10^5 cells/ml) were cultured for 48 hours in media alone or conditioned media from untreated, HA or nanoHA treated macrophages before being cultured for a further 7 days in osteogenic media. **(A)** Cells were then stained with AR and imaged under an inverted microscope. Magnification =20x. Scale bar = 50µm. **(B)** Cells were destained using 10% cetylpyridinium chloride and AR dye was quantified by measuring absorbance at 540 nm. Data (n=3) is represented as mean ± SEM was analysed using one-way ANOVA with Tukey post-test (*p<0.05, **p<0.01, ***p<0.001).

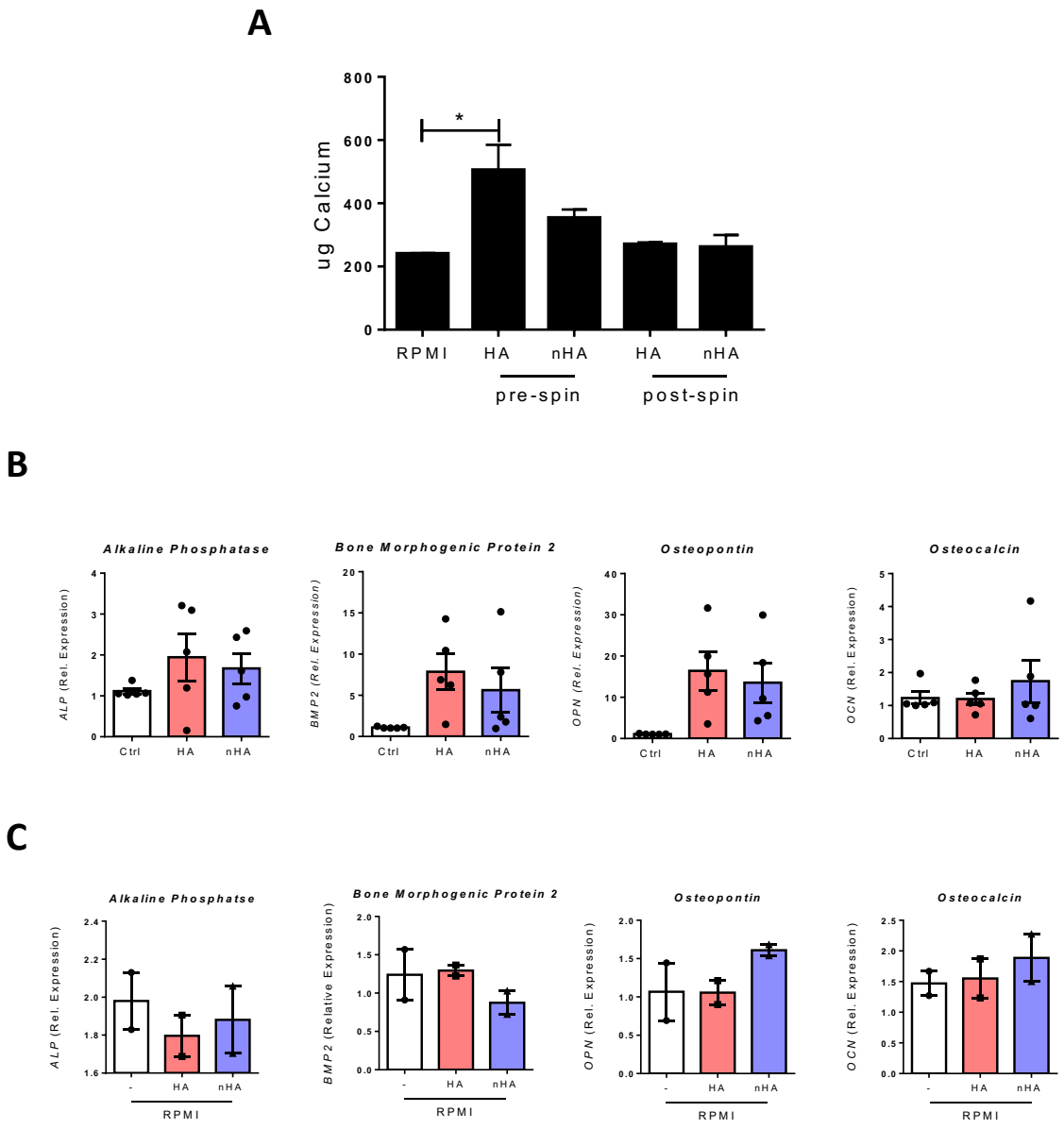

Figure 5.3: Direct effect of particles or material release on MSC osteogenesis. (A) Calcium content in media pre- and post-centrifugation was determined using the o-cresolphthalein complexone (oCPC) method where a violet coloured complex is formed between calcium ions reacting with oCPC246 (Sentinel Diagnostics). **(B)** Human MSCs (1x 10^5 cells/ml) were left untreated or stimulated with micron or nano particles directly for 48 hours. mRNA levels of ALP, BMP2, OPN and OCN were analysed by real-time PCR. **(C)** Human MSCs (1x 10^5 cells/ml) were cultured in media alone or particle conditioned media for 48 hours. mRNA levels of ALP, BMP2, OPN and OCN were analysed by real-time PCR. mRNA concentration was normalised to the housekeeping gene GAPDH. Gene expression, relative to media alone (-) control cells, was determined using the $2^{-\Delta\Delta CT}$ algorithm. Data (n=2-5) is represented as mean ± SEM was analysed using one-way ANOVA with Tukey post-test.

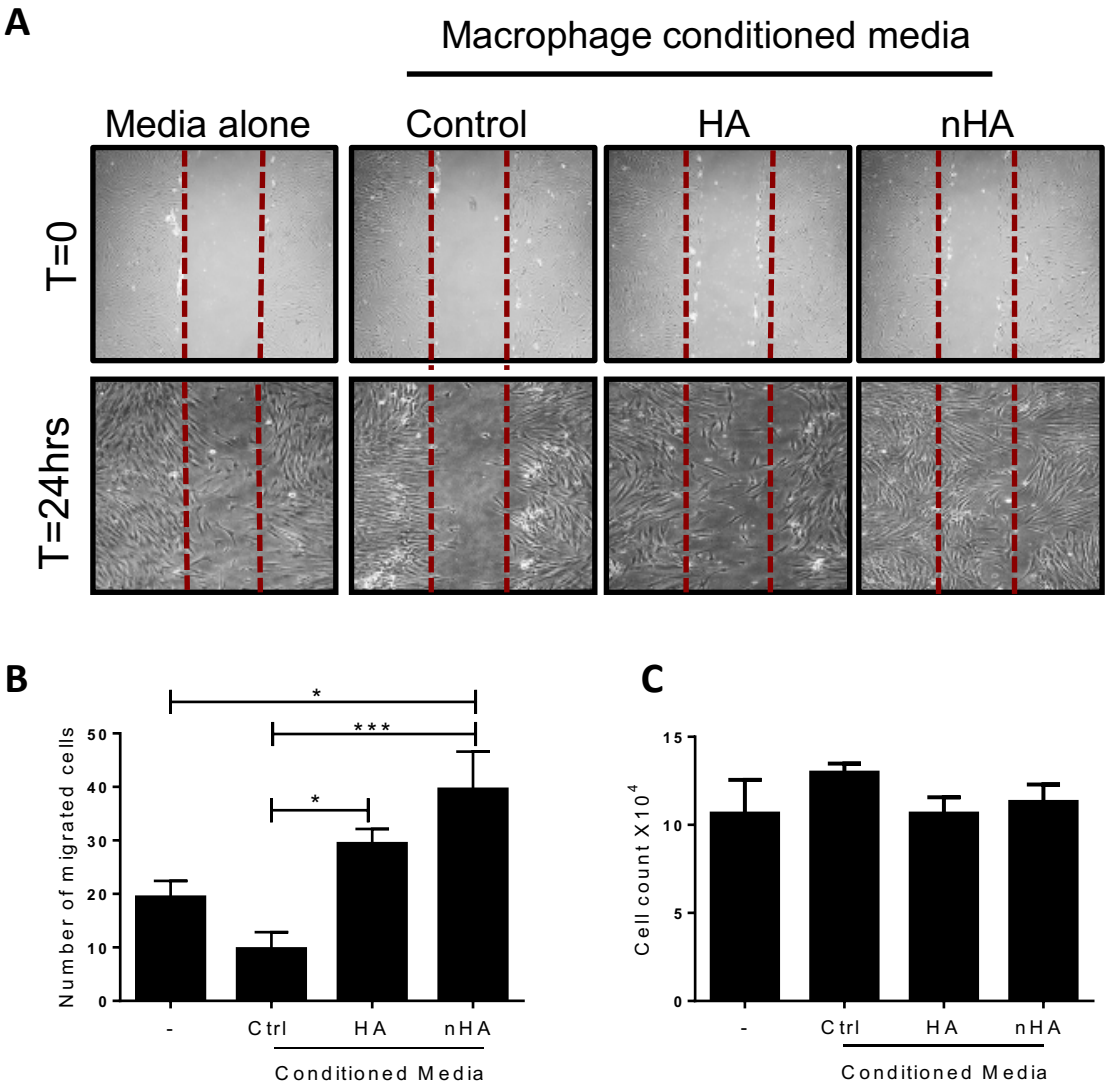

Figure 5.4: NanoHA conditioned media enhances migration of human MSCs. (A) Representative images displaying human MSC migration (at time of induced scratch, T=0 and after 24 hours, T=24) following culture in media alone, or conditioned media from untreated, HA or nanoHA treated macrophages. **(B)** Cells were counted by blinded individuals at 6 pre-determined imaged sites from each healthy donor and a mean value per donor was calculated and plotted. **(C)** Cell count of MSCs after 24 hours of culture in macrophage conditioned media. Data (n=3) is represented as mean ± SEM was analysed using one-way ANOVA with Tukey Post-Test (*p<0.05, ***p<0.001) versus media alone control).

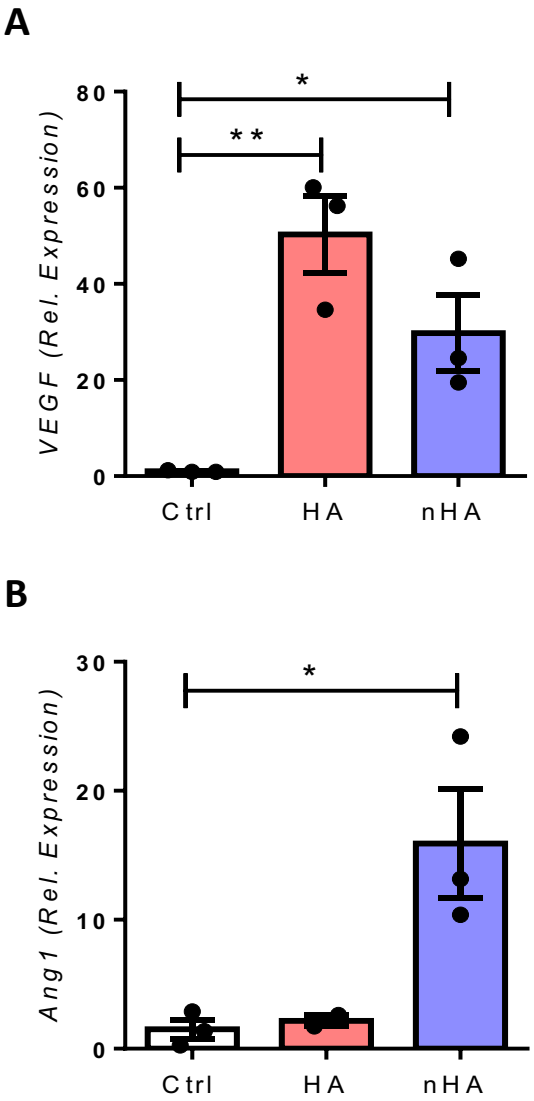

Figure 5.5: HA and nanoHA particles induce differential angiogenic gene expression in primary human macrophages. Primary human macrophages (1 x 10^6 cells/ml) were stimulated with HA or nanoHA particles (250 µg/ml) for 24 hours. mRNA levels of **(A)** VEGF and **(B)** Ang1 were analysed by real-time PCR. mRNA concentration was normalised to the housekeeping gene RPLPO ribosomal RNA. Gene expression, relative to untreated control cells, was determined using the $2^{-\Delta\Delta CT}$ algorithm. Data (n=3) is represented as mean ± SEM was analysed using one-way ANOVA with Tukey Post-Test (*p<0.05, **p<0.01 versus control).

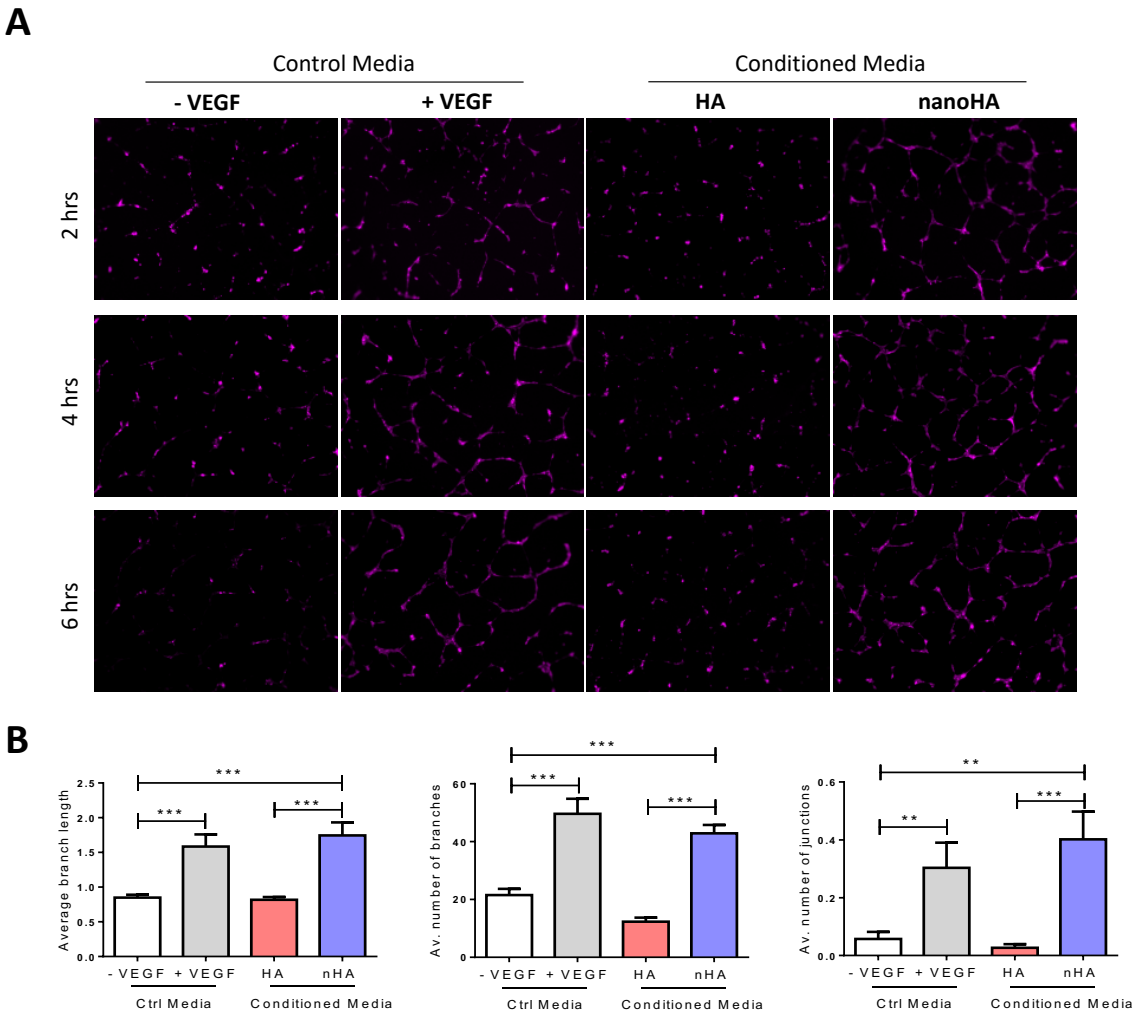

Figure 5.6: NanoHA particles drive endothelial cell tubule formation in human endothelial cells. Fluorescently tagged human umbilical vein endothelial cells (HUVECs) (2 x 10^4) were seeded onto Matrigel coated plates in serum-free control media (EGM-2MV) without or with VEGF (10 ng/ml) as negative and positive controls respectively. Alternatively, cells were seeded in 50% supplemented serum-free conditioned media from micronHA or nanoHA particle treated macrophages. **(A)** Cells were imaged using phase-contrast microscopy every 2 hours to assess endothelial cell tubule formation. **(B)** Average branch length, average number of branches and average number of junctions were quantified using ImageJ. Data (n=2) is represented as mean ± SEM was analysed using one-way ANOVA with Tukey post-test (**p<0.01, ***p<0.001).

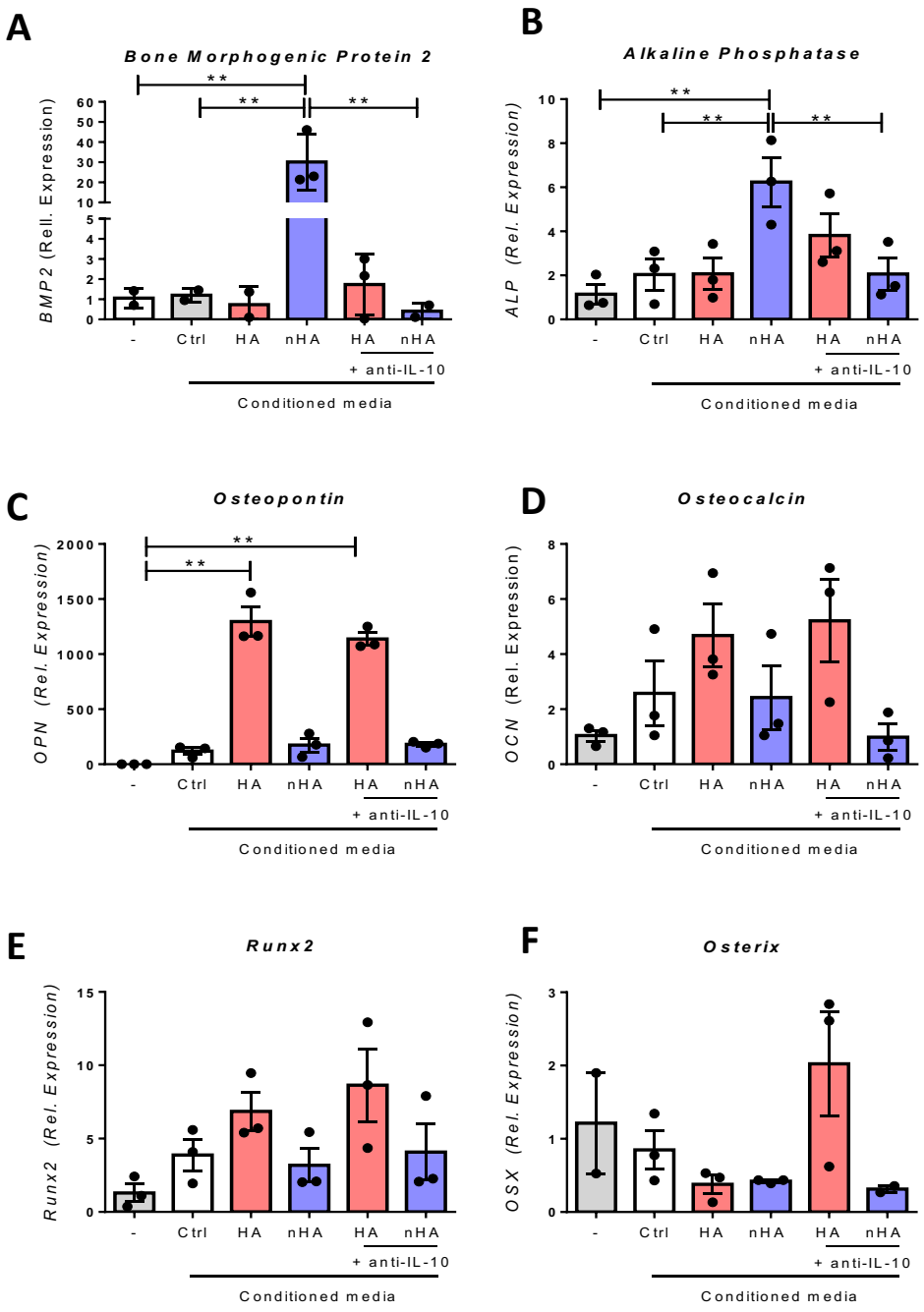

Figure 5.7: Conditioned media from nanoHA treated macrophages drives osteogenesis of human MSCs in an IL-10 dependent manner. Human MSCs (1 x 10^5 cells/ml) were cultured in media alone or conditioned media from untreated, micronHA or nanoHA particle treated (+/- pre-treatment with IL-10 neutralizing antibody (15 ng/ml)) macrophages for 48 hours. mRNA levels of **(A)** Bone Morphogenic Protein 2, **(B)** Alkaline Phosphatase, **(C)** Osteopontin, **(D)** Osteocalcin, **(E)** Runx2 and **(F)** Osterix were analysed by real-time PCR. mRNA concentration was normalised to the housekeeping gene GAPDH. Gene expression, relative to media alone (-) control cells, was determined using the $2^{-\Delta\Delta CT}$ algorithm. Data (n=3) is represented as mean ± SEM was analysed using one-way ANOVA with Tukey Post-Test (*p<0.05, **p<0.01, ***p<0.001).

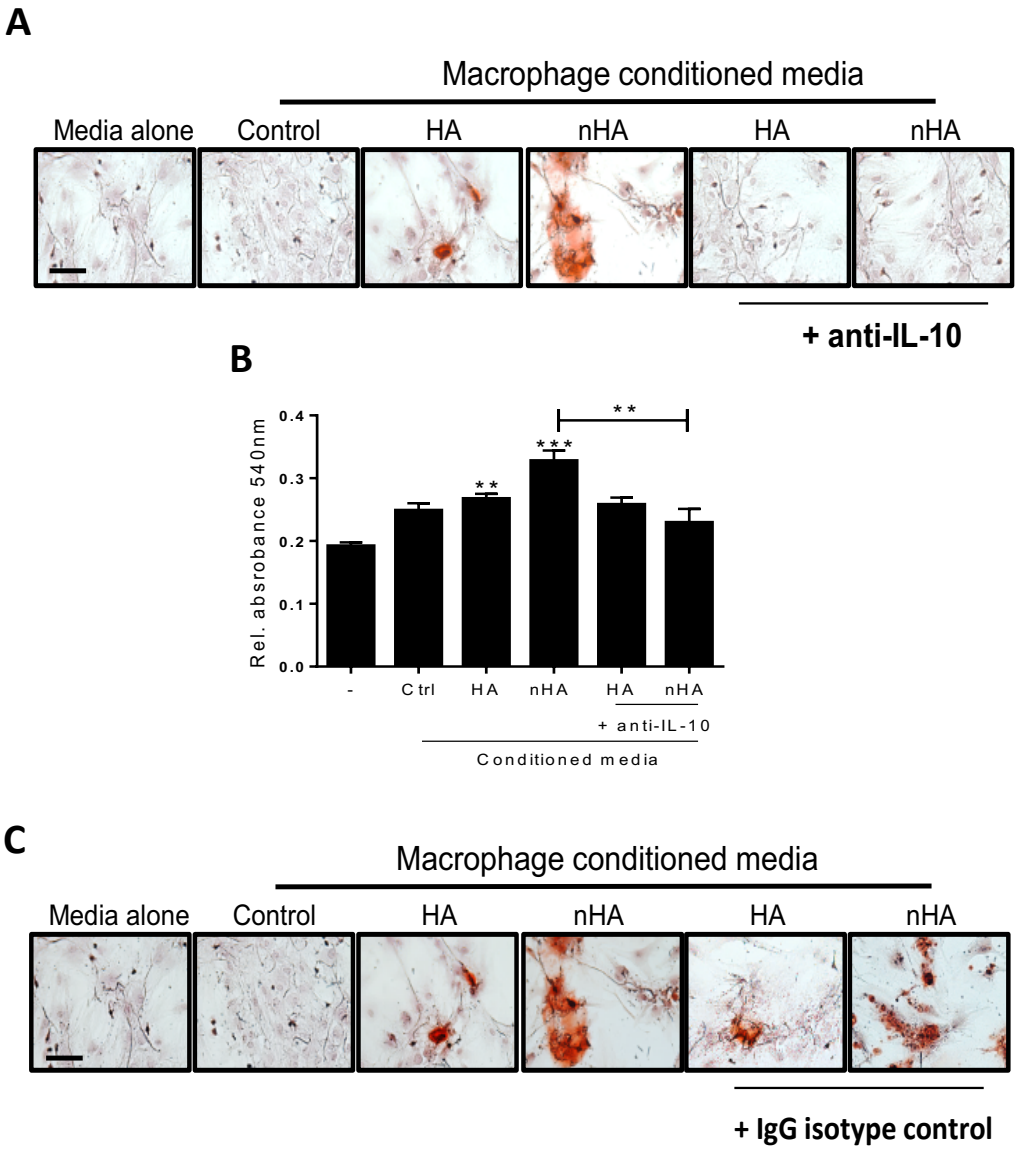

Figure 5.8: Conditioned media from nanoparticle treated macrophages drives mineralization of human MSCs in an IL-10 dependent manner. (A) Human MSCs (1 x 10^5 cells/ml) were cultured in media alone or conditioned media from untreated, micron or nano particle treated (+/- pre-treatment with an IL-10 neutralizing antibody (15 ng/ml)) macrophages for 48 hours before being cultured for a further 7 days in osteogenic media to look at downstream mineralization and calcification. **(A)** Cells were then stained with AR and imaged under an inverted microscope. **(B)** Cells were destained using 10% cetylpyridinium chloride and AR dye was quantified by measuring absorbance at 540nm. **(C)** Human MSCs (1x 10^5 cells/ml) were cultured in media alone or conditioned media from untreated, micron or nano particle treated (+/- pre-treatment with an IgG isotype control antibody) macrophages for 48 hours before being cultured for a further 7 days in osteogenic media assess downstream mineralization and calcification. Cells were then stained with Alizarin red (AR) and imaged under an inverted microscope. Magnification =20x Scale bar = 50 µm. Data (n=3) is represented as mean ± SEM was analysed using one-way ANOVA with Tukey post-test (*p<0.05, **p<0.01, ***p<0.001 versus media alone control).

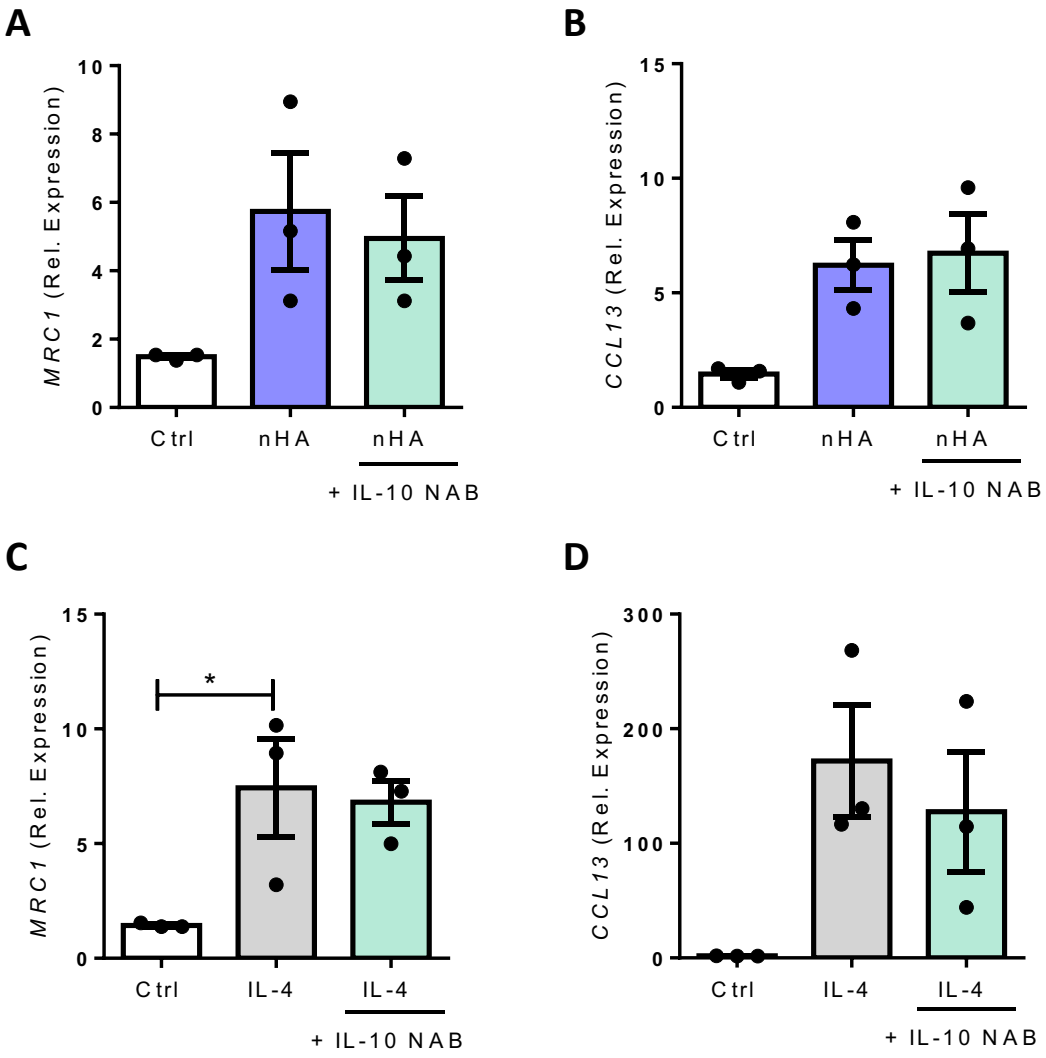

Figure 5.9: Neutralization of IL-10 does not affect nanoHA-induced M2 macrophage polarization. Primary human macrophages (1 x 10^6 cells/ml) were stimulated with nano particles alone or in the presence of an IL-10 neutralizing antibody (15 ng/ml) for 24 hours. mRNA levels of **(A)** MRC1 or **(B)** CCL13 were analysed by real-time PCR. As an alternative M2 polarizing stimulus, cells were stimulated with IL-4 (20 ng/ml) alone or in the presence of an IL-10 neutralizing antibody (15 ng/mL) for 24 hours. mRNA levels of **(C)** MRC1 or **(D)** CCL13 were analysed by real-time PCR. mRNA concentration was normalised to the housekeeping gene 18s Ribosomal RNA. Gene expression, relative to untreated control cells, was determined using the $2^{-\Delta\Delta CT}$ algorithm. Data (n=3) is represented as mean ± SEM was analysed using one-way ANOVA with Tukey post-test *p<0.05.

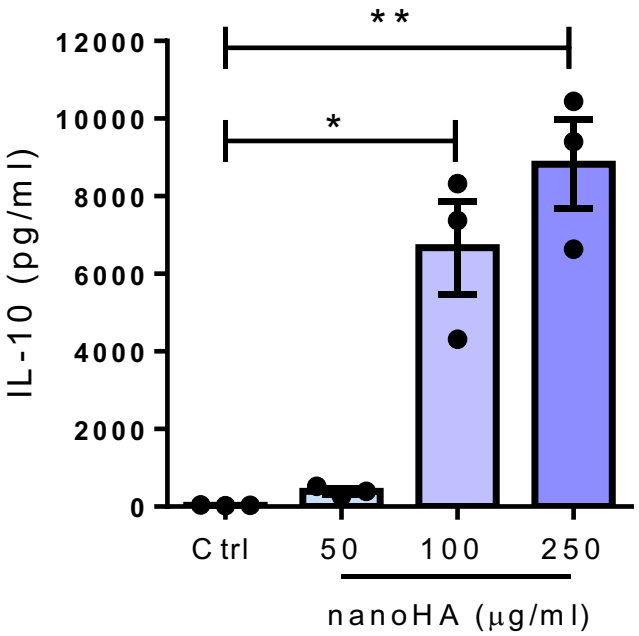

Figure 5.10: nanoHA particles drive IL-10 cytokine secretion in a dose-dependent manner. Primary human macrophages (1x 10^6 cells/ml) were stimulated with nanoHA (50, 100 or 250 µg/ml) for 24 hours. Cytokine production of cell supernatants was analysed by ELISA. Data (n=3) is represented as mean ± SEM was analysed using Kruskal Wallis with Dunn's post-test (*p<0.05, **p<0.01).

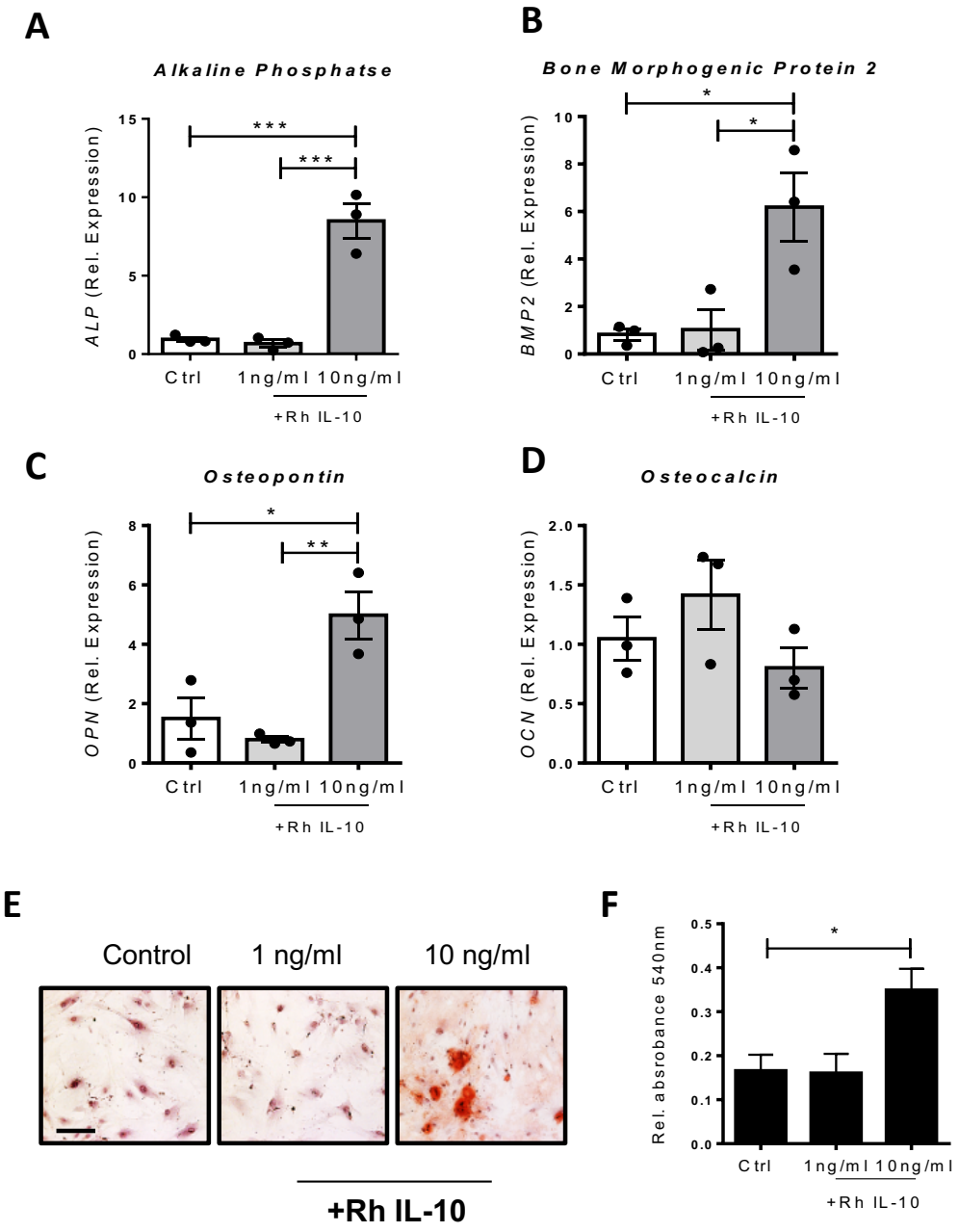

Figure 5.11: Supplementation of recombinant IL-10 to culture media drives osteogenic responses in human MSCs. Human MSCs (1x 10^5 cells/ml) were treated with recombinant human (Rh) IL-10 (1 ng/ml or 10 ng/ml) for 48 hours and mRNA levels of **(A)** Alkaline Phosphatase, **(B)** Bone Morphogenic Protein 2, **(C)** Osteopontin and **(D)** Osteocalcin were analysed by real-time PCR. mRNA concentration was normalised to the housekeeping gene GAPDH. Gene expression, relative to untreated control cells, was determined using the $2^{-\Delta\Delta CT}$ algorithm. **(E)** Standard expansion media for human MSCs was supplemented with Rh IL-10 (1 ng/ml or 10 ng/ml) and calcification as assessed by Alizarin Red staining was measured at day 7. Magnification = 20 x, Scale bar = 50µm. **(F)** Cells were destained using 10% cetylpyridinium chloride and AR dye was quantified by measuring absorbance at 540 nm. Data (n=3) is represented as mean ± SEM was analysed using one-way ANOVA with Tukey post-test (*p<0.05, **p<0.01, ***p<0.001).

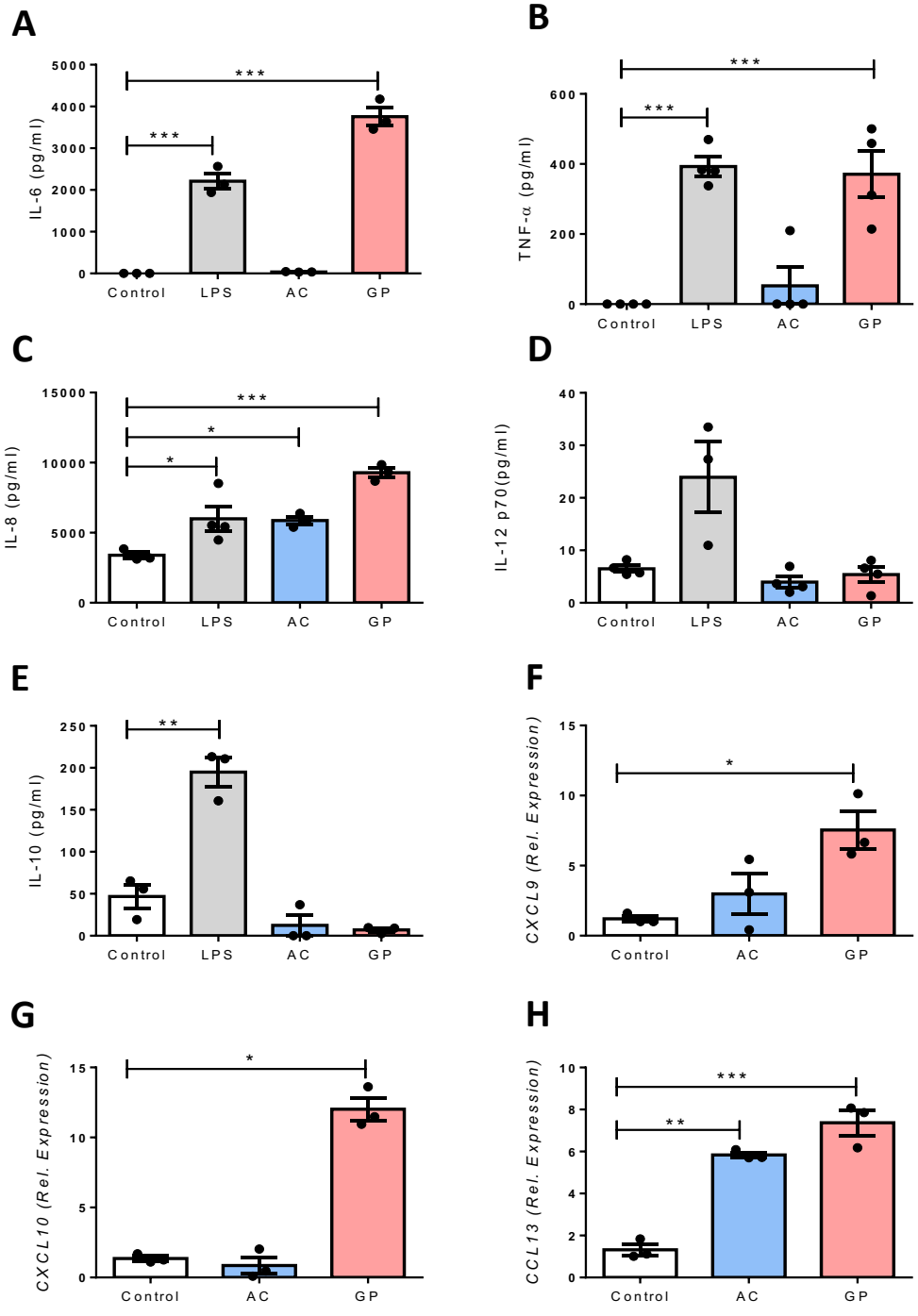

Figure 5.12: ECM derived from difference musculoskeletal tissue sources drive differential cytokine and chemokine responses in primary human macrophages. Primary human macrophages (1 x 10^6 cells/ml) were treated with solubilized ECM (GP or AC), or LPS (100 ng/ml) as a positive control for 24 hours. Cytokine levels of **(A)** IL-6, **(B)** TNFα **(C)** IL-8, **(D)** IL-12 and **(E)** IL-10 in cell supernatants were measured by ELISA. mRNA expression levels of **(F)** CXCL9, **(G)** CXCL10 and **(H)** CCL13 were analysed by real-time PCR. mRNA concentration was normalised to the housekeeping gene 18s Ribosomal RNA. Gene expression, relative to untreated control cells, was determined using the $2^{-\Delta\Delta CT}$ algorithm. Pooled data (n=3) is represented as mean ± SEM was analysed using one-way ANOVA with Tukey Post-Test (*p<0.05, **p<0.01, ***p<0.001).

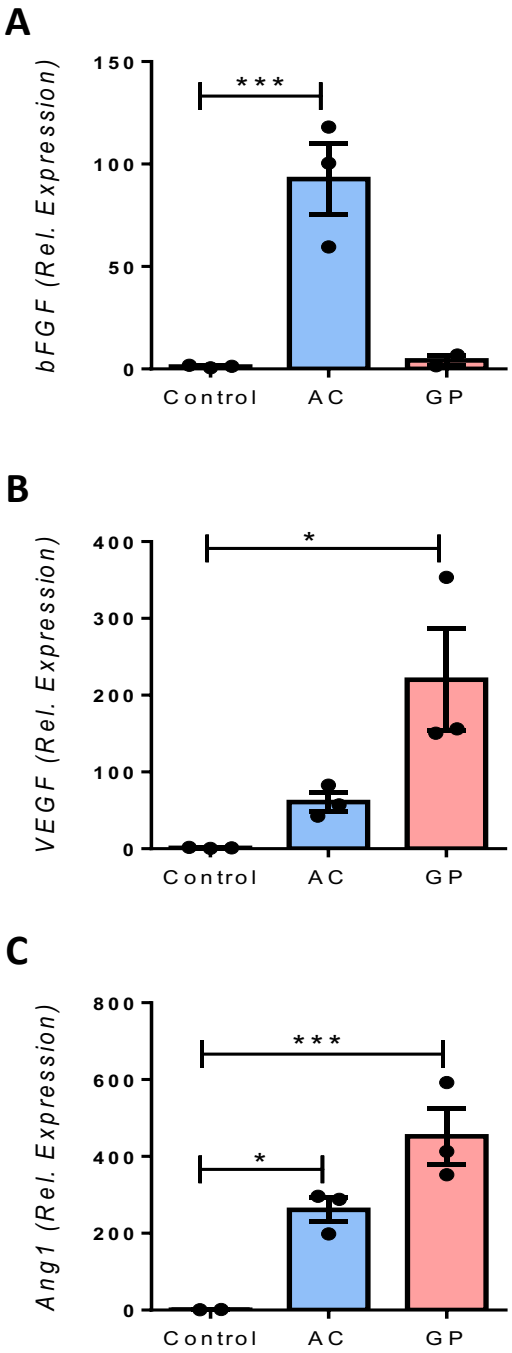

Figure 5.13: ECM derived from difference musculoskeletal tissue sources drive differential growth factors in primary human macrophages. Primary human macrophages (1 x 10^6 cells/ml) were treated with solubilized ECM (LIG, GP or AC), or LPS (100 ng/ml) as a positive control for 24 hours. mRNA expression levels of **(A)** bFGF, **(B)** VEGF and **(C)** Ang1 were analysed by real-time PCR. mRNA concentration was normalised to the housekeeping gene 18s Ribosomal RNA. Gene expression, relative to untreated control cells, was determined using the $2^{-\Delta\Delta CT}$ algorithm. Pooled data (n=3) is represented as mean ± SEM was analysed using one-way ANOVA with Tukey Post-Test (*p<0.05, **p<0.01, ***p<0.001).

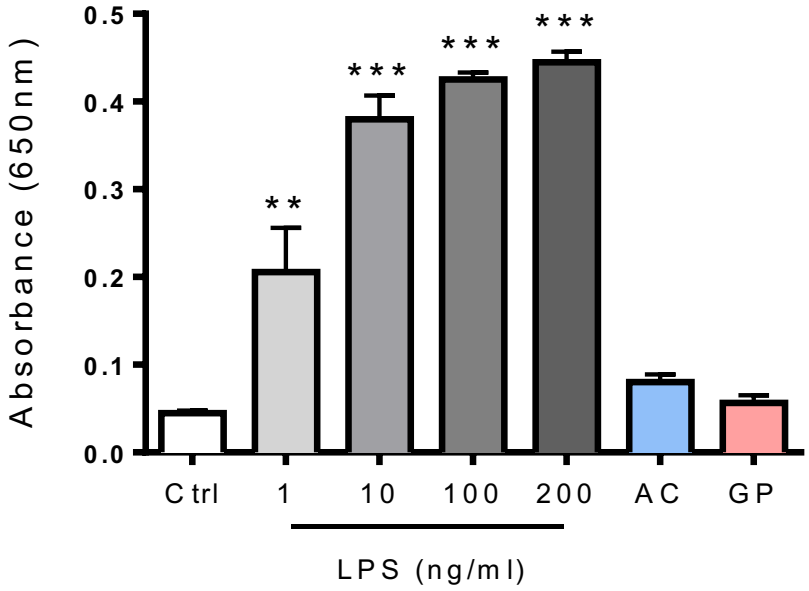

Figure 5.14: Solubilised ECM preparations are not contaminated with endotoxin. ECM preparations were shown to be endotoxin free, using the HEK-BlueTM hTLR4 assay system (Invivogen). The expression of SEAP, as measured by absorbance at 650nm, by ECM treated macrophages was comparable to untreated control cells. As a positive control, cells were treated with LPS (1 ng/ml, 10 ng/ml, 100 ng/ml or 200 ng/ml). Pooled data (n=2) is represented as mean ± SEM was analysed using one-way ANOVA with Tukey Post-Test (**p<0.01, ***p<0.001).

A

B

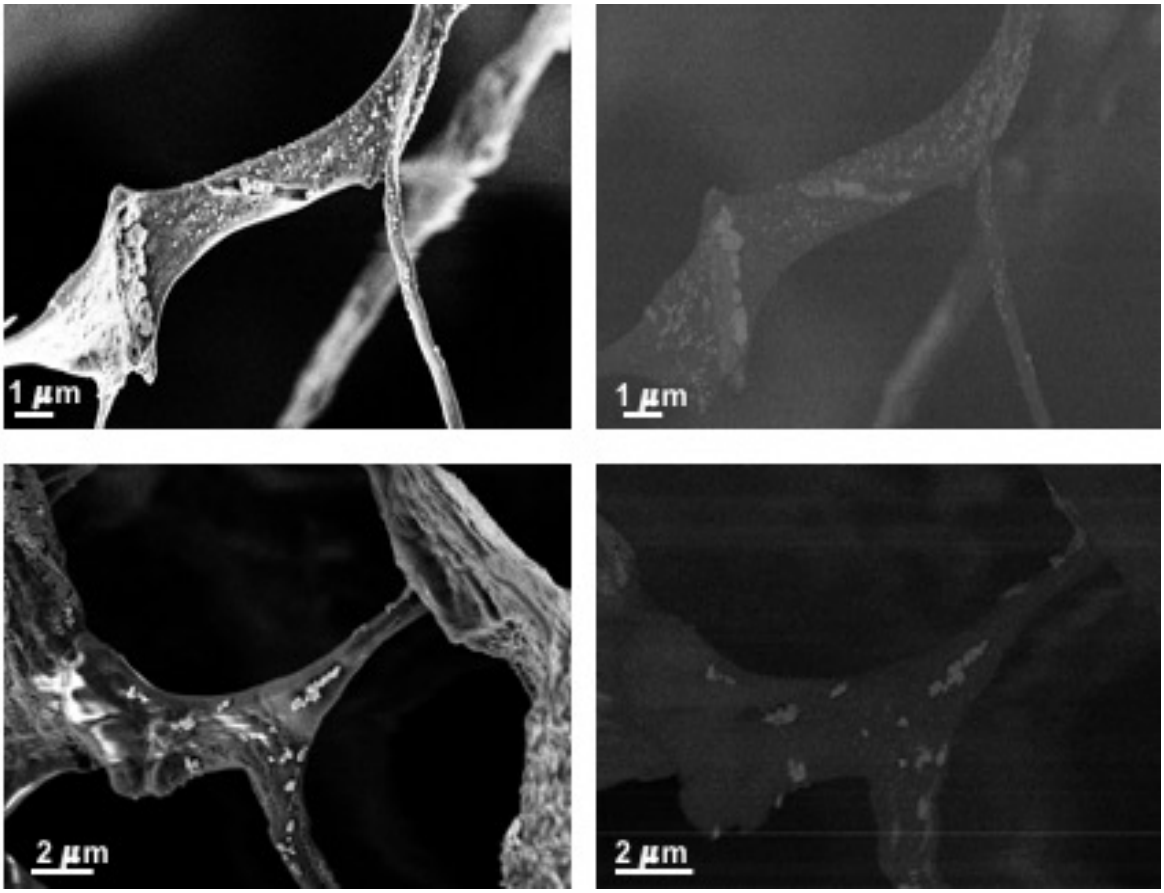

5.15: Characterisation of HA and nanoHA functionalised scaffolds. (Left) High magnification SEM images of **(A)** nanoHA or **(B)** micron HA functionalised scaffolds. (**Right)** SEM with energy selective backscatter (ESB) backscatter electron detector of scaffolds functionalised with **(A)** nanoHA or **(B)** micron HA particles. Images were obtained using a Zeiss Ultra Plus (Zeiss, Germany) with an acceleration voltage of 2kV and working distance of 5mm.

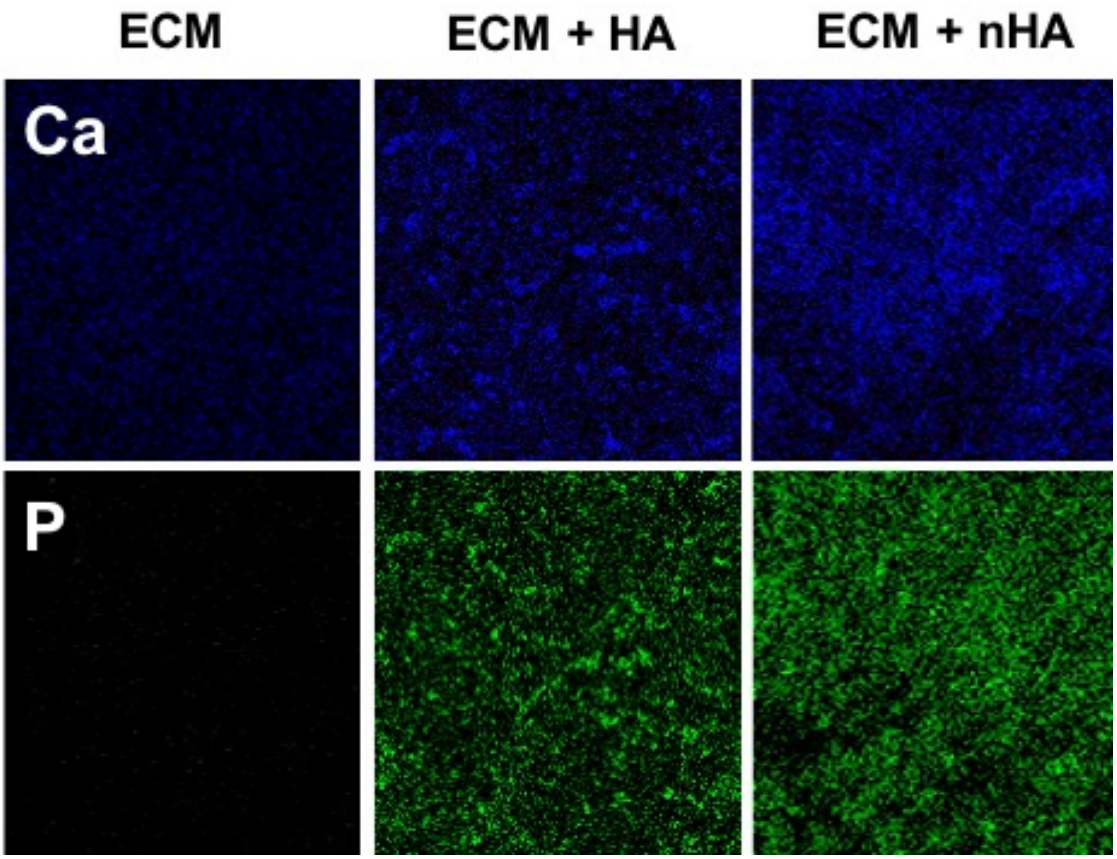

Figure 5.16: Hydroxyapatite particles remain in the ECM scaffold after the freeze-drying process. Representative Energy-dispersive X-ray spectroscopy (EDX) images of ECM scaffolds (+/- HA or nanoHA particles). Images were obtained using a Zeiss Ultra Plus (Zeiss, Germany) with an EDX detector with an acceleration voltage of 2kV and working distance of 5mm. (Ca=Calcium, P=Phosphorous)

A

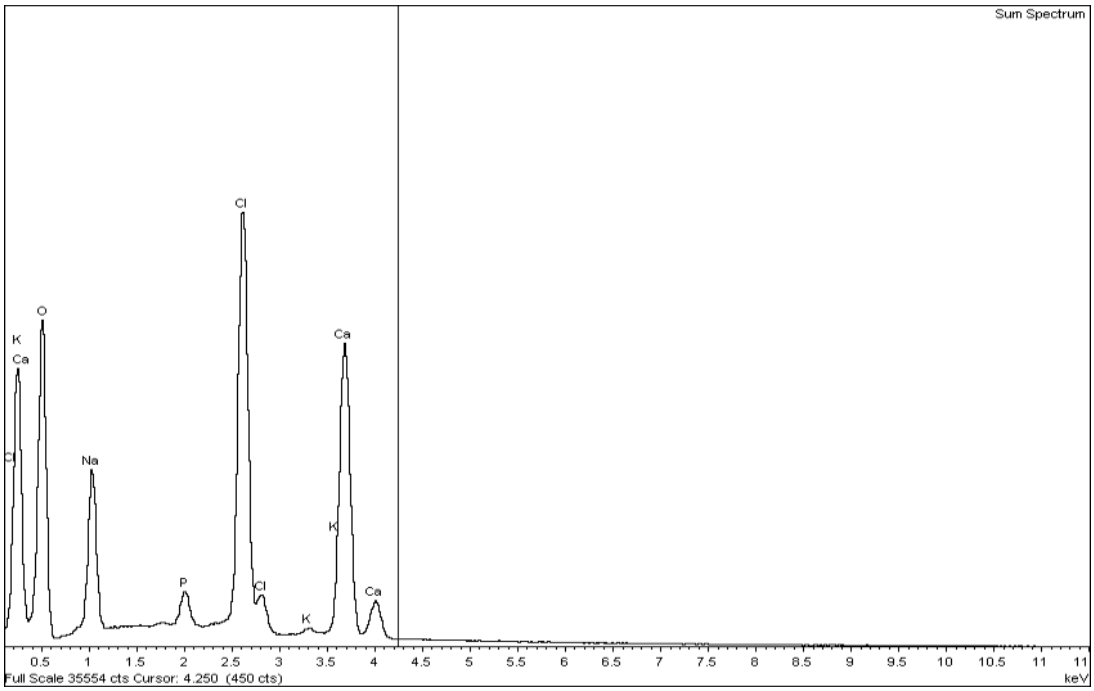

B

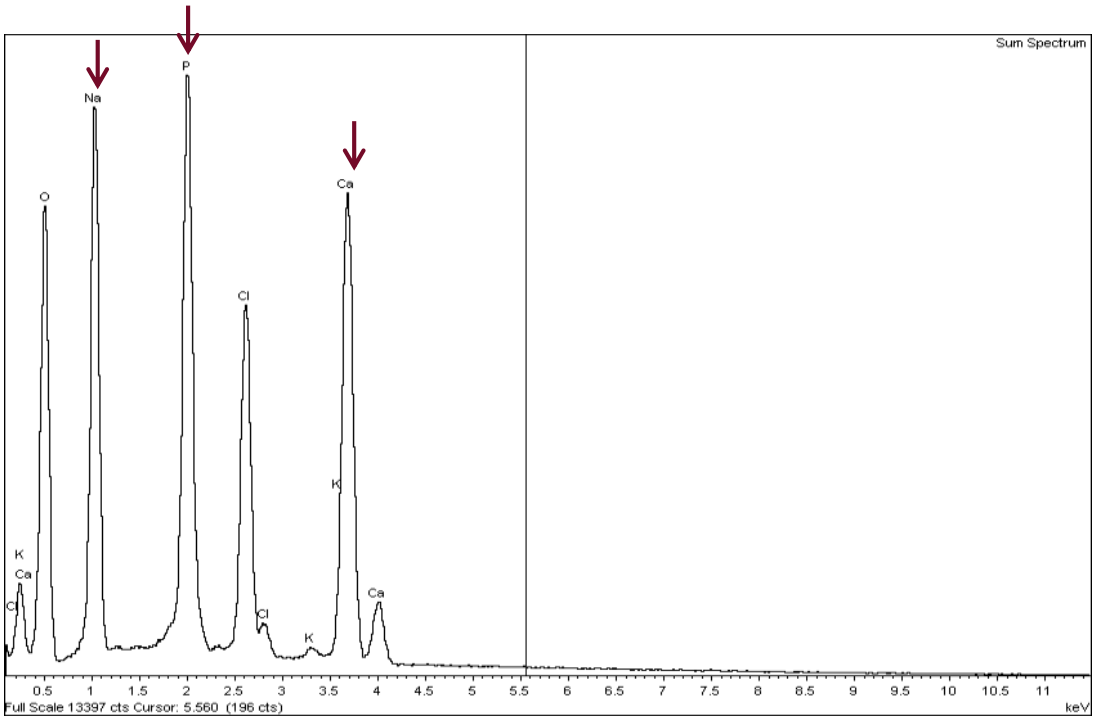

Figure 5.17: nanoHA particles remain in the ECM scaffold after the freeze drying process. EDX spectrum of chemical composition of ECM scaffolds (**A**: without nanoHA, **B**: with nanoHA).

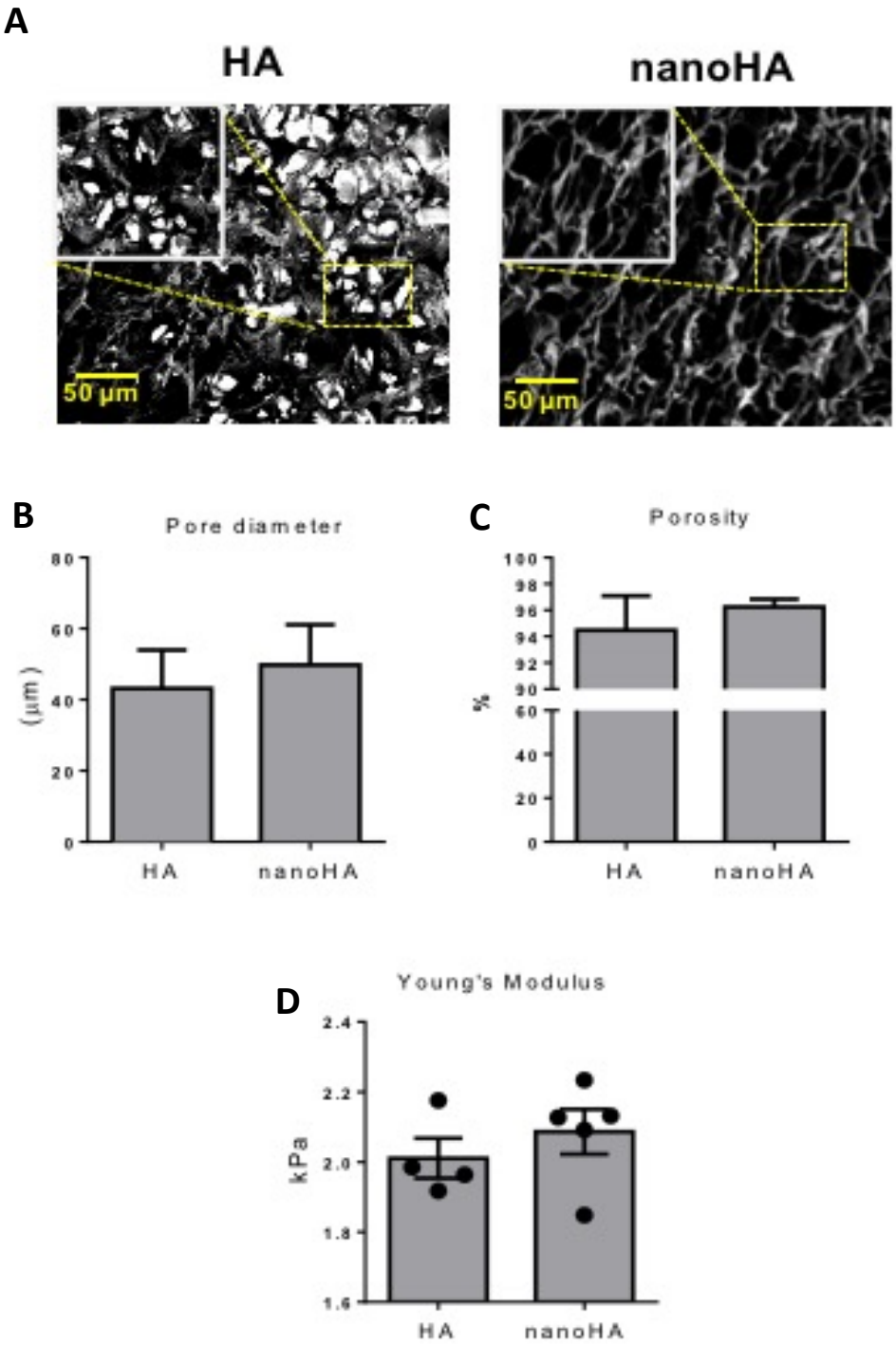

5.18: Characterisation of scaffold pore size and mechanical properties. (A) Scanning Electron Micrograph images of micron HA or nanoHA functionalised ECM scaffolds. **(B)** Scaffold pore size after functionalization was measured using Image J software. **(C)** Scaffold porosity was determined by gravimetry. **(D)** Mechanical strength was determined by uniaxial compression test. Data is represented as mean ± SEM was analysed using one-way ANOVA with Tukey Post-Test.

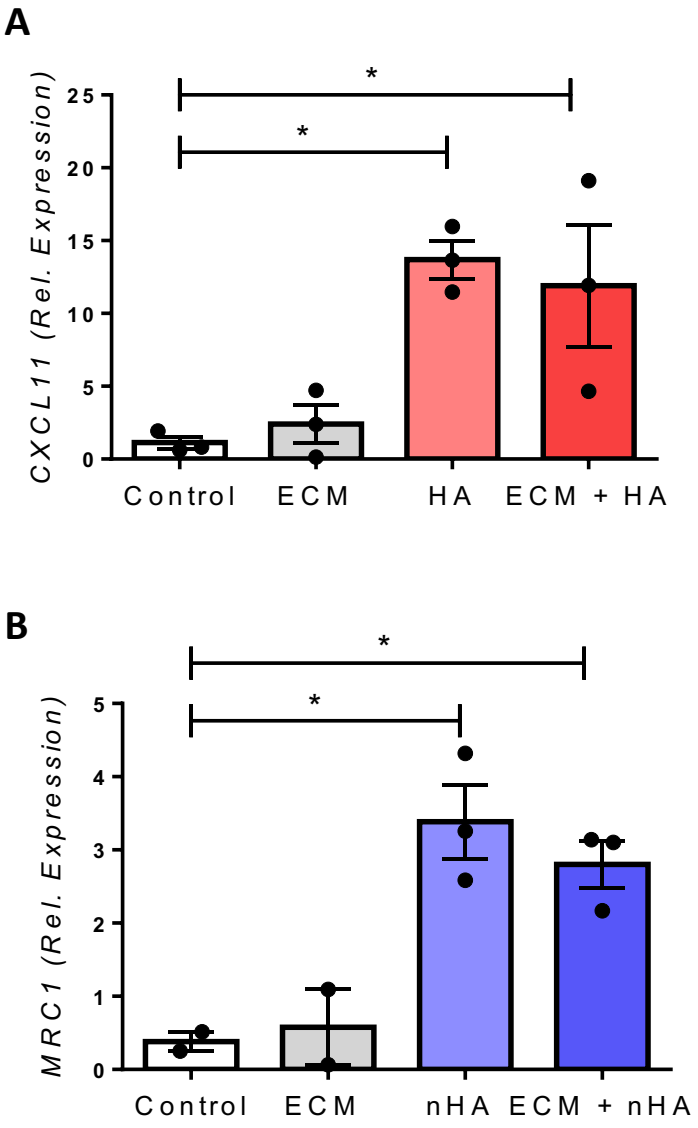

Figure 5.19: Particle functionalised scaffolds are capable of driving macrophage polarization. Primary human macrophages (1x 10^6 cells/ml) were stimulated with micron or nano particle functionalized ECM scaffolds for 24 hours. mRNA levels of **(A)** CXCL11 and **(B)** MRC1 were analysed by real-time PCR. mRNA concentration was normalised to the housekeeping gene 18s Ribosomal RNA. Gene expression, relative to untreated control cells, was determined using the $2^{-\Delta\Delta CT}$ algorithm. Pooled data (n=3) is represented as mean ± SEM was analysed using one-way ANOVA with Tukey Post-Test (*p<0.05).

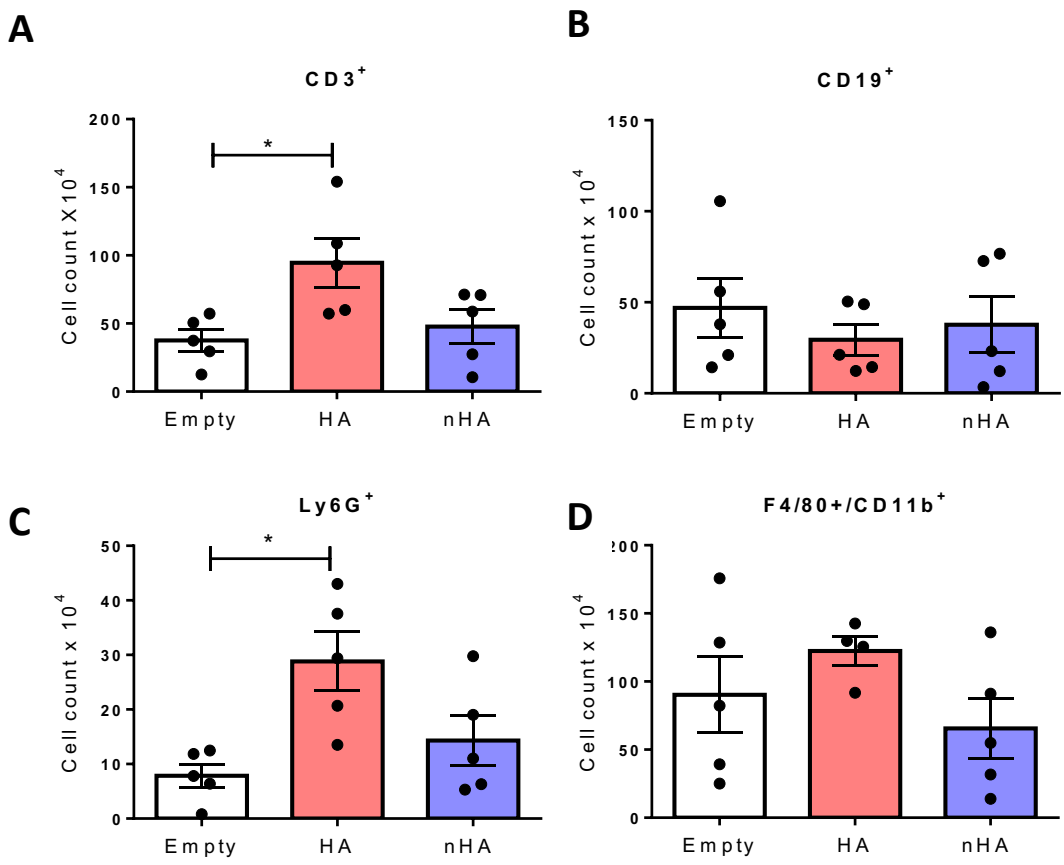

Figure 5.20: Characterization of immune cell subsets and phenotype following implantation of hydroxyapatite functionalized scaffolds into a rat femoral defect model. HA or nanoHA functionalised scaffolds were implanted into a 5mm rat femoral defect, or defect was left empty with no implant as a control. Tissue was harvested 1 week post implantation, digested and cells analysed by flow cytometry. **(A)** CD3+ T cells, **(B)** CD19+ B cells, **(C)** Ly6G+ neutrophils and **(D)** CD11b+/F4/80 macrophages were identified by flow cytometry. Statistical differences on n=5 rats were assessed using Kruskal Wallis test with Dunn's post-test (*p<0.05).

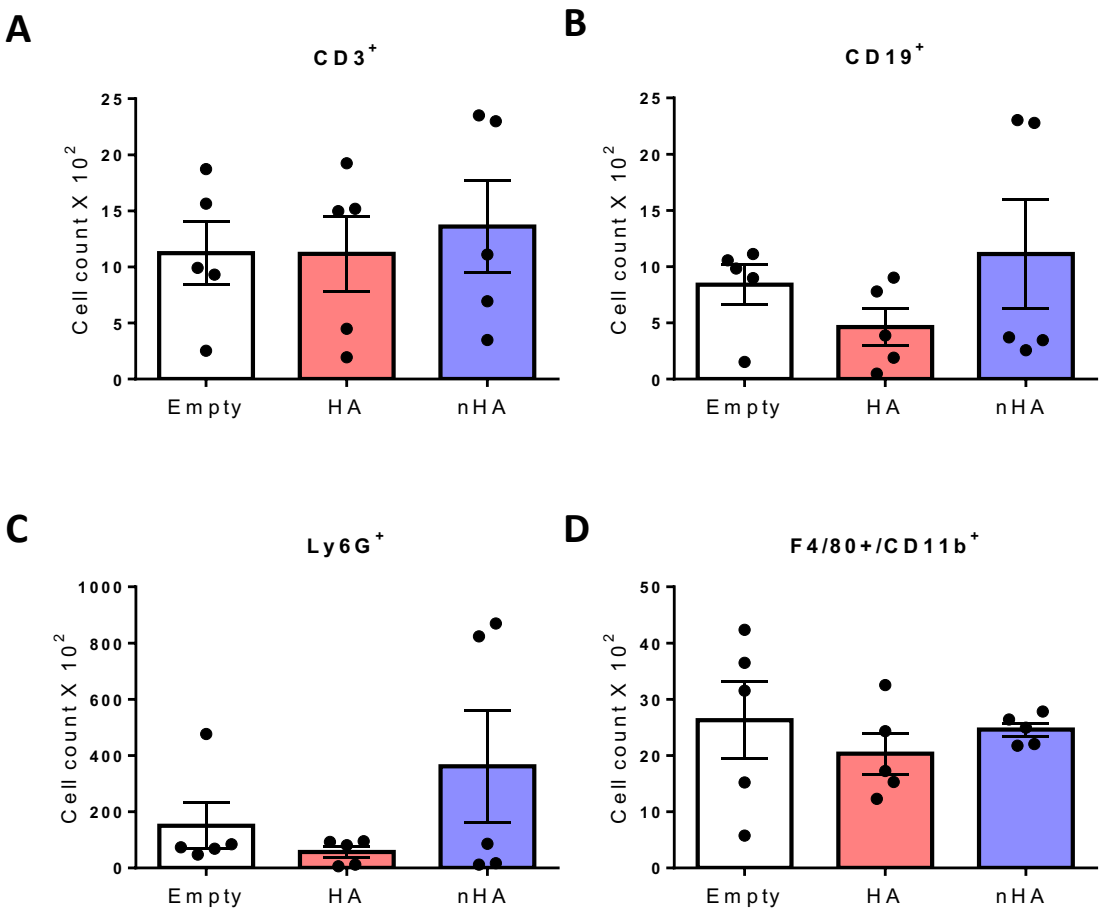

Figure 5.21: Flow cytometric analysis of immune cell subsets outside the defect site 1 week after implantation. Outer tissue surrounding the defect site was isolated and digested. **(A)** CD3+ T cells, **(B)** CD19+ B cells, **(C)** Ly6G+ neutrophils and **(D)** CD11b+/F4/80 macrophages were identified by flow cytometry. Statistical differences on n=5 rats were assessed using Kruskal Wallis test with Dunn's post-test.

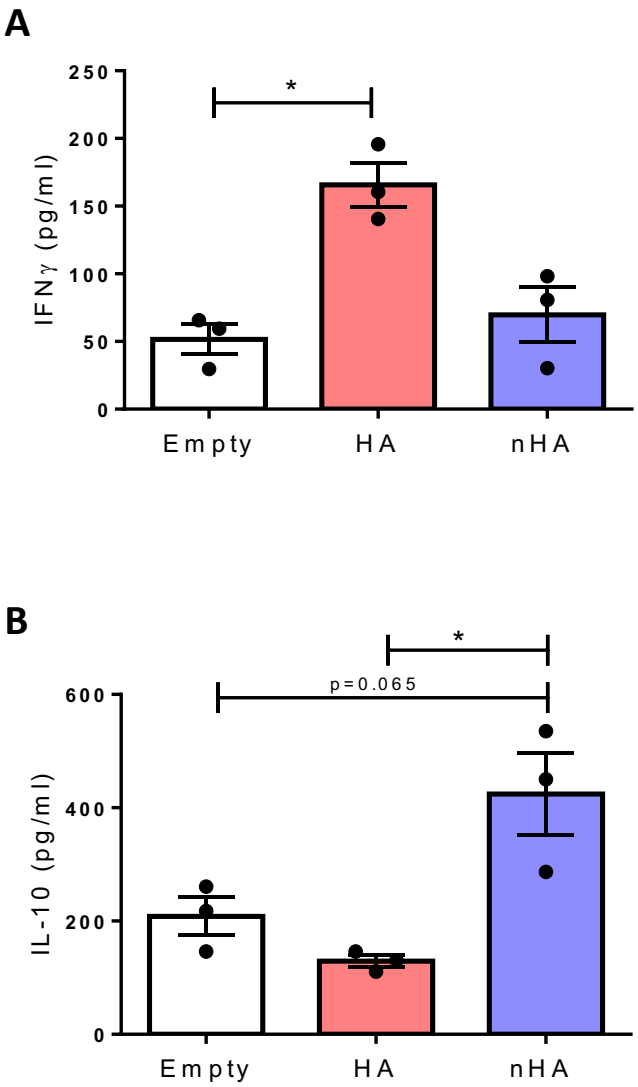

Figure 5.22: Characterization of immune cell subsets and phenotype following implantation of hydroxyapatite functionalized scaffolds into a rat femoral defect model. HA or nanoHA functionalised scaffolds were implanted into a 5mm rat femoral defect, or defect was left empty with no implant as a control. Cardiac punctures were performed 1 week post implantation and serum was isolated from blood samples. **(A)** IL-10 and **(B)** IFNγ cytokine levels were by ELISA. Statistical differences on n=5 rats were assessed using Kruskal Wallis test with Dunn's post-test (*p<0.05).

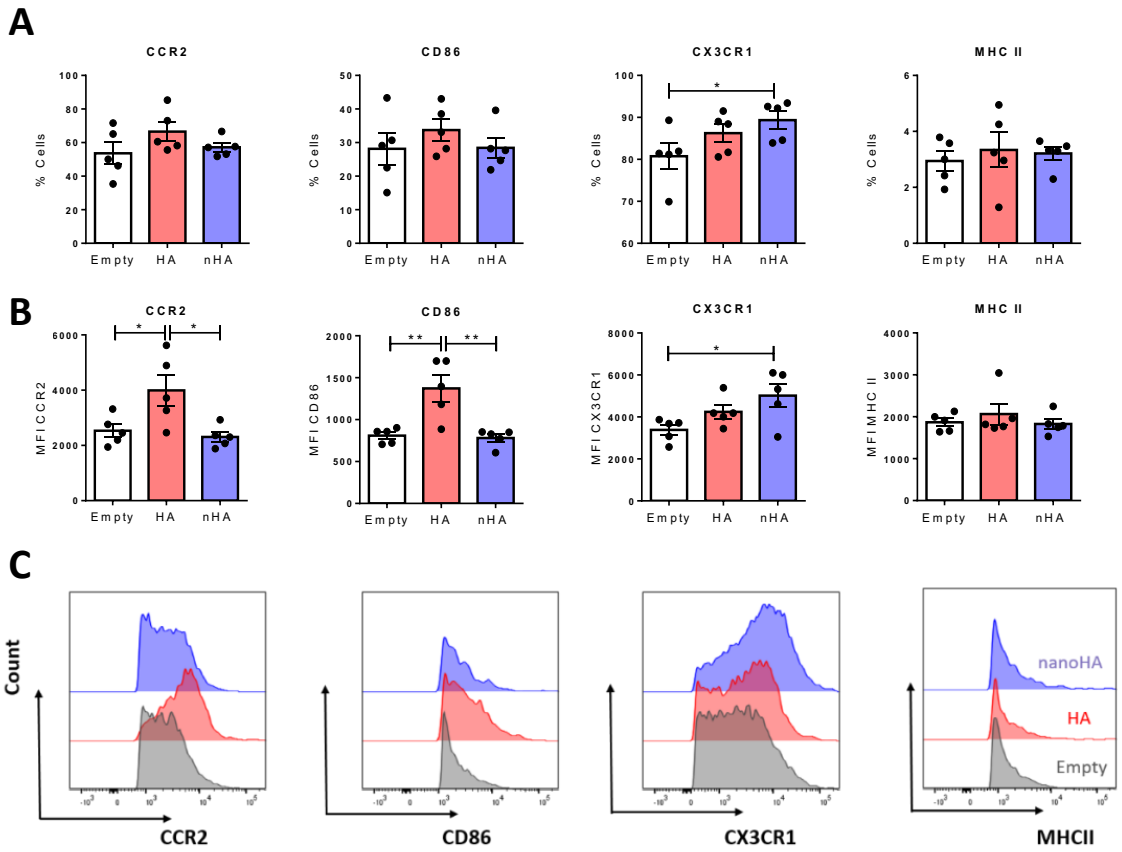

Figure 5.23: Characterization of macrophage phenotype following implantation of hydroxyapatite functionalized scaffolds into a rat femoral defect model. HA or nanoHA functionalised scaffolds were implanted into a 5mm rat femoral defect, or defect was left empty with no implant as a control. Tissue was harvested 1 week post implantation, digested and macrophage populations at defect site were analysed by flow cytometry. Macrophages were gated as F4/80+/CD11b+ and their phenotype assessed by surface marker expression. **(A)** Percentages of macrophages expressing CCR2, CD86, CX3CR1 and MHCII. **(B)** Mean Fluorescence intensity (MFI) for CCR2, CD86, CX3CR1 and MHCII **(C)** with representative histograms of each marker. Statistical differences on n=5 rats were assessed using Kruskal Wallis test with Dunn's post-test (*p<0.05, **p<0.01).

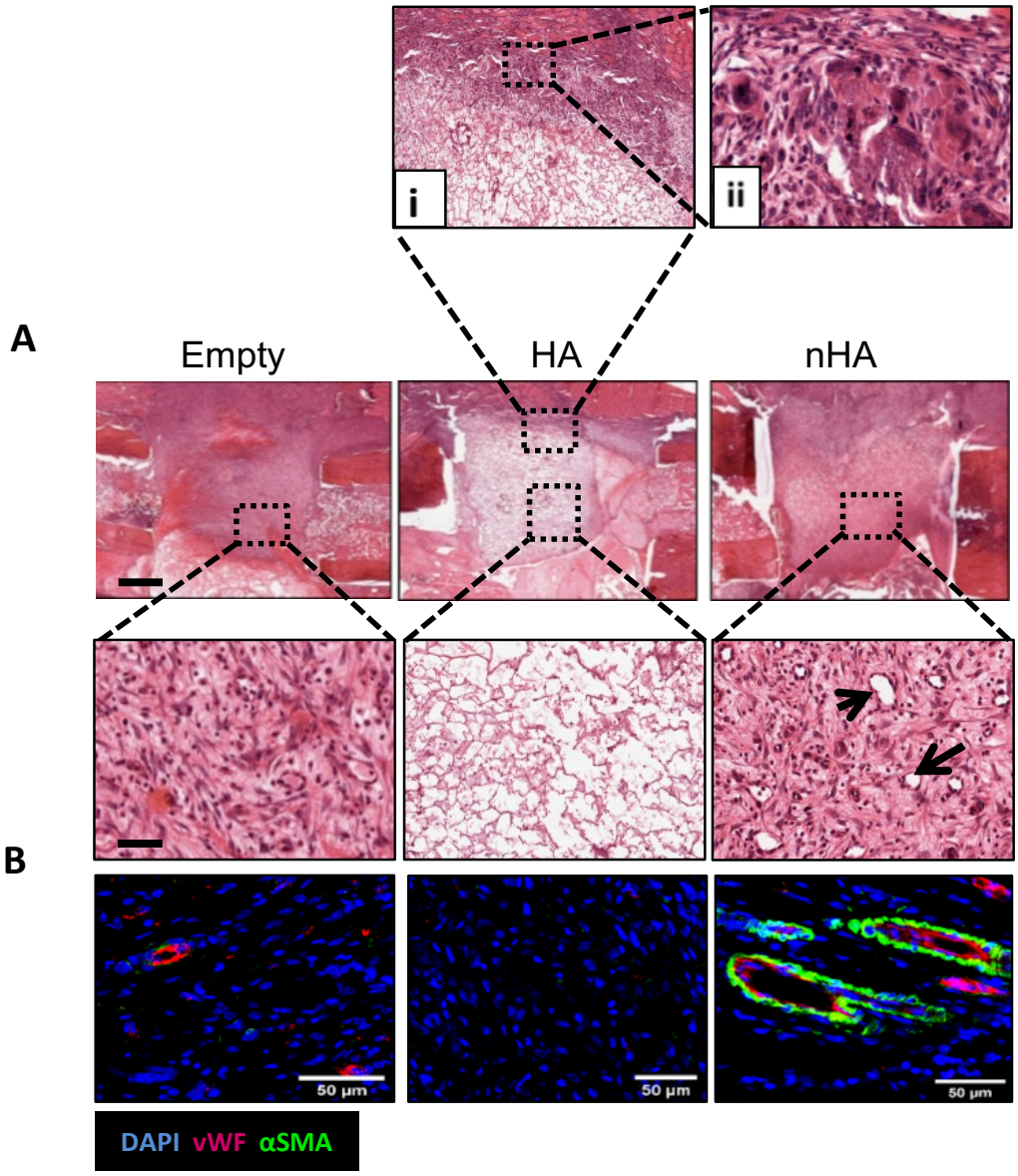

Figure 5.24: Nanoparticle functionalized scaffolds promote early vessel formation following implantation into a rat femoral defect model. (A) Representative images of low magnification H & E stained tissue at the defect site 1 week post implantation. Images taken at 2 x (upper panel, scale-bar 1 mm) and 10 x (lower panel, scale-bar 200 µm). Arrows indicate the presence of vessel like structures. High magnification of H & E stained samples showing fibrous encapsulation (i) and multinucleated cell formation (ii) **(B)** Representative images of vessel formation 1 week post-implantation. Von Willibrand factor (vWF) shown in red, α-SMA in shown in green and DAPI in blue. Scale bar = 50 µm.

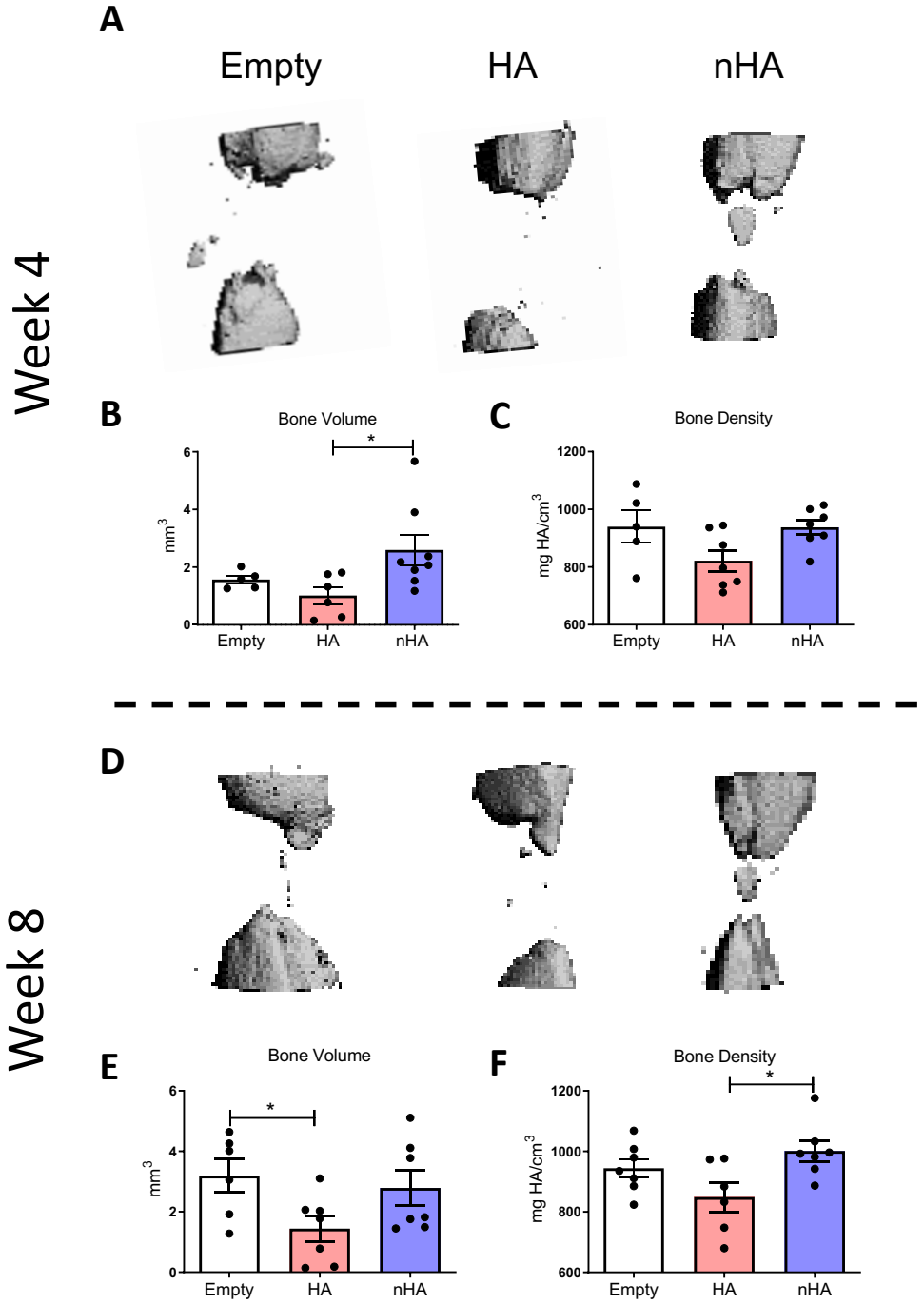

Figure 5.25: NanoHA, but not micron HA functionalized scaffolds, support bone tissue repair following implantation into a rat femoral defect model. (A) Reconstructed in vivo μCT analysis of bone formation at the defect site at 4 weeks. **(B)** Graphs represent quantification of total bone volume (mm^3) and **(C)** average bone density (mg HA/cm^3) at the defect site. **(D)** Reconstructed in vivo μCT analysis of bone formation at the defect site at 8 weeks. **(E)** Graphs represent quantification of total bone volume (mm^3) and (F) average bone density (mg HA/cm^3) at the defect site. Statistical differences (n=7 rats) were assessed using Kruskal Wallis test with Dunn's post-test (*p<0.05).

5.4 Discussion

It has now become increasingly apparent that engineering a pro-regenerative immune response following scaffold implantation is integral to downstream functional tissue regeneration. Despite the progress being made in designing biomaterials for bone regeneration, development of the 'ideal implant' has been hampered by the lack of detailed understanding of the immune response and, more specifically, the macrophage phenotype induced by various materials. The immune response to implanted biomaterials is determined by multiple factors, including biophysical cues such as material stiffness, topography and particle size. One such bioactive material that is commonly used in bone tissue engineering strategies is hydroxyapatite (HA) due to its similarity to natural bone and its osteoinductive properties. The results presented in this chapter demonstrate that nanoHA particle treated macrophages enhance mesenchymal stem cell (MSC) osteogenesis in vitro and this occurs in an IL-10 dependent manner, demonstrating a direct pro-osteogenic role for this cytokine. Characterization of the immune profile following incorporation of functionalized scaffolds into a rat femoral defect model revealed that micron-sized hydroxyapatite functionalized scaffolds elicited pro-inflammatory responses characterized by infiltrating T cells and elevated expression of M1 macrophages markers compared to nanoHA functionalized scaffolds which promoted M2 macrophage polarization. Furthermore, a higher concentration of circulating IL-10 was observed in rats implanted with nanoHA functionalized scaffolds. Moreover, rats implanted with nanoHA functionalized scaffolds exhibited enhanced vascularisation and bone volume compared to rats implanted with micron HA functionalized scaffolds. Taken together these results demonstrate that nano-sized hydroxyapatite has immunomodulatory potential and is capable of directing anti-inflammatory innate immune-mediated responses that are associated with tissue repair and regeneration.

There is now substantial evidence indicating that immune cells interact with the skeletal system and play a temporal role in post injury healing responses (365, 366, 378). Inflammation peaks at 24 hours post bone injury and is characterized by the expression

of pro-inflammatory cytokines and factors that contribute to early angiogenesis. This is followed by a renewal phase 7-10 days after injury, where bone forms via intramembranous ossification (378–380). Pro-inflammatory mediators are absent during the renewal phase, which is driven by factors influencing endochondral bone formation, such as TGF-β1-3 and bone morphogenetic proteins (378, 381). An imbalance in immune-mediated responses during early fracture healing is hypothesized to disturb the regeneration cascade leading to suboptimal bone healing, hence, the incorporation of bioactive cues into ECM scaffolds that are capable of polarizing immune responses has been hailed as a potential strategy to enhance constructive bone remodelling. In chapter 4, it was demonstrated that nanoHA particles preferentially polarize human macrophages towards an M2 phenotype and specifically enhance production of the anti-inflammatory cytokine, IL-10. In this chapter, these findings were further expanded and the data herein demonstrates that the secretome from nanoHA treated macrophages enhances MSC osteogenesis in an IL-10 dependent manner, demonstrating a direct pro-osteogenic role for this cytokine. IL-10 has previously been reported to promote chondrogenic differentiation and chondrocyte proliferation via the BMP pathway and can induce cartilage specific proteins such as collagen II and aggrecan (382, 383). The same study also demonstrated that IL-10 deficient mice developed smaller skulls, had less mineralised bone matrix and exhibit a reduction in the proliferation zone of embryonic growth plates (382). The work in this chapter further supports the concept that IL-10 may have a role in osteogenesis as the secretome of nanoHA-treated macrophages was found to enhance expression of the osteogenic genes, BMP2 and ALP in human MSCs, in addition to enhancing downstream mineralisation. In support of this, blockade of IL-10 reduced subsequent calcification and mineralization, further establishing a direct role for IL-10 in osteogenic differentiation. Increased expression of BMP2, ALP and OPN was also observed in the presence of recombinant IL-10, and while IL-10 was capable of driving OPN expression in MSCs, the same was not observed for nanoHA particles. While the work in this chapter offers compelling evidence of functional involvement of M2 macrophages, and for the first time a novel osteogenic role for IL-10 at least in an in vitro setting, an in-depth proteomic analysis is required to provide further information regarding the composition of the nanoHA-macrophage

secretome as there are likely a number of factors, in addition to IL-10, that are contributing to the observed outputs.

Interestingly, the enhanced TNFα and IL-1β observed with micron sized HA particle treatment, resulted in minimal downstream mineralisation of human MSCs. TNFα is normally expressed early during fracture healing, peaking at 24 hours after bone injury and while IL-1β acts through a distinct molecular signalling pathway, its expression pattern after bone fracture overlaps with that of TNFα; peaking immediately after injury and is undetectable after 72 hours (378, 379). This suggests that while these cytokines may have a role in the initial healing phase, they may be detrimental at the later tissue healing and remodelling phase. Indeed more efficient bone repair of calvarial defects was observed in IL-1R1 KO mice, while direct supplementation of media with recombinant human IL-1β *in vitro* inhibited MSC proliferation and differentiation into osteoblasts (366). Conflicting data still remains as to the role of TNFα in osteogenesis. While Hess *et al* demonstrated that TNFα can promote osteogenic differentiation of human MSCs, Lacey *et al* reported that TNFα has an inhibitory effect on osteogenesis in rodent MSCs (365, 367). Although work in this chapter demonstrated enhanced TNFα upon stimulation with micron sized particles, significant levels of IL-1β were also observed. Given the recent inhibitory role attributed to IL-1β in human MSC osteogenesis proposed by Martino *et al*, it is plausible that this cytokine, in combination with TNFα, are not conducive to osteogenesis and it is therefore not surprising that conditioned media from HA treated macrophages had no effect on MSC osteogenesis.

In addition to osteogenic differentiation of MSCs, migration of these cells to the site of implantation is an important aspect of the healing response in order to sustain tissue regeneration, however the chemotactic signals that guide MSCs to the implant site have not been extensively studied. Conditioned media from nanoHA treated macrophages significantly enhanced MSC migration. However further studies to characterise the growth factors and cytokines secreted by nanoHA stimulated macrophages are needed to ascertain what chemotactic factors may be responsible for this induction of MSC migration.

Treatment of macrophages with nanoHA particles upregulated the expression of VEGF and Ang1, which are known to contribute to vascularisation, and blood vessel maturation and stability, respectively (384, 385). Furthermore, conditioned media from nanoHA-treated macrophages significantly enhanced angiogenic processes in the HUVEC endothelial cell line. This data represents a very interesting finding in the context of functional bone tissue engineering, as a key requirement of the bone repair process, is adequate vascularisation. Loading of VEGF onto scaffolds is a strategy that has been used to improve vascularisation and has been shown to promote infiltration and proliferation of endothelial cells into engineered scaffolds (386). However, the data presented in this chapter demonstrates inherent pro-angiogenic properties of nanoHA particles, which may obviate the need to exogenously load in growth factors such as VEGF. The enhanced osteogenesis and migration of MSCs, and the pro-angiogenic responses in macrophages and endothelial cells, suggest that nanoHA particles elicit a more favourable immune response that may be more conducive to pro-regenerative responses, at least in an *in vitro* setting.

Bone is composite material, consisting of a mineral phase (HA) and an organic phase. The organic phase consists primarily of collagen type I and II, and provides flexibility to the tissue, therefore, in order to recapitulate a bone-like scaffold for implantation, a collagen-HA composite scaffold was fabricated. Collagen-nanoHA composite scaffolds have been used recently for in vivo bone regeneration applications and clinical applications (361, 370). In line with previous findings, the data presented here demonstrates that ECM materials derived from different musculoskeletal tissue sources differentially influence macrophage phenotype and cytokine profile and therefore the source of ECM tissue is an important factor to consider in the design of scaffolds (206). Fabrication of AC derived ECM scaffolds functionalised with either HA or nanoHA particles displayed comparable mechanical properties. This is important as mechanical cues such as scaffold stiffness has been shown recently to alter macrophage phenotype (387). Furthermore, pore size and porosity were similar in both scaffold groups with an average size of 50 μm. This is in line with previous studies reporting that a pore size of between 20μm-200μm allows for optimal attachment to accommodate cellular infiltration (388). Importantly HA particles remained within the construct after the

freeze-drying process, and therefore can be used as a 3D construct for further *in vivo* studies of bone regeneration.

In vivo characterisation of the immune response to particle-functionalised scaffolds using a rat femoral defect model revealed immune profiles similar to that of the *in vitro* study. Interestingly, analysis of cell subsets in micron HA scaffold groups revealed no discernible difference in the numbers of B cells, however significantly higher numbers of neutrophils and T cells were observed at the defect site. Chemokines such as CXCL9 and CXCL10, which were found to be enhanced in macrophages stimulated with micron HA particles, are known to be involved in the recruitment of T cells. Therefore, the enhanced T cell infiltration observed in the micron HA group may be attributed to micron particle-induced chemokine expression. Furthermore, macrophages present at the defect site expressed high levels of the surface markers, CCR2 and CD86, indicative of an M1-like profile. In contrast, implantation of nanoHA functionalized ECM scaffolds into critically sized bone defects resulted in an anti-inflammatory profile with upregulation of circulating IL-10, alongside higher numbers of anti-inflammatory CX3CR1+ macrophages. This translates our earlier in vitro findings of IL-10 induction and M2 macrophage polarization by nanoHA particles to a more pertinent *in vivo* setting.

Of note, as well as being associated with a more pro-resolution and anti-inflammatory profile, CX3CR1+ cells have also been shown to play an important role in neovascularization and the promotion of angiogenesis (389). There is an intimate link between bone regeneration, angiogenesis and inflammation, and impaired angiogenesis has been reported with prolonged administration of inflammatory cytokines in several in vivo models (374, 375). In line with this, implantation of micron HA functionalised scaffolds into the defect site did not promote new vessel formation. In contrast, nanoHA functionalised scaffolds appeared to promote the formation of vessel-like structures expressing vWF and αSMA, indicating the presence of vascular endothelial cells and mature vessels. MSCs can behave as pericyte-like cells and stabilise new vessel formation by endothelial cells (390). Given the enhanced MSC migration and pro-angiogenic response in endothelial cells observed in nanoHA conditioned media, it is tempting to speculate that this M2-like secretome may not only enhance angiogenic

endothelial cell responses, but also promote the recruitment of host MSCs that stabilise newly forming vessels. Subcutaneous injection of M2 macrophage-laden matrigels into C57/BL/6 mice has been shown to increase CD31+ endothelial cell numbers after 14 days, while higher numbers of M2 macrophages, which expressed high levels of potent pro-angiogenic stimulators, correlated with enhanced biomaterial vascularization (376, 377). Furthermore, it has previously been reported that higher numbers of M2 macrophages enhance angiogenic responses, with enhanced endothelial cell numbers and anastomosis of blood vessels in vivo (376, 377). Angiopoietin 2 (Ang2) is mainly involved in vessel formation, and Ang 1, involved in recruitment of pericyte to the vessel for stability and preventing endothelial cell apoptosis (391) while also promoting migration of MSCs (363). While further work is required to identify the factors specifically promoting the observed pro-angiogenic responses in this study, the enhanced Ang1 expression in nanoHA treated macrophages observed in vitro suggests that Ang1 secretion by macrophages may promote early vessel formation. Furthermore, CX3CR1+ cells have been shown to play an important role in neovascularization and the promotion of angiogenesis in a model of hind-limb ischemia (389), suggesting that the nanoHA-induced CX3CR1+ cell subset may well may be directly influencing vascularization in our femoral defect model. While further *in vivo* study is required to assess blood vessel formation and vascularization, this data further supports the pro-angiogenic potential of the nanoHA particles.

Given the inflammatory profile of the micron HA-functionalized scaffolds and the apparent lack of tissue vascularization, which is a crucial component of functional bone regeneration (374), it was not surprising that these early responses coincided with a lack of bone regeneration. Defect bridging was absent at 4 and 8 weeks post-implantation and there appeared be an appreciable decrease in bone density. This complements earlier *in vivo* work suggesting that while the presence of inflammatory signals early on in fracture healing may be beneficial (356), prolonged administration can hamper healing (374, 375). Furthermore, this is in line with recent reports demonstrating that RAG knockout mice, which lack a functional adaptive immune system and therefore T cell responses, exhibit accelerated mineralisation and remodelling (211). While the role of individual adaptive cell subsets has not yet been established in the bone repair

process, this data, in tandem with recent studies, suggest that T cells may not be permissive to efficient bone regeneration. Further studies examining specific T cell subsets during the healing process is necessary to determine the exact role of adaptive cells in this regeneration process.

In contrast, and in line with our *in vitro* findings, implantation of nanoHA functionalized ECM scaffolds in critical bone defects resulted in significantly more bone volume compared to both empty defect and HA functionalized scaffolds. While the extent of bone tissue repair overall was limited and full defect bridging was absent in the nanoHA scaffold group, even at 8 weeks, future studies will explore combining M2-polarizing nanoHA particles into-cell laden scaffolds to determine if this will synergistically enhance long-term matrix deposition, tissue repair and functional bone regeneration. Furthermore, mechanical reinforcement of the current scaffold design may enhance long-term tissue repair, as one potential limitation of the current ECM scaffold design may be the rate of degradation of the scaffold itself.

In summary, current strategies being explored to enhance bone healing in vivo include incorporating anti-inflammatory cytokines such as IL-10 or IL-4 into scaffolds (392–394). However, the data presented here offers compelling evidence that nanoHA particles themselves are inherently anti-inflammatory and supportive of osteogenesis. Therefore, this positions this particle as a particularly attractive immune-modulatory biomaterial that may be incorporated into various 3D constructs and may avoid the need to exogenously load cytokines into constructs. A summary of the results generated in this study is provided in figure 5.26.

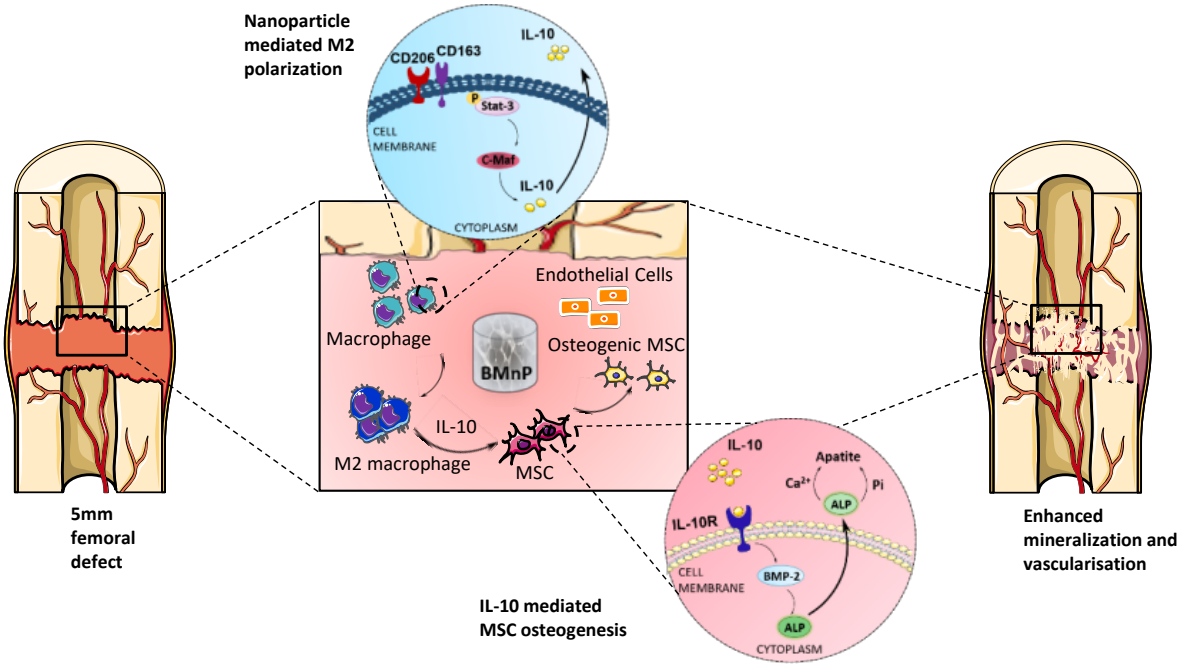

Figure 5.26: Model of nanoHA mediated bone regeneration

Chapter 6: General Discussion

6.1 General Discussion

OA is the most prevalent form of arthritis affecting nearly 10% of the population worldwide. In Ireland, it is estimated that nearly half a million individuals currently suffer from OA and this figure is set to rise as both life expectancy increases and the obesity epidemic worsens. It is estimated that 9.6% of men and 18% of women over the age of 60 suffer from OA and this number rises to 80% of individuals by the age of 75 (395). This highly prevalent disease represents a significant economic and healthcare burden.

Early stage OA can be classified as an osteochondral defect, characterised by damage to both articular cartilage and the underlying subchondral bone. Macrophage-driven inflammation propagates this damage via the secretion of cytokines such as TNFα and IL-1β. These mediators are particularly detrimental to the joint as they can enhance expression of various cartilage degrading enzymes such as MMP-1, MMP-9 and MMP-13, resulting in catabolism of cartilage within the joint (396). Furthermore, maintenance of healthy cartilage in the joint by aggrecan and collagen type II is inhibited by IL-1β (23, 397) and underlying subchondral bone eventually becomes exposed. As the bone no longer has a protective covering that would normally prevent friction and provide lubrication, bone erosion ensues, and often the damage is so severe that individuals require a total joint arthroplasty. Wear debris generated from prosthetic implants over time has been reported to trigger inflammatory processes that lead to a complication known as periprosthetic osteolysis which results in degradation of the surrounding bone, loosening of the implant and therefore the need for revision surgery (128). Revision surgeries are associated with a drastically increased recovery time and, in the case of young implant recipients, the limited lifespan of the prosthesis means that individuals may have to undergo several surgeries during their lifetime.

The lack of progression in the development of disease-modifying drugs for OA is largely due to a limited understanding of the initial triggers and molecular events involved in driving early cartilage destruction and subsequent inflammation associated with the disease. This is complicated by the fact that OA is initially asymptomatic and often progresses to a more severe state prior to the onset of symptoms, when prevention is

too late. While multiple factors are likely to contribute to disease pathogenesis, it is well established that particulates in the form of BCP crystals play a pathogenic role in OA (99, 102). Chapter 3 of this thesis provided insight into the effects of BCP crystals on macrophage metabolism, and results suggest that a BCP-induced switch favouring glycolysis is linked to M1 macrophage polarization. While the field of immunometabolism is still in its infancy and much remains to be learned regarding the impact of metabolic reprogramming on disease pathogenesis, the data presented here supports the idea that it may be possible to modulate metabolic changes in polarized macrophages by specifically targeting key glycolytic enzymes. This study could also be extended to other DAMPs e.g. S100A8, in order to determine if DAMP-induced metabolic reprogramming represents a novel therapeutic avenue for the treatment of OA.

In the case of end-stage OA, total joint replacements are required, however and as mentioned above, these surgeries are associated with complications, particularly as patient age increases. It has previously been demonstrated that periprosthetic tissues exhibit increased M1/M2 macrophage ratios compared to non-operated osteoarthritic synovial tissues and that PMMA bone cement particles can enhance the expression of the M1 macrophage marker, iNOS (140). The findings presented in Chapter 4 demonstrate that both HA and PMMA particles enhance M1 marker expression and induce a more activated macrophage state, while decreasing the expression of M2 markers. Consistent with reports on atherosclerosis-associated cholesterol crystals and OA-associated BCP crystals, this study demonstrates that HA and PMMA particles induce the production of IL-1β by human macrophages in an NLRP3-dependent manner, as evidenced by decreased IL-1β cytokine production in the presence of the novel small molecule inhibitor of NLRP3, MCC950. This compound has been reported to have therapeutic potential for the treatment of inflammatory diseases such as Multiple Sclerosis and Muckle-Wells Syndrome (398) and, while further *in vivo* study is required, it may also have potential use in biomedical engineering.

Previous work in the Dunne laboratory has demonstrated that cholesterol and BCP crystals induce IL-1β and MMP production via MATS, which involves direct binding of

particulates to the cell membrane resulting in lipid raft formation and aggregation of (ITAM)-containing molecules which mediate the recruitment and activation of Syk (247). Results from this study demonstrate that both HA and PMMA particles are also capable of inducing the phosphorylation of Syk in macrophages and that inhibition of Syk reduces the secretion of IL-1β, IL-6 and TNFα. Furthermore, depletion of cholesterol from the cell membrane abrogated HA and PMMA particle induced cytokine secretion. Interestingly this is not the case for particle induced IL-8 suggesting that this cytokine is regulated in a distinct manner. Future studies, using for example atomic force microscopy, are warranted to fully confirm that these particles are indeed exerting their effects through direct membrane binding.

Activation of ERK MAP kinase is associated with increased cell proliferation, while active p38 MAP kinase plays a key role in cell differentiation. The results presented in Chapter 4 also demonstrate that HA and PMMA particles induce the phosphorylation of both ERK and p38 in human macrophages, which may promote cell survival and activation at the prosthetic implant site. Similar to Syk inhibition, specific blockade of ERK and p38 MAP kinases significantly reduced particle-induced IL-6 and TNFα production while also blocking particle mediated M1 gene expression. Future experiments will investigate the effect of Syk and MAP kinase inhibitors on particle induced inflammatory responses in synovial macrophages of patients with OA given that their immune profile would differ from that of healthy subjects and they are likely to exhibit high M1 to M2 ratios.

Future approaches to lessen inflammation at the joint site and improve the lifespan of orthopaedic implants could also involve the coating of implants with Syk or MAP kinase small molecule inhibitors. Given that Syk appears to play a role at such an early stage of particle-induced signal transduction, inhibiting its activity may prevent the initiation of a range of detrimental downstream cellular responses including inflammatory cytokine secretion, MMP expression and osteoclast maturation. The Syk inhibitor, R788, used in this study is available as an orally administered drug which showed promising results in phase I and phase II clinical trials by AstraZeneca for the treatment of Rheumatoid Arthritis (RA) (339). Unfortunately, adverse side effects reported during the phase III trial led to termination. However, as the nature of OA, periprosthetic osteolysis and RA

differ in their immune response, R788 or a modification of the drug itself when administered locally may still prove effective as a therapy for osteolysis. Indeed, a number of pharmaceutical companies are currently pursuing alternative Syk inhibitors.

Another key aspect of Chapter 4 was characterisation of the immune response to in-house generated nano HA. Natural bone consists of nanometre scale HA on the outer surface of the bone, however micron sized HA is currently used for orthopaedic coatings. This may therefore result in poor integration of the implant with surrounding bone followed by dissolution of the coating and initiation of inflammatory responses. Nanometre or submicron surface structures imitate the geometry and arrangement of components of natural bone tissue, however, the host immune response to nanoHA particles still remains largely unknown (119, 189). Results demonstrated that, in contrast to larger HA particles, nanoHA particles preferentially polarize macrophages towards an M2 phenotype as evidenced by enhanced mRNA expression of MRC1 and CCL13, as well as increased expression of the M2 surface markers, CD206 and CD163. Furthermore, the M2 associated cytokine, IL-10, was significantly enhanced upon stimulation with nanoHA particles. Preliminary data generated in this study suggest that these responses may be coupled to metabolic changes in macrophages as micron sized HA particles were found to drive a metabolic switch favouring glycolysis while concomitantly dampening mitochondrial biogenesis. However, further research into the relationship between the metabolic and immunologic effects of biomaterial based particulates are required to confirm this hypothesis. These results have a number of important implications for both particle-induced immune responses and immunometabolism research and open up new possibilities in the search for biomaterials that can regulate the metabolic status, and therefore, immune phenotype of cells. Taken together this data suggests that nanoHA may be a more favourable bioceramic to use for orthopaedic implants when compared to micron sized HA particles, and the use of such material clinically may result in superior host integration as well as reduced periprosthetic inflammation.

It is anticipated that in the future, strategies to repair and regenerate damaged tissue in situ will be developed (208). Current tissue engineering approaches typically involve fabrication of scaffolds functionalised with growth factors or bioactive cues that can direct functional tissue regeneration (399). In the case of bone tissue regeneration,

incorporation of nanoHA as a bioactive and osteoinductive cue is being widely explored and has shown some success in animal models (361), however there have been relatively few examples of successful bone tissue regeneration in humans using biomaterial scaffolds. One of the key factors identified in the failure of tissue engineered constructs and, similar to the failure of current orthopaedic implants, is insufficient integration with host tissue. This may be attributed to poor surface interaction of biomaterials with the host tissue as well as adverse immunological responses to certain types of biomaterials. As mentioned, it is now well accepted that an appropriate immune response, involving a temporal switch from a pro-inflammatory response (comprising M1 macrophages) to an anti-inflammatory response (comprising M2 macrophages) is integral to successful tissue regeneration with increased numbers of M2 macrophages associated with more positive remodelling outcomes (206, 400). Biomaterial scaffolds are often designed to modulate the later stages of the healing processes, such as stem cell differentiation, with less focus placed on the early immune responses. However, it is becoming increasingly apparent that modulation of the immune response post-implantation may prove to be a beneficial strategy to maximize the regenerative capacity of progenitor cells and minimize the destructive effects of prolonged inflammation. In the case of bone fracture healing, the requirement of macrophages during the repair process has been demonstrated as depletion of macrophages leads to inferior fracture healing. Studies characterising macrophage phenotypes during the ossification phase revealed a predominantly M2 phenotype, with low numbers of M1 macrophages present by day 7. Furthermore, enhancement of an M2 phenotype using IL-4 and IL-13 significantly increased bone formation at 3 weeks (358). However, modulation of the immune responses in a critically sized defect, which has very little capacity for repair, has not yet been assessed. The data presented in Chapter 5 not only offers compelling evidence that nanoHA particle-mediated M2 macrophage polarization enhances MSC osteogenesis in an IL-10 dependent manner in vitro, but also demonstrates that nanoHA particles are capable of directing anti-inflammatory, wound repair immune responses that are associated with enhanced bone tissue repair and regeneration *in vivo.*

While this study focused specifically on modulating HA particle characteristics, modulation of various other parameters of scaffold design are being explored, including choice of crosslinker, substrate stiffness and 3D geometric cues (fibre orientation) (399). These parameters can therefore be tailored in order to promote a desired immune response *in vivo*. For example, carbodiimide and glutaraldehyde crosslinking is commonly used to tune the stiffness of biomimetic scaffolds in order to modulate stem cell differentiation *in vitro*, however the use of such chemical crosslinking during scaffold fabrication can have a profound influence on macrophage phenotype and disrupt host tissue remodelling *in vivo*. Crosslinking with Genipin has been shown to elicit a more favourable immune response, by driving a predominantly M2 macrophage phenotype at the implant site (401). The most targeted method of controlling the immune response to biomaterial implantation is to release factors such as cytokines that overwhelm native signalling and direct macrophage polarization. This could be achieved by incorporating growth factors or small molecule drugs into controlled release systems (399). For example, binding of IL-4 to decellularised bone scaffolds has been used to promote vasculogenesis in vivo and control macrophage polarization in vitro (374). Silk protein has been used to form biopolymer films that can release cytokines such as IFNγ and IL-4. The solubility of the films can be altered to allow for short or longer-term release, and have been shown to effectively polarize macrophages into M1 or M2 phenotypes (402). More recently, silk-based 3D bioprinted hydrogels have been designed which allows for highly organized 3D constructs to be fabricated while also permitting a tunable delivery system for controlled cytokine release (403). Based on the data presented in this thesis is also possible that, by specifically tailoring HA particle characteristics, immune responses induced after biomaterial implantation may be modulated without the need for the delivery of exogenous cytokines or growth factors.

In conclusion, this data presented herein highlights the crucial role of the innate immune response in modulating the regenerative capacity of stem cells and the importance of integrating control of the host immune microenvironment into regenerative medicine strategies. Continued work in this field will provide new insights into the pathogenesis of OA and has real potential for the development of specific treatments for this form of arthritis which will become steadily more prevalent as the aging population increases.

6.2 Future Directions

- Having identified a novel pro-osteogenic role for the IL-10, we now propose to develop an IL-10 functionalised scaffold for bone tissue repair. Recombinant human IL-10 could therefore be conjugated to the current ECM scaffolds, or alternatively, to 3D bioprinted constructs, where degradation rate may be tuned to allow for controlled release of the cytokine.
- Further work into the role of biomaterial-induced metabolic changes in macrophages will be conducted in order to determine if metabolic reprogramming is specific to hydroxyapatite or whether other biomaterial based nano/micron particles impact differentially on immune cell metabolism. Furthermore, the impact of specific metabolites (e.g. itaconate – an anti-inflammatory metabolite) on stem cell differentiation will be explored.
- Given the limited defect bridging in the femoral defect model, we hypothesise that one limitation of the current scaffold design was the mechanical strength and rapid degradation rate of the scaffold itself. In order to overcome the shortcomings of this current design, two approaches will be taken. In the first instance, the extent of crosslinking will be modified to create a more mechanically stable scaffold which may slow down the degradation rate. Alternatively, mechanical reinforcement of the scaffold may be performed by 3D printing a supporting structure in the scaffold (e.g. co-printing ECM into a polymer) which will potentially improve overall mechanical integrity.
- Further analysis of the role of the adaptive immune response following scaffold implantation will be carried out given that this arm of the immune system also plays an integral role in the tissue healing response.

References

1. van den Bosch, M. H. J. 2019. Inflammation in osteoarthritis: is it time to dampen the alarm(in) in this debilitating disease? *Clin. Exp. Immunol.* 195: 153–166.
2. Goldring, M. B., and S. R. Goldring. 2007. Osteoarthritis. *J. Cell. Physiol.* 213: 626–634.
3. Ayral, X., E. H. Pickering, T. G. Woodworth, N. Mackillop, and M. Dougados. 2005. Synovitis: a potential predictive factor of structural progression of medial tibiofemoral knee osteoarthritis – results of a 1 year longitudinal arthroscopic study in 422 patients. *Osteoarthr. Cartil.* 13: 361–367.
4. Wieland, H. A., M. Michaelis, B. J. Kirschbaum, and K. A. Rudolphi. 2005. Osteoarthritis - an untreatable disease? *Nat. Rev. Drug Discov.* 4: 331–344.
5. Goldring, M. B. 2000. The role of the chondrocyte in osteoarthritis. *Arthritis Rheum.* 43: 1916–1926.
6. Sophia Fox, A. J., A. Bedi, and S. A. Rodeo. 2009. The basic science of articular cartilage: structure, composition, and function. *Sports Health* 1: 461–468.
7. Gottardi, R., U. Hansen, R. Raiteri, M. Loparic, M. Duggelin, D. Mathys, N. F. Friederich, P. Bruckner, and M. Stolz. 2016. Supramolecular Organization of Collagen Fibrils in Healthy and Osteoarthritic Human Knee and Hip Joint Cartilage. *PLoS One* 11: e0163552.
8. Buckland-Wright, C. 2004. Subchondral bone changes in hand and knee osteoarthritis detected by radiography. *Osteoarthr. Cartil.* 12: 10–19.
9. Burr, D. B. 2004. Anatomy and physiology of the mineralized tissues: Role in the pathogenesis of osteoarthrosis. *Osteoarthr. Cartil.* 12: 20–30.
10. Sherwood, J. C., J. Bertrand, S. E. Eldridge, and F. Dell'accio. 2014. Cellular and molecular mechanisms of cartilage damage and repair. *Drug Discov. Today* 19: 1172–1177.
11. Karsdal, M. A., A. C. Bay-Jensen, R. J. Lories, S. Abramson, T. Spector, P. Pastoureau, C. Christiansen, M. Attur, K. Henriksen, S. R. Goldring, and V. Kraus. 2014. The coupling of bone and cartilage turnover in osteoarthritis: Opportunities for bone antiresorptives and anabolics as potential treatments? *Ann. Rheum. Dis.* 73: 336–348.
12. Scanzello, C. R., and S. R. Goldring. 2012. The role of synovitis in osteoarthritis pathogenesis. *Bone* 51: 249–257.
13. Kennedy, A., U. Fearon, D. J. Veale, and C. Godson. 2011. Macrophages in synovial

inflammation. *Front. Immunol.* 2: 1–9.

14. Scanzello, C. R., B. McKeon, B. H. Swaim, E. Dicarlo, E. U. Asomugha, V. Kanda, A. Nair, D. M. Lee, J. C. Richmond, J. N. Katz, M. K. Crow, and S. R. Goldring. 2011. Synovial inflammation in patients undergoing arthroscopic meniscectomy: Molecular characterization and relationship to symptoms. *Arthritis Rheum.* 63: 391–400.

15. Benito, M. J., D. J. Veale, O. FitzGerald, W. B. Van Den Berg, and B. Bresnihan. 2005. Synovial tissue inflammation in early and late osteoarthritis. *Ann. Rheum. Dis.* 64: 1263–1267.

16. McInnes, I. B., and G. Schett. 2011. The pathogenesis of rheumatoid arthritis. *N. Engl. J. Med.* 365: 2205–2219.

17. Liu-bryan, R. and R. T. 2015. Emerging regulators of the inflammatory process in osteoarthritis. *Nat. Rev. Rheumatol.* 11: 35–44.

18. Berenbaum, F. 2013. Osteoarthritis as an inflammatory disease (osteoarthritis is not osteoarthrosis!). *Osteoarthr. Cartil.* 21: 16–21.

19. Blom, A. B., P. L. E. M. van Lent, A. E. M. Holthuysen, P. M. van der Kraan, J. Roth, N. van Rooijen, and W. B. van den Berg. 2004. Synovial lining macrophages mediate osteophyte formation during experimental osteoarthritis. *Osteoarthr. Cartil.* 12: 627–635.

20. Blom, A. B., P. L. Van Lent, S. Libregts, A. E. Holthuysen, P. M. Van Der Kraan, N. Van Rooijen, and W. B. Van Den Berg. 2007. Crucial role of macrophages in matrix metalloproteinase-mediated cartilage destruction during experimental osteoarthritis: Involvement of matrix metalloproteinase 3. *Arthritis Rheum.* 56: 147–157.

21. Katona, G. 1984. Osteoarthritis - an inflammatory disease? *Int. J. Tissue React.* 6: 453–461.

22. Smith, M. D., S. Triantafillou, A. Parker, P. P. Youssef, and M. Coleman. 1997. Synovial membrane inflammation and cytokine production in patients with early osteoarthritis. *J. Rheumatol.* 24: 365–371.

23. Goldring, M. B., J. Birkhead, L. J. Sandell, T. Kimura, and S. M. Krane. 1988. Interleukin 1 suppresses expression of cartilage-specific types II and IX collagens and increases types I and III collagens in human chondrocytes. *J. Clin. Invest.* 82: 2026–2037.

24. Chevalier, X., B. Giraudeau, T. Conrozier, J. Marliere, P. Kiefer, and P. Goupille.

2005. Safety study of intraarticular injection of interleukin 1 receptor antagonist in patients with painful knee osteoarthritis: A multicenter study. *J. Rheumatol.* 32: 1317–1323.

25. Schlaak, J. F., I. Pfers, K. H. Meyer Zum Buschenfelde, and E. Marker-Hermann. 1996. Different cytokine profiles in the synovial fluid of patients with osteoarthritis, rheumatoid arthritis and seronegative spondylarthropathies. *Clin. Exp. Rheumatol.* 14: 155–162.

26. Zhang, X., Y. Zhu, X. Chen, Y. Zhang, Y. Zhang, Y. Jia, H. Wang, Y. Liu, and L. Xiao. 2014. Baicalein ameliorates inflammatory-related apoptotic and catabolic phenotypes in human chondrocytes. *Int. Immunopharmacol.* 21: 301–308.

27. Magnano, M. D., E. F. Chakravarty, C. Broudy, L. Chung, A. Kelman, J. Hillygus, and M. C. Genovese. 2007. A pilot study of tumor necrosis factor inhibition in erosive/inflammatory osteoarthritis of the hands. *J. Rheumatol.* 34: 1323–1327.

28. Sandy, J. D., P. J. Neame, R. E. Boynton, and C. R. Flannery. 1991. Catabolism of aggrecan in cartilage explants: Identification of a major cleavage site within the interglobular domain. *J. Biol. Chem.* 266: 8683–8685.

29. Kashiwagi, M., J. J. Enghild, C. Gendron, C. Hughes, B. Caterson, Y. Itoh, and H. Nagase. 2004. Altered Proteolytic Activities of ADAMTS-4 Expressed by C-terminal Processing. *J. Biol. Chem.* 279: 10109–10119.

30. Stanton, H., F. M. Rogerson, C. J. East, S. B. Golub, K. E. Lawlor, C. T. Meeker, C. B. Little, K. Last, P. J. Farmer, I. K. Campbell, A. M. Fourie, and A. J. Fosang. 2005. ADAMTS5 is the major aggrecanase in mouse cartilage in vivo and in vitro. *Nature* 434: 648–652.

31. Verma, R. P., and C. Hansch. 2007. Matrix metalloproteinases (MMPs): Chemical-biological functions and (Q)SARs. *Bioorganic Med. Chem.* 15: 2223–2268.

32. Yuan, G. H., M. Tanaka, K. Masuko-Hongo, A. Shibakawa, T. Kato, K. Nishioka, and H. Nakamura. 2004. Characterization of cells from pannus-like tissue over articular cartilage of advanced osteoarthritis. *Osteoarthr. Cartil.* 12: 38–45.

33. Maiotti, M., G. Monteleone, U. Tarantino, G. F. Fasciglione, S. Marini, and M. Coletta. 2000. Correlation between osteoarthritic cartilage damage and levels of proteinases and proteinase inhibitors in synovial fluid from the knee joint. *Arthroscopy* 16: 522–526.

34. Bondeson, J., S. D. Wainwright, S. Lauder, N. Amos, and C. E. Hughes. 2006. The role of synovial macrophages and macrophage-produced cytokines in driving aggrecanases, matrix metalloproteinases, and other destructive and inflammatory responses in osteoarthritis. *Arthritis Res. Ther.* 8: R187.
35. Ra, H. J., and W. C. Parks. 2007. Control of matrix metalloproteinase catalytic activity. *Matrix Biol.* 26: 587–596.
36. Ishiguro, N., T. Ito, H. Ito, H. Iwata, H. Jugessur, M. Ionescu, and A. R. Poole. 1999. Relationship of matrix metalloproteinases and their inhibitors to cartilage proteoglycan and collagen turnover: Analyses of synovial fluid from patients with osteoarthritis. *Arthritis Rheum.* 42: 129–136.
37. Little, C. B., A. Barai, D. Burkhardt, S. M. Smith, A. J. Fosang, Z. Werb, M. Shah, and E. W. Thompson. 2009. Matrix metalloproteinase 13-deficient mice are resistant to osteoarthritic cartilage erosion but not chondrocyte hypertrophy or osteophyte development. *Arthritis Rheum.* 60: 3723–3733.
38. Neuhold, L. A., L. Killar, W. Zhao, M. L. A. Sung, L. Warner, J. Kulik, J. Turner, W. Wu, C. Billinghurst, T. Meijers, A. R. Poole, P. Babij, and L. J. DeGennaro. 2001. Postnatal expression in hyaline cartilage of constitutively active human collagenase-3 (MMP-13) induces osteoarthritis in mice. *J. Clin. Invest.* 107: 35–44.
39. Liu, Y., J. A. Ranish, R. Aebersold, and S. Hahn. 2001. Identification and Enzymatic Characterization of Two Diverging Murine Counterparts of Human Interstitial Collagenase (MMP-1) Expressed at Sites of Embryo Implantation. *J. Biol. Chem.* 276: 7169–7175.
40. Akram, M. 2014. Citric Acid Cycle and Role of its Intermediates in Metabolism. *Cell Biochem. Biophys.* 68: 475–478.
41. O'Neill, L. A. J., R. J. Kishton, and J. Rathmell. 2016. A guide to immunometabolism for immunologists. *Nat Rev Immunol* 16: 553–565.
42. Glatz, J. F. C., and J. J. F. P. Luiken. 2015. Fatty acids in cell signaling: Historical perspective and future outlook. *Prostaglandins Leukot. Essent. Fat. Acids* 92: 57–62.
43. Stincone, A., A. Prigione, T. Cramer, M. M. C. Wamelink, K. Campbell, E. Cheung, V. Olin-Sandoval, N. M. Grüning, A. Krüger, M. Tauqeer Alam, M. A. Keller, M. Breitenbach, K. M. Brindle, J. D. Rabinowitz, and M. Ralser. 2015. The return of metabolism: Biochemistry and physiology of the pentose phosphate pathway. *Biol.*

Rev. 90: 927–963.
44. Saxton, R. A., and D. M. Sabatini. 2017. mTOR Signaling in Growth, Metabolism, and Disease. *Cell* 168: 960–976.
45. Düvel, K., J. L. Yecies, S. Menon, P. Raman, A. I. Lipovsky, A. L. Souza, E. Triantafellow, Q. Ma, R. Gorski, S. Cleaver, M. G. Vander Heiden, J. P. MacKeigan, P. M. Finan, C. B. Clish, L. O. Murphy, and B. D. Manning. 2010. Activation of a metabolic gene regulatory network downstream of mTOR complex 1. *Mol. Cell* 39: 171–183.
46. Majmundar, A. J., W. J. Wong, and M. C. Simon. 2010. Hypoxia-Inducible Factors and the Response to Hypoxic Stress. *Mol. Cell* 40: 294–309.
47. Lee, M. N., S. H. Ha, J. Kim, A. Koh, C. S. Lee, J. H. Kim, H. Jeon, D.-H. Kim, P.-G. Suh, and S. H. Ryu. 2009. Glycolytic Flux Signals to mTOR through Glyceraldehyde-3-Phosphate Dehydrogenase-Mediated Regulation of Rheb. *Mol. Cell. Biol.* 29: 3991–4001.
48. Sancak, Y., L. Bar-Peled, R. Zoncu, A. L. Markhard, S. Nada, and D. M. Sabatini. 2010. Ragulator-rag complex targets mTORC1 to the lysosomal surface and is necessary for its activation by amino acids. *Cell* 141: 290–303.
49. Diskin, C., and E. M. Pålsson-McDermott. 2018. Metabolic Modulation in Macrophage Effector Function. *Front. Immunol.* 9: 270.
50. Rodriguez-Prados, J.-C., P. G. Traves, J. Cuenca, D. Rico, J. Aragones, P. Martin-Sanz, M. Cascante, and L. Bosca. 2010. Substrate Fate in Activated Macrophages: A Comparison between Innate, Classic, and Alternative Activation. *J. Immunol.* 185: 605–614.
51. Cramer, T., Y. Yamanishi, B. E. Clausen, I. Förster, R. Pawlinski, N. Mackman, V. H. Haase, R. Jaenisch, M. Corr, V. Nizet, G. S. Firestein, H. P. Gerber, N. Ferrara, and R. S. Johnson. 2003. HIF-1α is essential for myeloid cell-mediated inflammation. *Cell* 112: 645–657.
52. Lunt, S. Y., and M. G. Vander Heiden. 2011. Aerobic Glycolysis: Meeting the Metabolic Requirements of Cell Proliferation. *Annu. Rev. Cell Dev. Biol.* 27: 441–464.
53. Taylor, C. T., and S. P. Colgan. 2017. Regulation of immunity and inflammation by hypoxia in immunological niches. *Nat. Rev. Immunol.* 17: 774–785.
54. Weinberg, J. B., M. A. Misukonis, P. J. Shami, S. N. Mason, D. L. Sauls, W. A. Dittman, E. R. Wood, G. K. Smith, B. McDonald, and K. E. Bachus. 1995. Human

mononuclear phagocyte inducible nitric oxide synthase (iNOS): analysis of iNOS mRNA, iNOS protein, biopterin, and nitric oxide production by blood monocytes and peritoneal macrophages. *Blood* 86: 1184–1195.

55. Thomas, A. C., and J. T. Mattila. 2014. "Of mice and men": Arginine metabolism in macrophages. *Front. Immunol.* 5: 1–7.

56. Van den Bossche, J., J. Baardman, N. A. Otto, S. van der Velden, A. E. Neele, S. M. van den Berg, R. Luque-Martin, H. J. Chen, M. C. S. Boshuizen, M. Ahmed, M. A. Hoeksema, A. F. de Vos, and M. P. J. de Winther. 2016. Mitochondrial Dysfunction Prevents Repolarization of Inflammatory Macrophages. *Cell Rep.* 17: 684–696.

57. Everts, B., E. Amiel, G. J. W. Van Der Windt, T. C. Freitas, R. Chott, K. E. Yarasheski, E. L. Pearce, and E. J. Pearce. 2012. Commitment to glycolysis sustains survival of NO-producing inflammatory dendritic cells. *Blood* 120: 1422–1431.

58. Papathanassiu, A. E., J. H. Ko, M. Imprialou, M. Bagnati, P. K. Srivastava, H. A. Vu, D. Cucchi, S. P. McAdoo, E. A. Ananieva, C. Mauro, and J. Behmoaras. 2017. BCAT1 controls metabolic reprogramming in activated human macrophages and is associated with inflammatory diseases. *Nat. Commun.* 8: 1–13.

59. Vats, D., L. Mukundan, J. I. Odegaard, L. Zhang, K. L. Smith, C. R. Morel, D. R. Greaves, P. J. Murray, and A. Chawla. 2006. Oxidative metabolism and PGC-1β attenuate macrophage-mediated inflammation. *Cell Metab.* 4: 13–24.

60. Huang, S. C. C., B. Everts, Y. Ivanova, D. O'Sullivan, M. Nascimento, A. M. Smith, W. Beatty, L. Love-Gregory, W. Y. Lam, C. M. O'Neill, C. Yan, H. Du, N. A. Abumrad, J. F. Urban, M. N. Artyomov, E. L. Pearce, and E. J. Pearce. 2014. Cell-intrinsic lysosomal lipolysis is essential for alternative activation of macrophages. *Nat. Immunol.* 15: 846–855.

61. Galván-Peña, S., and L. A. J. O'Neill. 2014. Metabolic reprogramming in macrophage polarization. *Front. Immunol.* 5: 1–6.

62. Sag, D., D. Carling, R. D. Stout, and J. Suttles. 2008. Adenosine 5'-Monophosphate-Activated Protein Kinase Promotes Macrophage Polarization to an Anti-Inflammatory Functional Phenotype. *J. Immunol.* 181: 8633–8641.

63. Fearon, U., M. Canavan, M. Biniecka, and D. J. Veale. 2016. Hypoxia, mitochondrial dysfunction and synovial invasiveness in rheumatoid arthritis. *Nat. Rev. Rheumatol.* 12: 385–397.

64. Fearon, U., M. M. Hanlon, S. M. Wade, and J. M. Fletcher. 2019. Altered metabolic pathways regulate synovial inflammation in rheumatoid arthritis. *Clin. Exp. Immunol.* 197: 170–180.
65. Biniecka, M., M. Canavan, T. McGarry, W. Gao, J. McCormick, S. Cregan, L. Gallagher, T. Smith, J. J. Phelan, J. Ryan, J. O'Sullivan, C. T. Ng, D. J. Veale, and U. Fearon. 2016. Dysregulated bioenergetics: a key regulator of joint inflammation. *Ann. Rheum. Dis.* 75: 2192 LP – 2200.
66. McGarry, T., M. Biniecka, W. Gao, D. Cluxton, M. Canavan, S. Wade, S. Wade, L. Gallagher, C. Orr, D. J. Veale, and U. Fearon. 2017. Resolution of TLR2-induced inflammation through manipulation of metabolic pathways in Rheumatoid Arthritis. *Sci. Rep.* 7: 43165.
67. Mobasheri, A., M. P. Rayman, O. Gualillo, J. Sellam, P. van der Kraan, and U. Fearon. 2017. The role of metabolism in the pathogenesis of osteoarthritis. *Nat Rev Rheumatol* 13: 302–311.
68. Grishko, V. I., R. Ho, G. L. Wilson, and A. W. Pearsall. 2009. Diminished mitochondrial DNA integrity and repair capacity in OA chondrocytes. *Osteoarthritis Cartilage* 17: 107–113.
69. Gobelet, C., and J. C. Gerster. 1984. Synovial fluid lactate levels in septic and non-septic arthritides. *Ann. Rheum. Dis.* 43: 742–745.
70. Bulysheva, A. A., N. Sori, and M. P. Francis. 2018. Direct crystal formation from micronized bone and lactic acid: The writing on the wall for calcium-containing crystal pathogenesis in osteoarthritis? *PLoS One* 13: e0202373–e0202373.
71. Saïd-Sadier, N., and D. M. Ojcius. 2014. Alarmins, Inflammasomes and Immunity Pattern recognition receptors in innate immunity. 35: 437–449.
72. Chen, G. Y., and G. Nuñez. 2010. Sterile inflammation: Sensing and reacting to damage. *Nat. Rev. Immunol.* 10: 826–837.
73. Kumahashi, N., K. Naitou, H. Nishi, K. Oae, Y. Watanabe, S. Kuwata, M. Ochi, M. Ikeda, and Y. Uchio. 2011. Correlation of changes in pain intensity with synovial fluid adenosine triphosphate levels after treatment of patients with osteoarthritis of the knee with high-molecular-weight hyaluronic acid. *Knee* 18: 160–164.
74. Han, M. Y., J. J. Dai, Y. Zhang, Q. Lin, M. Jiang, X. Y. Xu, and Q. Liu. 2012. Identification of osteoarthritis biomarkers by proteomic analysis of synovial fluid. *J. Int.*

Med. Res. 40: 2243–2250.

75. Sunahori, K., M. Yamamura, J. Yamana, K. Takasugi, M. Kawashima, H. Yamamoto, W. J. Chazin, Y. Nakatani, S. Yui, and H. Makino. 2006. The S100A8/A9 heterodimer amplifies proinflammatory cytokine production by macrophages via activation of nuclear factor kappa B and p38 mitogen-activated protein kinase in rheumatoid arthritis. *Arthritis Res. Ther.* 8: 1–12.

76. García-Arnandis, I., M. I. Guillén, F. Gomar, J. P. Pelletier, J. Martel-Pelletier, and M. J. Alcaraz. 2010. High mobility group box 1 potentiates the pro-inflammatory effects of interleukin-1β in osteoarthritic synoviocytes. *Arthritis Res. Ther.* 12: 1–12.

77. Qin, Y., Y. Chen, W. Wang, Z. Wang, G. Tang, P. Zhang, Z. He, Y. Liu, S. M. Dai, and Q. Shen. 2014. HMGB1-LPS complex promotes transformation of osteoarthritis synovial fibroblasts to a rheumatoid arthritis synovial fibroblast-like phenotype. *Cell Death Dis.* 5: 1–10.

78. Kubo, T., C. A. Towle, H. J. Mankin, and B. V. Treadwell. 1985. Stress-induced proteins in chondrocytes from patients with osteoarthritis. *Arthritis Rheum.* 28: 1140–1145.

79. Takahashi, K., T. Kubo, Y. Arai, J. Imanishi, M. Kawata, and Y. Hirasawa. 1997. Localization of heat shock protein in osteoarthritic cartilage. *Scand. J. Rheumatol.* 26: 368–375.

80. Siebelt, M., H. Jahr, H. C. Groen, M. Sandker, J. H. Waarsing, N. Kops, C. Müller, W. Van Eden, M. De Jong, and H. Weinans. 2013. Hsp90 inhibition protects against biomechanically induced osteoarthritis in rats. *Arthritis Rheum.* 65: 2102–2112.

81. McCarthy, G. M., and A. Dunne. 2018. Calcium crystal deposition diseases — beyond gout. *Nat. Rev. Rheumatol.* 14: 592–602.

82. Zreiqat, H., D. Belluoccio, M. M. Smith, R. Wilson, L. A. Rowley, K. Jones, Y. Ramaswamy, T. Vogl, J. Roth, J. F. Bateman, and C. B. Little. 2010. S100A8 and S100A9 in experimental osteoarthritis. *Arthritis Res. Ther.* 12: R16.

83. Chen, Y. S., W. Yan, C. L. Geczy, M. A. Brown, and R. Thomas. 2009. Serum levels of soluble receptor for advanced glycation end products and of S100 proteins are associated with inflammatory, autoantibody, and classical risk markers of joint and vascular damage in rheumatoid arthritis. *Arthritis Res. Ther.* 11: 1–11.

84. Van Lent, P. L. E. M., L. Grevers, A. B. Blom, A. Sloetjes, J. S. Mort, T. Vogl, W.

Nacken, W. B. Van Den Berg, and J. Roth. 2008. Myeloid-related proteins S100A8/S100A9 regulate joint inflammation and cartilage destruction during antigen-induced arthritis. *Ann. Rheum. Dis.* 67: 1750–1758.

85. Van Lent, P. L. E. M., A. B. Blom, R. F. P. Schelbergen, A. Slöetjes, F. P. J. G. Lafeber, W. F. Lems, H. Cats, T. Vogl, J. Roth, and W. B. Van Den Berg. 2012. Active involvement of alarmins S100A8 and S100A9 in the regulation of synovial activation and joint destruction during mouse and human osteoarthritis. *Arthritis Rheum.* .

86. Schelbergen, R. F. P., W. De Munter, M. H. J. Van Den Bosch, F. P. J. G. Lafeber, A. Sloetjes, T. Vogl, J. Roth, W. B. Van Den Berg, P. M. Van Der Kraan, A. B. Blom, and P. L. E. M. Van Lent. 2016. Alarmins S100A8/S100A9 aggravate osteophyte formation in experimental osteoarthritis and predict osteophyte progression in early human symptomatic osteoarthritis. *Ann. Rheum. Dis.* 75: 218–225.

87. Van Lent, P. L. E. M., L. C. Grevers, A. B. Blom, O. J. Arntz, F. A. J. Van De Loo, P. Van Der Kraan, S. Abdollahi-Roodsaz, G. Srikrishna, H. Freeze, A. Sloetjes, W. Nacken, T. Vogl, J. Roth, and W. B. Van Den Berg. 2008. Stimulation of chondrocyte-mediated cartilage destruction by S100A8 in experimental murine arthritis. *Arthritis Rheum.* 58: 3776–3787.

88. Turovskaya, O., D. Foell, P. Sinha, T. Vogl, R. Newlin, J. Nayak, M. Nguyen, A. Olsson, P. P. Nawroth, A. Bierhaus, N. Varki, M. Kronenberg, H. H. Freeze, and G. Srikrishna. 2008. RAGE, carboxylated glycans and S100A8/A9 play essential roles in colitis-associated carcinogenesis. *Carcinogenesis* 29: 2035–2043.

89. Schelbergen, R. F. P., A. B. Blom, M. H. J. van den Bosch, A. Slöetjes, S. Abdollahi-Roodsaz, B. W. Schreurs, J. S. Mort, T. Vogl, J. Roth, W. B. van den Berg, and P. L. E. M. van Lent. 2012. Alarmins S100A8 and S100A9 elicit a catabolic effect in human osteoarthritic chondrocytes that is dependent on Toll-like receptor 4. *Arthritis Rheum.* 64: 1477–1487.

90. Liu, Y. Z., A. P. Jackson, and S. D. Cosgrove. 2009. Contribution of calcium-containing crystals to cartilage degradation and synovial inflammation in osteoarthritis. *Osteoarthr. Cartil.* 17: 1333–1340.

91. Ea, H. K., C. Nguyen, D. Bazin, A. Bianchi, J. Guicheux, P. Reboul, M. Daudon, and F. Lioté. 2011. Articular cartilage calcification in osteoarthritis: Insights into crystal-induced stress. *Arthritis Rheum.* 63: 10–18.

92. Stack, J., and G. McCarthy. 2016. Basic calcium phosphate crystals and osteoarthritis pathogenesis: Novel pathways and potential targets. *Curr. Opin. Rheumatol.* 28: 122–126.
93. Dreier, R. 2010. Hypertrophic differentiation of chondrocytes in osteoarthritis: The developmental aspect of degenerative joint disorders. *Arthritis Res. Ther.* 12: 216.
94. Conway, R., and G. M. McCarthy. 2018. Calcium-Containing Crystals and Osteoarthritis: an Unhealthy Alliance. *Curr. Rheumatol. Rep.* 20: 13.
95. McCarthy, G. M., J. A. Augustine, A. S. Baldwin, P. A. Christopherson, H. S. Cheung, P. R. Westfall, and R. I. Scheinman. 1998. Molecular Mechanism of Basic Calcium Phosphate Crystal-induced Activation of Human Fibroblasts: ROLE OF NUCLEAR FACTOR κB, ACTIVATOR PROTEIN 1, AND PROTEIN KINASE C. *J. Biol. Chem.* 273: 35161–35169.
96. Reuben, P. M., M. A. Brogley, Y. Sun, and H. S. Cheung. 2002. Molecular Mechanism of the Induction of Metalloproteinases 1 and 3 in Human Fibroblasts by Basic Calcium Phosphate Crystals. *J. Biol. Chem.* 277: 15190–15198.
97. Nasi, S., A. So, C. Combes, M. Daudon, and N. Busso. 2016. Interleukin-6 and chondrocyte mineralisation act in tandem to promote experimental osteoarthritis. *Ann. Rheum. Dis.* 75: 1372 LP – 1379.
98. Pazár, B., H.-K. Ea, S. Narayan, L. Kolly, N. Bagnoud, V. Chobaz, T. Roger, F. Lioté, A. So, and N. Busso. 2011. Basic Calcium Phosphate Crystals Induce Monocyte/Macrophage IL-1β Secretion through the NLRP3 Inflammasome In Vitro. *J. Immunol.* 186: 2495–2502.
99. Corr, E. M., C. C. Cunningham, L. Helbert, G. M. McCarthy, and A. Dunne. 2017. Osteoarthritis-associated basic calcium phosphate crystals activate membrane proximal kinases in human innate immune cells. *Arthritis Res. Ther.* 19: 23.
100. Cunningham, C. C., E. Mills, L. a. Mielke, L. K. O'Farrell, E. Lavelle, A. Mori, G. M. McCarthy, K. H. G. Mills, and A. Dunne. 2012. Osteoarthritis-associated basic calcium phosphate crystals induce pro-inflammatory cytokines and damage-associated molecules via activation of Syk and PI3 kinase. *Clin. Immunol.* 144: 228–236.
101. Jin, C., P. Frayssinet, R. Pelker, D. Cwirka, B. Hu, A. Vignery, S. C. Eisenbarth, and R. a Flavell. 2011. NLRP3 inflammasome plays a critical role in the pathogenesis of hydroxyapatite-associated arthropathy. *Proc. Natl. Acad. Sci. U. S. A.* 108: 14867–

14872.
102. Ea, H.-K., V. Chobaz, C. Nguyen, S. Nasi, P. van Lent, M. Daudon, A. Dessombz, D. Bazin, G. McCarthy, B. Jolles-Haeberli, A. Ives, D. Van Linthoudt, A. So, F. Lioté, and N. Busso. 2013. Pathogenic Role of Basic Calcium Phosphate Crystals in Destructive Arthropathies. *PLoS One* 8: e57352.
103. Nasi, S., H. K. Ea, A. So, and N. Busso. 2017. Revisiting the role of interleukin-1 pathway in osteoarthritis: Interleukin-1α and -1β, and NLRP3 inflammasome are not involved in the pathological features of the murine menisectomy model of osteoarthritis. *Front. Pharmacol.* 8: 282.
104. Cunningham, C. C., E. M. Corr, G. M. McCarthy, and A. Dunne. 2016. Intra-articular basic calcium phosphate and monosodium urate crystals inhibit anti-osteoclastogenic cytokine signalling. *Osteoarthr. Cartil.* 24: 2141–2152.
105. Nasi, S., H. K. Ea, F. Lioté, A. So, and N. Busso. 2016. Sodium thiosulfate prevents chondrocyte mineralization and reduces the severity of murine osteoarthritis. *PLoS One* 11: e0158196.
106. Qvist, P., A.-C. Bay-Jensen, C. Christiansen, E. B. Dam, P. Pastoureau, and M. A. Karsdal. 2008. The disease modifying osteoarthritis drug (DMOAD): Is it in the horizon? *Pharmacol. Res.* 58: 1–7.
107. Sinusas, K. 2012. Osteoarthritis: diagnosis and treatment. *Am. Fam. Physician* 85: 49–56.
108. Richardson, P. G., B. Barlogie, J. Berenson, S. Singhal, S. Jagannath, D. Irwin, S. V. Rajkumar, G. Srkalovic, M. Alsina, R. Alexanian, D. Siegel, R. Z. Orlowski, D. Kuter, S. A. Limentani, S. Lee, T. Hideshima, D.-L. Esseltine, M. Kauffman, J. Adams, D. P. Schenkein, and K. C. Anderson. 2003. A Phase 2 Study of Bortezomib in Relapsed, Refractory Myeloma. *N. Engl. J. Med.* 348: 2609–2617.
109. Fioravanti, A., M. Fabbroni, A. Cerase, and M. Galeazzi. 2009. Treatment of erosive osteoarthritis of the hands by intra-articular infliximab injections: A pilot study. *Rheumatol. Int.* 29: 961–965.
110. Berenbaum, F. 2010. Targeted therapies in osteoarthritis: a systematic review of the trials on www.clinicaltrials.gov. *Best Pract. Res. Clin. Rheumatol.* 24: 107–119.
111. Campbell, B. J. 2016. American Academy of Orthopaedic Surgeons. .
112. Rodriguez-Gonzalez, F. Á. 2009. Introduction to biomaterials in orthopaedic

surgery. *Biomater. Orthop. Surg.* 1–10.

113. Rajamaki, K., J. Lappalainen, K. Oorni, E. Valimaki, S. Matikainen, P. T. Kovanen, and K. K. Eklund. 2010. Cholesterol crystals activate the NLRP3 inflammasome in human macrophages: a novel link between cholesterol metabolism and inflammation. *PLoS One* 5: e11765.

114. Hallab, N. J., and J. J. Jacobs. 2009. Biologic Effects of Implant Debris. *Bull. NYU Hosp. Jt. Dis.* 67: 182–188.

115. Abu-Amer, Y., I. Darwech, and J. C. Clohisy. 2007. Aseptic loosening of total joint replacements: mechanisms underlying osteolysis and potential therapies. *Arthritis Res. Ther.* 9 Suppl 1: S6.

116. Howie, D. W., S. D. Neale, D. R. Haynes, O. T. Holubowycz, M. a. McGee, L. B. Solomon, S. a. Callary, G. J. Atkins, and D. M. Findlay. 2013. Periprosthetic osteolysis after total hip replacement: Molecular pathology and clinical management. *Inflammopharmacology* 21: 389–396.

117. Nich, C., Y. Takakubo, J. Pajarinen, M. Ainola, A. Salem, T. Sillat, A. J. Rao, M. Raska, Y. Tamaki, M. Takagi, Y. T. Konttinen, S. B. Goodman, and J. Gallo. 2013. Macrophages-Key cells in the response to wear debris from joint replacements. *J. Biomed. Mater. Res. A* 101: 3033–3045.

118. Schmalzried, T. P., M. Jasty, and W. H. Harris. 1992. Periprosthetic bone loss in total hip arthroplasty. Polyethylene wear debris and the concept of the effective joint space. *J. Bone Joint Surg. Am.* 74: 849–863.

119. Laquerriere, P., A. Grandjean-Laquerriere, E. Jallot, G. Balossier, P. Frayssinet, and M. Guenounou. 2003. Importance of hydroxyapatite particles characteristics on cytokines production by human monocytes in vitro. *Biomaterials* 24: 2739–2747.

120. Bitar, D. 2015. Biological response to prosthetic debris. *World J. Orthop.* 6: 172.

121. Pajarinen, J., V.-P. Kouri, E. Jämsen, T.-F. Li, J. Mandelin, and Y. T. Konttinen. 2013. The response of macrophages to titanium particles is determined by macrophage polarization. *Acta Biomater.* 9: 9229–9240.

122. Horowitz, S. M., S. B. Doty, J. M. Lane, and A. H. Burstein. 1993. Studies of the mechanism by which the mechanical failure of polymethylmethacrylate leads to bone resorption. *J. Bone Joint Surg. Am.* 75: 802–813.

123. Haynes, D. R., S. D. Rogers, S. Hay, M. J. Pearcy, and D. W. Howie. 1993. The

differences in toxicity and release of bone-resorbing mediators induced by titanium and cobalt-chromium-alloy wear particles. *J. Bone Joint Surg. Am.* 75: 825–834.
124. McKellop, H. A., P. Campbell, S. H. Park, T. P. Schmalzried, P. Grigoris, H. C. Amstutz, and A. Sarmiento. 1995. The origin of submicron polyethylene wear debris in total hip arthroplasty. *Clin. Orthop. Relat. Res.* 3–20.
125. Bitar, D., and J. Parvizi. 2015. Biological response to prosthetic debris. *World J. Orthop.* 6: 172–189.
126. Purdue, P. E., P. Koulouvaris, B. J. Nestor, and T. P. Sculco. 2006. The central role of wear debris in periprosthetic osteolysis. *HSS J.* 2: 102–113.
127. Noordin, S., and B. Masri. 2012. Periprosthetic osteolysis: Genetics, mechanisms and potential therapeutic interventions. *Can. J. Surg.* 55: 408–417.
128. Goodman, S. B. 2007. Wear particles, periprosthetic osteolysis and the immune system. *Biomaterials* 28: 5044–5048.
129. Farrera, C., K. Bhattacharya, B. Lazzaretto, F. T. Andon, K. Hultenby, G. P. Kotchey, A. Star, and B. Fadeel. 2014. Extracellular entrapment and degradation of single-walled carbon nanotubes. *Nanoscale* 6: 6974–6983.
130. Vitkov, L., W.-D. Krautgartner, A. Obermayer, W. Stoiber, M. Hannig, M. Klappacher, and D. Hartl. 2015. The initial inflammatory response to bioactive implants is characterized by NETosis. *PLoS One* 10: e0121359.
131. Jhunjhunwala, S., S. Aresta-DaSilva, K. Tang, D. Alvarez, M. J. Webber, B. C. Tang, D. M. Lavin, O. Veiseh, J. C. Doloff, S. Bose, A. Vegas, M. Ma, G. Sahay, A. Chiu, A. Bader, E. Langan, S. Siebert, J. Li, D. L. Greiner, P. E. Newburger, U. H. von Andrian, R. Langer, and D. G. Anderson. 2015. Neutrophil Responses to Sterile Implant Materials. *PLoS One* 10: e0137550.
132. Munoz, L. E., R. Bilyy, M. H. C. Biermann, D. Kienhofer, C. Maueroder, J. Hahn, J. M. Brauner, D. Weidner, J. Chen, M. Scharin-Mehlmann, C. Janko, R. P. Friedrich, D. Mielenz, T. Dumych, M. D. Lootsik, C. Schauer, G. Schett, M. Hoffmann, Y. Zhao, and M. Herrmann. 2016. Nanoparticles size-dependently initiate self-limiting NETosis-driven inflammation. *Proc. Natl. Acad. Sci. U. S. A.* 113: E5856–E5865.
133. Biermann, M. H. C., M. J. Podolska, J. Knopf, C. Reinwald, D. Weidner, C. Maueroder, J. Hahn, D. Kienhofer, A. Barras, R. Boukherroub, S. Szunerits, R. Bilyy, M. Hoffmann, Y. Zhao, G. Schett, M. Herrmann, and L. E. Munoz. 2016. Oxidative Burst-

Dependent NETosis Is Implicated in the Resolution of Necrosis-Associated Sterile Inflammation. *Front. Immunol.* 7: 557.

134. Purdue, P. E. 2008. Alternative macrophage activation in periprosthetic osteolysis. *Autoimmunity* 41: 212–217.

135. Blaine TA, Rosier RN, P. J. et al. 1996. Increased levels of Tumor Necrosis Factor Alpha and Interleukin-6 protein and messanger RNA in Human Peripheral Blood monocytes due to titanium particles. *J. bone Jt. surgery.* 78: 1181–1192.

136. Ren, W., S.-Y. Yang, and P. H. Wooley. 2004. A novel murine model of orthopaedic wear-debris associated osteolysis. *Scand. J. Rheumatol.* 33: 349–357.

137. Wooley, P. H., R. Morren, J. Andary, S. Sud, S. Y. Yang, L. Mayton, D. Markel, A. Sieving, and S. Nasser. 2002. Inflammatory responses to orthopaedic biomaterials in the murine air pouch. *Biomaterials* 23: 517–526.

138. Schwarz, E. M., E. B. Benz, a. P. Lu, J. J. Goater, a. V. Mollano, R. N. Rosier, J. E. Puzas, and R. J. O'Keefe. 2000. Quantitative small-animal surrogate to evaluate drug efficacy in preventing wear debris-induced osteolysis. *J. Orthop. Res.* 18: 849–855.

139. Ingham, E., and J. Fisher. 2005. The role of macrophages in osteolysis of total joint replacement. *Biomaterials* 26: 1271–1286.

140. Rao, A. J., E. Gibon, T. Ma, Z. Yao, R. L. Smith, and S. B. Goodman. 2012. Revision joint replacement, wear particles, and macrophage polarization. *Acta Biomater.* 8: 2815–2823.

141. Antonios, J. K., Z. Yao, C. Li, A. J. Rao, and S. B. Goodman. 2013. Macrophage polarization in response to wear particles in vitro. *Cell. Mol. Immunol.* 10: 471–82.

142. Sabokbar, A., I. Itonaga, S. G. Sun, O. Kudo, and N. a. Athanasou. 2005. Arthroplasty membrane-derived fibroblasts directly induce osteoclast formation and osteolysis in aseptic loosening. *J. Orthop. Res.* 23: 511–519.

143. Yao, J., T. T. Glant, M. W. Lark, K. Mikecz, J. J. Jacobs, N. I. Hutchinson, L. a Hoerrner, K. E. Kuettner, and J. O. Galante. 1995. The potential role of fibroblasts in periprosthetic osteolysis: fibroblast response to titanium particles. *J. Bone Miner. Res.* 10: 1417–1427.

144. Wei, X., X. Zhang, M. J. Zuscik, M. H. Drissi, E. M. Schwarz, and R. J. O'Keefe. 2005. Fibroblasts express RANKL and support osteoclastogenesis in a COX-2-dependent manner after stimulation with titanium particles. *J. Bone Miner. Res.* 20: 1136–1148.

145. Manlapaz, M., W. J. Maloney, and R. L. Smith. 1996. In vitro activation of human fibroblasts by retrieved titanium alloy wear debris. *J. Orthop. Res.* 14: 465–472.
146. Koreny, T., M. Tunyogi-Csapó, I. Gál, C. Vermes, J. J. Jacobs, and T. T. Glant. 2006. The role of fibroblasts and fibroblast-derived factors in periprosthetic osteolysis. *Arthritis Rheum.* 54: 3221–3232.
147. Lin, T. H., Y. Tamaki, J. Pajarinen, H. a. Waters, D. K. Woo, Z. Yao, and S. B. Goodman. 2014. Chronic inflammation in biomaterial-induced periprosthetic osteolysis: NF-κB as a therapeutic target. *Acta Biomater.* 10: 1–10.
148. Tamaki, Y., K. Sasaki, A. Sasaki, Y. Takakubo, H. Hasegawa, T. Ogino, Y. T. Konttinen, J. Salo, and M. Takagi. 2008. Enhanced osteolytic potential of monocytes/macrophages derived from bone marrow after particle stimulation. *J. Biomed. Mater. Res. B. Appl. Biomater.* 84: 191–204.
149. Ritchlin, C. T., E. M. Schwarz, R. J. O'Keefe, and R. J. Looney. 2004. RANK, RANKL and OPG in inflammatory arthritis and periprosthetic osteolysis. *J. Musculoskelet. Neuronal Interact.* 4: 276–284.
150. Haynes, D. R., T. N. Crotti, a E. Potter, M. Loric, G. J. Atkins, D. W. Howie, and D. M. Findlay. 2001. The osteoclastogenic molecules RANKL and RANK are associated with periprosthetic osteolysis. *J. Bone Joint Surg. Br.* 83: 902–911.
151. Veigl, D., J. Niederlová, and O. Kryštůfková. 2007. Periprosthetic osteolysis and its association with RANKL expression. *Physiol. Res.* 56: 455–462.
152. Childs, L. M., J. J. Goater, R. J. O'Keefe, and E. M. Schwarz. 2001. Efficacy of etanercept for wear debris-induced osteolysis. *J. Bone Miner. Res.* 16: 338–347.
153. Jeffrey Goater, J., R. J. O'Keefe, R. N. Rosier, J. Edward Puzas, and E. M. Schwarz. 2002. Efficacy of ex vivo OPG gene therapy in preventing wear debris induced osteolysis. *J. Orthop. Res.* 20: 169–173.
154. Yang, S.-Y., L. Mayton, B. Wu, J. J. Goater, E. M. Schwarz, and P. H. Wooley. 2002. Adeno-associated virus-mediated osteoprotegerin gene transfer protects against particulate polyethylene-induced osteolysis in a murine model. *Arthritis Rheum.* 46: 2514–2523.
155. Abbas, S., J. C. Clohisy, and Y. Abu-Amer. 2003. Mitogen-activated protein (MAP) kinases mediate PMMA-induction of osteoclasts. *J. Orthop. Res.* 21: 1041–1048.
156. Yamanaka, Y., Y. Abu-Amer, R. Faccio, and J. C. Clohisy. 2006. Map kinase c-JUN N-

terminal kinase mediates PMMA induction of osteoclasts. *J. Orthop. Res.* 24: 1349–1357.

157. Clohisy, J. C., Y. Yamanaka, R. Faccio, and Y. Abu-Amer. 2006. Inhibition of IKK activation, through sequestering NEMO, blocks PMMA-induced osteoclastogenesis and calvarial inflammatory osteolysis. *J. Orthop. Res.* 24: 1358–1365.

158. Rao, A. J., E. Gibon, T. Ma, Z. Yao, R. L. Smith, and S. B. Goodman. 2012. Acta Biomaterialia Revision joint replacement , wear particles , and macrophage polarization. *Acta Biomater.* 8: 2815–2823.

159. Carmody, E. E., E. M. Schwarz, J. E. Puzas, R. N. Rosier, and R. J. O'Keefe. 2002. Viral interleukin-10 gene inhibition of inflammation, osteoclastogenesis, and bone resorption in response to titanium particles. *Arthritis Rheum.* 46: 1298–1308.

160. Fleisch, H. A. 1997. Bisphosphonates: Preclinical aspects and use in osteoporosis. *Ann. Med.* 29: 55–62.

161. Trevisan, C., V. Nava, M. Mattavelli, and C. G. Parra. 2013. Bisphosphonate treatment for osteolysis in total hip arthroplasty. A report of four cases. *Clin. Cases Miner. Bone Metab.* 10: 61–64.

162. Teng, S., C. Yi, C. Krettek, and M. Jagodzinski. 2015. Bisphosphonate Use and Risk of Implant Revision after Total Hip/Knee Arthroplasty: A Meta-Analysis of Observational Studies. *PLoS One* 10: e0139927.

163. Horowitz, S. M., S. A. Algan, and M. A. Purdon. 1996. Pharmacologic inhibition of particulate-induced bone resorption. *J. Biomed. Mater. Res.* 31: 91–96.

164. Shanbhag, A. S., C. T. Hasselman, and H. E. Rubash. 1997. The John Charnley Award. Inhibition of wear debris mediated osteolysis in a canine total hip arthroplasty model. *Clin. Orthop. Relat. Res.* 33–43.

165. von Knoch, F., A. Heckelei, C. Wedemeyer, G. Saxler, G. Hilken, F. Henschke, F. Loer, and M. von Knoch. 2005. The effect of simvastatin on polyethylene particle-induced osteolysis. *Biomaterials* 26: 3549–3555.

166. Ulrich-Vinther, M., E. E. Carmody, J. J. Goater, K. Soøballe, R. J. O'Keefe, and E. M. Schwarz. 2002. Recombinant adeno-associated virus-mediated osteoprotegerin gene therapy inhibits wear debris-induced osteolysis. *J. Bone Jt. Surg. - Ser. A* 84: 1405–1412.

167. Schwarz, E. M., D. Campbell, S. Totterman, A. Boyd, R. J. O'Keefe, and R. J. Looney.

2003. Use of volumetric computerized tomography as a primary outcome measure to evaluate drug efficacy in the prevention of peri-prosthetic osteolysis: A 1-year clinical pilot of etanercept vs. placebo. *J. Orthop. Res.* 21: 1049–1055.
168. Pollice, P. F., R. N. Rosier, R. J. Looney, J. E. Puzas, E. M. Schwarz, and R. J. O'Keefe. 2001. Oral pentoxifylline inhibits release of tumor necrosis factor-alpha from human peripheral blood monocytes : a potential treatment for aseptic loosening of total joint components. *J. Bone Joint Surg. Am.* 83-A: 1057–1061.
169. Yannaki, E., A. Papadopoulou, E. Athanasiou, P. Kaloyannidis, A. Paraskeva, D. Bougiouklis, P. Palladas, M. Yiangou, and A. Anagnostopoulos. 2010. The proteasome inhibitor bortezomib drastically affects inflammation and bone disease in adjuvant-induced arthritis in rats. *Arthritis Rheum.* 62: 3277–3288.
170. Lee, S. W., J. H. Kim, Y. B. Park, and S. K. Lee. 2009. Bortezomib attenuates murine collagen-induced arthritis. *Ann. Rheum. Dis.* 68: 1761–1767.
171. Steadman, J. R., W. G. Rodkey, and K. K. Briggs. 2010. Microfracture: Its history and experience of the developing surgeon. *Cartilage* 1: 78–86.
172. Minas, T., T. Ogura, and T. Bryant. 2016. Autologous chondrocyte implantation. *JBJS Essent. Surg. Tech.* 6: 1–11.
173. Matsusue, Y., T. Yamamuro, and H. Hama. 1993. Arthroscopic multiple osteochondral transplantation to the chondral defect in the knee associated with anterior cruciate ligament disruption. *Arthroscopy* 9: 318–321.
174. Ulstein, S., A. Årøen, J. H. Røtterud, S. Løken, L. Engebretsen, and S. Heir. 2014. Microfracture technique versus osteochondral autologous transplantation mosaicplasty in patients with articular chondral lesions of the knee: A prospective randomized trial with long-term follow-up. *Knee Surgery, Sport. Traumatol. Arthrosc.* 22: 1207–1215.
175. Huey, D. J., J. C. Hu, and K. Athanasiou. 2012. Unlike bone, cartilage regeneration remains elusive. *Science* 338: 917–21.
176. Johnstone, B., M. Alini, M. Cucchiarini, G. R. Dodge, D. Eglin, F. Guilak, H. Madry, A. Mata, R. L. Mauck, C. E. Semino, and M. J. Stoddart. 2013. Tissue engineering for articular cartilage repair - the state of the art. *Eur. Cell. Mater.* 25: 248–67.
177. Newman, A. P. 1998. Articular cartilage repair. *Am. J. Sports Med.* 26: 309–324.
178. Murphy, C. M., F. J. O'Brien, D. G. Little, and A. Schindeler. 2013. Cell-scaffold

interactions in the bone tissue engineering triad. *Eur. Cells Mater.* 26: 120–132.
179. Le Blanc, K., and D. Mougiakakos. 2012. Multipotent mesenchymal stromal cells and the innate immune system. *Nat. Rev. Immunol.* 12: 383–396.
180. Glenn, J. D. 2014. Mesenchymal stem cells: Emerging mechanisms of immunomodulation and therapy. *World J. Stem Cells* 6: 526.
181. Lennon, D. P., and A. I. Caplan. 2006. Isolation of human marrow-derived mesenchymal stem cells. *Exp. Hematol.* 34: 1604–1605.
182. Farrell, E., F. J. O'Brien, P. Doyle, J. Fischer, I. Yannas, B. A. Harley, B. O'Connell, P. J. Prendergast, and V. A. Campbell. 2006. A collagen-glycosaminoglycan scaffold supports adult rat mesenchymal stem cell differentiation along osteogenic and chondrogenic routes. *Tissue Eng.* 12: 459–468.
183. Caplan, A. I. 2005. Review: mesenchymal stem cells: cell-based reconstructive therapy in orthopedics. *Tissue Eng.* 11: 1198–1211.
184. Uccelli, A., L. Moretta, and V. Pistoia. 2006. Immunoregulatory function of mesenchymal stem cells. *Eur. J. Immunol.* 36: 2566–2573.
185. Shi, Y., J. Su, A. I. Roberts, P. Shou, A. B. Rabson, and G. Ren. 2012. How mesenchymal stem cells interact with tissue immune responses. *Trends Immunol.* 33: 136–143.
186. Gao, C., J. Seuntjens, G. N. Kaufman, N. Tran-Khanh, A. Butler, A. Li, H. Wang, M. D. Buschmann, E. J. Harvey, and J. E. Henderson. 2012. Mesenchymal stem cell transplantation to promote bone healing. *J. Orthop. Res.* 30: 1183–1189.
187. Vinardell, T., E. J. Sheehy, C. T. Buckley, and D. J. Kelly. 2012. A comparison of the functionality and in vivo phenotypic stability of cartilaginous tissues engineered from different stem cell sources. *Tissue Eng. - Part A* 18: 1161–1170.
188. Savkovic, V., H. Li, J.-K. Seon, M. Hacker, and S. F. and J.-C. Simon. 2014. Mesenchymal Stem Cells in Cartilage Regeneration. *Curr. Stem Cell Res. Ther.* 9: 469–488.
189. Mestres, G., M. Espanol, W. Xia, C. Persson, M.-P. Ginebra, and M. K. Ott. 2015. Inflammatory response to nano- and microstructured hydroxyapatite. *PLoS One* 10: e0120381.
190. Yamasaki, H., and H. Sakai. 1992. Osteogenic response to porous hydroxyapatite ceramics under the skin of dogs. *Biomaterials* 13: 308–312.

191. Klein, C., K. de Groot, W. Chen, Y. Li, and X. Zhang. 1994. Osseous substance formation induced in porous calcium phosphate ceramics in soft tissues. *Biomaterials* 15: 31–34.
192. Webster, T. J., R. W. Siegel, and R. Bizios. 1999. Osteoblast adhesion on nanophase ceramics. *Biomaterials* 20: 1221–1227.
193. Webster, T. J., C. Ergun, R. H. Doremus, R. W. Siegel, and R. Bizios. 2000. Specific proteins mediate enhanced osteoblast adhesion on nanophase ceramics. *J. Biomed. Mater. Res.* 51: 475–483.
194. Gonzalez-Fernandez, T., B. N. Sathy, C. Hobbs, G. M. Cunniffe, H. O. McCarthy, N. J. Dunne, V. Nicolosi, F. J. O'Brien, and D. J. Kelly. 2017. Mesenchymal stem cell fate following non-viral gene transfection strongly depends on the choice of delivery vector. *Acta Biomater.* 55: 226–238.
195. Badylak, S. F. 2007. The extracellular matrix as a biologic scaffold material. *Biomaterials* 28: 3587–3593.
196. Badylak, S. F. 2005. Regenerative medicine and developmental biology: the role of the extracellular matrix. *Anat. Rec. B. New Anat.* 287: 36–41.
197. Gilbert, T. W. 2012. Strategies for tissue and organ decellularization. *J. Cell. Biochem.* 113: 2217–2222.
198. Caplan, A. I. 1986. The extracellular matrix is instructive. *Bioessays* 5: 129–132.
199. Sawkins, M. J., W. Bowen, P. Dhadda, H. Markides, L. E. Sidney, A. J. Taylor, F. R. A. J. Rose, S. F. Badylak, K. M. Shakesheff, and L. J. White. 2013. Hydrogels derived from demineralized and decellularized bone extracellular matrix. *Acta Biomater.* 9: 7865–7873.
200. Sadtler, K., A. Singh, M. T. Wolf, X. Wang, D. M. Pardoll, and J. H. Elisseeff. 2016. Design, clinical translation and immunological response of biomaterials in regenerative medicine. *Nat. Rev. Mater.* 1.
201. Sridharan, R., A. R. Cameron, D. J. Kelly, C. J. Kearney, and F. J. O'Brien. 2015. Biomaterial based modulation of macrophage polarization: a review and suggested design principles. *Mater. Today* 18: 313–325.
202. Laboratories, B. 2016. Macrophage Polarization Mini Review. .
203. Badylak, S. F., J. E. Valentin, A. K. Ravindra, G. P. McCabe, and A. M. Stewart-Akers. 2008. Macrophage phenotype as a determinant of biologic scaffold remodeling.

Tissue Eng. Part A 14: 1835–1842.
204. Brown, B. N., J. E. Valentin, A. M. Stewart-Akers, G. P. McCabe, and S. F. Badylak. 2009. Macrophage phenotype and remodeling outcomes in response to biologic scaffolds with and without a cellular component. *Biomaterials* 30: 1482–1491.
205. Godwin, J. W., A. R. Pinto, and N. A. Rosenthal. 2013. Macrophages are required for adult salamander limb regeneration. *Proc. Natl. Acad. Sci. U. S. A.* 110: 9415–9420.
206. Brown, B. N., R. Londono, S. Tottey, L. Zhang, K. a. Kukla, M. T. Wolf, K. a. Daly, J. E. Reing, and S. F. Badylak. 2012. Macrophage phenotype as a predictor of constructive remodeling following the implantation of biologically derived surgical mesh materials. *Acta Biomater.* 8: 978–987.
207. Sicari, B. M., J. L. Dziki, B. F. Siu, C. J. Medberry, C. L. Dearth, and S. F. Badylak. 2014. The promotion of a constructive macrophage phenotype by solubilized extracellular matrix. *Biomaterials* 35: 8605–8612.
208. Julier, Z., A. J. Park, P. S. Briquez, and M. M. Martino. 2017. Promoting tissue regeneration by modulating the immune system. *Acta Biomater.* 53: 13–28.
209. Reinke, S., S. Geissler, W. R. Taylor, K. Schmidt-Bleek, K. Juelke, V. Schwachmeyer, M. Dahne, T. Hartwig, L. Akyüz, C. Meisel, N. Unterwalder, N. B. Singh, P. Reinke, N. P. Haas, H.-D. Volk, and G. N. Duda. 2013. Terminally Differentiated CD8⁺ T Cells Negatively Affect Bone Regeneration in Humans. *Sci. Transl. Med.* 5: 177ra36 LP-177ra36.
210. Liu, Y., L. Wang, T. Kikuiri, K. Akiyama, C. Chen, X. Xu, R. Yang, W. J. Chen, S. Wang, and S. Shi. 2011. Mesenchymal stem cell-based tissue regeneration is governed by recipient T lymphocytes via IFN-γ and TNF-α. *Nat. Med.* 17: 1594–1601.
211. Toben, D., I. Schroeder, T. El Khassawna, M. Mehta, J.-E. Hoffmann, J.-T. Frisch, H. Schell, J. Lienau, A. Serra, A. Radbruch, and G. N. Duda. 2011. Fracture healing is accelerated in the absence of the adaptive immune system. *J. Bone Miner. Res.* 26: 113–124.
212. Nosbaum, A., N. Prevel, H.-A. Truong, P. Mehta, M. Ettinger, T. C. Scharschmidt, N. H. Ali, M. L. Pauli, A. K. Abbas, and M. D. Rosenblum. 2016. Cutting Edge: Regulatory T Cells Facilitate Cutaneous Wound Healing. *J. Immunol.* 196: 2010–2014.
213. Lai, L. W., K. C. Yong, and Y. H. H. Lien. 2012. Pharmacologic recruitment of regulatory T cells as a therapy for ischemic acute kidney injury. *Kidney Int.* 81: 983–

992.
214. Gandolfo, M. T., H. R. Jang, S. M. Bagnasco, G. J. Ko, P. Agreda, M. J. Soloski, M. T. Crow, and H. Rabb. 2010. Mycophenolate mofetil modifies kidney tubular injury and Foxp3+ regulatory T cell trafficking during recovery from experimental ischemia-reperfusion. *Transpl. Immunol.* 23: 45–52.
215. Burzyn, D., W. Kuswanto, D. Kolodin, J. L. Shadrach, M. Cerletti, Y. Jang, E. Sefik, T. G. Tan, A. J. Wagers, C. Benoist, and D. Mathis. 2013. A Special Population of regulatory T Cells Potentiates muscle repair. *Cell* 155: 1282–1295.
216. Jameson, J., K. Ugarte, N. Chen, P. Yachi, E. Fuchs, R. Boismenu, and W. L. Havran. 2002. A Role for Skin γδ T Cells in Wound Repair. *Science (80-.).* 296: 747 LP – 749.
217. Ono, T., K. Okamoto, T. Nakashima, T. Nitta, S. Hori, Y. Iwakura, and H. Takayanagi. 2016. IL-17-producing γδT cells enhance bone regeneration. *Nat. Commun.* 7: 1–9.
218. Arpaia, N., J. A. Green, B. Moltedo, A. Arvey, S. Hemmers, S. Yuan, P. M. Treuting, and A. Y. Rudensky. 2015. A Distinct Function of Regulatory T Cells in Tissue Protection. *Cell* 162: 1078–1089.
219. Evans, R. W., H. S. Cheung, and D. J. McCarty. 1984. Cultured human monocytes and fibroblasts solubilize calcium phosphate crystals. *Calcif. Tissue Int.* 36: 645–650.
220. Cunniffe, G. M., F. J. O'Brien, S. Partap, T. J. Levingstone, K. T. Stanton, and G. R. Dickson. 2010. The synthesis and characterization of nanophase hydroxyapatite using a novel dispersant-aided precipitation method. *J. Biomed. Mater. Res. A* 95: 1142–1149.
221. Daly, A. C., P. Pitacco, J. Nulty, G. M. Cunniffe, and D. J. Kelly. 2018. 3D printed microchannel networks to direct vascularisation during endochondral bone repair. *Biomaterials* 162: 34–46.
222. Loeser, R. F., J. A. Collins, and B. O. Diekman. 2016. Ageing and the pathogenesis of osteoarthritis. *Nat Rev Rheumatol* 12: 412–420.
223. Mobasheri, A. 2013. The Future of Osteoarthritis Therapeutics: Targeted Pharmacological Therapy. *Curr. Rheumatol. Rep.* 15: 364.
224. Pearce, E. L., and E. J. Pearce. 2013. Metabolic pathways in immune cell activation and quiescence. *Immunity* 38: 633–643.
225. Pearce, E. L., M. C. Poffenberger, C.-H. Chang, and R. G. Jones. 2013. Fueling immunity: insights into metabolism and lymphocyte function. *Science* 342: 1242454.

226. Loftus, R. M., and D. K. Finlay. 2016. Immunometabolism: Cellular Metabolism Turns Immune Regulator. *J. Biol. Chem.* 291: 1–10.
227. San-Millán, I., and G. A. Brooks. 2017. Reexamining cancer metabolism: Lactate production for carcinogenesis could be the purpose and explanation of the Warburg Effect. *Carcinogenesis* 38: 119–133.
228. Palsson-McDermott, E. M., and L. A. J. O'Neill. 2013. The Warburg effect then and now: From cancer to inflammatory diseases. *BioEssays* 35: 965–973.
229. Dang, E. V, J. Barbi, H.-Y. Yang, D. Jinasena, H. Yu, Y. Zheng, Z. Bordman, J. Fu, Y. Kim, H.-R. Yen, W. Luo, K. Zeller, L. Shimoda, S. L. Topalian, G. L. Semenza, C. V Dang, D. M. Pardoll, and F. Pan. 2011. Control of T(H)17/T(reg) balance by hypoxia-inducible factor 1. *Cell* 146: 772–784.
230. Russell, D. G., L. Huang, and B. C. VanderVen. 2019. Immunometabolism at the interface between macrophages and pathogens. *Nat. Rev. Immunol.* .
231. Osborn, O., and J. M. Olefsky. 2012. The cellular and signaling networks linking the immune system and metabolism in disease. *Nat Med* 18: 363–374.
232. Yin, Y., S.-C. Choi, Z. Xu, D. J. Perry, H. Seay, B. P. Croker, E. S. Sobel, T. M. Brusko, and L. Morel. 2015. Normalization of CD4+ T cell metabolism reverses lupus. *Sci. Transl. Med.* 7: 274ra18 LP-274ra18.
233. Lee, C.-F., Y.-C. Lo, C.-H. Cheng, G. J. Furtmüller, B. Oh, V. Andrade-Oliveira, A. G. Thomas, C. E. Bowman, B. S. Slusher, M. J. Wolfgang, G. Brandacher, and J. D. Powell. 2017. Preventing Allograft Rejection by Targeting Immune Metabolism. *Cell Rep.* 13: 760–770.
234. Bettencourt, I. A., and J. D. Powell. 2017. Targeting Metabolism as a Novel Therapeutic Approach to Autoimmunity, Inflammation, and Transplantation. *J. Immunol.* 198: 999 LP – 1005.
235. June, R. K., R. Liu-Bryan, F. Long, and T. M. Griffin. 2016. Emerging role of metabolic signaling in synovial joint remodeling and osteoarthritis. *J. Orthop. Res.* 34: 2048–2058.
236. Liu-Bryan, R. 2015. Inflammation and intracellular metabolism: new targets in OA. *Osteoarthr. Cartil.* 23: 1835–1842.
237. Kluzek, S., J. L. Newton, and N. K. Arden. 2015. Is osteoarthritis a metabolic disorder? *Br. Med. Bull.* 115: 111–121.

238. Rachow, J. W., L. M. Ryan, D. J. Mccarty, and P. C. Halverson. 1988. Synovial fluid inorganic pyrophosphate concentration and nucleotide pyrophosphohydrolase activity in basic calcium phosphate deposition arthropathy and milwaukee shoulder syndrome. *Arthritis Rheum.* 31: 408–413.

239. Dalbeth, N., T. Smith, B. Nicolson, B. Clark, K. Callon, D. Naot, D. O. Haskard, F. M. McQueen, I. R. Reid, and J. Cornish. 2008. Enhanced osteoclastogenesis in patients with tophaceous gout: Urate crystals promote osteoclast development through interactions with stromal cells. *Arthritis Rheum.* 58: 1854–1865.

240. Desai, J., S. Steiger, and H. J. Anders. 2017. Molecular Pathophysiology of Gout. *Trends Mol. Med.* 23: 756–768.

241. Lai, S., and X. Zhou. 2013. Inflammatory Cells in Tissues of Gout Patients and Their Correlations with Comorbidities. *Open Rheumatol. J.* 7: 26–31.

242. Jay, S. M., E. A. Skokos, J. Zeng, K. Knox, and T. R. Kyriakides. 2010. Macrophage fusion leading to foreign body giant cell formation persists under phagocytic stimulation by microspheres in vitro and in vivo in mouse models. *J. Biomed. Mater. Res. - Part A* 93: 189–199.

243. Nadra, I., J. C. Mason, P. Philippidis, O. Florey, C. D. W. Smythe, G. M. McCarthy, R. C. Landis, and D. O. Haskard. 2005. Proinflammatory activation of macrophages by basic calcium phosphate crystals via protein kinase C and MAP kinase pathways: A vicious cycle of inflammation and arterial calcification? *Circ. Res.* 96: 1248–1256.

244. Bertani, F. R., P. Mozetic, M. Fioramonti, M. Iuliani, G. Ribelli, F. Pantano, D. Santini, G. Tonini, M. Trombetta, L. Businaro, S. Selci, and A. Rainer. 2017. Classification of M1/M2-polarized human macrophages by label-free hyperspectral reflectance confocal microscopy and multivariate analysis. *Sci. Rep.* 7: 1–9.

245. Liu, B., M. Zhang, J. Zhao, M. Zheng, and H. Yang. 2018. Imbalance of M1/M2 macrophages is linked to severity level of knee osteoarthritis. *Exp. Ther. Med.* 16: 5009–5014.

246. Dominguez-Gutierrez, P. R., S. Kusmartsev, B. K. Canales, and S. R. Khan. 2018. Calcium Oxalate Differentiates Human Monocytes Into Inflammatory M1 Macrophages. *Front. Immunol.* 9: 1863.

247. Ng, G., K. Sharma, S. M. Ward, M. D. Desrosiers, L. A. Stephens, W. M. Schoel, T. Li, C. A. Lowell, C.-C. Ling, M. W. Amrein, and Y. Shi. 2008. Receptor-Independent,

Direct Membrane Binding Leads to Cell-Surface Lipid Sorting and Syk Kinase Activation in Dendritic Cells. *Immunity* 29: 807–818.
248. Corr, E. M., C. C. Cunningham, L. Helbert, G. M. McCarthy, and A. Dunne. 2017. Osteoarthritis-associated basic calcium phosphate crystals activate membrane proximal kinases in human innate immune cells. *Arthritis Res. Ther.* 19.
249. Banchereau, J., F. Briere, C. Caux, J. Davoust, S. Lebecque, Y. Liu, B. Pulendran, and K. Palucka. 2000. Mmunobiology of. *Annu. Rev. Immunol.* 18: 767–811.
250. Schulz, D., Y. Severin, V. R. T. Zanotelli, and B. Bodenmiller. 2019. In-Depth Characterization of Monocyte-Derived Macrophages using a Mass Cytometry-Based Phagocytosis Assay. *Sci. Rep.* 9: 1925.
251. Murray, P. J., J. E. Allen, S. K. Biswas, E. A. Fisher, D. W. Gilroy, S. Goerdt, S. Gordon, J. A. Hamilton, L. B. Ivashkiv, T. Lawrence, M. Locati, A. Mantovani, F. O. Martinez, J.-L. Mege, D. M. Mosser, G. Natoli, J. P. Saeij, J. L. Schultze, K. A. Shirey, A. Sica, J. Suttles, I. Udalova, J. A. van Ginderachter, S. N. Vogel, and T. A. Wynn. 2014. Macrophage Activation and Polarization: Nomenclature and Experimental Guidelines. *Immunity* 41: 14–20.
252. Roszer, T. 2015. Understanding the Mysterious M2 Macrophage through Activation Markers and Effector Mechanisms. *Mediators Inflamm.* 2015: 816460.
253. Van den Bossche, J., L. A. O'Neill, and D. Menon. 2017. Macrophage Immunometabolism: Where Are We (Going)? *Trends Immunol.* 38: 395–406.
254. Krawczyk, C. M., T. Holowka, J. Sun, J. Blagih, E. Amiel, R. J. DeBerardinis, J. R. Cross, E. Jung, C. B. Thompson, R. G. Jones, and E. J. Pearce. 2010. Toll-like receptor-induced changes in glycolytic metabolism regulate dendritic cell activation. *Blood* 115: 4742–4749.
255. Bonora, M., S. Patergnani, A. Rimessi, E. de Marchi, J. M. Suski, A. Bononi, C. Giorgi, S. Marchi, S. Missiroli, F. Poletti, M. R. Wieckowski, and P. Pinton. 2012. ATP synthesis and storage. *Purinergic Signal.* 8: 343–357.
256. Aderem, A. 2003. Phagocytosis and the Inflammatory Response. *J. Infect. Dis.* 187: S340–S345.
257. Sharp, F. A., D. Ruane, B. Claass, E. Creagh, J. Harris, P. Malyala, M. Singh, D. T. O'Hagan, V. Pétrilli, J. Tschopp, L. A. J. O'Neill, and E. C. Lavelle. 2009. Uptake of particulate vaccine adjuvants by dendritic cells activates the NALP3 inflammasome.

Proc. Natl. Acad. Sci. U. S. A. 106: 870–875.

258. Marie-Anaïs, F., J. Mazzolini, F. Herit, and F. Niedergang. 2016. Dynamin-Actin Cross Talk Contributes to Phagosome Formation and Closure. *Traffic* 17: 487–499.

259. Kelly, B., and L. A. J. O'Neill. 2015. Metabolic reprogramming in macrophages and dendritic cells in innate immunity. *Cell Res.* 25: 771–784.

260. Everts, B., E. Amiel, S. C. C. Huang, A. M. Smith, C. H. Chang, W. Y. Lam, V. Redmann, T. C. Freitas, J. Blagih, G. J. W. Van Der Windt, M. N. Artyomov, R. G. Jones, E. L. Pearce, and E. J. Pearce. 2014. TLR-driven early glycolytic reprogramming via the kinases TBK1-IKKε supports the anabolic demands of dendritic cell activation. *Nat. Immunol.* 15: 323–332.

261. Malinarich, F., K. Duan, R. A. Hamid, A. Bijin, W. X. Lin, M. Poidinger, A.-M. Fairhurst, and J. E. Connolly. 2015. High Mitochondrial Respiration and Glycolytic Capacity Represent a Metabolic Phenotype of Human Tolerogenic Dendritic Cells. *J. Immunol.* 194: 5174–5186.

262. McCarthy, G. M., P. R. Westfall, I. Masuda, P. A. Christopherson, H. S. Cheung, and P. G. Mitchell. 2001. Basic calcium phosphate crystals activate human osteoarthritic synovial fibroblasts and induce matrix metalloproteinase-13 (collagenase-3) in adult porcine articular chondrocytes. *Ann. Rheum. Dis.* 60: 399 LP – 406.

263. Bai, G., D. S. Howell, G. A. Howard, B. A. Roos, and H. S. Cheung. 2001. Basic calcium phosphate crystals up-regulate metalloproteinases but down-regulate tissue inhibitor of metalloproteinase-1 and -2 in human fibroblasts. *Osteoarthr. Cartil.* 9: 416–422.

264. Morgan, M. P., L. C. Whelan, J. D. Sallis, C. J. McCarthy, D. J. Fitzgerald, and G. M. McCarthy. 2004. Basic calcium phosphate crystal–induced prostaglandin E2 production in human fibroblasts: Role of cyclooxygenase 1, cyclooxygenase 2, and interleukin-1β. *Arthritis Rheum.* 50: 1642–1649.

265. Björk, P., A. Björk, T. Vogl, M. Stenström, D. Liberg, A. Olsson, J. Roth, F. Ivars, and T. Leanderson. 2009. Identification of human S100A9 as a novel target for treatment of autoimmune disease via binding to quinoline-3-carboxamides. *PLoS Biol.* 7: 0800–0812.

266. Schelbergen, R. F., E. J. Geven, M. H. J. Van Den Bosch, H. Eriksson, T. Leanderson, T. Vogl, J. Roth, F. A. J. Van De Loo, M. I. Koenders, P. M. Van Der Kraan, W. B. Van Den

Berg, A. B. Blom, and P. L. E. M. Van Lent. 2015. Prophylactic treatment with S100A9 inhibitor paquinimod reduces pathology in experimental collagenase-induced osteoarthritis. *Ann. Rheum. Dis.* 74: 2254–2258.

267. Cesaro, A., N. Anceriz, A. Plante, N. Pagé, M. R. Tardif, and P. A. Tessier. 2012. An Inflammation Loop Orchestrated by S100A9 and Calprotectin Is Critical for Development of Arthritis. *PLoS One* 7.

268. Bengtsson, A. A., G. Sturfelt, C. Lood, L. Rönnblom, R. F. Van Vollenhoven, B. Axelsson, B. Sparre, H. Tuvesson, M. W. Öhman, and T. Leanderson. 2012. Pharmacokinetics, tolerability, and preliminary efficacy of paquinimod (ABR-215757), a new quinoline-3-carboxamide derivative: Studies in lupus-prone mice and a multicenter, randomized, double-blind, placebo-controlled, repeat-dose, dose-ranging study in . *Arthritis Rheum.* 64: 1579–1588.

269. Ruan, G., J. Xu, K. Wang, S. Zheng, J. Wu, F. Bian, B. Chang, Y. Zhang, T. Meng, Z. Zhu, W. Han, and C. Ding. 2019. Associations between serum IL-8 and knee symptoms, joint structures, and cartilage or bone biomarkers in patients with knee osteoarthritis. *Clin. Rheumatol.* 38: 3609–3617.

270. Pierzchala, A. W., D. J. Kusz, and G. Hajduk. 2011. CXCL8 and CCL5 expression in synovial fluid and blood serum in patients with osteoarthritis of the knee. *Arch. Immunol. Ther. Exp. (Warsz).* 59: 151–155.

271. Takahashi, A., M. C. de Andres, K. Hashimoto, E. Itoi, and R. O. Oreffo. 2015. Epigenetic regulation of interleukin-8, an inflammatory chemokine, in osteoarthritis. *Osteoarthr. Cartil.* 23: A191–A192.

272. Haraden, C. A., J. L. Huebner, M. F. Hsueh, Y. J. Li, and V. B. Kraus. 2019. Synovial fluid biomarkers associated with osteoarthritis severity reflect macrophage and neutrophil related inflammation. *Arthritis Res. Ther.* 21: 1–9.

273. Bonnet, C. S., and D. A. Walsh. 2005. Osteoarthritis, angiogenesis and inflammation. *Rheumatology* 44: 7–16.

274. Kraan, M. C., D. D. Patel, J. J. Haringman, M. D. Smith, H. Weedon, M. J. Ahern, F. C. Breedveld, and P. P. Tak. 2001. The development of clinical signs of rheumatoid synovial inflammation is associated with increased synthesis of the chemokine CXCL8 (interleukin-8). *Arthritis Res.* 3: 65–71.

275. Wang, S., R. Song, Z. Wang, Z. Jing, S. Wang, and J. Ma. 2018. S100A8/A9 in

Inflammation . *Front. Immunol.* 9: 1298.

276. Johnson, K., A. Jung, A. Murphy, A. Andreyev, J. Dykens, and R. Terkeltaub. 2000. Mitochondrial oxidative phosphorylation is a downstream regulator of nitric oxide effects on chondrocyte matrix synthesis and mineralization. *Arthritis Rheum.* 43: 1560–1570.

277. Wang, Y., X. Zhao, M. Lotz, R. Terkeltaub, and R. Liu-Bryan. 2015. Mitochondrial Biogenesis Is Impaired in Osteoarthritis Chondrocytes but Reversible via Peroxisome Proliferator–Activated Receptor γ Coactivator 1α. *Arthritis Rheumatol.* 67: 2141–2153.

278. Maneiro, E., M. A. Martín, M. C. de Andres, M. J. López-Armada, J. L. Fernández-Sueiro, P. del Hoyo, F. Galdo, J. Arenas, and F. J. Blanco. 2003. Mitochondrial respiratory activity is altered in osteoarthritic human articular chondrocytes. *Arthritis Rheum.* 48: 700–708.

279. Blanco, F. J., M. J. López-Armada, and E. Maneiro. 2004. Mitochondrial dysfunction in osteoarthritis. *Mitochondrion* 4: 715–728.

280. Muz, B., H. Larsen, L. Madden, S. Kiriakidis, and E. M. Paleolog. 2012. Prolyl hydroxylase domain enzyme 2 is the major player in regulating hypoxic responses in rheumatoid arthritis. *Arthritis Rheum.* 64: 2856–2867.

281. Tsai, C.-H., Y.-C. Chiang, H.-T. Chen, P.-H. Huang, H.-C. Hsu, and C.-H. Tang. 2013. High glucose induces vascular endothelial growth factor production in human synovial fibroblasts through reactive oxygen species generation. *Biochim. Biophys. Acta - Gen. Subj.* 1830: 2649–2658.

282. Ren, K., A. Dusad, Y. Zhang, and D. Wang. 2013. Therapeutic intervention for wear debris-induced aseptic implant loosening. *Acta Pharm. Sin. B* 3: 76–85.

283. Huang, Z., T. Ma, P.-G. Ren, R. L. Smith, and S. B. Goodman. 2010. Effects of orthopedic polymer particles on chemotaxis of macrophages and mesenchymal stem cells. *J. Biomed. Mater. Res. Part A* 94A: 1264–1269.

284. Ren, P.-G., A. Irani, Z. Huang, T. Ma, S. Biswal, and S. B. Goodman. 2011. Continuous Infusion of UHMWPE Particles Induces Increased Bone Macrophages and Osteolysis. *Clin. Orthop. Relat. Res.* 469: 113–122.

285. Ren, P.-G., S.-W. Lee, S. Biswal, and S. B. Goodman. 2008. Systemic trafficking of macrophages induced by bone cement particles in nude mice. *Biomaterials* 29: 4760–4765.

286. Ingham, E., T. R. Green, M. H. Stone, R. Kowalski, N. Watkins, and J. Fisher. 2000. Production of TNF-α and bone resorbing activity by macrophages in response to different types of bone cement particles. *Biomaterials* 21: 1005–1013.
287. Blaine, T. A., R. N. Rosier, J. E. Puzas, R. J. Looney, P. R. Reynolds, S. D. Reynolds, and R. J. O'Keefe. 1996. Increased levels of tumor necrosis factor-alpha and interleukin-6 protein and messenger RNA in human peripheral blood monocytes due to titanium particles. *J. Bone Joint Surg. Am.* 78: 1181–1192.
288. Goodman, S. B., P. Huie, Y. Song, D. Schurman, W. Maloney, S. Woolson, and R. Sibley. 1998. Cellular profile and cytokine production at prosthetic interfaces: Study of tissues retrieved from revised hip and knee replacements. *J. Bone Jt. Surg.* 80: 531–539.
289. Nakashima, Y., D. H. Sun, M. C. Trindade, W. J. Maloney, S. B. Goodman, D. J. Schurman, and R. L. Smith. 1999. Signaling pathways for tumor necrosis factor-alpha and interleukin-6 expression in human macrophages exposed to titanium-alloy particulate debris in vitro. *J. Bone Joint Surg. Am.* 81: 603–615.
290. Merkel, K. D., J. M. Erdmann, K. P. McHugh, Y. Abu-Amer, F. P. Ross, and S. L. Teitelbaum. 1999. Tumor Necrosis Factor-α Mediates Orthopedic Implant Osteolysis. *Am. J. Pathol.* 154: 203–210.
291. Mandelin, J., T. F. Li, M. Liljestrom, M. E. Kroon, R. Hanemaaijer, S. Santavirta, and Y. T. Konttinen. 2003. Imbalance of RANKL/RANK/OPG system in interface tissue in loosening of total hip replacement. *J. Bone Joint Surg. Br.* 85: 1196–1201.
292. Haynes, D. R., T. N. Crotti, and H. Zreiqat. 2004. Regulation of osteoclast activity in peri-implant tissues. *Biomaterials* 25: 4877–4885.
293. Zhang, X., S. G. Morham, R. Langenbach, D. a Young, L. Xing, B. F. Boyce, E. J. Puzas, R. N. Rosier, R. J. O'Keefe, and E. M. Schwarz. 2001. Evidence for a direct role of cyclo-oxygenase 2 in implant wear debris-induced osteolysis. *J. bone Miner. Res.* 16: 660–70.
294. Im, G.-I., B.-C. Kwon, and K.-B. Lee. 2004. The effect of COX-2 inhibitors on periprosthetic osteolysis. *Biomaterials* 25: 269–275.
295. Cunniffe, G. M., C. M. Curtin, E. M. Thompson, G. R. Dickson, and F. J. O'Brien. 2016. Content-Dependent Osteogenic Response of Nanohydroxyapatite: An in Vitro and in Vivo Assessment within Collagen-Based Scaffolds. *ACS Appl. Mater. Interfaces* 8:

23477–23488.
296. Goodman, S. B., Z. Yao, M. Keeney, and F. Yang. 2013. The future of biologic coatings for orthopaedic implants. *Biomaterials* 34: 3174–3183.
297. Malik, A. F., R. Hoque, X. Ouyang, A. Ghani, E. Hong, K. Khan, L. B. Moore, G. Ng, F. Munro, R. A. Flavell, Y. Shi, T. R. Kyriakides, and W. Z. Mehal. 2011. Inflammasome components Asc and caspase-1 mediate biomaterial-induced inflammation and foreign body response. *Proc. Natl. Acad. Sci.* 108: 20095–20100.
298. Yue, H., W. Wei, Z. Yue, P. Lv, L. Wang, G. Ma, and Z. Su. 2010. Particle size affects the cellular response in macrophages. *Eur. J. Pharm. Sci.* 41: 650–657.
299. Murray, P. J., J. E. Allen, S. K. Biswas, E. A. Fisher, D. W. Gilroy, S. Goerdt, S. Gordon, J. A. Hamilton, L. B. Ivashkiv, T. Lawrence, M. Locati, A. Mantovani, F. O. Martinez, J.-L. Mege, D. M. Mosser, G. Natoli, J. P. Saeij, J. L. Schultze, K. A. Shirey, A. Sica, J. Suttles, I. Udalova, J. A. van Ginderachter, S. N. Vogel, and T. A. Wynn. 2014. Macrophage activation and polarization: nomenclature and experimental guidelines. *Immunity* 41: 14–20.
300. Corr, E. M., C. C. Cunningham, and A. Dunne. 2016. Cholesterol crystals activate Syk and PI3 kinase in human macrophages and dendritic cells. *Atherosclerosis* 251: 197–205.
301. Shanbhag, A. S., A. M. Kaufman, K. Hayata, and H. E. Rubash. 2007. Assessing osteolysis with use of high-throughput protein chips. *J. Bone Joint Surg. Am.* 89: 1081–1089.
302. Wang, H., T.-H. Jia, N. Zacharias, W. Gong, H.-X. Du, P. H. Wooley, and S.-Y. Yang. 2013. Combination gene therapy targeting on interleukin-1[beta] and RANKL for wear debris-induced aseptic loosening. *Gene Ther* 20: 128–135.
303. Christo, S. N., K. R. Diener, J. Manavis, M. A. Grimbaldeston, A. Bachhuka, K. Vasilev, and J. D. Hayball. 2016. Inflammasome components ASC and AIM2 modulate the acute phase of biomaterial implant-induced foreign body responses. *Sci. Rep.* 6: 20635.
304. Narayan, S., B. Pazar, H.-K. Ea, L. Kolly, N. Bagnoud, V. Chobaz, F. Lioté, T. Vogl, D. Holzinger, A. Kai-Lik So, and N. Busso. 2011. Octacalcium phosphate crystals induce inflammation in vivo through interleukin-1 but independent of the NLRP3 inflammasome in mice. *Arthritis Rheum.* 63: 422–433.

305. Lin, Y.-C., D.-Y. Huang, J.-S. Wang, Y.-L. Lin, S.-L. Hsieh, K.-C. Huang, and W.-W. Lin. 2015. Syk is involved in NLRP3 inflammasome-mediated caspase-1 activation through adaptor ASC phosphorylation and enhanced oligomerization. *J. Leukoc. Biol.* 97: 825–835.

306. King, W. G., M. D. Mattaliano, T. O. Chan, P. N. Tsichlis, and J. S. Brugge. 1997. Phosphatidylinositol 3-kinase is required for integrin-stimulated AKT and Raf-1/mitogen-activated protein kinase pathway activation. *Mol. Cell. Biol.* 17: 4406–4418.

307. Mócsai, A., J. Ruland, and V. L. J. Tybulewicz. 2010. The SYK tyrosine kinase: a crucial player in diverse biological functions. *Nat Rev Immunol* 10: 387–402.

308. Wang, Y., S. Von Euw, F. M. Fernandes, S. Cassaignon, M. Selmane, G. Laurent, G. Pehau-Arnaudet, C. Coelho, L. Bonhomme-Coury, M.-M. Giraud-Guille, F. Babonneau, T. Azaïs, and N. Nassif. 2013. Water-mediated structuring of bone apatite. *Nat. Mater.* 12: 1144–1153.

309. Von Euw, S., Y. Wang, G. Laurent, C. Drouet, F. Babonneau, N. Nassif, and T. Azaïs. 2019. Bone mineral: new insights into its chemical composition. *Sci. Rep.* 9: 8456.

310. Lebre, F., R. Sridharan, M. J. Sawkins, D. J. Kelly, F. J. O'Brien, and E. C. Lavelle. 2017. The shape and size of hydroxyapatite particles dictate inflammatory responses following implantation. *Sci. Rep.* 7: 2922.

311. Oleszycka, E., S. McCluskey, F. A. Sharp, N. Muñoz-Wolf, E. Hams, A. L. Gorman, P. G. Fallon, and E. C. Lavelle. 2018. The vaccine adjuvant alum promotes IL-10 production that suppresses Th1 responses. *Eur. J. Immunol.* 48: 705–715.

312. Xu, J., Y. Yang, G. Qiu, G. Lai, Z. Wu, D. E. Levy, and Y. Ding. 2009. c-Maf Regulates IL-10 Expression during Th17 polarization. *Journal* 48: 5437–5447.

313. Cao, S., J. Liu, L. Song, and X. Ma. 2005. The Protooncogene c-Maf Is an Essential Transcription Factor for IL-10 Gene Expression in Macrophages. *J. Immunol.* 174: 3484–3492.

314. Rostam, H. M., P. M. Reynolds, M. R. Alexander, N. Gadegaard, and A. M. Ghaemmaghami. 2017. Image based Machine Learning for identification of macrophage subsets. *Sci. Rep.* 7: 1–11.

315. Shayan, M., J. Padmanabhan, A. H. Morris, B. Cheung, R. Smith, J. Schroers, and T. R. Kyriakides. 2018. Nanopatterned bulk metallic glass-based biomaterials modulate macrophage polarization. *Acta Biomater.* 75: 427–438.

316. Foroozandeh, P., and A. A. Aziz. 2018. Insight into Cellular Uptake and Intracellular Trafficking of Nanoparticles. *Nanoscale Res. Lett.* 13.

317. Blacker, T. S., Z. F. Mann, J. E. Gale, M. Ziegler, A. J. Bain, G. Szabadkai, and M. R. Duchen. 2014. Separating NADH and NADPH fluorescence in live cells and tissues using FLIM. *Nat. Commun.* 5.

318. Takeda, N., E. L. O'Dea, A. Doedens, J. W. Kim, A. Weidemann, C. Stockmann, M. Asagiri, M. C. Simon, A. Hoffmann, and R. S. Johnson. 2010. Differential activation and antagonistic function of HIF-α isoforms in macrophages are essential for NO homeostasis. *Genes Dev.* 24: 491–501.

319. Tan, H. Y., N. Wang, S. Li, M. Hong, X. Wang, and Y. Feng. 2016. The Reactive Oxygen Species in Macrophage Polarization: Reflecting Its Dual Role in Progression and Treatment of Human Diseases. *Oxid. Med. Cell. Longev.* 2016.

320. Teeny, S. M., S. C. York, J. W. Mesko, and R. E. Rea. 2003. Long-term follow-up care recommendations after total hip and knee arthroplasty. *J. Arthroplasty* 18: 954–962.

321. Kurtz, S., K. Ong, E. Lau, F. Mowat, and M. Halpern. 2007. Projections of primary and revision hip and knee arthroplasty in the United States from 2005 to 2030. *J. Bone Joint Surg. Am.* 89: 780–5.

322. Sedlik, C., D. Orbach, P. Veron, E. Schweighoffer, F. Colucci, R. Gamberale, A. Ioan-Facsinay, S. Verbeek, P. Ricciardi-Castagnoli, C. Bonnerot, V. L. J. Tybulewicz, J. Di Santo, and S. Amigorena. 2003. A Critical Role for Syk Protein Tyrosine Kinase in Fc Receptor-Mediated Antigen Presentation and Induction of Dendritic Cell Maturation. *J. Immunol.* 170: 846 LP – 852.

323. Flach, T. L., G. Ng, A. Hari, M. D. Desrosiers, P. Zhang, S. M. Ward, M. E. Seamone, A. Vilaysane, A. D. Mucsi, Y. Fong, E. Prenner, C. C. Ling, J. Tschopp, D. A. Muruve, M. W. Amrein, and Y. Shi. 2011. Alum interaction with dendritic cell membrane lipids is essential for its adjuvanticity. *Nat Med* 17: 479–487.

324. Desaulniers, P., M. Fernandes, C. Gilbert, S. G. Bourgoin, and P. H. Naccache. 2001. Crystal-induced neutrophil activation. VII. Involvement of Syk in the responses to monosodium urate crystals. *J. Leukoc. Biol.* 70: 659–668.

325. Nagao, G., K. Ishii, K. Hirota, K. Makino, and H. Terada. 2010. Role of lipid rafts in phagocytic uptake of polystyrene latex microspheres by macrophages. *Anticancer Res.*

30: 3167–3176.
326. Cui, X., T. Liang, C. Liu, Y. Yuan, and J. Qian. 2016. Correlation of particle properties with cytotoxicity and cellular uptake of hydroxyapatite nanoparticles in human gastric cancer cells. *Mater. Sci. Eng. C* 67: 453–460.
327. Nabi, I. R., and P. U. Le. 2003. Caveolae/raft-dependent endocytosis. *J. Cell Biol.* 161: 673–677.
328. Kou, L., J. Sun, Y. Zhai, and Z. He. 2013. The endocytosis and intracellular fate of nanomedicines: Implication for rational design. *Asian J. Pharm. Sci.* 8: 1–10.
329. Subtil, A., I. Gaidarov, K. Kobylarz, M. A. Lampson, J. H. Keen, and T. E. Mcgraw. 1999. Acute cholesterol depletion inhibits clathrin-coated pit budding. *Proc. Natl. Acad. Sci. U. S. A.* 96: 6775–6780.
330. Grimmer, S., B. van Deurs, and K. Sandvig. 2002. Membrane ruffling and macropinocytosis in A431 cells require cholesterol. *J. Cell Sci.* 115: 2953–2962.
331. Lai, S. K., K. Hida, S. T. Man, C. Chen, C. Machamer, T. A. Schroer, and J. Hanes. 2007. Privileged delivery of polymer nanoparticles to the perinuclear region of live cells via a non-clathrin, non-degradative pathway. *Biomaterials* 28: 2876–2884.
332. Rakshit, D. S., K. Ly, T. K. Sengupta, B. J. Nestor, T. P. Sculco, L. B. Ivashkiv, and P. E. Purdue. 2006. Wear Debris Inhibition of Anti-Osteoclastogenic Signaling by Interleukin-6 and Interferon-γ: Mechanistic Insights and Implications for Periprosthetic Osteolysis. *JBJS* 88.
333. Moreau, M. F., C. Guillet, P. Massin, S. Chevalier, H. Gascan, M. F. Basle, and D. Chappard. 2007. Comparative effects of five bisphosphonates on apoptosis of macrophage cells in vitro. *Biochem. Pharmacol.* 73: 718–723.
334. Millett, P. J., M. J. Allen, and M. P. G. Bostrom. 2002. Effects of alendronate on particle-induced osteolysis in a rat model. *J. Bone Joint Surg. Am.* 84-A: 236–249.
335. von Knoch, M., C. Wedemeyer, A. Pingsmann, F. von Knoch, G. Hilken, C. Sprecher, F. Henschke, B. Barden, and F. Loer. 2005. The decrease of particle-induced osteolysis after a single dose of bisphosphonate. *Biomaterials* 26: 1803–1808.
336. Fleisch, H. A. 1997. Bisphosphonates: preclinical aspects and use in osteoporosis. *Ann. Med.* 29: 55–62.
337. Bi, F., Z. Shi, C. Zhou, A. Liu, Y. Shen, and S. Yan. 2015. Intermittent Administration of Parathyroid Hormone [1-34] Prevents Particle-Induced Periprosthetic Osteolysis in a

Rat Model. *PLoS One* 10: e0139793.

338. Ren, K., A. Dusad, Y. Zhang, and D. Wang. 2013. Therapeutic intervention for wear debris-induced aseptic implant loosening. *Acta Pharm. Sin. B* 3: 76–85.

339. Weinblatt, M. E., A. Kavanaugh, R. Burgos-Vargas, A. H. Dikranian, G. Medrano-Ramirez, J. L. Morales-Torres, F. T. Murphy, T. K. Musser, N. Straniero, A. V Vicente-Gonzales, and E. Grossbard. 2008. Treatment of rheumatoid arthritis with a syk kinase inhibitor: A twelve-week, randomized, placebo-controlled trial. *Arthritis Rheum.* 58: 3309–3318.

340. Zwerina, J., S. Hayer, M. Tohidast-Akrad, H. Bergmeister, K. Redlich, U. Feige, C. Dunstan, G. Kollias, G. Steiner, J. Smolen, and G. Schett. 2004. Single and combined inhibition of tumor necrosis factor, interleukin-1, and RANKL pathways in tumor necrosis factor–induced arthritis: Effects on synovial inflammation, bone erosion, and cartilage destruction. *Arthritis Rheum.* 50: 277–290.

341. Glimcher, M. J. 2006. Bone: Nature of the Calcium Phosphate Crystals and Cellular, Structural, and Physical Chemical Mechanisms in Their Formation. *Rev. Mineral. Geochemistry* 64: 223–282.

342. Von Euw, S., W. Ajili, T.-H.-C. Chan-Chang, A. Delices, G. Laurent, F. Babonneau, N. Nassif, and T. Azaïs. 2017. Amorphous surface layer versus transient amorphous precursor phase in bone – A case study investigated by solid-state NMR spectroscopy. *Acta Biomater.* 59: 351–360.

343. Rey, C., C. Combes, C. Drouet, H. Sfihi, and A. Barroug. 2007. Physico-chemical properties of nanocrystalline apatites: Implications for biominerals and biomaterials. *Mater. Sci. Eng. C* 27: 198–205.

344. Schoenenberger, A. D., A. Schipanski, V. Malheiro, M. Kucki, J. G. Snedeker, P. Wick, and K. Maniura-Weber. 2016. Macrophage Polarization by Titanium Dioxide (TiO_2) Particles: Size Matters. *ACS Biomater. Sci. Eng.* 2: 908–919.

345. Dos Santos, T., J. Varela, I. Lynch, A. Salvati, and K. A. Dawson. 2011. Quantitative assessment of the comparative nanoparticle-uptake efficiency of a range of cell lines. *Small* 7: 3341–3349.

346. Desai, M. P., V. Labhasetwar, E. Walter, R. J. Levy, and G. L. Amidon. 1997. The mechanism of uptake of biodegradable microparticles in Caco-2 cells is size dependent. *Pharm. Res.* 14: 1568–1573.

347. Kumari, S., S. Mg, and S. Mayor. 2010. Endocytosis unplugged: Multiple ways to enter the cell. *Cell Res.* 20: 256–275.
348. Oh, N., and J. H. Park. 2014. Endocytosis and exocytosis of nanoparticles in mammalian cells. *Int. J. Nanomedicine* 9: 51–63.
349. Dutta, D., and J. G. Donaldson. 2012. Search for inhibitors of endocytosis. *Cell. Logist.* 2: 203–208.
350. Ma, C., M. L. Kuzma, X. Bai, and J. Yang. 2019. Biomaterial-Based Metabolic Regulation in Regenerative Engineering. *Adv. Sci.* 6.
351. Reilly, G. C., and A. J. Engler. 2010. Intrinsic extracellular matrix properties regulate stem cell differentiation. *J. Biomech.* 43: 55–62.
352. Murphy, C. M., A. Matsiko, M. G. Haugh, J. P. Gleeson, and F. J. O'Brien. 2012. Mesenchymal stem cell fate is regulated by the composition and mechanical properties of collagen–glycosaminoglycan scaffolds. *J. Mech. Behav. Biomed. Mater.* 11: 53–62.
353. Lee, J.-H., H.-K. Park, and K. S. Kim. 2016. Intrinsic and extrinsic mechanical properties related to the differentiation of mesenchymal stem cells. *Biochem. Biophys. Res. Commun.* 473: 752–757.
354. Sadtler, K., K. Estrellas, B. W. Allen, M. T. Wolf, H. Fan, A. J. Tam, C. H. Patel, B. S. Luber, H. Wang, K. R. Wagner, J. D. Powell, F. Housseau, D. M. Pardoll, and J. H. Elisseeff. 2016. Developing a pro-regenerative biomaterial scaffold microenvironment requires T helper 2 cells. *Science* 352: 366–370.
355. Grotenhuis, N., S. F. H. De Witte, G. J. V. M. van Osch, Y. Bayon, J. F. Lange, and Y. M. Bastiaansen-Jenniskens. 2016. Biomaterials Influence Macrophage–Mesenchymal Stem Cell Interaction *In Vitro*. *Tissue Eng. Part A* 22: 1098–1107.
356. Glass, G. E., J. K. Chan, A. Freidin, M. Feldmann, N. J. Horwood, and J. Nanchahal. 2011. TNF- promotes fracture repair by augmenting the recruitment and differentiation of muscle-derived stromal cells. *Proc. Natl. Acad. Sci.* 108: 1585–1590.
357. Hashimoto, J., H. Yoshikawa, K. Takaoka, N. Shimizu, K. Masuhara, T. Tsuda, S. Miyamoto, and K. Ono. 1989. Inhibitory effects of tumor necrosis factor alpha on fracture healing in rats. *Bone* 10: 453–457.
358. Schlundt, C., T. El Khassawna, A. Serra, A. Dienelt, S. Wendler, H. Schell, N. van Rooijen, A. Radbruch, R. Lucius, S. Hartmann, G. N. Duda, and K. Schmidt-Bleek. 2015.

Macrophages in bone fracture healing: Their essential role in endochondral ossification. *Bone* .

359. Almeida, H. V., G. M. Cunniffe, T. Vinardell, C. T. Buckley, F. J. O'Brien, and D. J. Kelly. 2015. Coupling Freshly Isolated CD44 + Infrapatellar Fat Pad-Derived Stromal Cells with a TGF-β3 Eluting Cartilage ECM-Derived Scaffold as a Single-Stage Strategy for Promoting Chondrogenesis. *Adv. Healthc. Mater.* n/a-n/a.

360. Benders, K. E. M., P. R. van Weeren, S. F. Badylak, D. B. F. Saris, W. J. A. Dhert, and J. Malda. 2013. Extracellular matrix scaffolds for cartilage and bone regeneration. *Trends Biotechnol.* 31: 169–176.

361. Cunniffe, G. M., G. R. Dickson, S. Partap, K. T. Stanton, and F. J. O'Brien. 2010. Development and characterisation of a collagen nano-hydroxyapatite composite scaffold for bone tissue engineering. *J. Mater. Sci. Mater. Med.* 21: 2293–2298.

362. Filipowska, J., K. A. Tomaszewski, Ł. Niedźwiedzki, J. A. Walocha, and T. Niedźwiedzki. 2017. The role of vasculature in bone development, regeneration and proper systemic functioning. *Angiogenesis* 20: 291–302.

363. Ponte, A. L., E. Marais, N. Gallay, A. Langonne, B. Delorme, O. Herault, P. Charbord, and J. Domenech. 2007. The in vitro migration capacity of human bone marrow mesenchymal stem cells: comparison of chemokine and growth factor chemotactic activities. *Stem Cells* 25: 1737–1745.

364. Chiu, L. L. Y., and M. Radisic. 2010. Scaffolds with covalently immobilized VEGF and Angiopoietin-1 for vascularization of engineered tissues. *Biomaterials* 31: 226–241.

365. Lacey, D. C., P. J. Simmons, S. E. Graves, and J. A. Hamilton. 2009. Proinflammatory cytokines inhibit osteogenic differentiation from stem cells: implications for bone repair during inflammation. *Osteoarthr. Cartil.* 17: 735–742.

366. Martino, M. M., K. Maruyama, G. A. Kuhn, T. Satoh, O. Takeuchi, R. Muller, and S. Akira. 2016. Inhibition of IL-1R1/MyD88 signalling promotes mesenchymal stem cell-driven tissue regeneration. *Nat. Commun.* 7: 11051.

367. Hess, K., A. Ushmorov, J. Fiedler, R. E. Brenner, and T. Wirth. 2009. TNFalpha promotes osteogenic differentiation of human mesenchymal stem cells by triggering the NF-kappaB signaling pathway. *Bone* 45: 367–376.

368. Crapo, P. M., T. W. Gilbert, and S. F. Badylak. 2011. An overview of tissue and

whole organ decellularization processes. *Biomaterials* 32: 3233–43.
369. Browe, D. C., A. Dunne, C. T. Buckley, and D. J. Kelly. Glyoxal cross-linking of solubilised extracellular matrix to produce highly porous , elastic and chondro-permissive scaffolds for orthopaedic tissue engineering. .
370. Cunniffe, G. M., P. J. Diaz-Payno, J. S. Ramey, O. R. Mahon, A. Dunne, E. M. Thompson, F. J. O'Brien, and D. J. Kelly. 2017. Growth plate extracellular matrix-derived scaffolds for large bone defect healing. *Eur. Cell. Mater.* 33: 130–142.
371. Cunniffe, G. M., P. J. Díaz-Payno, E. J. Sheehy, S. E. Critchley, H. V. Almeida, P. Pitacco, S. F. Carroll, O. R. Mahon, A. Dunne, T. J. Levingstone, C. J. Moran, R. T. Brady, F. J. O'Brien, P. A. J. Brama, and D. J. Kelly. 2018. Tissue-specific extracellular matrix scaffolds for the regeneration of spatially complex musculoskeletal tissues. *Biomaterials* 188: 63–73.
372. Landsman, L., L. Bar-on, A. Zernecke, K. Kim, R. Krauthgamer, S. A. Lira, I. L. Weissman, C. Weber, S. Jung, W. Dc, and E. Shagdarsuren. 2009. CX3CR1 is required for monocyte homeostasis and atherogenesis by promoting cell survival. *Blood* 113: 963–972.
373. Geissmann, F., S. Jung, and D. R. Littman. 2018. Blood Monocytes Consist of Two Principal Subsets with Distinct Migratory Properties Frederic. *Immunity* 129: 470–485.
374. Spiller, K. L., S. Nassiri, C. E. Witherel, R. R. Anfang, J. Ng, K. R. Nakazawa, T. Yu, and G. Vunjak-Novakovic. 2015. Sequential delivery of immunomodulatory cytokines to facilitate the M1-to-M2 transition of macrophages and enhance vascularization of bone scaffolds. *Biomaterials* 37: 194–207.
375. Schmidt-Bleek, K., H. Schell, N. Schulz, P. Hoff, C. Perka, F. Buttgereit, H. D. Volk, J. Lienau, and G. N. Duda. 2012. Inflammatory phase of bone healing initiates the regenerative healing cascade. *Cell Tissue Res.* 347: 567–573.
376. Spiller, K. L., R. R. Anfang, K. J. Spiller, J. Ng, K. R. Nakazawa, J. W. Daulton, and G. Vunjak-Novakovic. 2014. The role of macrophage phenotype in vascularization of tissue engineering scaffolds. *Biomaterials* 35: 4477–4488.
377. Jetten, N., S. Verbruggen, M. J. Gijbels, M. J. Post, M. P. J. De Winther, and M. M. P. C. Donners. 2014. Anti-inflammatory M2, but not pro-inflammatory M1 macrophages promote angiogenesis in vivo. *Angiogenesis* 17: 109–118.
378. Gerstenfeld, L. C., D. M. Cullinane, G. L. Barnes, D. T. Graves, and T. A. Einhorn.

2003. Fracture healing as a post-natal developmental process: molecular, spatial, and temporal aspects of its regulation. *J. Cell. Biochem.* 88: 873–884.
379. Kon, T., T. J. Cho, T. Aizawa, M. Yamazaki, N. Nooh, D. Graves, L. C. Gerstenfeld, and T. A. Einhorn. 2001. Expression of osteoprotegerin, receptor activator of NF-kappaB ligand (osteoprotegerin ligand) and related proinflammatory cytokines during fracture healing. *J. Bone Miner. Res.* 16: 1004–1014.
380. Dimitriou, R., E. Tsiridis, and P. V. Giannoudis. 2005. Current concepts of molecular aspects of bone healing. *Injury* 36: 1392–1404.
381. Cheng, N.-C., B. T. Estes, H. A. Awad, and F. Guilak. 2009. Chondrogenic differentiation of adipose-derived adult stem cells by a porous scaffold derived from native articular cartilage extracellular matrix. *Tissue Eng. Part A* 15: 231–241.
382. Jung, Y.-K., G.-W. Kim, H.-R. Park, E.-J. Lee, J.-Y. Choi, F. Beier, and S.-W. Han. 2013. Role of interleukin-10 in endochondral bone formation in mice: anabolic effect via the bone morphogenetic protein/Smad pathway. *Arthritis Rheum.* 65: 3153–3164.
383. Muller, R. D., T. John, B. Kohl, A. Oberholzer, T. Gust, A. Hostmann, M. Hellmuth, D. Laface, B. Hutchins, G. Laube, R. W. Veh, S. K. Tschoeke, W. Ertel, and G. Schulze-Tanzil. 2008. IL-10 overexpression differentially affects cartilage matrix gene expression in response to TNF-alpha in human articular chondrocytes in vitro. *Cytokine* 44: 377–385.
384. Wernike, E., M. O. Montjovent, Y. Liu, D. Wismeijer, E. B. Hunziker, K. A. Siebenrock, W. Hofstetter, and F. M. Klenke. 2010. Vegf incorporated into calcium phosphate ceramics promotes vascularisation and bone formation in vivo. *Eur. Cells Mater.* 19: 30–40.
385. Conway, E., D. Collen, and P. Carmeliet. 2001. Molecular mechanisms of blood vessel formation. *Trends Biochem. Sci.* 22: 251–256.
386. Shen, Y. H., M. S. Shoichet, and M. Radisic. 2008. Vascular endothelial growth factor immobilized in collagen scaffold promotes penetration and proliferation of endothelial cells. *Acta Biomater.* 4: 477–489.
387. Sridharan, R., B. Cavanagh, A. R. Cameron, D. J. Kelly, and F. J. O'Brien. 2019. Material stiffness influences the polarization state, function and migration mode of macrophages. *Acta Biomater.* 89: 47–59.
388. Almeida, H. V, A. D. Dikina, K. J. Mulhall, F. J. O'Brien, E. Alsberg, and D. J. Kelly.

2017. Porous Scaffolds Derived from Devitalized Tissue Engineered Cartilaginous Matrix Support Chondrogenesis of Adult Stem Cells. *ACS Biomater. Sci. Eng.* 3: 1075–1082.

389. Park, Y., J. Lee, J.-Y. Kwak, K. Noh, E. Yim, H.-K. Kim, Y. J. Kim, H. E. Broxmeyer, and J.-A. Kim. 2017. Fractalkine induces angiogenic potential in CX3CR1-expressing monocytes. *J. Leukoc. Biol.* jlb.1A0117-002RR.

390. Avolio, E., V. V. Alvino, M. T. Ghorbel, and P. Campagnolo. 2017. Perivascular cells and tissue engineering: Current applications and untapped potential. *Pharmacol. Ther.* 171: 83–92.

391. Metheny-Barlow, L. J., and L. Y. Li. 2003. The enigmatic role of angiopoietin-1 in tumor angiogenesis. *Cell Res.* 13: 309–317.

392. Glass, K. A., J. M. Link, J. M. Brunger, F. T. Moutos, C. A. Gersbach, and F. Guilak. 2014. Tissue-engineered cartilage with inducible and tunable immunomodulatory properties. *Biomaterials* 35: 5921–5931.

393. Dumont, C. M., J. Park, and L. D. Shea. 2015. Controlled release strategies for modulating immune responses to promote tissue regeneration. *J. Control. Release* 219: 155–166.

394. Holladay, C., K. Power, M. Sefton, T. O'Brien, W. M. Gallagher, and A. Pandit. 2011. Functionalized scaffold-mediated interleukin 10 gene delivery significantly improves survival rates of stem cells in vivo. *Mol. Ther.* 19: 969–978.

395. Arden, N., and M. C. Nevitt. 2006. Osteoarthritis: epidemiology. *Best Pract. Res. Clin. Rheumatol.* 20: 3–25.

396. Attur, M. G., I. R. Patel, R. N. Patel, S. B. Abramson, and A. R. Amin. 1998. Autocrine production of IL-1 beta by human osteoarthritis-affected cartilage and differential regulation of endogenous nitric oxide, IL-6, prostaglandin E2, and IL-8. *Proc. Assoc. Am. Physicians* 110: 65–72.

397. Pfander, D., N. Heinz, P. Rothe, H.-D. Carl, and B. Swoboda. 2004. Tenascin and aggrecan expression by articular chondrocytes is influenced by interleukin 1beta: a possible explanation for the changes in matrix synthesis during osteoarthritis. *Ann. Rheum. Dis.* 63: 240–244.

398. Coll, R. C., A. a B. Robertson, J. J. Chae, S. C. Higgins, R. Muñoz-Planillo, M. C. Inserra, I. Vetter, L. S. Dungan, B. G. Monks, A. Stutz, D. E. Croker, M. S. Butler, M.

Haneklaus, C. E. Sutton, G. Núñez, E. Latz, D. L. Kastner, K. H. G. Mills, S. L. Masters, K. Schroder, M. a Cooper, and L. a J. O'Neill. 2015. A small-molecule inhibitor of the NLRP3 inflammasome for the treatment of inflammatory diseases. *Nat. Med.* 21: 248–55.

399. Sridharan, R., A. R. Cameron, D. J. Kelly, C. J. Kearney, and F. J. O'Brien. 2015. Biomaterial based modulation of macrophage polarization: a review and suggested design principles. *Mater. Today* 18: 313–325.

400. Mahon, O. R., and A. Dunne. 2018. Disease-associated particulates and joint inflammation; mechanistic insights and potential therapeutic targets. *Front. Immunol.* 9.

401. Wang, Y., J. Bao, X. Wu, Q. Wu, Y. Li, Y. Zhou, L. Li, and H. Bu. 2016. Genipin crosslinking reduced the immunogenicity of xenogeneic decellularized porcine whole-liver matrices through regulation of immune cell proliferation and polarization. *Sci. Rep.* 6: 24779.

402. Reeves, A. R. D., K. L. Spiller, D. O. Freytes, G. Vunjak-Novakovic, and D. L. Kaplan. 2015. Controlled release of cytokines using silk-biomaterials for macrophage polarization. *Biomaterials* 73: 272–283.

403. Kumar, M., J. Coburn, D. L. Kaplan, and B. B. Mandal. 2016. Immuno-Informed 3D Silk Biomaterials for Tailoring Biological Responses. *ACS Appl. Mater. Interfaces* 8: 29310–29322.

Appendix

1. Flow Cytometry gating strategies

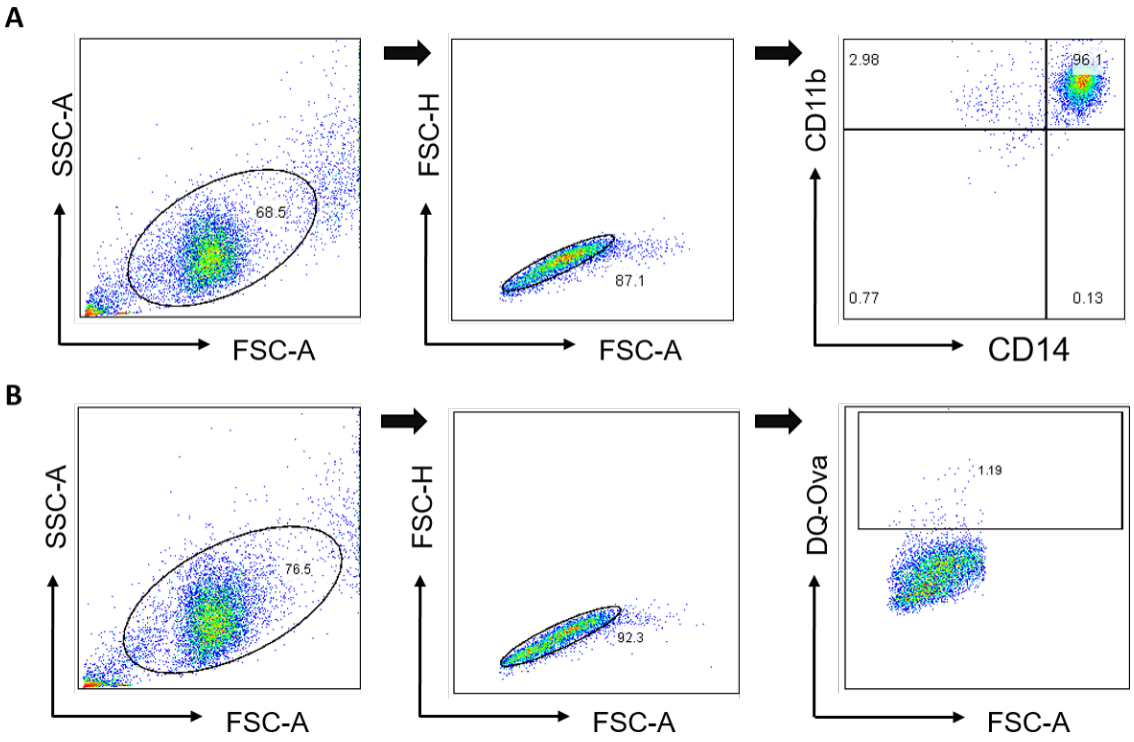

Figure app.1.1: Flow cytometry gating strategy for antigen uptake assays. (A) To assess expression of the maturation markers CD40, CD80 and CD86 by macrophages, the macrophage population was first selected by FSC and SSC. Single cells were then gated on by FSC area and height. Viable cells were then selected on the basis of viability dye exclusion. Fully differentiated macrophages were selected for by co-expression of CD14 and CD11b. **(B)** To measure DQ -Ova uptake, the macrophage population was first selected on the basis of FSC and SSC in order to exclude debris and dying cells. Single cells were then selected based on FSC area and height. The DQ-Ova+ cell gate was then drawn using control cells which were not incubated with DQ-Ova.

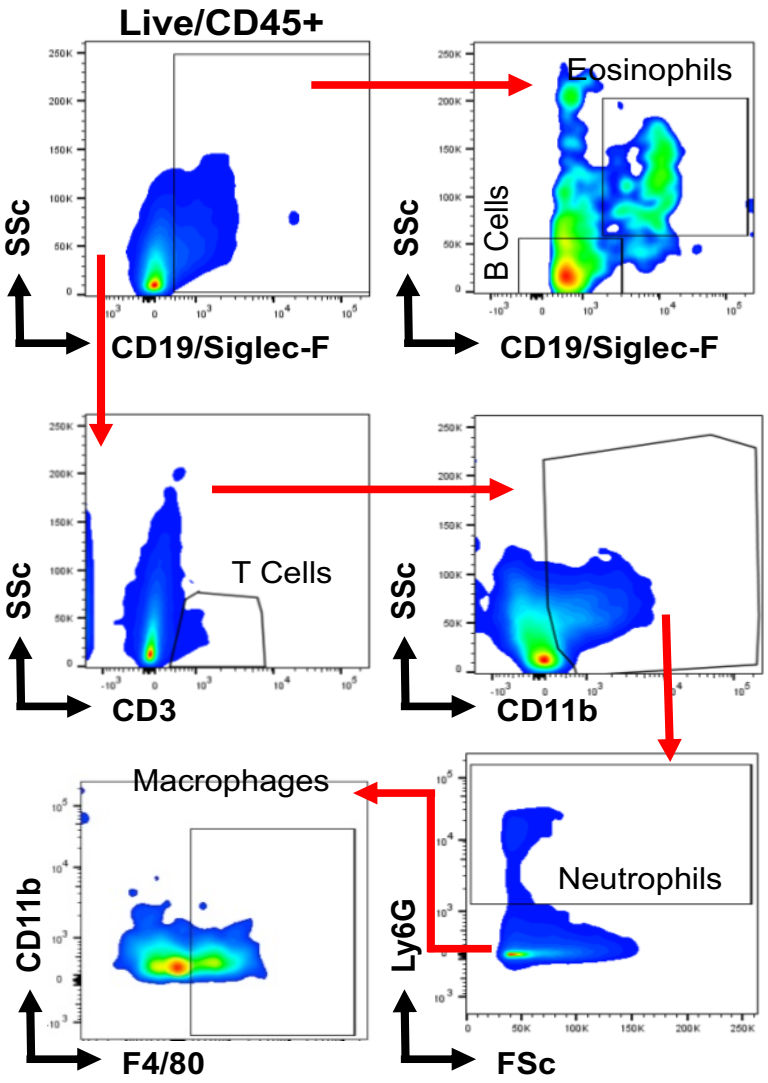

Figure app.1.2. Gating strategy for immune cell populations. Cells generated by digest of the tissue were antibody stained and analysed by flow cytometry. Firstly, live/CD45+ immune cells were selected and basophils and eosinophils were gated on based on CD19/Siglec F expression. T cells were then selected for on the basis of their SSC area and CD3 expression. Total CD11b population was gated on and neutrophils were selected on their LY6G expression. Finally, CD11b/F4/80 double positive cells were selected as the macrophage population.

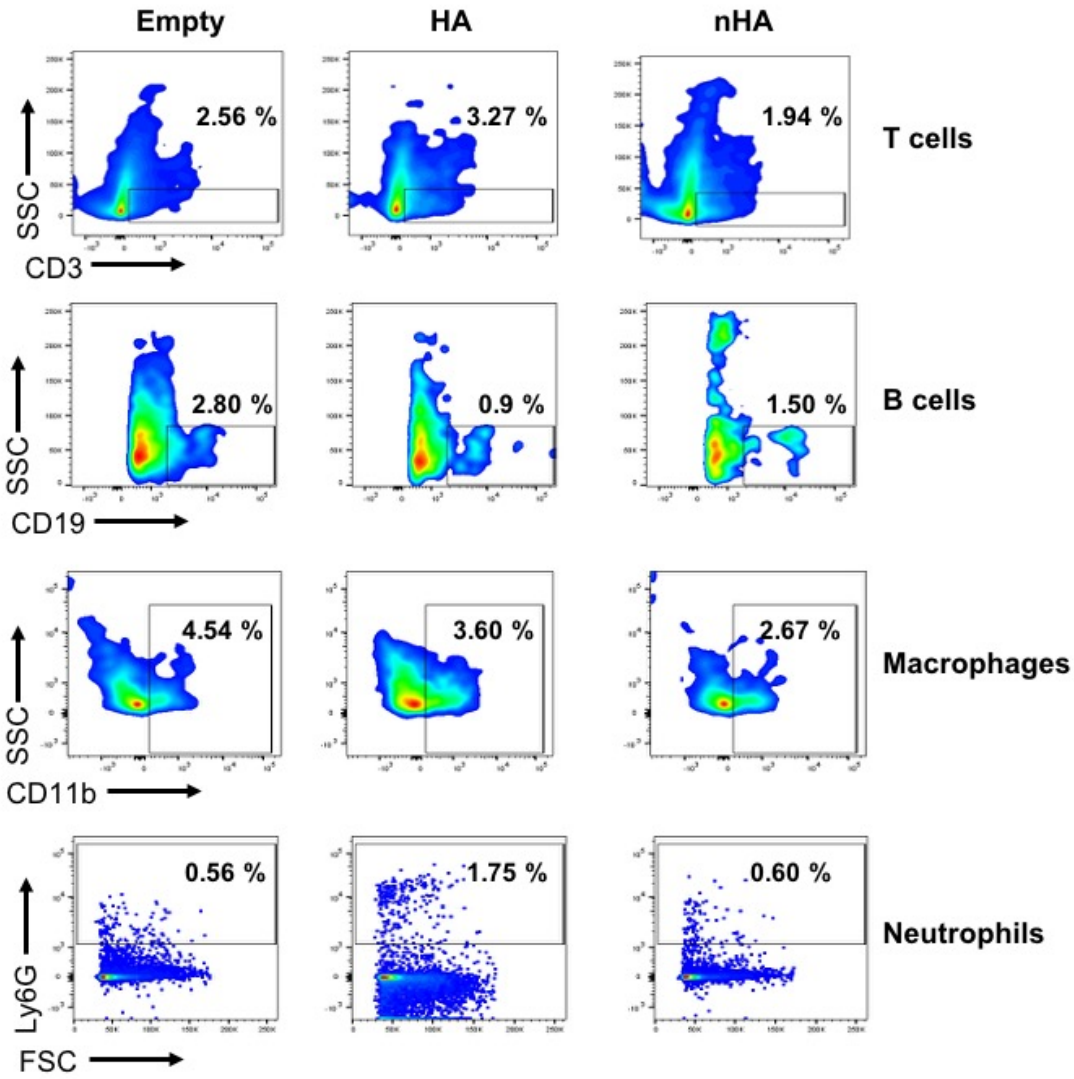

Figure app.1.3. Cell populations at defect site. Cells generated by digest of the tissue were antibody stained and analysed by flow cytometry. Representative dot plots of individual cell subsets for each implant group with average percentage for n=5 rats. Gating strategy in Figure app.1.2

2. Assesment of inhibitors and vehicle controls on pro-inflammatory macrophage profile

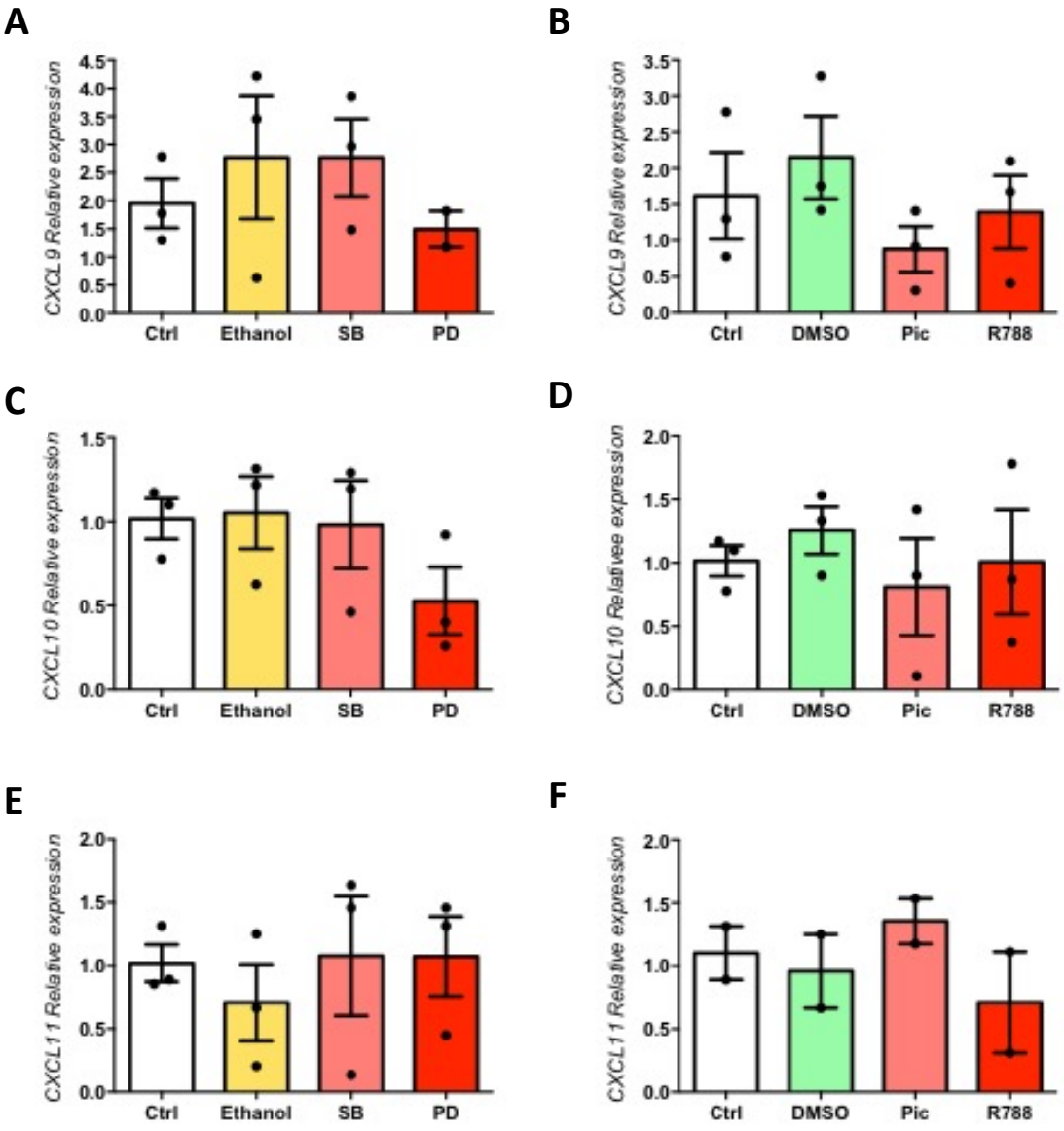

Figure app.2. Effect of inhibitors and vehicle controls alone on macrophage pro-inflammatory profile. Primary human macrophages (1 x 10^6 cells/ml) were stimulated with SB203580, PD98059 (both 20 µM) or ethanol **(A, C & E)** or Piceatannol (20 µM), R788 (25 µM) or DMSO **(B, D, F)** for 24 hours. mRNA levels of **(A & B)** CXCL9, **(C & D)** CXCL10 and **(E & F)** CXCL11 were analysed by real-time PCR. mRNA concentration was normalised to the housekeeping gene 18s ribosomal RNA. Gene expression, relative to untreated control cells, was determined using the $2^{-\Delta\Delta CT}$ algorithm. Pooled data (n=2-3) is represented as mean ± SEM. Data was analysed using one-way ANOVA with Tukey post-test.

3. Assesment of endotoxin levels in partilce preparations

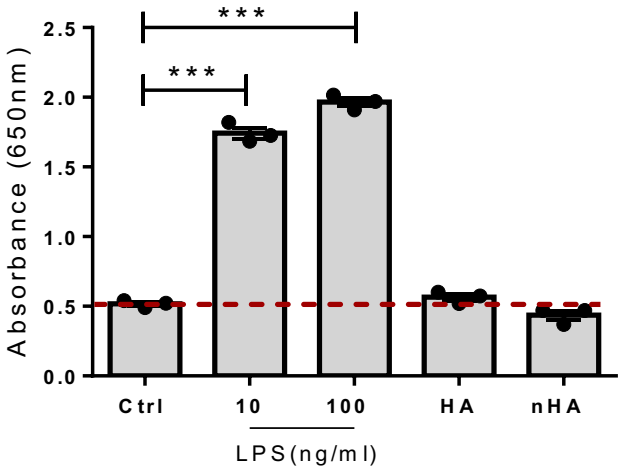

Figure app.3. Analysis of endotoxin levels in micron and nanoHA preparations. Both micron and nano Hydroxyapatite particle preparations were shown to be endotoxin free, using the HEK-Blue^{TM} hTLR4 assay system (Invivogen). The expression of SEAP, as measured by absorbance at 650nm, by particle treated macrophages was comparable to untreated control cells. As a positive control, cells were treated with LPS (10 ng/ml or 100 ng/ml). Data (n=3) is represented as mean ± SEM was analysed using one-way ANOVA with Tukey post-test (****p<0.0001 vs untreated control).

4. Proteomic analysis of ECM tissue

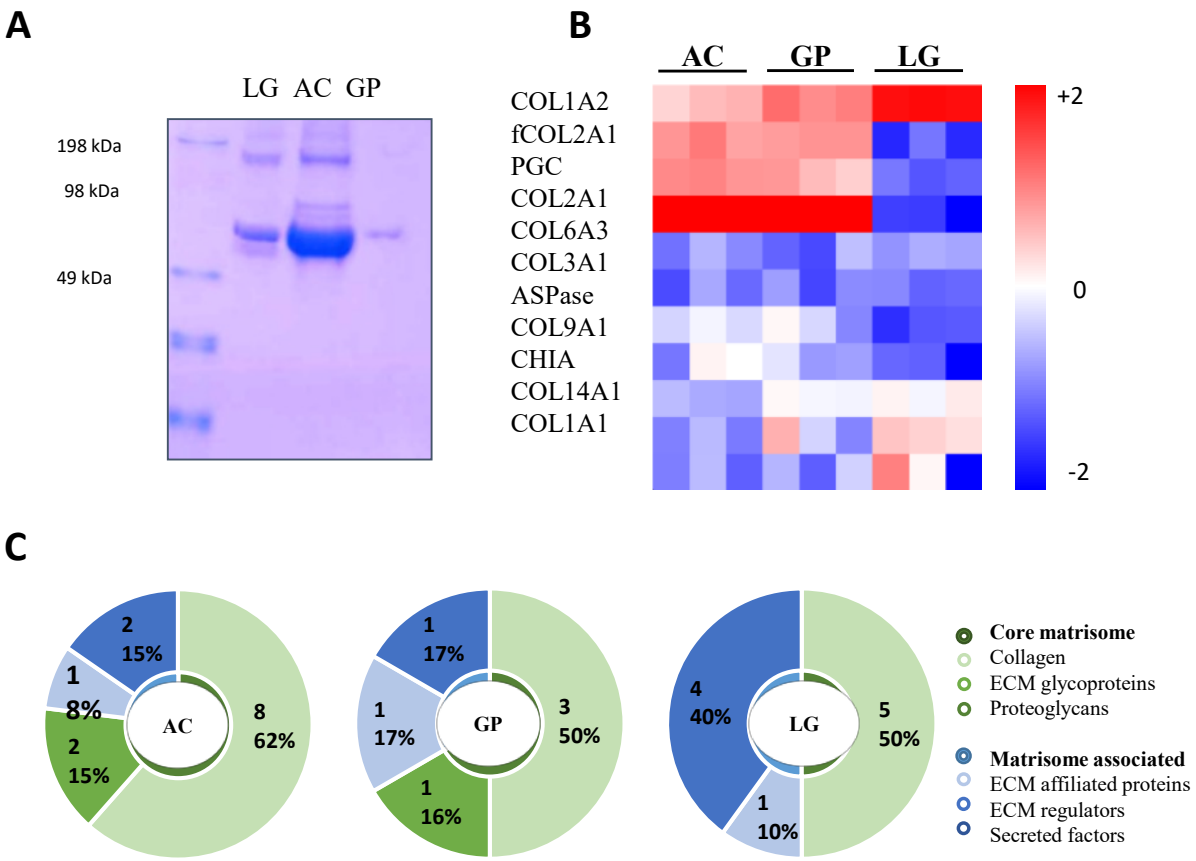

Figure app.4. Relative abundance of functional proteins in articular cartilage (AC), growth plate (GP) and ligament (LG) tissue. (A) Coomassie stained gel of solubilised AC, GP and LG. **(B)** Heat map pf solubilised AC, GP and LG**. (C)** Bioinformatics analysis and filtering through Matrisome Database |(DB).

5. Inflammatory profile of AC or GP ECM scaffolds in rat femoral defect

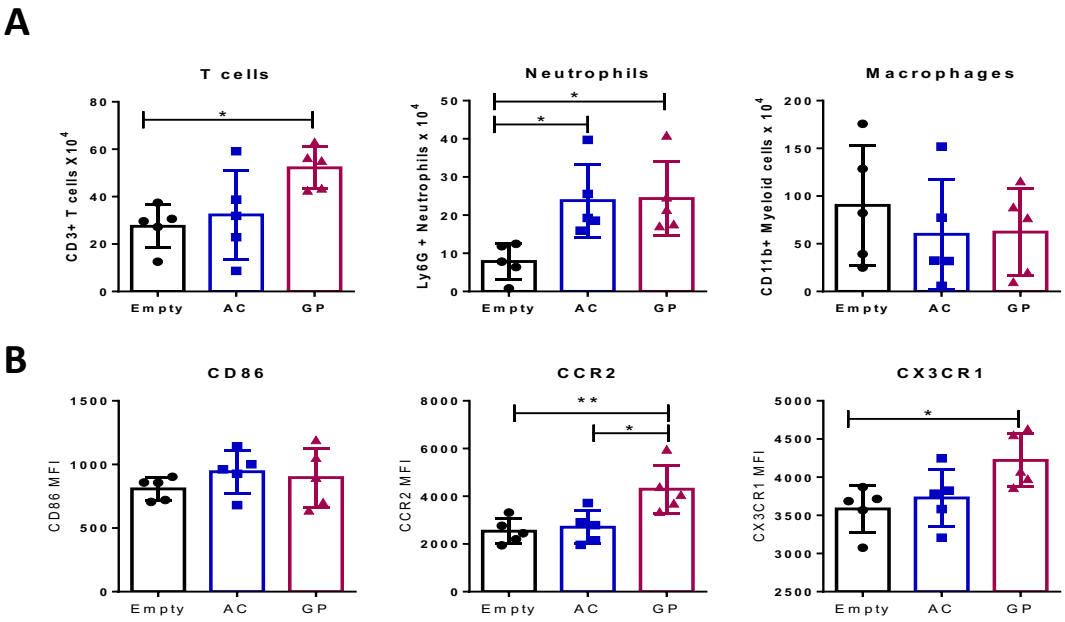

Figure app.5. Characterization of immune cell subsets and phenotype following implantation of AC or GP ECM scaffolds into a rat femoral defect model. (A) Flow cytometric analysis of immune cell subsets within the defect site 1 week after implantation. **(B)** Analysis of macrophage population at defect site expressing CCR2, CD86, and CX3CR1. Statistical differences on n=5 rats were assessed using Kruskal Wallis test with Dunn's post-test, *p<0.05, **p<0.01.